Universitat de València

Facultat de Física

Departament de Física Atòmica, Molecular i Nuclear

Irradiated Silicon Detectors for HL-LHC: Characterization and Simulations

TESIS DOCTORAL PRESENTADA POR

Mercedes Miñano Moya

2012

El Dr. SALVADOR MARTÍ GARCÍA, Científico Titular del Consejo Superior de Investigaciones Científicas (CSIC) destinado en el Instituto de Física Corpuscular (IFIC)

CERTIFICA:

Que la presente memoria, "***Irradiated Silicon Detectors for HL-LHC: Characterization and Simulations***", ha sido realizada bajo mi dirección en el Departamento de Física Atómica, Molecular y Nuclear de la Universidad de Valencia por Mercedes Miñano Moya y constituye su tesis para optar al grado de doctor en Física por la Universidad de Valencia.

Y para que así conste, en cumplimiento de la legislación vigente, firmo el presente Certificado en Burjassot a de de 20 .

Dr. Salvador Martí García

Declaration

This dissertation is the result of my own work, except where explicit reference is made to the work of others, and has not been submitted for another qualification to this or any other university.

Mercedes Miñano Moya

Desmayarse, atreverse, estar furioso,
áspero, tierno, liberal, esquivo,
alentado, mortal, difunto, vivo,
leal, traidor, cobarde y animoso;

no hallar fuera del bien centro y reposo,
mostrarse alegre, triste, humilde, altivo,
enojado, valiente, fugitivo,
satisfecho, ofendido, receloso;

huir el rostro al claro desengaño,
beber veneno por licor suave,
olvidar el provecho, amar el daño;

creer que un cielo en un infierno cabe,
dar la vida y el alma a un desengaño;
ésto es amor, quien lo probó lo sabe.

Lope de Vega

Contents

Preface

The excellent LHC performance in 2010 and 2011 has brought hints of new physics, notably narrowing the range of masses available to the Higgs particle to a window of just 16 GeV. Within this window, both the ATLAS and CMS experiments have seen hints that a Higgs might exist in the mass range 124-126 GeV. However, to turn those hints into a discovery, or to rule out the Standard Model Higgs particle altogether, requires one more years worth of data. During 2012, the machine will be running at a collision energy of 8 TeV. The bunch spacing remains at 50 ns. The data target is 15 fb^{-1} throughout this year for ATLAS (and CMS), three times larger the total untill now. Then a long shutdown will be taken for around 18 months in order to prepare operation at its full design collision energy of 14 TeV reaching the nominal luminosity of $1 \times 10^{34}\ cm^{-2}\ s^{-1}$. It has been proposed a high luminosity upgrade of the LHC for the next decade (the HL-LHC Project), so it can not be left behind the research activity on the sub-detectors to withstand much higher instantaneous luminosity and to operate after 3000 fb^{-1} of integrated data. The goal is to achieve the same or better performance at the HL-LHC as at the LHC, despite the large increase in event rate and final integrated dose.

This thesis is focused on the development of silicon microstrip detectors enough radiation hard to cope with the particle fluence expected at the ATLAS Inner Detector region under HL-LHC conditions that imply total fluences of fast hadrons above $10^{16}\ cm^{-2}$. The work is framed on the CERN RD50 Collaboration which proposes to develop a semiconductor detector technology that can operate beyond the limits of present devices under environments as for example the described above.

Following a short review in chapter 1 of the Standard Model which is the actual theory that describes elementary particles and their interactions, the physics accessible with the Large Hadron Collider including the search of the Higgs boson and the motivations to go beyond are given. In chapter 2 a general description of the LHC facilities at CERN is shown. The experiments around the machine are presented, focusing on the ATLAS Tracker. Furthermore, in this chapter both the expected physics and the machine plans for HL-LHC are related. A more detailed description of the upgrade concerning ATLAS and particularly the Inner Detector is found. Finally, in the chapter 2 the main objectives of the CERN RD50 Collaboration are listed.

The semiconductor physics concerning silicon detectors is treated in chapter 3. First, the basic concepts required to understand the operating principles of silicon detectors are explained. This covers topics as the *Band Theory* or the pn-junction. Secondly, the main structural features of silicon microstrip detectors are described followed by the processes by which the signal is created and collected. The chapter ends with the discussion of the spatial resolution required

to these sensitive position detectors and the sources of noise involved in the signal acquisition. Since due to the ATLAS Inner Detector will face the harsher radiation environment, a description of the basic radiation mechanisms in silicon detectors is also given in chapter 4.

In chapter 5, the ISE-TCAD software package used to carried out semiconductor device simulations is presented. Every stage in a simulation project is explained, starting with the device generator, the device simulation and analysis of the results obtained by TCAD tools. A second part of this chapter develops simulations of a simplified two dimensional silicon microstrip sensor in order to find a model that describes a real silicon sensor as accurate as possible. Chapter 6 describes the experimental procedures for the electrical characterization of silicon microstrip detectors and the readout acquisition systems in order to performance charge collection measurements. It is presented the Alibava acquisition system. This new analogue readout system for microstrip silicon sensors was developed as a result of a collaboration between the University of Liverpool, CNM (Barcelona) and IFIC (Valencia) and this thesis presents one of the first work plan using the Alibava acquisiton system. Finally, in this chapter, a description of the irradiation facilities is also given.

p-Type silicon microstrip sensors have been showing a promising performance under high radiation environments. Chapters 7 is devoted to present the results from the characterization of p-type silicon microstrip detectors irradiated at the expected fluences for the strip region of the ATLAS Inner Detector upgrade. The validation of sensor samples from different manufacturers are covered in terms of charge collection efficiency and signal to noise ratio. Different sensor parameters has been also compared and any potential issue has been discussed in order to find the most appropiate properties which better face with radiation.

The second part of this thesis that corresponds to the chapter 8, concerns studies of the effect of very high instantaneous ionization in a microstrip silicon detector. It is considered a n-type silicon sensor, the current detector technology fot the ATLAS SCT, with the objective to apply the results to a possible beam loss scenario under the operating conditions at LHC.

The final chapter, number 9, contains all the conclusions reached in this thesis.

Chapter 1

Theoretical Physics Motivations

The Standard Model [1] is the theoretical framework that provides the most accurate description of the interactions among elementary particles. It has been incredibly successful in explaining most particle physics measurements. There is, however, one missing ingredient to this recipe that has not been yet discovered and that is the Higgs boson. Despite the experimental success of the Standard Model, there are some aspects which are not fully satisfactory. For instance, it contains no treatment of gravity or general relativity nor it includes any mathematical mechanism to solve the hierarchy problem. The LHC has a rich physics potential, ranging for more precise measurements of Standard Model Parameters including the search of the elusive Higgs boson to the search for new physics phenomena.

1.1 Standard Model Review

The Standard Model (SM) is a highly successful theory that describes how the elementary particles interact. This model has been able to describe results obtained at previous experiments up to energies of around 200 *GeV* [2] but it is not a complete description of observed physical phenomena. The Standard Model is a quantum field theory consistent with quantum mechanics and the special theory of relativity.

According to the SM, the matter constituents are pointlike particles of spin 1/2 (fermions). Moreover, each particle has an antimatter counterpart with exactly the same properties except the electric charge (which has an opposite sign). In addition to the electric charge, all the particles of matter may carry as well a color charge (for the strong interaction) and an isospin charge (for the weak interaction). These charges are the responsible of the particle interactions which in the SM happen via exchange of gauge particles of spin 1 (bosons) [1]. One of the merits of the SM is to unify the electromagnetic, nuclear weak and strong interactions under the same framework. Thus the SM is a gauge theory based on the $\mathrm{SU}_C(3) \otimes \mathrm{SU}_L(2) \otimes U_Y(1)$ symmetry group.

The SM can be described by three types of fields, the matter field, which corresponds to the

[1] Gravity, the fourth interaction, is not contained in the SM and is extremely weak when compared to the other interactions at these energy scales.

	1st generation	2nd generation	3rd generation
Quarks	u (up)	c (charm)	t (top)
	charge:+2/3	charge:+2/3	charge:+2/3
	d (down)	s (strange)	b (bottom)
	charge:−1/3	charge:−1/3	charge:−1/3
Leptons	e^- (electron)	μ^- (muon)	τ^- (tau)
	charge:-1	charge:-1	charge:-1
	ν_e (e^- neutrino)	ν_μ (μ^- neutrino)	ν_τ (τ^- neutrino)

Table 1.1: The fundamental matter particles of the Standard Model. Particles are grouped in generations according to the increasing mass of the particles. It is noted that only the 1st generation, i.e. *(u, d)* and *(e, ν_e)* are found in ordinary matter.

	Theory	Coupling constant	Range [m]	Mass [GeV/c^2]
γ (photon)	QED	$\alpha = 1/137$	∞	0
Z^0, $W^\pm$	electroweak	$G_F\, m_p \approx 10^{-5}$	10^{-18}	91.2, 80.2
g_i (gluons)	QCD	$\alpha_s \approx 1$	10^{-15}	0
G (Graviton)	-	$G\, m_p \approx 10^{-39}$	∞	0

Table 1.2: The gauge bosons (force carriers) of the Standard Model.

fermionic leptons and quarks summarised in Table 1.1; the gauge fields, from which the gauge bosons appear and the Higgs scalar fields, which explain the generation of particles and gauge bosons (Z and W) masses. The gauge bosons are 8 massless gluons for the strong interaction, 1 massless photon for the electromagnetic interaction and 3 massive bosons, Z and $W^\pm$ for the weak interaction as summarised in Table 1.2.

The weak interaction can be unified with the electromagnetic interaction into the electroweak interaction (EW) [3]. The EW theory predicts the existence of 4 physical vector bosons (γ, Z and $W^\pm$). A theoretical prediction is that they are massless but the vector bosons for the weak interaction (Z and $W^\pm$) were experimentally found to be massive. For the model to allow for massive gauge bosons, an additional scalar field that breaks the electroweak symmetry has to be introduced. This is called spontaneous symmetry breaking [4]. The scalar field will not only provide masses for the gauge bosons but also predicts an additional scalar particle, the Higgs boson [5]. The fermionic particles couple to the Higgs field to obtain mass.

Hadron is the name of a non-elementary particle which is built of quarks held together by the strong force. Moreover, the hadrons are sub-classified in *baryons* and *mesons* depending if they are formed by $3q$ or $q\overline{q}$, respectively. Mathematically, quarks are triplets of the $SU_C(3)$ gauge group and it has been mentioned they carry color charges which are responsible for their participation in the strong interaction (Quantum ChromoDynamics theory, QCD). The 8 massless gluons mediate this interaction and they carry color charges themselves (thus self-interacting) and they are supposed to be massless within the SM. On one hand, quarks are never observed freely, they are always confined in bound states (i.e. in hadrons since they are color singlets). This property is known as *color confinement*. It is due to the fact that gluons, that are color

charged, interact with each other, leading to an increase of the strong coupling constant (α_S) at large distances. On the other hand, at small distances (i.e. high energy) the strong coupling constant decreases and therefore quarks and gluons can be understood as free particles with the so-called property *asymptotic freedom*. In that freedom state, quarks can exchange gluons which can produce additional $q\overline{q}$ pairs. Finally, the interaction between all these quarks and gluons can produce collimated groups of hadrons in the direction of the parent quark (so-called jets).

1.2 The search of the Higgs boson

The Higgs particle predicted by the model remains to be discovered at the time of writing. However, several theoretical arguments strongly indicate that if the Higgs boson exits, it could be discovered at the LHC.

One of the main topics at LHC (at the ATLAS and CMS experiments) is the search of the last missing piece of the Standard Model: The Higgs boson. Its mass is not predicted by the theory. If the SM has to remain a viable effective theory up to the Planck energy scale ($\Lambda_P \sim 10^{19}\ GeV$) and the Higgs mechanism is valid, the Higgs boson mass must lie in the narrow interval of 130-180 GeV/c^2. The lower and upper bounds with respect to the energy scale are plotted in Fig. 1.1. For energy scales(Λ) $\sim 1\ TeV$, the Higgs mass is constrained to lie in the range $50\ GeV < m_H < 800\ GeV/c^2$. The LHC will be able to explore the Higgs mass range up to $1\ TeV/c^2$.

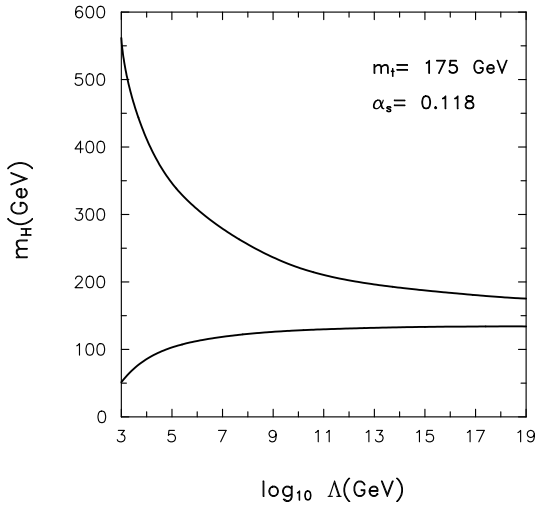

Figure 1.1: The predicted bounds from theory as a function of the energy scale Λ. The top quark mass is taken to be $m_t = 175\ GeV/c^2$. From a small window of Higgs masses around $160\ GeV/c^2$ the Standard Model is valid to the Planck scale ($\approx 10^{19}\ GeV$). For other values of the Higgs mass the Standard Model is only an effective theory at low energy and new physics has to set in at some scale Λ (from [6])

.

All LEP experiments have searched for the SM Higgs boson with together 2465 pb^{-1} of e^+e^- data untill energies of 209 GeV/c^2. At these energies the Higgs boson mass is expected to be produced mainly in association with a Z boson through the annihilation of an electron and a positron as shown in Fig. 1.2. The direct search of the Higgs boson has only provided a lower bound on its mass, $m_H > 114\ GeV/c^2$ (95% C.L.), resulting from the exclusion of the kinematical range accesible to the accelerator. A global fit to all electroweak data [7] leads to a Higgs mass close to the lower limit and an upper limit of $\sim 200\ GeV/c^2$, (95% C.L.).

In addition, Tevatron increased the exclusion range of the mass for the Higgs of 158-175 GeV/c^2 [8]. As due to the fits of all Standard Model parameters, a light Higgs boson is preferred. A mass of the Higgs boson, $m_H > 175\ GeV$ has a much lower probability than the range $114\ GeV < m_H < 158\ GeV$. Including the ATLAS and CMS combination data up to half of 2011, the presence of the standard model Higgs is excluded in the mass range 141-476 GeV/c^2 at > 95% C.L.. Indeed, the region from 146 to 443 GeV is excluded at 99% C.L.. These limits for the Higgs mass are recopilated to Fig. 1.3.

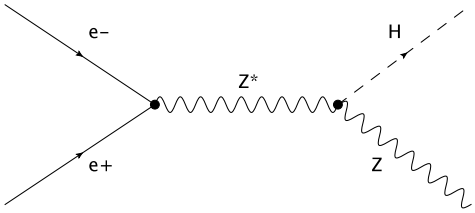

Figure 1.2: In this Feynman diagram, an electron and a positron annihilate, producing a virtual Z boson that becomes a Z boson and a Higgs boson. This process is called Higgs-strahlung and it is the dominant production process for a standard model Higgs.

Higher order corrections to the electroweak observables are in most cases dependent on the Higgs boson mass. Precise electroweak measurements performed at LEP are accurate enough to be sensitive to the mass of the Higgs boson through these radiative corrections. It results in a theoretical limit of $M_H \leq 212\ GeV/c^2$ [9]. The SM will not be able to survive without modifications if the Higgs mass is above 1TeV.

The searh for the Standard Model Higgs boson has been used as a benchmark to establish the performance of important systems of the LHC experiments. They are designed to cover the different signatures of the Higgs boson, consisting in the identification of the predicted decay modes and production mechanisms, with statistical significance over all the mass range as presented in figure 1.4.

At low masses ($m_H < 2m_Z$), the Higgs width would be a few MeV, and so the observed width would be defined by the instrumental resolution. The predominant decay mode would be into hadrons ($H \rightarrow b\bar{b}$) with a branching ratio of ~ 90 % but with the constraint to detect the channel due to large QCD two-jet backgrounds. The significance of the $H \rightarrow b\bar{b}$ can be increased with the associated production of the Higgs with a W or Z or a $t\bar{t}$ pair but these channels have smaller cross sections. A cleaner decay mode would be $H \rightarrow \gamma\gamma$. The branching ratio is small, $O\ (10^{-3})$ and this decay mode is observable over a limited Higgs mass region, between 80 and 150 GeV/c^2. The signal detection in this channel requires the rejection of the large backgrounds

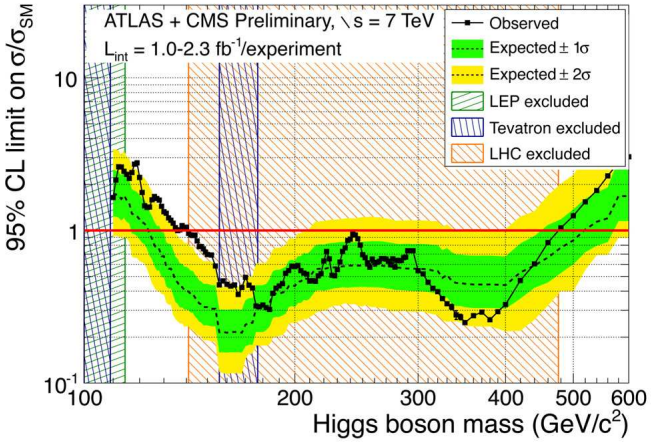

Figure 1.3: Experimental limits from the LHC on standard model Higgs production in the mass range 100-600 GeV. The solid curve reflects the observed experimental limits for the production of Higgs of each possible mass value (horizontal axis). The region for which the solid curve is below the horizontal line at the value of 1 is excluded with a 95% confidence level (CL). The dashed curve shows the expected limit in the absence of the Higgs boson, based on simulations. The green and yellow bands correspond, respectively to 68%, and 95% confidence level regions from the expected limits. The hatched regions show the exclusions from the searches at the different colliders. *Results from november 2011*.

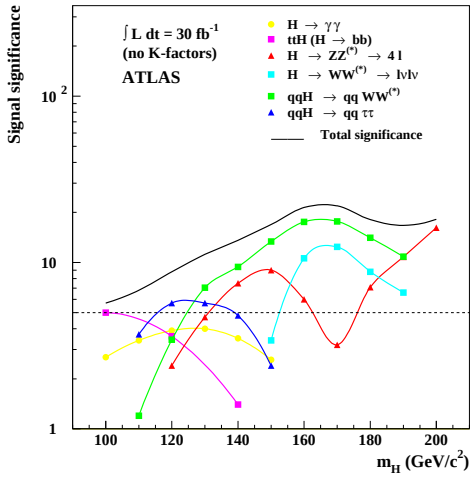

Figure 1.4: Signal significance of the various SM-Higgs discovery channels as well as for the combination of channels, after one year or 100 fb^{-1} (from [10]).

from the $\gamma\gamma$ continuum production and the two photon decay mode of the neutral pions $\pi^0 \rightarrow \gamma\gamma$.

In the intermediate Higgs mass region, $m_H > 150\,GeV/c^2$, the channel, $H \rightarrow ZZ \rightarrow llll$, where each Z decays to a pair oppositely charged leptons provides a very clean signature. Below the ZZ production threshold, one of the Z bosons is virtual and the mass can not be used as a constraint. Nevertheless, the signal provided by the decay channel $H \rightarrow ZZ^* \rightarrow llll$ can still be observed with large significance. Also, $H \rightarrow WW^* \rightarrow l\nu l\nu$ would provide a experimentally clean channel to study the properties of the Higgs boson.

For large masses, $m_H > 600\,GeV$, the decay modes $H \rightarrow WW \rightarrow l\nu jj$ (where j stands for jet) and $H \rightarrow ZZ \rightarrow ll\nu\nu$ are the only possible signatures. The rates for those remain high, since all three flavours of neutrino are available.

1.3 Limitations of the Standard Model

The SM appears as a successful theory describing the strong and electroweak interactions of elementary particles. The status of experimental measurements in particle physics are in good agreement with the SM predictions. Nevertheless there is still some issues unresolved within SM which can point to beyond SM Physics at the TeV or higher scales.

Some of the deficiencies in the SM are enumerated below.

1. **Grand Unification**. The SM does not unify the strong and EW forces. Although the strong interaction is described by the SM, it is not as good described as the EW force. Is the Grand Unifying Theory (GUT) that really unifies these forces [11]. But this theory had also experimental problems because GUTs allow proton decays and its lifetime depends on the GUT scale. Very precise experiments have put lower limits on the proton lifetime and up to now no proton decays has been observed, implying that at least the proton lifetime is longer than the one predicted by GUT. Furthermore, gravity is not included. Thus, new theories should be proposed.

2. **Renormalization**. A reasonable theory for physics should not produce any infinites for measurable quantities. As the SM is renormalizable, infinites on measurable quantities can be absorved into non-measurable quantities. So that, all quantities predicted by the theory are well defined and have a finite value. This leads to the fact, that these quantities depend on the energy scale at which they are measured. Therefore, the interaction coupling constants, which set the strength for the interactions, present the so-called *running coupling constants* [12]. This principle applies to the coupling constants of the SM as well as to masses. As the three coupling constants (electromagnetic, weak and strong) are all running, one could assume that they all cross at one point and are unified there. But this is not the case for SM as seen in Fig. 1.5(a). However, with some possible extensions of the SM such as the minimal supersymmetric standard model (MSSM) [12], with particles of masses around 1 TeV, an unification of the three forces of the SM is possible as seen in Fig. 1.5(b).

3. **Hierarchy problem**. It is related to the huge gap between two fundamental scales of

physics: the EW scale ($\Lambda_{EW} \sim 10^2\ GeV$) and the Planck scale ($\Lambda_P \sim 10^{19}\ GeV$) where the gravitacional interaction becomes important.

One of the consequences is that if no new physics exists between these two scales, and therefore the SM is valid up to the Planck mass, then the Higgs mass diverges, unless it is unnaturally tuned. The observable Higgs mass is composed of a bare mass (M_{H0}) and radiative corrections (δM_H) and the correct physical value M_H may be obtained as:

$$M_H^2 \sim M_{H0}^2 + \delta M_H^2 \tag{1.1}$$

The leading term of the radiative corrections is quadratically dependent on the coupling constant of the corresponding interaction and thus on the energy scale. This can be associated to the GUT scale ($\Lambda_{GUT} \sim 10^{16}\ GeV$) in order to be consistent with a relatively light Higgs boson ($M_H < 1\ TeV/c^2$). So that, the value M_{H0}^2 is required to be accurate in one part in 10^{16} in order to compensate the divergent corrections. This problem, which is known as the *fine tunning* problem of the SM, is still unresolved within the SM context.

If this large difference between the only fundamental energy scale in nature and the energy scale of the Higgs mass (and of the rest of the elementary particles in general) exits, the SM can be considered as a low-energy effective theory of a more general unified theory, where the lower energy scale would follow from symmetry breaking processes implied and described in the theory. Anyhow, the hierarchy problem indicates that the SM is incomplete at the TeV scale where the LHC will be able to explore, and therefore new physics should either stabilize the Higgs mass, or if the Higgs does not exist, provide mass to the weak gauge bosons by some other yet unknown mechanism. Both posibilities will of course be known at the same time once this energy range is explored.

4. **The fermion mass hierarchy problem**. Beyond the ordinarily observed matter content that can be constituted by the following fermions (ν_e, e^-, u, d), the measurements have confirmed the existence of ≥ 3 families: (ν_μ, μ^-, c, s) and (ν_τ, τ^-, t, b) are heavier copies of the first family with no obvious explanation in the SM. The SM gives no prediction for the number of fermion generations. Furthermore, there is no explanation or prediction of their masses, which are observed to have hierarchical pattern spanning over 6 orders of magnitude between the top quark and the electron. Even more mysterious are the neutrinos, which are lighter still by many orders of magnitude.

5. **Neutrino masses**. The neutrinos are massless particles in the SM. However, from different experiments it is known that these particles have masses. The new models have to explain this fact.

6. **Cosmological consideration**. It is theorized that the baryon matter density is ~ 4 %. The rest of the universe is made up of ~ 24 % dark matter and ~ 72 % dark energy [13]. SM neither provides any explanation for dark energy nor it has a suitable dark matter candidate. Similarly, the observed asymmetry between matter and anti-matter in the universe can not be explained within the framework of the SM.

1.4 Beyond Standard Model

Some of the above mentioned problems could be solved with the help of the theoretical extensions of the SM. Ambitious examples of these models are Supersymmetry or Extra dimensions that are described detailed in the next sections. However, there are other important models. The 2 Higgs-Doublet Models (2HDM) are one of the simplest possible extensions of the SM that includes enlargement of the scalar sector, a 4th generation of fermions, Baryogenesis (it could provide an explanation for the matter-antimatter asymmetry of the universe) and Dark matter (in the case of the *inert higgs doublet model*, for instance). A complete review of these models can be found in the reference [14]. All these theories will be subjected of extensive searches at the LHC.

1.4.1 Supersymmetry

An extension of the SM is the supersymmetry [15]. The simplest supersymmetric extension of the SM is the Minimal Supersymmetric Model (MSSM) [12]. This gauge theory assumes that every particle on the SM would have its own superpartner with the same quantum numbers but with the spin differing by $1/2$ (each fermion has a bosonic counterpart, the squarks and sleptons, and the bosons have fermionic superpartners called gluinos and gauginos). It implies the discovery, identification and the study of a whole new spectrum of particles, including no less than 5 Higgs particles. The entire parameter space of the MSSM can be studied at LHC.

All superpartners would be degenerated in mass with the ordinary particles if supersymmetry was not broken. This breaking leads to the superpartners acquire large masses. The possibility of supersymmetric extension of the SM relies on strong arguments derived from theory. SUSY would lead to the solving of the different unexplained issues regarding the SM exposed above. Within SUSY, the unification of the gauge couplings for the strong, weak, and electromagnetic interactions is possible at the GUT energy scale (see Figure 1.5). The supersymmetric particles effectively contribute to the running of the coupling constants for energies above the typical SUSY mass scale.

Adding the supersymmetric partner particles leads to radiative corrections which cancel the quadratically divergent terms of the Higgs mass, hereby solving the *fine tunning* problem of the SM.

Another issue which remains still unresolved is the *dark matter* in the universe. Most of the missing dark matter is suggested to be in the form of non-relativistic cold dark matter, consisting in weakly interactive massive particles (WIMPs). The decays of supersymmetric particles, such as squarks and gluinos, would involve cascades which always contain a neutralino (χ^0), the lightest neutral weakly-interacting supersymmetric particle. Supersymmetry provides the χ^0 as a perfect candidate for cold dark matter. It is considered to be stable in the MSSM and hence expected to exist in the universe today. As the χ^0 would interact very weakly with the detector, the experiment would measure a significant missing transverse energy, E_T^{miss}, in the final state. The rest of the cascade would result in a number of leptons and jets.

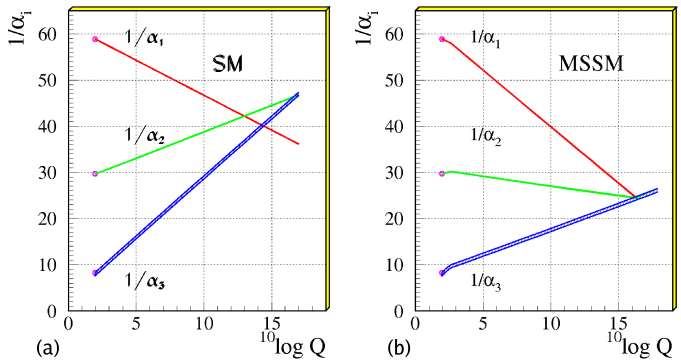

Figure 1.5: Running coupling constants of the three Standard Model interactions. It is shown the inverse of the three Standard Model couplings α_i with i =1, 2, and 3 for the $U(1)_Y$, $SU(2)_L$ and $SU(3)_C$ symmetry groups respectively as a function of the sliding scale Q (in GeV) in (a) for the Standard Model and in (b) for the minimal supersymmetric extension of the Standard Model (MSSM). The gauge couplings meet almost exactly in one point, somewhere around 10^{16} *GeV*, usually referred to as the GUT scale (Gran Unification Theory).

1.4.2 Extra dimensions theories

Several new models propose the existence of extra dimensions [16] leading to a characteristic energy scale of quantum gravity in the TeV region and therefore, solving the hierarchy problem. Extra dimensions models add more space dimensions on top of the usual three spatial dimensions. In these theories, the SM fields are confined to a 4-dimensional manifold, while gravity can propagate through all the dimensions. Then, the observed weakness of the gravitational interaction (compared with other interactions) is not fundamental, it is merely a consequence of the existence of the extra dimensions. Moreover, these extra dimensions are assumed to be curled up, such that their small size explains why they would be invisible to us.

These extra dimensions may become detectable at very high energies. One possible experimental signature could lead to the emission of gravitons which scape into extra dimensions and therefore generate E_T^{miss} or miniature black-hole production with spectacular decays involving democratic production of fundamental final states such as jets, leptons, photons, neutrinos, W's and Z's [17].

Chapter 2

Experimental Framework

2.1 The Large Hadron Collider at CERN

The *Large Hadron Collider* (LHC) [18, 19] at CERN near Geneva is currently the largest ever built accelerator. It is installed in the existing 26.7 *km* tunnel that was constructed between 1984 and 1989 for the *Large Electron-Positron Collider* (LEP).

It is designed to collide proton beams with a nominal centre-of-mass energy of 14 TeV and a luminosity peak of $10^{34}\ cm^{-2}\ s^{-1}$. It can also collide heavy (Pb) ions with an energy of 2.8 TeV per nucleon and a peak luminosity of $10^{27}\ cm^{-2}\ s^{-1}$.

In order to accelerate the proton beams the existing CERN accelerator complex is used (see Figure 2.1). It starts with 50 *MeV* protons generated by the LINAC2 linear accelerator. The Proton Synchroton Booster (PSB) increases the energy to 1.4 *GeV* before the SPS accelerates the beam to 450 *GeV* and injects it into the LHC. The maximum energy which can be transferred to the beams is directly related with the accelerator radius ($p(GeV/c) = 0.3qBr$ being p the transverse momentum of the particles, B the strength of the magnetic field in Teslas and r the radius of the curvature of the circular accelerator in units of meters). There are two transfer tunnels, approximately 2.5 *km* in length, linking the LHC to the CERN accelerator complex that acts as injector.

Each beam has an internal structure as they are arranged in bunches separated in space which condense up to 1.15×10^{11} protons. Collisions will have a rate of 40 *MHz* (i.e. one collision every 25 *ns*). The machine will run up to the design luminosity of $10^{34}\ cm^{-2}\ s^{-1}$. A total integrated luminosity of 300 fb^{-1} is expected to be collected. At the time of writing, the LHC is working at a peak luminosity of $3.65 \times 10^{33}\ cm^{-2}\ s^{-1}$. The LHC performance for the recent years 2010-2011 achieves the foreseen plans as shown in the table 2.1.

The collider consists in two rings with counter-rotating beams. A magnetic field of 8.33 Tesla is generated to bend the trajectory of the 7 TeV proton beams along the LHC tunnel. It is achieved by 1232 superconducting dipole magnets. This kind of magnets uses twin bore magnets which consist of two sets of coils and beam channels within the same mechanical structure and cryostat. This design comes to the fact that the LHC magnets have to accelerate

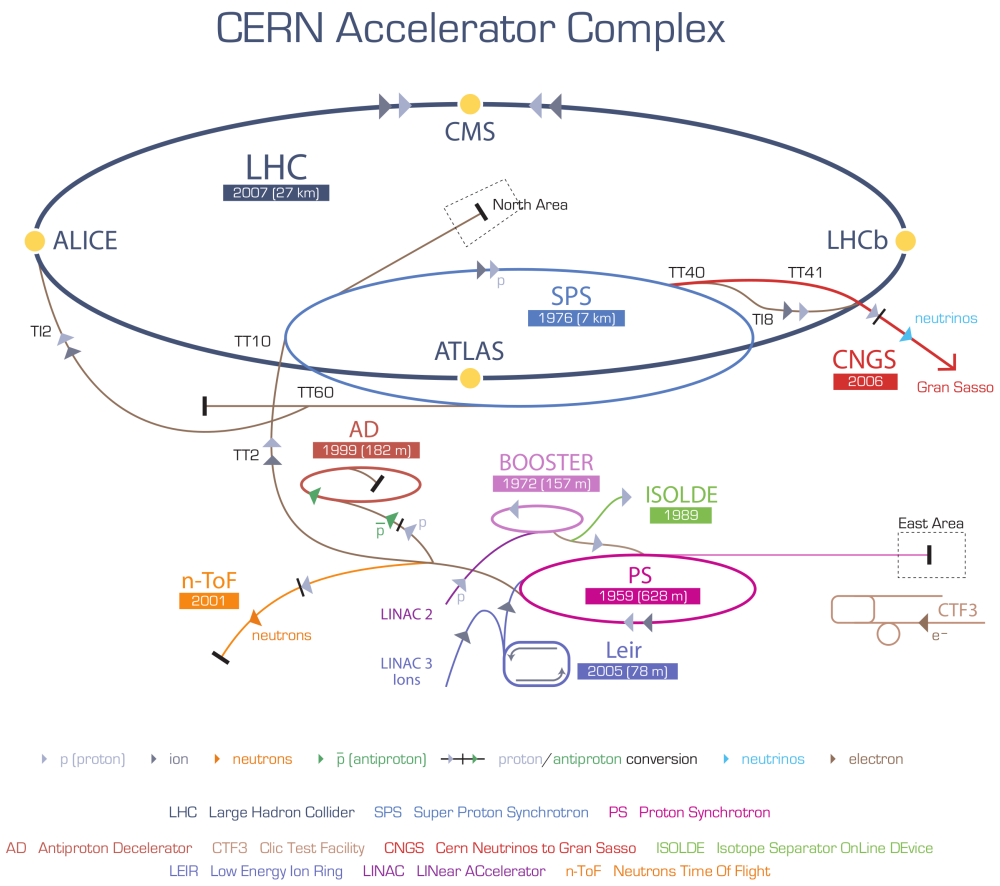

Figure 2.1: Configuration of the CERN accelerator complex and locations of the four LHC experiments.

Data taking year	Integrated luminosity recorded by ATLAS	peak luminosity
2010	45 pb^{-1}	$2.1 \times 10^{32}\ cm^{-2}s^{-1}$
2011	5.257 fb^{-1}	$3.65 \times 10^{33}\ cm^{-2}s^{-1}$

Table 2.1: LHC luminosity for the year 2010 and untill october for the year 2011 for collisions at $\sqrt{s} = 7\ TeV$.

two beams of equally charged particles but in opposite directions and there are obvious room constraints. The coils are made of niobium-titanium (NbTi) which is a material that allows to reach the superconducting regime when it is at 1.9 K [19]. A detailed cross section of a dipole magnet is shown in Fig. 2.2 where all its parts are depicted.

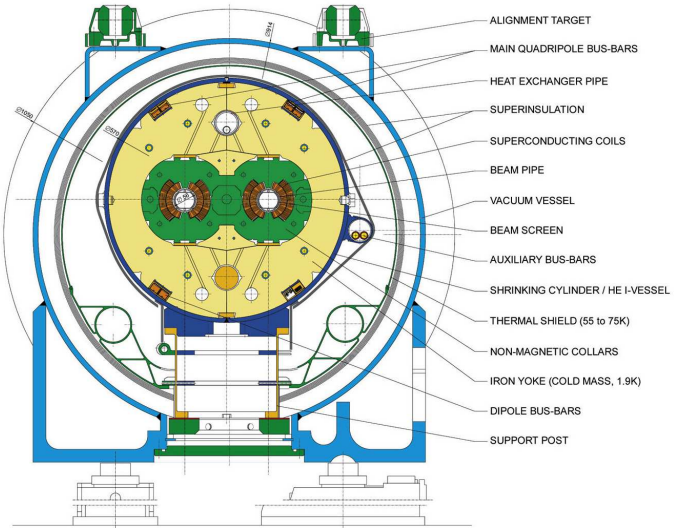

Figure 2.2: Cross section of a LHC dipole magnet design showing its components.

In addition, 392 quadrupolar magnets are used to focus and correct the beams. Also there are sextupole, octupole and decapole magnets mainly for compensating the systematic non-linearities. Some of the most relevant LHC parameters are summarized in Table 2.2.

The aim of the LHC is to reveal the physics beyond the Standard Model from proton-proton collisions with a centre of mass energy of up to 14 TeV. In addition, LHC serves also for precision measurements of the Standard Model parameters. The formidable LHC luminosity and resulting interaction rate are needed because of the small cross sections expected for the most interesting physics processes which will be discussed later. However, with an inelastic cross section of 80 mb, the LHC will produce a total rate of 10^9 inelastic events per second at design luminosity. This presents a serious experimental difficulty as it implies that every candidate event for new physics will on the average be accompanied by 23 inelastic events per bunch crossing.

	Nominal Parameters
Intensity per bunch	1.15×10^{11} protons per bunch
Number of bunches per beam	2.808
Bunch spacing	25 *ns*
Average radius of a beam at interaction point (IP)	16 μm
Crossing angle	300 μrad
Magnet field strength	8.33 *T*
Dipole magnet temperature	1.9 *K*
Total beam current	0.584 *A*
Inelastic proton-proton cross section	80 *mb*
Collisions per bunch crossing	23
Track multiplicity	700

Table 2.2: LHC general parameters at the high luminosity of $10^{34}\ cm^{-2}\ s^{-1}$

The number of events per second generated in the LHC collisions is given by:

$$N_{event} = L\sigma_{event} \tag{2.1}$$

where σ_{event} is the cross section for the event under study and L the integrated luminosity which is defined by

$$L = \int \mathcal{L}\, dt \tag{2.2}$$

$\mathcal{L}$ is the machine instantaneous luminosity which depends only on the beam parameters. It can be written for a Gaussian beam distribution as:

$$\mathcal{L} = \frac{N_b^2 n_b f_{rev} \gamma_r}{4\pi\epsilon_n\beta^*} F \tag{2.3}$$

$$F = \frac{1}{\sqrt{1 + (\frac{\Theta_c \sigma_z}{2\sqrt{\epsilon_n\beta^*}})^2}} \tag{2.4}$$

where N_b is the number of particles per bunch, n_b the number of bunches per beam, f_{rev} the revolution frequency, γ_r the relativistic gamma factor, ϵ_n the normalized transverse beam emmittance, β^* the amplitude function at the collision point. The latter two parameters together describe the beamsize at interaction:ϵ_n is a beam quality concept reflecting the concept of bunch preparation and β^* is a beam optics quantity and is determined by the accelerator magnet configuration at the interaction point. F is the geometric luminosity reduction factor due to the crossing angle at the interaction point. It is dependent on the full crossing angle, Θ_c, and the bunch length, σ_z.

Theoretically, the luminosity can be increased by increasing both the number of particles per bunch and the number of bunches, and by reducing the intersection area between them.

Nevertheless, this is hard to achieve in practice since the major limitation comes from beam-to-beam effects. The proton bunch creates a hugely non-linear electromagnetic field which modifies the trajectory of particles from their ideal orbits. The force on the particle is proportional to the number of protons on the bunch, and limits the bunch intensity to $\sim 10^{11}$ protons.

The LHC has two general purpose experiments, ATLAS [20] and CMS [21], both aiming at a peak luminosity of $\mathcal{L} = 10^{34}\ cm^{-2}s^{-1}$ for proton-proton operation. There are also two low luminosity experiments: LHCb [22] for b-physics, aiming at a peak luminosity of $\mathcal{L} = 10^{32}\ cm^{-2}s^{-1}$, and TOTEM [23](integrated into CMS) for the detection of protons from elastic scattering at small angles, aiming at a peak luminosity of $\mathcal{L} = 2\times10^{29}\ cm^{-2}s^{-1}$. In addition to the proton beams, the LHC has also operated with ion beams. The LHC has one dedicated ion experiment, ALICE [24], aiming at a peak luminosity of $\mathcal{L} = 10^{27}\ cm^{-2}s^{-1}$. Pb-Pb nuclei collisions will be studied at a centre of mass energy of 5.5 TeV per nucleon. Related to the LHC running with Pb-Pb nuclei collisions for the years 2010-2011, there has been a peak luminosity of $3.68\times10^{26}\ cm^{-2}s^{-1}$ with collisions at $\sqrt{s} = 2.76\ TeV$. The LHC experiments can be seen in the figure 2.3.

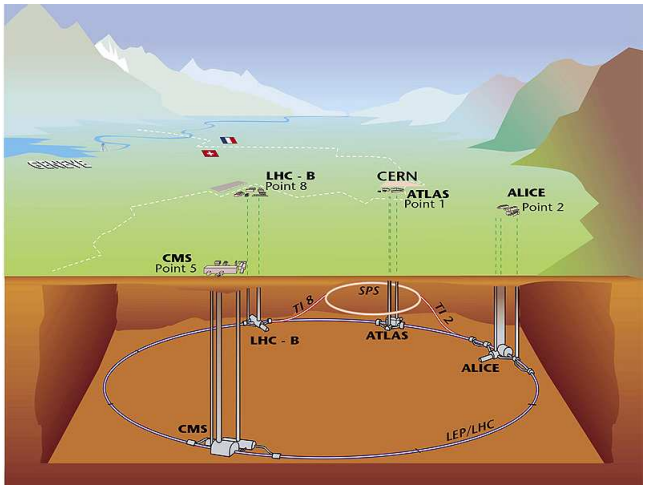

Figure 2.3: Representation of the LHC ring with its experimental underground caverns and services at the surface buildings.

LHC experiment requirements

These LHC physics goals can be turned into a set of general requirements for the LHC detectors:

- Fast, radiation hard electronics and sensor elements in order to cope with the harsh radiation environment. High detector granularity to reduce the overlapping events.
- Good charge-particle momentum resolution and reconstruction efficiency in the inner tracker are essential to observe secondary vertices.

- Very good electromagnetic calorimetry for electron and photon identification and complemented by full-coverage hadronic calorimetry for accurate jet and missing transverse energy measurements.
- Good muon identification and momentum resolution over a wide range of momenta.
- Highly efficient triggering on low transverse momemtum objects with sufficient background rejection.

2.2 LHC Experiments

This section is devoted to a general description of the LHC experiments. A schematic view of them can be found in Fig. 2.4. A more detailed description will be focused on the high luminosity experiment ATLAS and in particular its silicon tracker which constitutes the main subject of this thesis work.

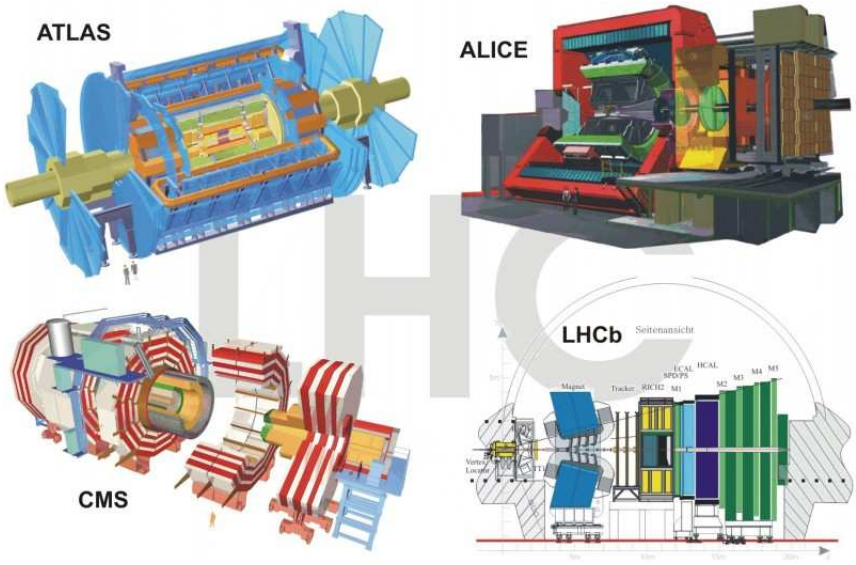

Figure 2.4: Graphical simulation of the huge LHC experiments (not to scale).

2.2.1 A Toroidal LHC ApparatuS (ATLAS)

ATLAS [25] is a general purpose experiment for high luminosity (up to $10^{34}\ cm^{-2}\ s^{-1}$). Its design has been optimized to be sensitive to a wide range of physics signatures in order to fully exploit the discovery potential of the hadron collider.

The experiment will perform high precision measurements on SM parameters and the Higgs boson search. The relevant decay modes of the SM Higgs boson at the LHC energies were explained before. These searches fix a set of requirements in terms of detector performance. For example, from the $H \rightarrow \gamma\gamma$ decay mode, a very good electromagnetic calorimetry for electron and photon identification and energy measurements is required, with good π^0 rejection and efficient photon isolation.

ATLAS is the largest LHC detector with 44 m long and 25 m high. Its weight is 7000 tons. The overall ATLAS detector layout is shown in figure 2.5.

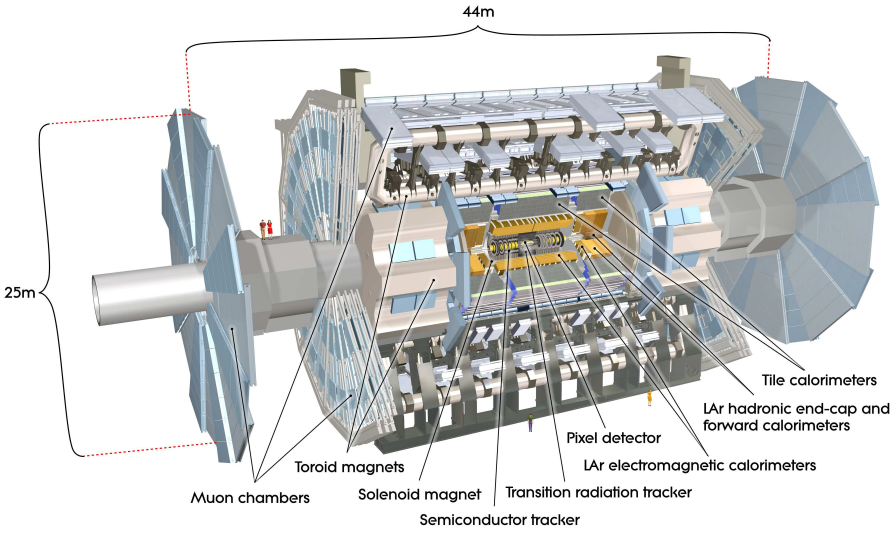

Figure 2.5: General view of the ATLAS detector. The dimensions are 25 *m* in height and 44 *m* in lenght. The overall weight of the detector is approximately 7000 *tons*.

The ATLAS detector is nominally forward-backward symmetric with respect to the interaction point. It comprises three main subsystems: tracking sytem, calorimeters and muon detectors. From the inside out:

- The **Inner Detector** (ID) combines high resolution discrete silicon detectors in the innermost layers (pixel and microstrips detectors) with a continuous gaseous straw drift-tube detector in the outermost radii. It is immersed in a 2 T solenoid field. It ensures a robust pattern recognition and momentum determination, precise vertex measurements, electron indentification, and pion separation. The ID will be described in more detail later.
- The **Electromagnetic Calorimeter** (ECAL) for the identification and energy measurements of electrons and photons. With an hermetic coverage, it uses liquid argon (LAr) as an ionization medium (it is also known as LAr calorimeter), with lead absorbers arranged in a accordion geometry. The high granularity of the detector elements allows to work with excellent performance in terms of energy and position resolution. It is surrounded by cryostat as it needs very low temperatures to operate.

- The **Hadronic Calorimeter** (HCAL) for the measurements of hadronic jets and missing energy (E_T^{miss}). The barrel calorimeter (TileCal) is provided by an iron absorber and plastic scintillator plates (called tiles). HCAL is separated into a large barrel (TileCal) and two smaller extended barrel cylinders, one on either side of the central barrel. In the end-caps, LAr technology is also used for the hadronic calorimeters providing both electromagnetic and hadronic energy measurements.

  The showers produced by particles such as the γ and $e^{\pm}$ are practically contained in the electromagnetic calorimeter, as they can penetrate much less than hadrons and produce narrower showers. Often a hadronic shower will start in the electromagnetic calorimeter and most of which will be absorbed in the hadronic calorimeter.

- The **Muon Spectrometer**, a stand-alone tracking device for muon detection including:

  – High precision tracking chambers: the Monitored Drift Tubes (MDT) and the Cathode Strip Chambers (CSC), for an excellent measurement of the muon momenta.

  – Trigger chambers with very fast response (timing resolution $\sim$1.5-4 ns) and bunch crossing identification: the Resistive Plate Chambers (RPC) and the Thin Gap Chambers (TGC).

  An air-core toroid magnet system generates strong bending power in a large volume within a light and open structure. This magnetic system has a barrel (25 m long, with an inner bore of 9.4 m and an outer diameter of 20.1 m) and two inserted end-cap magnets (with a length of 5.0 m, an inner bore of 1.65 m and an outer diameter of 10.7 m). The barrel toroid consists of eight flat coils assembled radially and symmetrically around the beam axis. The magnetic field provides for typical bending powers of 3 Tm in the barrel and 6 Tm in the end-caps.

To select events of interest, a three-level trigger system is used. The hardware-based level-1 (L1) uses a subset of detector information to reduce the event rate to a design value of 75 kHz. It uses information from the calorimeters and muon trigger chambers. The two software-based trigger levels, level-2 and the event filter, are collectively known as the High Level Trigger (HLT) and reduce the event rate to about 200 Hz. This reduction is possible because the HLT uses seeded, step-wise and fast selection algorithms based on the reconstruction of potentially interesting physical objects like electrons, muons, jets, tracks, and missing E_T and can provide the earliest possible rejection of background events.

2.2.2 Compact Muon Solenoid (CMS)

CMS [26] is the other general purpose experiment for high luminosity (up to 10^{34} cm^{-2} s^{-1}) and it has the same discovery potential as ATLAS although its hardware and software design is different. It is smaller than ATLAS (21×15 m^2) although heavier with 12500 tons. The layout of the experiment is shown on figure2.6. At the heart of CMS sits a 13 m long, 6 m inner diameter, 4 T superconducting solenoid providing a large bending power (12 Tm) sorrounded by massive iron return yoke with 4 inserted muon chambers. Each muon chamber consists of several layer of aluminum drift tubes (DT) in the barrel region and cathode strip chambers (CSC) in the endcap region where the muon rate and the neutron background are higher. The muon

system is complemented by resistive plate chambers (RPC), dedicated to the trigger system and are used in the barrel as well as the endcap regions.

The inner part is large enough to accommodate the inner tracker and the calorimeter inside. The electromagnetic calorimeter (ECAL) uses over 80 000 scintillating lead tungstate ($PbWO_4$) crystals. The scintillation light is detected by silicon avalanche photodiodes (APDs) in the barrel region and vacuum phototriodes (VPTs) in the endcap region. A preshower system is installed in front of the endcap ECAL for ϕ^0 rejection.

The ECAL is surrounded by a brass/scintillator sampling hadron calorimeter (HCAL). The light is detected by photodetectors (hybrid photodiodes, or HPDs) that can provide gain and operate in high axial magnetic fields. Two very-forward hadronic calorimeters exist outside the coil, located at each end of the detector in a harsh radiation field and can therefore not be constructed of conventional materials. Instead the absorbers are made of steel, which suffers less activation under radiation than copper, and the showers are sampled by radiation resistant quartz fibres.

The tracking volume is given by a cylinder of 5.8 *m* length and 2.6 *m* diameter. CMS employs 10 layers of silicon microstrip detectors, which provide the required granularity and precision. In addition, 3 layers of silicon pixel detectors are placed at radii between 4.4 *cm* and 10.2 *cm*; the closest to the interaction region in order to improve the measurement of the impact parameter of charged-particle tracks, as well as the position of secondary vertices. Each subsystem is completed by endcaps which consists of 2 disks in the pixel detector and 9 plus 2 disks in the strip tracker on each side of the barrel (see Table 2.3). The expected flux at a radius of 4 *cm* is 3×10^{15} cm^{-2}. For the strip region, at 22 *cm* from the interaction point is expected 2×10^{14} cm^{-2} whereas 2×10^{13} cm^{-2} are expected at 115 *cm*. These fluxes are simulated [26] at an integrated luminosity of 500 fb^{-1} corresponding to about 10 years of LHC operation.

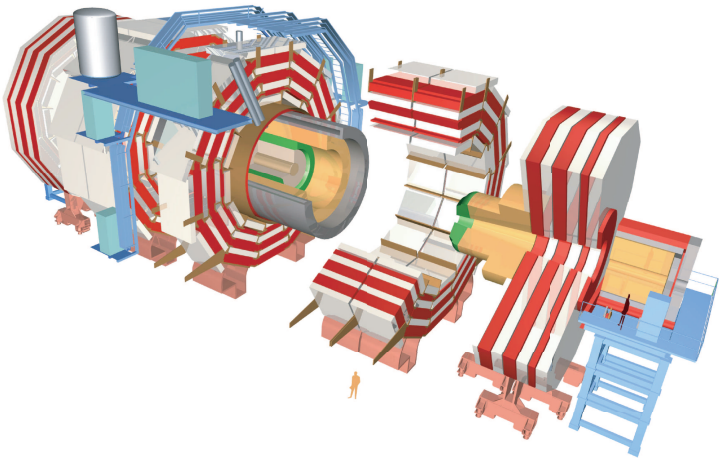

Figure 2.6: General view of the CMS detector. The dimensions are 15 *m* in height and 21 *m* in lenght. The overall weight of the detector is approximately 12500 *tones*.

Detector	distance from beamline	Technology	Area [m^2]	Channels [M]
Strip	$55 < R < 115\ cm$ $22 < R < 50\ cm$	p-on-n (500 μm thick) pitch $\sim 200\ \mu m$ p-on-n (320 μm thick) pitch $\sim 80\ \mu m$	210	66
Pixel	$< 20\ cm$	n-on-n (285 μm thick) oxygenated	1	9.3

Table 2.3: Technologies used in the CMS Silicon Tracker to match the specifications for radiation hardness and detector occupancy.

2.2.3 Large Hadron Collider beauty (LHCb)

LHCb [27] is a low luminosity experiment (up to $10^{32}\ cm^{-2}\ s^{-1}$) for measuring the parameters of *CP* violation in the interactions of *b*-hadrons. The LHCb detector is a single-arm spectrometer stretching for 20 metres along the beam pipe and with a forward angular coverage from approximately 10 mrad to 300 mrad in the bending plane. Its subdetectors are stacked behind each other like books on a shelf. The choice of the detector geometry is justified by the fact that at high energies both the *b*- and $\overline{b}$-hadrons are predominantly produced in the same forward or backward cone. The layout of the LHCb spectrometer can be seen in Fig. 2.7.

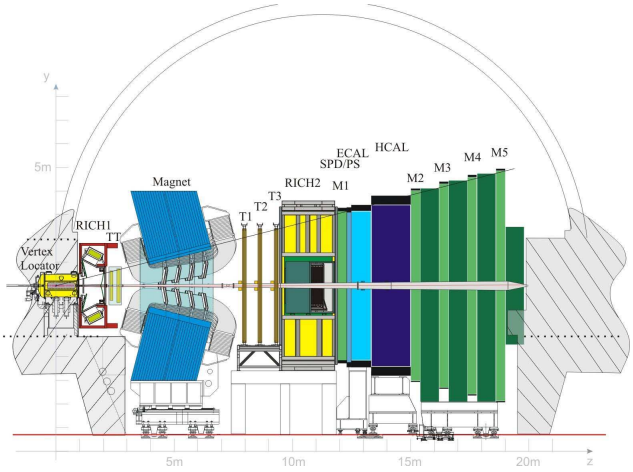

Figure 2.7: Schematic view of the LHCb detector.

It has a warm dipole spectrometer magnet providing an integrated field of 4 Tm. The LHCb tracking system consists of the VErtex LOcator system (including a pile-up veto counter) called VELO that uses silicon microstrip detectors and four planar tracking stations. The Tracker Turicensis (TT) is upstream of the spectrometer magnet (as VELO) and three tracking stations (T1-T3) behind the magnet, made of silicon microstrips in the inner parts (Inner Tracker, IT)

Detector	Technology	Pitch [μm]	Area [m^2]	Channels [n°]
VELO	n-on-n (300 μm thick)	[38-102]	-	$\sim$ 172 032
Silicon Tracker				
TT	p-on-n (500 μm thick)	183	8.4	143360
IT	p-on-n (320-410 μm thick)	198	4	129 024

Table 2.4: Technologies used in the LHCb Silicon Systems to match the specifications for radiation hardness and detector occupancy.

and Kapton/Al gas-tight straw-tubes for the outer parts (Outer Tracker, OT). The TT and the IT are called the Silicon Tracker.

The particle identification system consists of two Ring Imaging Cherencov counters (RICH 1 and RICH 2) to achieve excellent π-K separation in the momemtum range from 1 to 100 GeV/c, and Hybrid Photon Detectors. The upstream detector, RICH 1, covers the low momentum charged particle range $\sim$1-60 GeV/c using aerogel and $C_4\ F_{10}$ radiators, while the downstream detector, RICH 2, covers the high momentum range from $\sim$15 up to and beyond 100 GeV/c using a CF_4 radiator.

The calorimeter system is composed of a Preshower Detector (SPD/PS) in order to reject the high backgrounds of charged pions and a Scintillator Pad Detector to reject the background of π^0. After that, the classical structure of an electromagnetic calorimeter (scintillator/lead structure) followed by a hadron (scintillator/iron tiles) calorimeter is adopted. The muon detection system is composed of five stations (M1-M5) placed downstream of the magnet along the beam axis. It comprises 1368 Multi Wire Proportional Chambers (MWPC).

A more detailed description of the subsystems that use silicon technologies are provided in the following. The VELO consists of a series of silicon modules, each providing a measure of the r and ϕ coordinates, arranged along the beam direction. The track coordinates provided by the VELO are used to reconstruct production and decay vertices of beauty- and charm- hadrons, to provide an accurate measurement of their decay lifetimes and to measure the impact parameter of particles used to tag their flavour. The modules have a cylindrical geometry with circular strips centered as perfectly as possible around the beam axis. The innermost radius of the module limited by the required beam aperture is 5 mm. They are formed by two concentric semi-circular sensors. One of the two sensors of the module, called ϕ-sensor, provides information on the azimuthal coordinate around the beam. The other sensor, called R-sensor, provides information on the radial distance from the beam axis. The two halves should be aligned to better than 100 μm relative to each other in these coordinates. The damage to silicon in the most irradiated area for one nominal year of running, i.e. an accumulated luminosity of 2 fb^{-1}, is equivalent to that of 1 MeV neutrons with a fluence of $1.3\times10^{14}\ n_{eq}/cm^2$, whereas the irradiation in the outer regions does not exceed a fluence of $5\times10^{12}\ n_{eq}/cm^2$. The detector is required to sustain 3 years of nominal LHCb operation. Table 2.4 shows the technologies and some characteristics of the LHCb silicon subsystems.

During the production of VELO, the possibility of manufacturing full size n^+p sensors arose due to the advantages that presents this sensor technology (see Chapter 2), principally in cost of manufacture due to that doubled-side processing is not needed. One full size module was

produced in this technology and installed in one of the most upstream slots. It is foreseen to replace all the VELO modules after damage due to accumulated radiation or beam accidents.

About the Silicon Tracker (ST), both TT and IT uses silicon strip sensors with a pitch of about 200 μm. The IT covers a high cross shaped region in the centre of the three tracking stations (T1-T3). Each of the four ST stations has four detection layers with vertical strips in the first and the last layer and strips rotated by a stereo angle of -5° and +5° in the second and the third layer respectively. Related to radiation damage, for 10 years of operation at nominal luminosity, expected fluences in the innermost regions of the detectors do not exceed $5 \times 10^{14}\ n_{eq}/cm^2$ for the TT and $9 \times 10^{12}\ n_{eq}/cm^2$ for the IT.

2.2.4 A Large Ion Collider Experiment (ALICE)

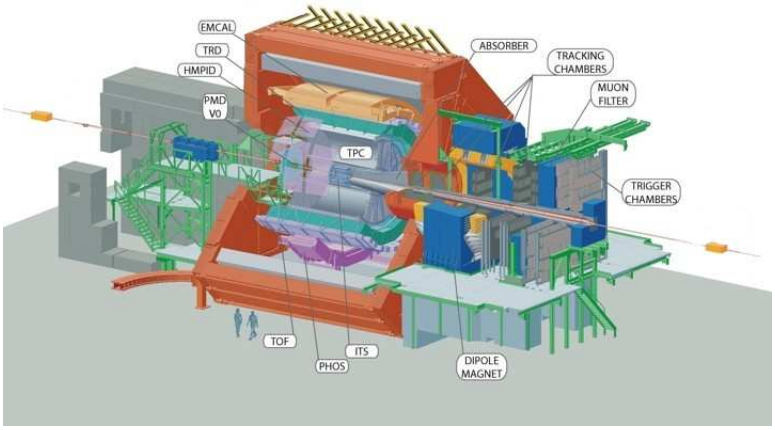

Figure 2.8: Schematic view of the ALICE detector.

ALICE [28] is a general purpose, heavy-ion detector which focuses on QCD, the strong interaction region of the Standard Model. It is designed to address the physics of strongly interacting matter and the quark gluon plasma at extreme values of energy density and temperature in nucleus-nucleus collisions. It will work at a peak luminosity of $10^{27}\ cm^{-2}\ s^{-1}$ for nominal Pb-Pb ion operation. Its overall dimensions are $16 \times 16 \times 26\ m^3$ with a total weight of approximately 10 000 tons.

It consists of a central barrel part and a forward muon spectrometer as seen in Fig. 2.8. The central part is embedded in a large solenoid magnet of 0.5 T. From the inside out, the barrel contains an Inner Tracking System (ITS) of six planes of high-resolution silicon pixel (SPD), drift (SDD), and strip (SSD), a cylindrical Time-Projection Chamber (TPC), three particle identification arrays of Time-of-Flight (TOF), Ring Imaging Cherenkov (HMPID) and Transition Radiation (TRD) detectors, and two electromagnetic calorimeters (PHOS and EMCal). Finally,

Detector - layer	Technology	Area [m^2]	Channels [$n°$]
SPD - 1	n-type pixel, 200 μm thick	0.07	3 276 800
SPD - 2	n-type pixel, 200 μm thick	0.14	6 553 600
SDD - 3	drift, 300 μm thick	0.42	43 008
SDD - 4	drift, 300 μm thick	0.89	90 112
SSD - 5	strip, 200 μm thick	2.2	1 148 928
SSD - 6	strip, 200 μm thick	2.8	1 459 200

Table 2.5: Technologies and dimensions used in the ITS detectors of ALICE to match the specifications for radiation hardness and detector occupancy.

the forward muon system consists of a complex arrangement of absorbers, a large dipole magnet (3 Tm) and fourteen planes of tracking and triggering chambers located up to 14 m from the interaction point.

Focusing on the tracking in the central part, it is divided into the ITS, and the TPC. The need for efficient and robust tracking has led to the choice of a TPC as the main tracking detector. The TRD will also be used for tracking in the central region improving the p_t resolution at high momentum. Because of the high particle density (50 particles per cm^2 is predicted for the inner layer), and in order to achieve the required impact parameter resolution, silicon pixel detectors have been chosen for the innermost two layers, and silicon drift detectors for the following two layers. The two outer layers, where the track density is expected to be below one particle per cm^2, are equipped with double-sided silicon microstrip detectors. All ITS is located at radii between 4 and 43 cm. The technologies used in the various layers of the ITS are summarized in Table 2.5. The expected fluence at the location of the inner layer (3.9 cm) of the ITS pixel detector is $3.5 \times 10^{12}\ n_{eq}/cm^2$ for 10 years of nominal operation. The fluence at the outer layer of the ITS that is at 43 cm of the beam pipe is $2 \times 10^{11}\ n_{eq}/cm^2$.

2.3 The ATLAS Tracker: The Inner Detector

The ATLAS Inner Detector (ID) is a cylinder of length 6.2 m and a radius of 1.15 m and performs the pattern recognition, momentum and vertex measurements together with electron identification. These capabilites are achieved with a discrete high resolution silicon Pixel detector followed by a silicon microstrip detector, the SemiConductor Tracker (SCT) and in the outer part of the ID, the Transition Radiation Tracker (TRT) as seen in Fig. 2.9. The components of the ID are summarized in the Table 2.6. The ID operates embedded in a 2 T axial magnetic field generated by a solenoid. This magnetic field is used for bending the charged particles and measure their charge and momentum.

Mechanically, the ID is divided in three parts: a central barrel region and two symmetric end-caps. The barrel extends over ± 80 cm along the Z-axis. The silicon detectors are arranged on concentric cylinders around the beam axis (three pixel layers and four SCT layers) up to a radius of 56 cm. The Pixel and SCT modules at the end-caps are arranged on disks along planes perpendicular to the beam axis. The TRT consists of about 300 000 gaseous straw tubes arranged

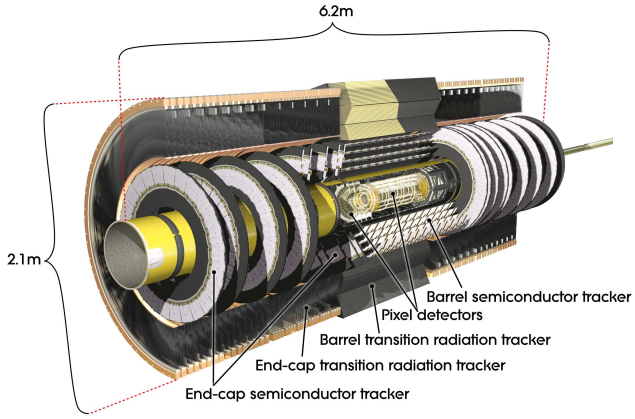

Figure 2.9: A cut-away view of the ATLAS Inner Detector, showing the various subdetectors.

in 73 layers in the barrel region and 2×160 straw planes in the end-cap regions providing an average number of 36 hits per track.

Due to the large track density expected at the LHC, the ID electronics and all the sensor elements must be fast enough and of course radiation hard. In addition, a very fine granularity is needed to handle the particle fluxes and to reduce the influence of overlapping events. For this purpose the ID has 5832 individual silicon modules (with about 86 million of readout channels).

2.3.1 The Pixel Detector

The pixel detector is the innermost subsytem of the ID. It is vital in order to achieve an excellent pattern recognition close to the collision point and very good *b*-tagging performance. It largely contributes to the impact parameter resolution and to the ability of the ID to determine secondary vertices.

The detector itself consists of one B-layer (for its importance in B-physics), two barrel layers

Detector	distance from beamline [cm]	Section	Layers	Area [m^2]	Channels [M]
Pixel	$R \sim 5.1$	B-layer	1	0.2	13.2
	$9.9 < R < 12.3\ cm$	Barrel	2	1.4	54
	$8.9 < R < 15\ cm$	End-cap	3	0.7	6.6
SCT	$25.5 < R < 55\ cm$	Barrel	4	34.4	3.2
	$25.1 < R < 61\ cm$	End-cap	9	26.7	3.0
TRT	$55.4 < R < 108.2\ cm$	Barrel			0.1
	$61.7 < R < 110.6\ cm$	End-cap			0.32

Table 2.6: Main parameters of the Inner Detector.

and two end-caps, with three disks each [29]. The B-layer is located at a radius of 5.1 *cm* from the interaction point (IP) and the two barrel layers at 9.9 *cm* and 12.3 *cm*. The two end-caps situated at each side of the barrel are located at $8.88 < R < 14.96$ *cm* from the beamline.

The pixel modules (identical for all regions) are single silicon sensors of 6.08×1.64 cm^2 divided in 46 080 pixels and a size of $50\ \mu m \times 400\ \mu m$ along the $R\phi$ and Z directions respectively. They are a n^+n silicon pixel array bump-bonded to 16 readout chips. The *pn* junction is located on the backside, with a multi-guard structure controlling the potencial drop towards the cutting-edges. These sensors have 250 μm of thickness. There are 1456 modules in the barrel and 288 in the end-caps.

2.3.2 SCT

The SCT detector is designed to provide four precision measurements per track at intermediate radii of the ID. Like the Pixel Detector, it consists of 4 barrel layers and 2 end-caps on each side of the barrel where silicon modules are mounted. The SCT has 4088 modules in total where 2112 are barrel modules and 1976 are end-cap modules.

The four barrels are located at 29.9 *cm*, 37.1 *cm*, 44.3 *cm*, and 51.4 *cm* respectively from the IP. On each barrel, the modules are placed in rows parallel to the beam axis. There are 12 modules in each row with a total of 2112 modules [30]. A barrel module consists of two pairs of single-sided p^+n silicon detectors glued back-to-back at 40 *mrad* angle and separated by a heat transport plate. Each silicon wafer is 6×6 cm^2, 285 μm thick, and has 768 readout strips with 80 μm pitch. On each side of the module, two wafers are wire-bonded together to form 12 *cm* long strips. Combining the measurements from both sides, a two-dimensional space-point is created. The readout is performed by means of 12 binary ABCD front-end chips and mounted above the detectors on a hybrid. The readout chain consists of a front-end amplifier and discriminator, followed by a binary pipeline which stores the hits above threshold until the level-1 trigger decision.

Each end-cap consists of 9 disks supported by a cylinder with modules arranged in rings within a disk. The disks are located at a $27.5 < R < 56$ *cm* from the beamline. The end-cap modules are identical to the barrels, except in their shape, trapezoidal in this case for a ϕ-arrangement within a ring, but otherwise similar to the barrel modules in electronics and readout. A disk may have up to three rings, therefore three types of end-cap modules (namely *inner*, *middle*, and *outer*) are needed [31]. The effective strip length after bonding is ~ 12 *cm* for *middle* and *outer* modules, and half this value for *inners* (with only one sensor per side). The strip pitch varies from 55 to 95 μm depending on the end-cap module type.

2.3.3 TRT

The TRT is based on straw detectors which measure the transition radiation produced when a relativistic charged particle crosses the boundary between media with different dielectric constants [32]. The transition radiation is emitted as X-rays in a very forward direction with respect to the parent particle trajectory.

The TRT geometry is optimized to maximize the production and detection of the transition radiation X-rays in the polypropylene radiatior material and the gaseous counters. The TRT

consists of about 300 000 gaseous straw tubes arranged into modules, and these mounted into a barrel and two end-caps on each side of the barrel. Each module contains a variable number of straw drift tubes depending on its position within the detector. The entire volume between straws is filled with a low-density foam (polypropylene) fibre radiator. Each straw is 144 cm long (for the barrel) and has a diameter of 4 mm, each fitted with a 30 μm diameter gold-plated tungsten wire [33]. They are filled with a mixture of 70% Xe, 27% CF_4, and 3% O_2 at atmospheric pressure.

The TRT barrel is made of three cylindrical concentric rings, each containing 32 identical modules. Three types of different modules are used (one per ring), identical in shape but differing in size. Starting from the IP, the barrel covers ± 78 cm along the beam direction. In the end-caps, the straws are arranged in 20 wheels per side, divided in two sets of identical wheels. The two sets, namely type A, and B, contain respectively twelve and eight wheels each. The straw length in the end-caps is 37 cm.

When a particle passes through the straw, it ionizes the gas and the electrons drift towards the central wire (anode) acting the straw wall as cathode. An avalanche is formed close to the wire where the electric field is high. The multiplication process is in the proportional regime, providing a signal amplification of $\sim 2.5 \times 10^4$. The measurement of the time the charge spends to drift towards the sense wire allows an stimation of where the particle crossed the straw with a position accuracy of $\sim 140 \mu m$.

2.3.4 Reference frame

The used ATLAS coodinate system is described following. The vector that points from the interaction point to the centre of the LHC ring defines the "+x" axis and the "+y" axis points upwards. The "+z" direction is along the beam axis. Besides the standard Cartesian coordinate system, especially for physics analyses, a coordinate system with (r, ϕ, θ) is useful. R is the transverse radius from beampipe and ϕ the azimutal angle, measured from the x-axis. θ can be used to directly measure the angle away from the beampipe.
For describing tracks of particles in a detector, the rapidity (y) is especially useful because $\triangle y$ is invariant under longitudinal (in z) Lorentz boosts. Rapidity is defined as

$$y = \frac{1}{2} \log \frac{E + p_L}{E - p_L} \tag{2.5}$$

where E is the energy of the particle and p_L is the longitudinal component of the momemtum of the particle. For a particle with zero rest mass, this equation is reduced to

$$\eta = -\log\left(\tan \frac{\theta}{2}\right) \tag{2.6}$$

where η is the pseudo-rapidity. η is also a good approximation for y in the relativistic limit. This parameter is convenient for describing the coverage of a detector. A high η coverage, meaning $\eta \gg 1$, means that a detector has good coverage in the forward regions.

The momemtum and vertex resolution requirements from physics call from high-precision measurements to be made with fine granularity detectors, given the very large track density

Detector	Section	η coverage	Resolution $\sigma[\mu m]$
Pixel	B-layer	± 2.5	$R\phi = 10, z = 115$
	Barrel	± 1.7	$R\phi = 10, z = 115$
	End-cap	1.7 - 2.5	$R\phi = 10, R = 77$
SCT	Barrel	± 1.4	$r\phi = 17, z = 580$
	End-cap	1.4 - 2.5	$r\phi = 16, R = 580$
TRT	Barrel	± 0.7	130
	End-cap	0.7 - 2.5	170

Table 2.7: η coverage of the Inner Detector parts and their nominal intrinsic resolution for a whole module as defined by the performance requirements of the ATLAS experiments [25].

expected at the LHC. The highest granularity is achieved around the vertex region using the silicon pixel detector. The total number of precision layers must be limited because of the material they introduce. Typically, three pixel layer and eight strip layers (four space points) will be crossed by each track. A large number of tracking points (typically 36 per track) is provided by the TRT. The combination of the two techniques give robust pattern recognition and high precision in both ϕ and z coordinates. The pixel layers are segmented in $r\phi$ and z, while the barrel SCT detector uses small angle (40 *mrad*) stereo strips to measure both coordinates, with one set of strips in each layer parallel to the beam direction, measuring $r\phi$. In the end-cap region, the detectors have a set of strips running radially and a set of stereo strips at an angle of 40 *mrad*. The detector has been designed to have spatial resolution of 17 μm in $r\phi$ and 580 μm in z per module, containing one $r\phi$ and one stereo measurement.
The TRT only provides $r\phi$ information, for which it has an intrinsic accuracy of 130 μm per straw. The barrel TRT straws are parallel to the beam direction and in the end-cap region, all the elements are perpendicular to the beam axis. The straw hits at the outer radius contribute significantly to the momentum measurement, since the lower precision per point compared to the silicon is compensated by the large number of measurements and longer measured track length. The expected measurement resolutions are summarized in table 2.7.

The Inner Detector layout provides full tracking coverage over $|\eta| \leq 2.5$(Fig. 2.10), including impact parameter measurements and vertexing for heavy-flavour and τ tagging. The secondary vertex measurement performance is enhanced by the innermost layer of pixels.

2.3.5 Radiation Levels

The high interaction rate in proton-proton collisions at a such high luminosity will lead to a very high radiation level in the detectors. It depends on the detector position relative to the IP. So, the most intense fluxes will be inside the inner tracker region.

Charged hadron secondaries mainly charged pions from inelastic proton-proton interactions dominate the radiation backgrounds at small radii. They constitute the most serious background for the innermost layers of the inner detector as seen in Fig. 2.11 above. It can also be seen that the charged hadron fluence contours run parallel to the beamline, which is a consequence of the flatness of the charged particle rapidity plateau of minimum bias events.

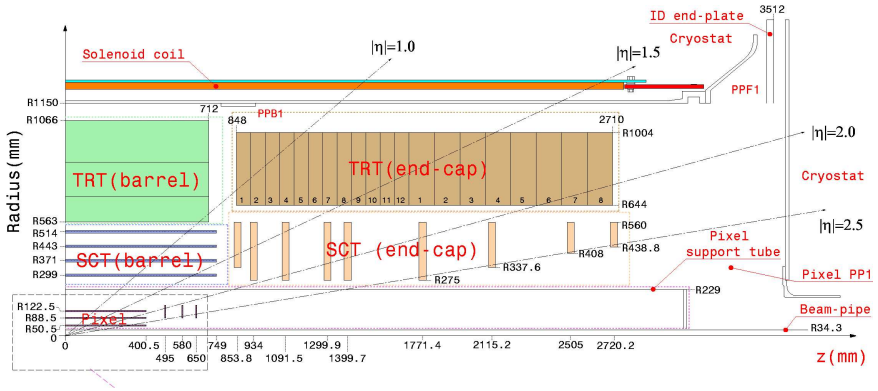

Figure 2.10: Position and η-coverage of the inner detector components.

The fluence map for all neutrons is shown in the Fig. 2.11 below. Close to the interaction point, charged pions dominate the bulk damage in silicon. However, further out in the SCT and TRT systems, neutrons are dominant. Some neutrons are originated from the interaction point, as well as secondaries from the beampipe, but most of them come from albedo (backsplash from the surfaces of the electromagnetic calorimeter). The dominant source of neutrons is from the endcap calorimeters, especially the FCAL. Table 2.8 shows projected radiation levels in key areas of the detector.

Location	f_{neq} (10^{14} cm^{-2})
Pixel B-layer	13.5
SCT layer 1	2
SCT disk 9	1
TRT outer radius	0.25

Table 2.8: The expected 1MeV neutron equivalent fluence, f_{neq} predicted for the inner detector after 10 years of operation.

The effects of background radiation fall into a number of general categories:

- increased background and occupancies (Fig. 2.12) leading to inefficiencies, worsened resolutions and fake tracks.
- radiation damage and ageing of detector components and electronics (Fig. 2.11).
- Interactions leading to anomalous deposits of local radiation can disrupt electronic signals (single events upsets) or destroy components (single event damage).

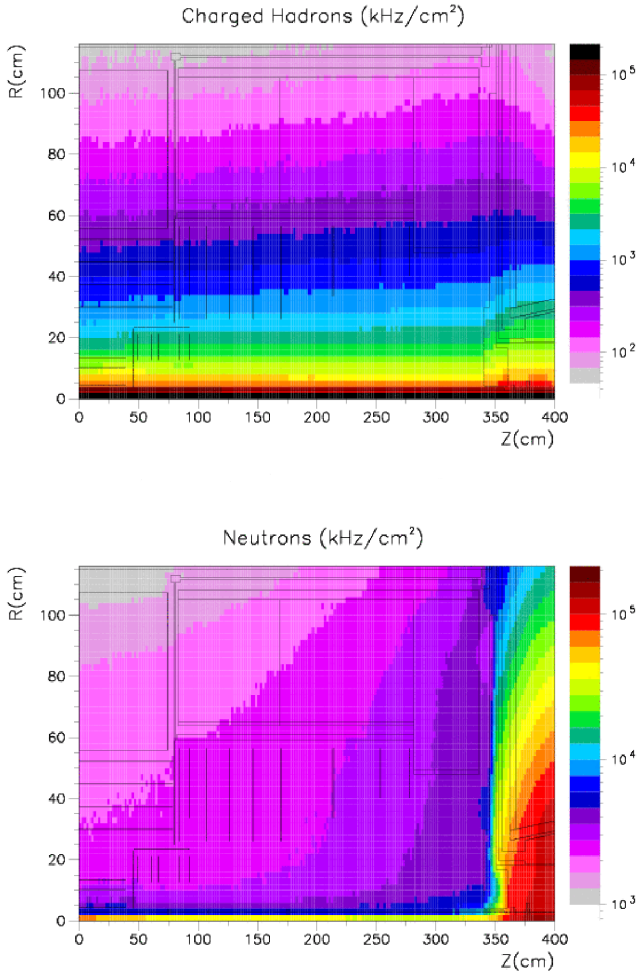

Figure 2.11: Above, charge hadron fluence rates in the inner detector, and below, total neutron fluence rates in the inner detector. These fluence maps are reported in units of kHz/cm^2 but it is noted that it does not imply periodically occuring events, the background fluence rates will follow a Poisson distribution (from [34]).

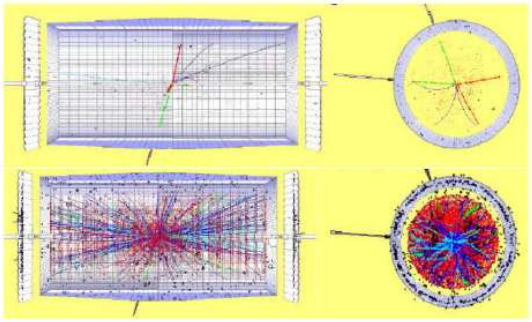

Figure 2.12: Higgs event: H $\rightarrow 2e\,2\mu$. In the upper part a "clean" event is shown. In the picture below, the same event is shown with the expected background for LHC design luminosity (from [35]).

2.4 The High Luminosity Large Hadron Collider

The LHC detectors have been designed for a nominal luminosity of $10^{34}\ cm^{-2}\ s^{-1}$. An upgrade of the LHC towards higher luminosities ($10^{35}\ cm^{-2}\ s^{-1}$) has been considered as an extension of the physics program [36]. This increase of almost one order of magnitude in luminosity will increase in the collision rate extending the sensitivity to new physics by roughly 20 – 30 % in terms of energy or particle mass, and allowing additional and more precise measurements to be performed. The upgraded machine project is called super Large Hadron Collider (sLHC). However, it has been stablished a maximum operation luminosity of $5\times10^{34}\ cm^{-2}\ s^{-1}$ in order to maximize the useful physics at high luminosity. This new project is denominated High Luminosity LHC (HL-LHC).

The increase in the number of collisions would also put greater demands on the detectors used in the experiments. Firstly, the number of particles produced in each bunch crossing would increase by a factor of 10. In order to reliably distinguish between the tracks produced by these particles, the granularity of many of the detectors would need to be increased. Secondly, the luminosity increase would also lead to a tenfold increase in the radiation damage received by the detectors. Therefore, their design must function within a much harder environment and yet preserve, if not improve, their ability to maximize the upgrade's physics opportunities. In preparation for this, several *R&D* programs are already working to provide guidelines for new detector technologies, which may be employed at the anticipated high radiation levels, as well as to study and design the new possible detector layouts, in order to be able to cope with the improved physics program.

2.4.1 Expected Physics

Data from LHC detectors should be able to cover most of the Standard Model (SM) physics program, in particular the Higgs discovery program. In addition, LHC should be able to probe the existence of physics beyond the SM, like SUSY, extradimensions or exotic phenomena (not

predicted by SM) as lepton and quark compositeness. The exact physics case for HL-LHC is hence difficult to predict today, since it depends very much on what the LHC will find or not find.

The main goal of HL-LHC, as it appears now, is to extend the discovery reach for physics beyond the SM and to improve the sensitivity for measurements which are rate-limited at the LHC. For this purpose, a large event statistics is essential. It is assumed that integrated luminosity of 100-300 fb^{-1} (1000-3000 fb^{-1}) per experiment will be collected at the LHC (HL-LHC). In addition, precision measurements of the SM parameters will be limited by systematic uncertainties already after the first five years of data taking at LHC. A few examples of physics case in which HL-LHC can improve with respect to LHC are discussed below. More details on the HL-LHC physics potential can be found in references [36–39].

When the LHC is running at design luminosity, if the Higgs exists, it should not scape from discovery in almost the whole mass range. Once it has been observed, however, parameters such as the mass and couplings will need to be measured. This may require more than 300 fb^{-1}. Due to small branching ratios for clean final states, there are insufficient statistics to measure the Higgs self-coupling at the LHC. As for the Higgs, if SUSY is observed at the LHC then the masses and model parameters will need to be determined, along with the connection to cosmology (e.g. dark matter), the impact on Higgs phenomenology and the SUSY breaking mechanism. Depending on the scenario in which SUSY will reveal itself, the measurements of masses and disentangling of different models could be difficult with the LHC.

If neither the Higgs nor SUSY is found, then other possibilities need investigation, such as other electroweak symmetry breaking mechanisms, extra dimensions, little Higgs models and Technicolor. Detecting such new physics may also be beyond the capabilities of the LHC.

2.4.2 Machine plan

At the time of writing this memory, the plans for the upgrade from LHC to HL-LHC is foreseen to occur in three phases, though they may change.

1. **Phase 0**.
   By 2012, more than 10 fb^{-1} of integrated luminosity is expected to be delivered with the peak luminosity above $10^{33}\ cm^{-2}\ s^{-1}$. Then, a 18 months long shutdown is scheduled. It is mainly for maintenance and technical consolidation for the machine performance and some concerning experiment issues (for instance, ATLAS will need to exchange the external beam pipes with light material one). After that, from ~ 2014, it is expected operation with an increase of its energy from the current energy of 7 TeV to 14 TeV reaching the nominal luminosity of $1 \times 10^{34}\ cm^{-2}\ s^{-1}$ (with few hundreds fb^{-1} of integrated luminosity) and a bunch crossing time of 25 ns.

2. **Phase I**.
   A second shutdown is anticipated at ~ 2018. At least, it will last 9 months to consolidate collimation, quadrupole focusing magnets replacement near interaction regions due to radiation damage and to prepare crab cavities (for an effective beam crossing scheme) and RF cryo system. This shutdown should make sure the machine to reach double the nominal luminosity. It is also foreseen to connect a new linac, called Linac-4 (replacing

the existing Linac 2) to the PSB as well as a PSB energy upgrade from 1.4 to 2 GeV injection to the PS.

It is expected an operation with a luminosity up to 2-3 $\times 10^{34}$ cm^{-2} s^{-1} and delivered a total of 300 fb^{-1} untill the end of this phase.

3. **Phase II**.
$\sim$2022-2023 with a previous shutdown (18 months will be needed to install and debug a new ATLAS ID detector). Experiments expect to accumulate up to 3000 fb^{-1} with a nominal luminosity up to 5×10^{34} cm^{-2} s^{-1} until $\sim$2030. Various options are under study to find the best way to deliver this luminosity, including luminosity levelling so that the high interaction rate will be sustained throughout the spill. Coping with the very high data rates and radiation levels at the HL-LHC will require major changes to ATLAS at this time.

2.4.3 The ATLAS upgrade

For the ATLAS experiment, the timescale of such a significant upgrade is driven by two major factors: An increase in pile-up of events per beam crossing from 20 to 200, and an increase of total fluence of particles. The former implies a finer granularity for the detectors to keep the occupancy acceptable low and trigger and data acquistion (DAQ) systems able to handle much higher event rates. The latter implies significant radiation damage on the detectors as well as the front-end electronics. In view of these limitations, the detector system will need to be replaced or technologically improved in order to keep their performance despite the large increase of event rates and total particle fluence. The detectors at low radii and large η are most affected, including the ID, forward calorimeter and forward muon wheels. On the contrary, the barrel calorimeters and muon chambers are left largely untouched.

The ATLAS plan foreseen for the upgrade period is the following [40]:

Phase 0

- With increasing the luminosity the muon spectrometer is exposed to significant backgrounds from low-energy neutrons and photons. Currently, the beam pipe in the forward region is made of stainless steel which produces high backgrounds in the muon system and becomes radiactive. A change of material in the beam pipe to beryllium beam pipe would significantly reduce the activation of the beam pipe by three orders of magnitude and hence the backgrounds rates in the muon spectrometer [41].

- The innermost layer of pixels, the B-layer, is the closest to the interaction region and therefore subject to the most severe radiation conditions. The original program of the B-layer replacement foresaw the extraction of the B-layer and its substitution with a new one. However, this turned out to be unfeasible, so it is planned now to exchange the beam pipe with a thinner one and use the additional space for a fourth pixel layer, an insertable B-layer (IBL). The IBL will serve as a backup in case of problems with the innermost layer, and will improve tracking and the determination of secondary vertices (b-tagging).

Phase I

During the second long shutdown, ATLAS detectors are being ready for ultimate luminosity by means of:

- To preserve Level-1 trigger sensitivity to high-p_T leptons despite pile-up and cavern backgrounds, various trigger upgrades are pursued: L1-Muon and L1-Calo trigger upgrades to combine them at L1 as well as possible new topological trigger elements. A hardware-based fast track finder is being developed which will provide massively parallel pattern recognition improving efficiencies in b- and τ-tagging and lepton isolation and completing global tracking at the beginning of Level-2 trigger.

- All the muon chambers on the forward small wheels (Cathode Strip Chambers) will be replaced with new chambers with more layers to secure tracking performance. In addition, new electronics is being developed for trigger improvements.

Phase II

- The forward region of the muon system has to be upgraded. A candidate option is to replace the current Monitored Drift Tubes (MDT) and the CSC muon system with smaller tubes with radius reduced from 30 to 15 mm. About 8 times less space charge is expected because the smaller cross section of the tube. Alternative option is to do both tracking and triggering with a single chamber. Several technologies are under study (micropattern gaseous detectors as *Micromegas*, MICRO Mesh Gas Structure, and *GEMs*, Gas Electron Multipliers) as currently used in the forward trigger system but optimised for higher rate operations.

- The forward calorimeter (FCAL) has to face intensive beam heating and radiation effects. Replacing forward calorimeter modules represents a serious logistical challenge, since it would require opening the end-cap cryostats and will take few years. To avoid this, ATLAS considers installing a *warm* forward calorimeter module in front of the current innermost module. This new forward calorimeter module would take the burden of the heat load, and would require new technology as well as additional shielding on its inner face, in order to protect the ID. In addition, the calorimeter systems will need a new generation of front-end electronics for better performance and a finer granularity, as well as for trigger improvements.

- At the HL-LHC conditions, the ATLAS TRT would experience extremely large occupancies, while radiation damage to the sensors and FE electronics of the silicon microstrip and pixel subsystems would seriously degrade their performance by 2019. For this phase, the ID will be entirely replaced with an all-silicon system with a finer granularity. At the same time, it is necessary to minimise the material profile of the ID: efforts are already underway to investigate increased service multiplexing and different construction schemes. In addition, increased heat generated by FE and readout electronics will require an upgraded cooling system.

2.4.4 The tentative ID upgrade

The most significant upgrade for ATLAS will be the full replacement of the whole ID foreseen at the phase II. In order to cope with the increase in pile-up events by about one order of magnitude at the higher luminosity, a silicon detector with enhanced radiation hardness is being designed.

The current ID utilizes silicon technology of pixel (Pixel detector), strips (SCT) and transition radiation technology (TRT) as seen in section 2.3. It has been designed to survive the fluence levels corresponding to 500 fb^{-1}. Operating the tracker beyond this point would lead to a degradation of the ATLAS tracking performance and hence, limit the physics output. In a typical recorded event at the HL-LHC, it is expected to have $\sim$ 200 collisions and about 10 000 tracks per bunch crossing (being $\sim$ 20 collisions and about 700 tracks per bunch crossing under the nominal LHC conditions). Simulations of the pile-up events expected from collisions under LHC and sLHC luminosities are compared in Fig. 2.13(a) and 2.13(b) (Plots provided by A. Abesselam).

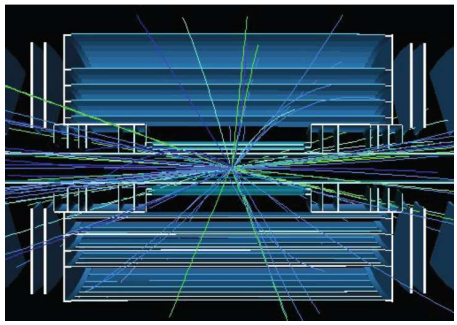

(a) Pile-up (5 collisions) at 2×10^{33} $cm^{-2}s^{-1}$.

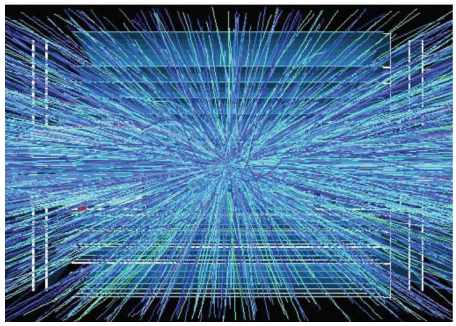

(b) Pile-up (400 collisions) at 10^{35} $cm^{-2}s^{-1}$ which includes a safety factor over the maximum expected 200.

Figure 2.13: Simulations of the pile-u events expected from proton collisions under LHC and sLHC luminosities.

To maintain the tracking performance at this increased occupancy of tracks, the upgraded

tracker must have a finer granularity than the current tracker. Fig. 2.14 shows a possible layout of a replacement tracker [42]. This layout would provide the required granularity to ensure good pattern recognition in all regions of the tracker.

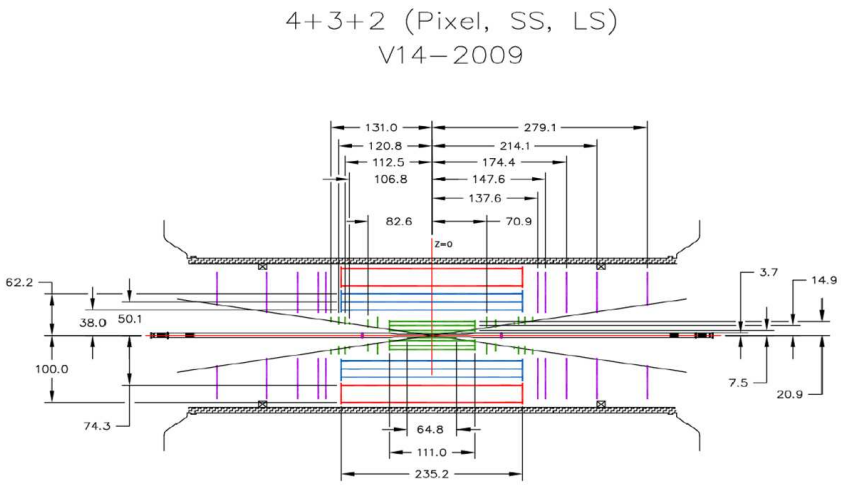

Figure 2.14: This is the current strawman layout for the upgrade of the ID, developed by the Utopia (task force to develop the upgrade inner tracker). Pixel barrel and endcap layers are shown in green. In blue the three short strip layers are represented and the two long strip layers in red. The five strip discs at each side are shown in purple. It is noted that all the TRT are replaced by strip silicon sensors.

For the upgrade at the phase-I, it is foreseen to add a 4^{th} low-mass pixel layer (at 3.3 *cm*) inside the present B-layer together with a new beampipe to improve the impact parameter resolution and compensate possible inefficiencies of the current pixel detector. It is the so-called the insertable B-layer (IBL). It is expected to have a radiation hardness up to $\sim 5\times10^{15}$ cm^{-2} at the designed peak luminosity of 3×10^{34} $cm^{-2}s^{-1}$.

For the phase-II, the pixel detector will be fully replaced by 4 barrel layers within a radius of about 3.7-20.9 cm. The barrel SCT will be extended to a 5 silicon microstrip layers at radii of 38, 49, 60, 75, and 95 cm. Currently it consists of only 4 layers from a radius of 30-51 cm. The three outer barrel SCT layers will replace the barrel TRT. The inner three layers are designed to contain short 24 mm-long strips. These are the *short strip* layers. The outer two barrel layers are the *long strip* layers. They are required to have 48 mm-long strip detectors. This design is expected to keep the occupancy below 1.6 % at the innermost radius, which is considered adequate. The tracker will be completed with a set of disks arranged normal to the beam axis.

As radiation damage scales with integrated luminosity, the radiation environment inside the tracker will increase. The short strip detectors are required to withstand 1.2×10^{15} n_{eq}/cm^2 which consists of approximately 50 % neutrons and 50 % charged hadrons, while the outer detectors will have to cope with 5×10^{14} n_{eq}/cm^2 consisting mostly in neutrons. The pixel region will withstand a radiation dose of 2×10^{16} n_{eq}/cm^2 at the innermost layer. These quantities are

summarized in Table 2.9.

All together, a detector with the described layout would have a total pixel area of about 4.5 m^2 with 300 million channels, and a total silicon-strip area of abour 150 m^2 and 40 million channels, a significant increase on the current inner tracker.

Location	f_{neq} (sLHC) [10^{15} cm^{-2}]
B-layer at 3.7 cm	22
Outer pixel layer at 21 cm	3
Middle strip layer at 38 cm	1.2
Outer strip layer at 95 cm	0.5

Table 2.9: The designed fluences, f_{neq}, predicted for the inner detector after $\sim$10 years of operation under the sLHC conditions.

A massive *R&D* program is under way to develop silicon sensors with sufficient radiation hardness [43] and to design of a ID scheme for an appropiate operation in terms of integration engineering, powering, thermal management and cooling.

2.5 RD50 Collaboration

Considering the expected total fluences of fast hadrons above 10^{16} cm^{-2} in the HL-LHC, the tracking detectors must be ultra radiation hard, provide a fast and efficient charge collection and be as thin as possible.

CERN has initiated a research program in order to find solutions for tracking systems at high radiation environment experiments as such in the HL-LHC. One of the projects is RD50[1] - ”Radiation hard semiconductor devices for very high luminosity colliders”- . It is a collaboration for research and development to provide a detector technology, which can operate safely and efficiently under an environment as described above.

The RD50 Collaboration was created in 2001 and approved in 2002. *IFIC-Valencia* is a founding member of the collaboration. Presently, RD50 counts a total of 256 members with 46 participating institutes. This comprises 38 institutes from 17 different countries in West and East Europe, 7 from North America (USA, Canada) and one from Middle East (Israel).

The main objective of the R&D program is:

To develop radiation hard semiconductor detectors that can operate beyond the limits of present devices. These devices should withstand fast hadrons fluences of the order of 10^{16} cm^{-2}, as expected for example for a recently discussed luminosity upgrade of the LHC to 10^{35} cm^{-2} s^{-1}.

Further objectives are:

[1] http://cern.ch/rd50

To develop new low-cost radiation hard technologies to instrument the tracker region.
The outline of recommendations to experiments on the optimum material, device, structure and operational conditions for detectors and on quality control procedures to ensure optimal radiation tolerance. These recomendations should be supported by tests performed on a generic demonstrator detector system tested under realistic operational conditions.
To achieve a deeper understanding of the radiation damage process in silicon and other detector relevant semiconductors with the aim to reach the above-mentioned goals and to support and collaborate with other HEP detector related research activities on radiation damage.

RD50 covers all possible semiconductor materials and technologies except diamond (RD42[2]) and cryogenic detectors (RD39[3]). The approach is to understand the relation between microscopic defects and macroscopic properties and to use the knowledge to engineer new materials with higher radiation hardness. In parallel new detector technologies are being explored and finally the improvements are applied to sensor prototypes for collider experiments.

The RD50 collaboration is organized in four research lines (see figure 2.15), which will be described in the following:

- **Defect and Material Characterization**

  The microscopic defect properties like type of defect, concentration, cross section and energy levels are determined by spectroscopic methods like *deep level transient spectroscopy* (DLTS), *thermally stimulated current* (TSC), *infrared spectroscopy*, and more. This characterization is applied to standard and new materials before and after certain radiation scenarios. A subproject of this research line is the WODEAN project, which concentrates on defect analysis on identical samples (about 240 samples irradiated with protons and neutrons) performed with the various tools available inside the RD50 network.

- **Detector Characterization**

  Simple pad detectors made from these new materials are studied by measurement of the current-voltage (IV) and capacitance-voltage (CV) characteristics, the charge collection efficiency (CCE) and trapping times as well as electric field profiles by means of the *transient current technique* (TCT). Device models are developed on basis of these measurements and optimal operational conditions are derived.

- **New Structures**

  In this research line new concepts are studied like production of thin sensors and 3D sensors. One important point is to find cost effective solutions.

- **Full Detector Systems**

  Here, the newly developed strip sensors undergo the final testing with LHC like electronics. Results from pad, ministrip and full strip sensors are being compared.

The *Full Detector Systems* can be considered as the main frame for the development of this work. This subproject is devoted to:

[2] http://graybook.cern.ch/programmes/experiments/RD42.html
[3] http://graybook.cern.ch/programmes/experiments/RD39.html

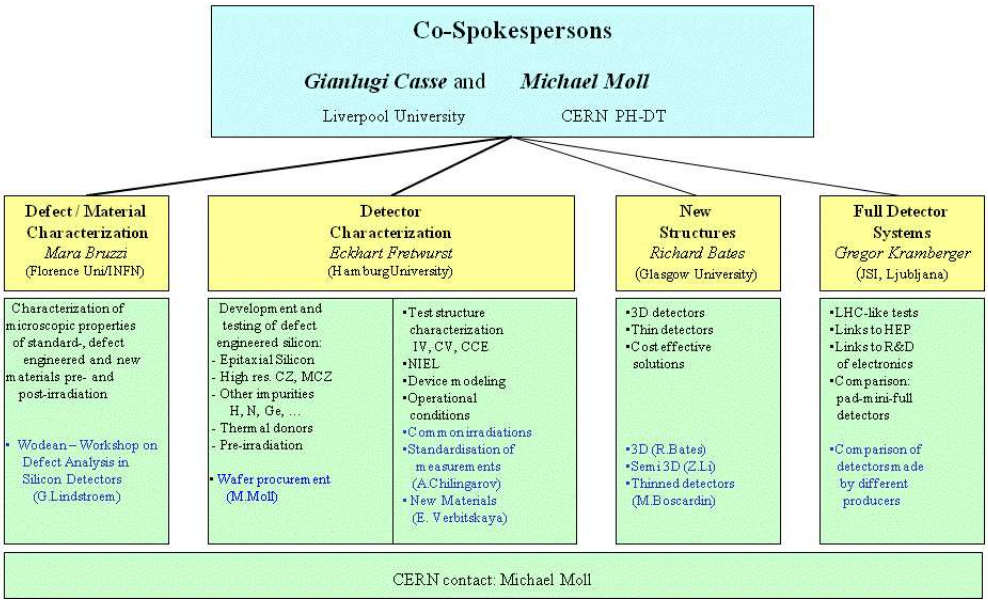

Figure 2.15: RD50 Organization: Research lines.

- Taking advantage of the LHC speed electronics to test the ultimate parameters for the present segmented detectors. Study of the lifetime limit of the system as a whole. Study the possible improvement of the present system to be implemented.
- Systematic evaluation of segmented detectors made of new RD50 materials and the studies of new structures.
- Anticpipation of the new problems connected with HL-LHC. Links to R&D on electronics.
- Device simulation of segmented devices.
- Design and realization of radiation hard pixel and microstrip detectors.
- Setup of low noise systems to measure microstrip and pixels made with thin detectors or new material to characterize very low signals.

Chapter 3

Silicon Detectors

Radiation can be detected via its interaction with the matter that constitutes suitable detectors. Charged particles and photons interact with the constituent atoms of the sensor material producing free charges that can be converted into a detectable signal. Silicon detectors have been used for energy measurements in nuclear physics since 1951 [44] and in particle physics since the 1970s. After the discovery of charmed particles in 1976, particle physicists started to develop position sensitive semiconductor detectors in order to reconstruct tracks. In 1980, Kemmer introduced the planar technique [45] for the production of silicon detectors which allowed the segmentation of the sensor.

3.1 Semiconductor theory

3.1.1 Crystal structure

Silicon is an element of the IV-th group of the periodic table, being characterised by four electrons in its outermost orbital (valence electrons) through the formation of covalent bonds in a diamond lattice structure (see Fig 3.1). Although silicon is very abundant on earth, it is rarely found in its crystalline form. Several crystal growth techniques have been developed to produce monocrystalline ingots, which will be used as the basic material for the production of detectors. These techniques will not be discussed here, but a good summary can be found in [46].

The lattice orientation of a silicon wafer is determined by the orientation of the seed used to grow the ingot. The crystal orientation is referred to the Miller indices of the cutting plane (wafer surface), denoted by (h,k,l). The notation <h,k,l> refers to the vector perpendicular to the plane (h,k,l). There are three possible orientations for a detector, namely <100>, <110>, and <111>, pictured in Fig. 3.2. The difference between the three orientations lies in the density of surface atoms near the cutting plane, and hence the density of unpaired electrons (broken covalent bonds). This will influence the surface parameters of the detectors. The <111> offers

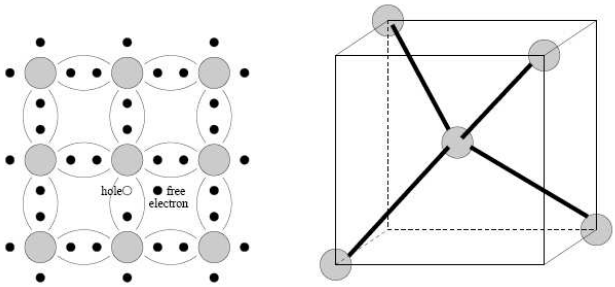

Figure 3.1: Schematic view of the covalent bonds between Si atoms and a cell of silicon lattice (diamond structure).

the tightest packaging of atom layers and thus obtains the highest energy loss for traversing particles. Nevertheless, the <100> crystal orientation is preferred as it has the lowest surface density. This improves the radiation hardness with respect to surface effects. Also, the bulk resistivity (the initial concentration of defects/doping of the wafer) will depend on the crystal growth technique as for detectors, the resistivity needs to be as high as possible in order to reach a full depletion at a low voltage.

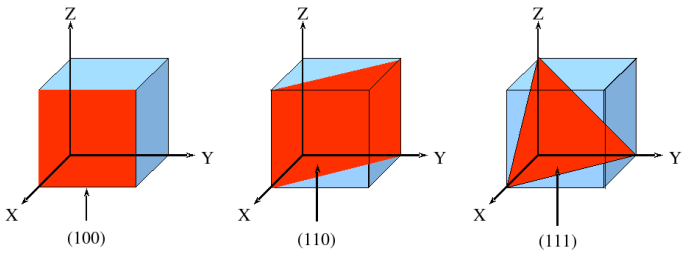

Figure 3.2: Respectively (100), (110), and (111) lattice orientation planes (pictured in red lines). The orientations <100>, <110>, and <111> refer to the perpendicular vector to the corresponding plane.

3.1.2 Band theory

For a complete understanding of the band structure, one may start considering isolated silicon atoms and then they are brought together. When the atoms are far apart, the possible energy levels which can be occupied by electrons are quantized into discrete energy levels and they are the same for each atom. As, for instance, two atoms are brought together, each of the energy level for each atom changes because of the influence of the other atom. However, since two electrons can not have the same quantum numbers according to the Pauli exclusion principle, the discrete energy level (atomic orbital) must split into two sublevels (molecular orbitals) in

order that each electron can occupy a distinct quantum state. The amount of splitting depends strongly on the internuclear distance of the two atoms. The closer the two nuclei, the stronger the perturbation and larger the splitting.

If three atoms are close together, a particular energy level splits into three separate levels of slightly different energies. If several atoms are brought together into a molecule, their atomic orbitals split and produce a number of molecular orbital proportional to the number of atoms. Figure 3.3 shows a schematic view of the evolution of the energy spectrum from an atom (a), to a molecule (b) and to a solid (c). It must be noted that the splitting also depends on the atomic orbital. For the deepest levels, the splitting is smaller because the orbital is tightly bound to its own nucleus and it is not greatly affected by the perturbation. In that orbitals, the electrons are found located in particular atoms even when the internuclear distance is small. Higher-energy levels, which have larger radii, are only loosely bound to their own nuclei. These levels are occupied by the valence electrons that are deslocated as they are part of the whole system.

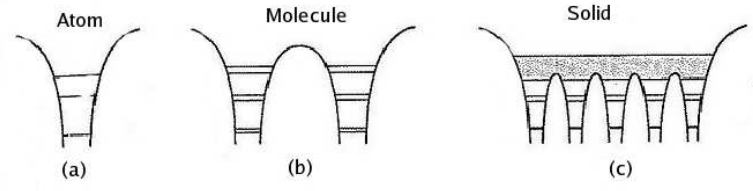

Figure 3.3: Schematic view of the evolution of the energy spectrum from an isolated atom (a), to a molecule (b) and to a solid (c).

When a large number of atoms (of order 10^{23} or more) are brought together to form a solid, the number of orbitals becomes exceedingly large, and the difference in energy becomes very small, so the levels may be considered to form a continuous band of energy than the discrete energy levels of single atoms. However, some intervals of energy contain no orbitals i.e., the forbidden energy levels form band gaps. As the energy range within a band depends on the internuclear distance and does not depends on the number of atoms in the system, the larger the number of atoms, every band will contain a larger number of energy levels distributed approximately in the same energy range for a particular internuclear distance.

The way how these bands are formed and filled determine whether the crystal has insulator, metal or semiconductor properties. The structure of an insulator, semiconductor and conductor are shown in Fig. 3.4. The lower-energy, almost fully occupied band is called the valence band and the upper-energy, almost unoccupied band is called the conduction band.

In a semiconductor, at $0K$ all the electrons will occupy the valence band and there can be no net current flow. There is an energy gap between this and the conduction band. At room temperature (300 K) some of the electrons become thermally excited to the conduction band leaving holes in their place. Any hole can be filled by an electron from a neighbour atom, thus resulting in the net flow of the hole. Holes can therefore be regarded as positive charges and can be described with a ”positive charge mobility”. Thermal excitation produces new electro-hole pairs while other pairs recombine.

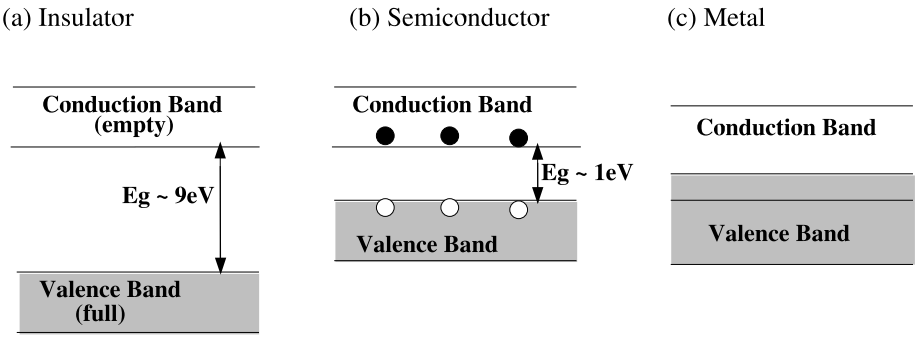

Figure 3.4: Band structures of (a) an insulator, (b) a semiconductor and (c) a conductor.

An insulator has similar band structure to a semiconductor, except that the bandgap energy is higher. This means that there are no free electrons and holes under ordinary temperatures. In a conductor, there is no band gap between the occupied and unoccupied states, which means that the electrons are able to move freely even at low temperatures.

Let consider silicon atoms. Figure 3.5 shows the band splitting of silicon whose atomic structure is $1s^2\ 2s^2\ 2p^6\ 3s^2\ 3p^2$.

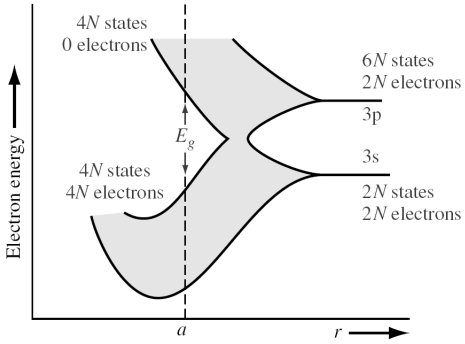

Figure 3.5: The splitting of the 3s and 3p states of silicon into the allowed and forbidden energy bands as a function of the distance between the atoms. N is the number of atoms.

Ten of the fourteen silicon atom electrons occupy deep energy levels ($n = 1, 2$) which are completely full and tightly bound to the nucleus. The four remaining valence electrons are relatively weakly bound to the nucleus at the $n = 3$ level. At a particular internuclear distance, the 3s and 3p states interact and overlap. The bands split but now four quantum states per atom are in the lower band and four quantum states are in the upper band. At absolute zero degrees, electrons are in the lowest energy state, so that all states in the lower band (valence band) will be filled and all states in the upper band (the conduction band) will be empty. The bandgap energy

E_g between the top of the valence band and the bottom of the conduction band is the width of the forbidden energy band. In silicon, the width of the gap is 1.12 eV.

The Bloch Teorem

It has been discussed qualitatively how and why bands of allowed and forbidden energies are formed in a crystal. These concepts can be developed more rigurously by considering quantum mechanics as shown here.

The behaviour of an electron in a crystalline solid is determined by studying the appropiate Schrödinger equation [47]. This may be written as

$$\left(-\frac{\hbar^2}{2m_e}\nabla^2 + V(\mathbf{r})\right)\psi(\mathbf{r}) = E\psi(\mathbf{r}) \tag{3.1}$$

where $V(\mathbf{r})$ is the crystal potential seen by the electron, and $\psi(\mathbf{r})$ and E are respectively, the wave function and the energy of this electron. The crystal potential has a periodic nature since the atoms in a crystal are located at regularly spaced well defined positions. For silicon atoms the lattice constant is 5.43095 Å at 300 K. Thus an electron propagating through a crystal will interact to every atom in the solid as well as with other electrons. Every electron will thus see a periodic potential satisfying,

$$V(\mathbf{r} + \mathbf{a}) = V(\mathbf{r}) \tag{3.2}$$

where a is the lattice constant. According to the *Bloch theorem* [47], the solution of equation 3.1 for a periodic potential has the form

$$\psi_{nk}(\mathbf{r}) = u_{nk}(\mathbf{r})\, e^{(ik\cdot r)} \tag{3.3}$$

and these functions are called Bloch functions. $u_{nk}(\mathbf{r})$ modulates the amplitude of the wave function associated with the free particle motion of electrons from one cell to the next, as shown in Figure 3.6 and has the same period as the lattice itself,

$$u_{nk}(\mathbf{r} + \mathbf{a}) = u_{nk}(\mathbf{r}) \tag{3.4}$$

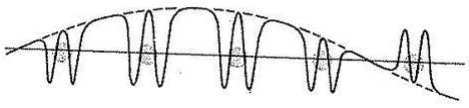

Figure 3.6: The Bloch function wave. The smooth curve represents the wave $e^{ik\mathbf{r}}$ which is modulated by the atomic like function $u_{nk}(\mathbf{r})$

The $\hbar k$ is referred to as the crystal momentum and k is a quantum number characteristic of the discrete translational symmetry of the periodic crystal. The second index n of the wave function is known as the band index.

The wave function, $\psi_{nk}(\mathbf{r})$ of a particular electron is a crystal orbital, as it is deslocalized through the solid, and not localized around any particular atom. Thus the electron is shared by the whole crystal. The probability density $|\psi_{nk}(\mathbf{r})|^2$, gives the probability of finding the electron at a particular position in the lattice.

The variation of the parameter k will lead to a continuous variation of the eigenvalues E_{nk} and this continuous variation of E_{nk} is what is meant the term band structure. The number of bands can be large and only the lowest ones are occupied by electrons. Each band covers a certain energy range. The energy intervals between the bands constitute the energy gaps, which are forbidden energies that cannot be occupied by electrons.

Electron Effective Mass

The movement of an electron in a lattice will be different from that of a free electron. The electron motion through the crystal is visualized as a localized wave packet composed of a superposition of Bloch functions of different wave momenta around an average wave momentum k. It is important to note that the same concepts are applied to the movement of a hole considering electrons and holes as charge carriers. In addition to an externally applied force, there are internal forces in the crystal which influence the motion of electrons/holes in the lattice. It can be written,

$$F_{total} = F_{ext} + F_{int} = m \cdot a \tag{3.5}$$

where F_{total}, F_{ext}, and F_{int} are the total force, the externally applied force and the internal forces, respectively, acting on a particle in a crystal. The parameter a is the acceleration and m is the rest mass of the particle.

Since it is difficult to take into account all the internal forces, it is written the equation,

$$F_{ext} = m^* \cdot a \tag{3.6}$$

where the acceleration a is now directly related to the external force. The parameter m^*, called the effective mass, takes into account the particle mass and also takes into account the effect of the internal forces.

It can be proved that the effective mass of an electron in a crystal is related to the dispersion relation of the energy E with the crystal momentum k, that is, to the band structure itself.

For a 1-D crystal, if an electric field, ϵ, is applied to the charge carrier, it is obtained

$$F_{ext} = -e\epsilon = m^* \cdot \frac{dv_g}{dt} \tag{3.7}$$

where v_g is the group velocity of the electron/hole wave packet that is given by

$$v_g = \frac{dw}{dk} = \frac{1}{\hbar} \nabla_k E \tag{3.8}$$

Using the equations 3.7 and 3.8, it is obtained

$$m^{*-1} = \frac{1}{\hbar^2} \nabla_k \nabla_k E \tag{3.9}$$

For an anisotropic band structure as for electrons in Si or Ge, the m^* can be larger along one direction than another, depending on the shape of the energy bands. To say that the mass depends on the direction just means that it depends on the values of k_x, k_y and k_z that determine the direction of the wave packet. In this case the scalar effective mass is formally replaced by an effective mass tensor, $\overleftrightarrow{m^*}$:

$$(\overleftrightarrow{m^*})^{-1}_{ij} = \frac{1}{\hbar^2} \frac{\partial^2 E(k)}{\partial k_i \partial k_j} \tag{3.10}$$

The effective mass is a parameter that relates the quantum mechanics to the classical force equations. In most instances, the electron (hole) in the conduction (valence) band can be thought of as a classical particle whose motion can be modeled by Newtonian mechanics, provided that the internal forces and quantum mechanical properties are taken into account through the effective mass. That is, a electron in a periodic potential is accelerated relative to the lattice in an applied electric (o magnetic) field as if the mass of the electron were equal to an effective mass.

3.1.3 Intrinsic silicon

The thermal excitation of an electron from the valence band to the conduction band creates free charge carriers in both bands (electrons in the conduction band and holes in the valence band). The number n of energy levels in the conduction band occupied by electrons in equilibrium is given by:

$$n = \int_{E_c} N_e(E) F_e(E) dE \tag{3.11}$$

where E_c is the energy value at the bottom of the conduction band. $N_e(E)$ is the density of states per unit volume for electrons which is given by [47]

$$N_e(E) = \frac{1}{2\pi^2} (\frac{2m_e^*}{\hbar})^{\frac{3}{2}} \sqrt{E - E_c} \tag{3.12}$$

The probability that a state of energy E is occupied by an electron comes from the Fermi-Dirac distribution, F(E):

$$F_e(E) = \frac{1}{1 + exp(\frac{E - E_F}{\kappa_B T})} \tag{3.13}$$

where κ_B is the Boltzmann constant and T is the absolute temperature with $\kappa_B T\ (300\ K) \sim 0.026\ eV$. E_F is the Fermi energy and typically corresponds to a point close to the halfpoint of the band gap for intrinsic silicon. It represents the energy level which is occupied with a probability of exactly 0.5. Therefore, the concentration of electrons in the conduction band is integrated to give:

$$n = N_C exp(-\frac{E_C - E_F}{\kappa_B T}) \tag{3.14}$$

with E_C being the energy at the bottom of the conduction band and the effective density of states in the conduction band, N_C, given by:

$$N_C = 2(\frac{m_e^* \kappa_B T}{2\pi\hbar^2})^{3/2} \tag{3.15}$$

where m_e^* is the effective mass of the electron in the conduction band.

It is useful to calculate the equilibrium concentration of holes, p, in the valence band. The distribution function $F_h(E)$ for holes is related to the electron distribution function $F_e(E)$ by:

$$F_h(E) = 1 - F_e(E) \tag{3.16}$$

because a hole is the absence of an electron in the valence band. From equations 3.13 and 3.16 one obtains:

$$F_h(E) = \frac{1}{exp(\frac{E_F - E}{\kappa_B T}) + 1} \tag{3.17}$$

If the holes near the top of the valence band behave as particles with effective mass, m_h^*, the density of states per unit volume for holes is given by

$$N_h(E) = \frac{1}{2\pi^2}(\frac{2m_h^*}{\hbar})^{\frac{3}{2}} \sqrt{E_v - E} \tag{3.18}$$

where E_V is the energy at the top of the valence band. Proceeding as in equation 3.14, one can compute the hole concentration in the valence band:

$$p = N_V exp(\frac{E_V - E_F}{\kappa_B T}) \tag{3.19}$$

where the effective density of states in the valence band, N_V, is given by:

$$N_V = 2(\frac{2\pi m_h^* \kappa_B T}{2\pi\hbar^2})^{3/2} \tag{3.20}$$

By taking the ratio of equations 3.14 and 3.19, the E_F is obtained,

$$E_F = \frac{E_C + E_V}{2} + \frac{\kappa_B T}{2} ln\left(\frac{N_V}{N_C}\right) \tag{3.21}$$

In an intrinsic semiconductor, the concentration of holes is equal to the concentration of free electrons and is called the intrinsic carrier density:

$$n = p = n_i = \sqrt{N_C N_V} exp(-\frac{E_G}{2\kappa_B T}) \propto T^{\frac{3}{2}} exp(\frac{-E_G}{2\kappa_B T}) \tag{3.22}$$

where $E_G = E_C - E_V$ denotes the gap energy (this decreases with the temperature, and for silicon at room temperature $E_G = 1.12\ eV$ [47]). The only assumption made is that the distance of the Fermi level from the edge of both bands is large in comparison with $\kappa_B T$. These results hold for impurity ionization as well.

Multiplying the two distributions results in

$$np = n_i^2 = N_C N_V exp(-\frac{E_G}{\kappa_B T}) \tag{3.23}$$

This property is referred to as the *mass action law*. It is valid for intrinsic or doped material in thermal equilibrium.

3.1.4 Doped silicon

It is possible to compute the intrinsic concentration of carriers in silicon from equation 3.23 being $1.45 \times 10^{10} cm^{-3}$ at 300 K [48]. Taking into account the density of the material (see appendix A), this implies that one out of 10^{12} atoms is ionised. To increase the concentration of carriers, silicon can be doped with impurity atoms. Such impurities must be atoms of the IIIrd or the Vth group of the periodic table. These will replace some silicon lattice atoms and form covalent bonds with the neighbouring atoms as shown in Fig. 3.7.

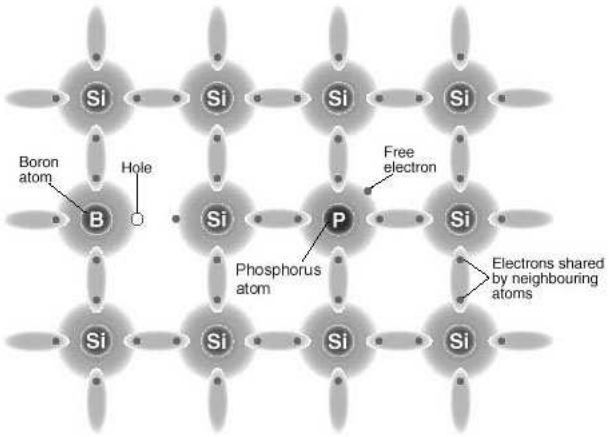

Figure 3.7: Schematic of doped silicon with Boron atoms which only have three valence electrons and leaving an extra hole and Phosphorous atoms with five electrons in its valence shell leaving an extra electron.

The elements of the Vth group, as Phosphorous (P), are called ”donors”. They have five electrons in the valence shell; four of them form covalent bonds with silicon atoms and the fifth one is only weakly bounded so that thermal energy is enough to bring it into the conduction band. From the band point of view, the donor atoms create energy levels near to the top of the band gap which corresponds to the states of the fifth electron apported by the donor atoms. As the energy gap of the new states with respect to the conduction band is rather small, at room temperature, all the donors are positively ionised thus, the concentration of free carriers is equal to the concentration N_d of impurities since $N_d >> n_i$. A silicon crystal doped with donors is called n-type because of the excess of free negative charge carriers. In this case, the conductivity in the crystal is determined by the flow of these electrons. They are the majority carriers while the holes are denoted minority carriers.

Another type of doping is due to the so-called ”acceptors”, elements of the IIIrd group as Boron (B). They have three electrons in the valence shell. It creates electron deficiencies when replace silicon atoms in the lattice. The resulting holes are easily filled by thermally excited electrons coming from silicon atoms. The acceptor atoms create energy levels near to the bottom of the band gap which corresponds to the unoccupied states of the hole left by the acceptor atoms. As the energy gap of the valence band to the new states is rather small, at room temperature they will be occupied and hence the impurity atoms are negatively ionised and holes are created in the silicon. The concentration of free carriers is equal to the concentration N_a of impurities since $N_a >> n_i$. A crystal doped with acceptors is denoted as p-type, and the conduction is mainly due to holes, its majority carriers. The two kinds of doped silicon is ilustrated in Fig. 3.8.

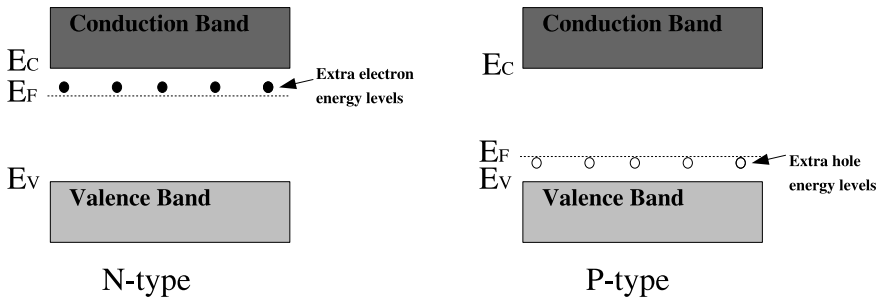

Figure 3.8: The extra levels in the band model created by the impurity atoms are shown for n-type and p-type silicon. In n-type material there are electron energy levels near the top of the band gap so that they can be easily excited into the conduction band. In p-type material, extra holes energy levels in the bandgap allow excitation of valence band electrons, leaving mobile holes in the valence band.

Carrier Transport

Free electrons and holes in a semiconductor are constantly undergoing random thermally motion, but this alone does not result in a net current flow. These charge carriers in silicon have a thermal velocity of the order $10^4\ m/s$ [49]. If now it is considered the application of an external electric field, E, the charge carriers suffer an acceleration. The carriers scatter frequently, losing momentum in each collision, nevertheless the charge carriers will travel at an average drift velocity given by,

$$v_{drift,e} = -\mu_e E \tag{3.24}$$

$$v_{drift,h} = \mu_h E \tag{3.25}$$

where μ_e and μ_h are the mobilities of the electrons in the conduction band and the mobility of the holes in the valence band respectively. It is defined to be positive for both e^- and holes. At lower electric fields, the drift velocity is small compared to the thermal velocity, and the scattering rate is independent of the field strength. So, the drift velocity increases linearly with the field strength, and the mobilities will be roughly constant. However, as the field strength and drift velocity get high, scattering occurs more frequently, and eventually the velocity saturates. Thus, a field dependence mobility model assumes

$$v(E) = \frac{\mu E}{1 + \frac{\mu E}{v_{sat}}} \tag{3.26}$$

where v_{sat} is the drift saturation velocity. The drift velocity of holes in silicon saturates at an applied electric field of approximately $10^5\ V/cm$ and it corresponds to a velocity of $10^7\ cm/s$. For electrons the maximum drift velocity is approximately $2\times10^7\ cm/s$, at a lower applied electric field of $4\times10^3\ V/cm$ [50].

Apart from this, it is important to note that the electron and hole mobilities may be different; for example, the electron mobility in silicon is about 3 times the hole mobility at 300 K as seen in Table 3.1. The hole motion is smaller due to the holes can be occupied by both free electrons and atomic electrons. Its effect is that the effective mass of holes in silicon is higher than the one of electrons [49] and the mobility is related to the charge carriers effective mass by means of equation 3.27.

$$\mu_{e,h} = e\tau_{e,h}/m^*_{e,h} \tag{3.27}$$

where $m^*_{e,h}$ is the effective mass of the electron or hole and $\tau_{e,h}$ refers to the average time taken between two collisions of the free moving carriers.

	$\mu_e(cm^2V^{-1}s^{-1})$	$\mu_h(cm^2V^{-1}s^{-1})$
Silicon	1350	480
Germanium	3900	1900

Table 3.1: Mobilities for electrons and holes at 300 K for silicon and germanium materials.

In addition, in silicon at a temperature range of $100 \leq T \leq 400\ K$ the mobility varies as T^{-m} where $m = 2.5$ for electrons and $m = 2.7$ for holes [49].

The drift current density, J_{drift}, is given by

$$J_{drift} = \rho v_{drift} = \rho \mu E \tag{3.28}$$

where ρ is the charge density. It depends on considering the electron or the hole current and is given by $\rho = qn$ for electrons and $\rho = qp$ for holes. The resistivity ϱ is defined as the proportionality constant between the electric field E and the drift current density J_{drift}:

$$E = \varrho J_{drift} \tag{3.29}$$

while it depends on the concentration of both free carriers (electrons and holes) and on their mobilities, μ_e and μ_h:

$$\varrho = \frac{E}{J_{drift}} = \frac{1}{q(\mu_e n + \mu_h p)} = \frac{1}{\sigma} \tag{3.30}$$

The conductivity, σ, is also defined in the above equation.

For intrinsic silicon, one obtains $\varrho \simeq 235\ K\Omega cm$. The charge neutrality condition governs the number of carriers:

$$n + N_a^- = p + N_d^+ \tag{3.31}$$

When the net impurity concetration $\mid N_d - N_a \mid$ is much larger than the intrinsic carrier concentration n_i, then $n = N_d - N_a$ in the conduction band and $p = N_a - N_d$ in the valence band. So, for p-type silicon,

$$\varrho \simeq \frac{1}{q\mu_h N_a} \tag{3.32}$$

and analogously for n-type silicon,

$$\varrho \simeq \frac{1}{q\mu_e N_d} \tag{3.33}$$

Both types of silicon can be used as bulk material for detectors. However, the p-type is preferred for very high radiation environment as expected at HL-LHC as it will be shown in chapter 4.

3.2 The pn-junction

A *pn* junction is one of the elementary building blocks of almost all semiconductor devices such as diodes, transistors, solar cells, LEDs, and integrated circuits. It basically the interface formed by contacting p-type and n-type silicon material. The p-type silicon is electrically neutral but has a population of holes in the valence band with a density of N_a and the n-type silicon is

also electrically neutral but has a population of electrons in the conduction band with a density of N_d. These charge carriers are free to move. When this two semiconductors are joined there is a gradient in these carriers concentrations resulting in the formation of two opposite currents across the junction:

- **Diffusion Current,** J_{diff}

  Due to the density gradients, the electrons of the n-side start to diffuse towards th p-side and recombine with the holes. The holes in the p-side diffuse into the other direction and recombine with the electrons in the n-side. It results in a diffusion current:

  $$J_{diff} = q(D_n \nabla n - D_p \nabla p) \tag{3.34}$$

  with ∇n and ∇p the charge carrier gradients across the junction and D_n and D_p the diffusion coeficients for electrons and holes respectively given by the Einstein relations [51]:

  $$D_{n,p} = \frac{\kappa_B T}{q} \mu_{e,h} \tag{3.35}$$

- **Drift Current,** J_{drift}

  The diffusion of the electrons (holes) leads to fixed positive charged (negative) ions in the n-type (p-type) silicon. Due to these space charge regions an electric field will be developed from the n-side towards the p-side. The electric potential can form a barrier for further diffusion and it will cause carrier drift in the opposite direction to diffusion. The drift current as explained above is given by:

  $$J_{drift} = q(\mu_e n + \mu_h p)E \tag{3.36}$$

The device will reach a state of equilibrium when the net current flow is zero,

$$J_{drift} + J_{diff} \equiv 0 \tag{3.37}$$

A ”depletion region” is created with much lower carrier concentration than the bulk material. Due to doping, the Fermi level will move towards the valence band for p-type material and towards the conduction band for n-type material. At thermal equilibrium, the Fermi level at the pn-junction has to line up. This will shift the valence and conduction band leading to a barrier potential [49]. If the Fermi levels were unequal, then net current flow would occur. The characterisctics of the pn-junction are plotted in Fig.3.9.

The height of this barrier potential depends on the purity of the material and, assuming that N_a and N_d is much bigger than n_i, it can be calculated from:

$$V_{bi} = \frac{kT}{q} ln \frac{N_a N_d}{n_i^2} \tag{3.38}$$

It is called the built-in potential and is of the order of a few hundred of milivolts. The barrier is high enough that few electrons can cross from n-type to p-type region reducing the diffusion current.

Hence by joining n- and p-type silicon together a region is created which is depleted of free charge carriers and experiences a built-in electric field due to the ionized atoms in the junction. This region is perfectly suited to the detection of radiation. Incident radiation on this region ionizes the silicon and the resultant electron-hole pairs will be accelerated under the built-in electric field. They will move in opposite directions to produce a measurable signal. It is the operation principle for radiation detectors in which the free space charge region has to be extended over the full sensitive area to increase the collected signal as will be discussed in the following.

Reverse bias

In equilibrium, the diffusion of electrons (holes) due to the unequal majority charge carrier concentrations in the n-type and p-type materials is compensated by the drift of electrons (holes) in the opposite direction induced by the space charge. An external voltage applied to the pn-junction will disturb this balance and influence the drift and diffusion currents of the charge carriers and therefore, the space charge region. The total current density through the junction of an ideal diode can be described by the Shockley equation [49]:

$$J = J_0(e^{\frac{qV}{\kappa_B T}} - 1) \tag{3.39}$$

The saturation current density, J_0 is given by

$$J_0 = \frac{qD_p p_{n0}}{L_p} + \frac{qD_n n_{p0}}{L_n} \tag{3.40}$$

where D_p and D_n are the diffusion coefficients for electrons and holes, p_{n0} and n_{p0} are the hole density in the n-side and the electron density in the p-side at thermal equilibrium, and $L_p = \sqrt{D_p \tau_p}$ and $L_n = \sqrt{D_n \tau_n}$ are the diffusion lengths of holes and electrons.

The space charge region may be extended by the application of an external potential of the same sign as V_{bi} across the junction. If a negative potential is applied to the p-side (or a positive potential to the n-side), the barrier for electrons moving from n- to p-side is increased and the diffusion current in this direction decreases exponentially resulting in a very small current. The pn-junction is said to be in the *reverse* bias region as seen in Fig. 3.10. The current in reverse bias direction is saturated at saturation current density J_0.

By changing the polarity of the applied voltage the barrier is reduced and the diffusion current increases through the junction as minority carriers are injected into the junction. Charge created in the neutral, non-depleted zone recombine with free carriers and is lost. In this case, the pn-junction is *forward* biased.

Generally, semiconductor radiation detectors work using reverse-biased pn junctions, where a positive bias is applied to the n-type region or a negative bias to the p-type region. In this scenario, the total potential across the junction is the sum of the built-in potential, V_{bi}, and the applied bias, V. Since the depletion region contains few charge carriers, the external bias produces very little current flow. Instead, electrons in the n-type and holes in the p-type will be attracted away from the edges of the depletion region, causing it to widen. The electric field and the width of the depletion zone can be calculated by solving the one-dimensional Poisson equation according to [49]

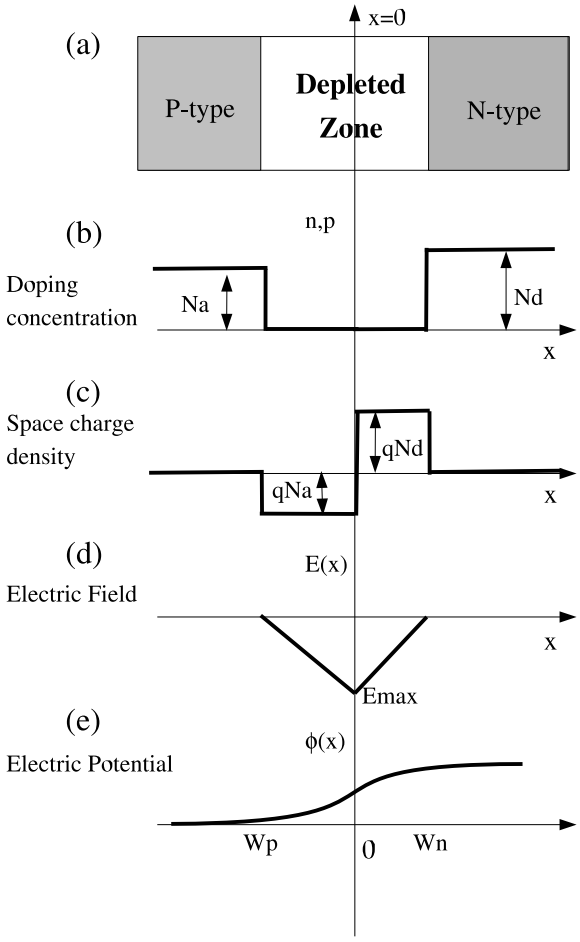

Figure 3.9: Diagram of the interface region of a pn-junction, each subdiagram shows a variable as a function of distance with $x = 0$ just in the junction. (a) The p-type and n-type silicon. (b) The free charge carriers concentration with N_a holes in the p-type side and N_d electrons in the n-type one; note the depletion of carriers in the depletion region. (c) The fixed space charge density equal to the doping concentration multiplied by the electron charge. (d) The electric field, E. (e) The electric potential, ϕ.

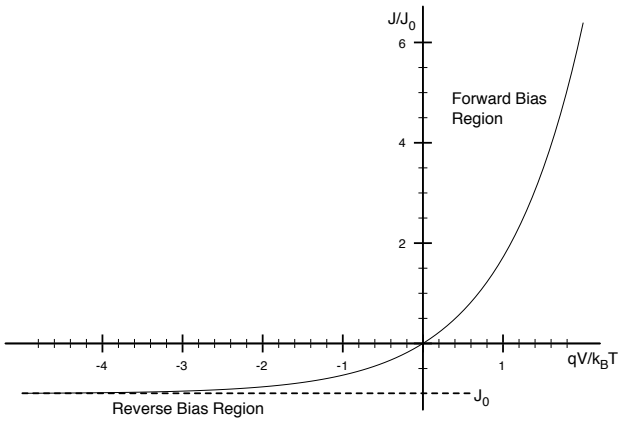

Figure 3.10: Ideal current-voltage characteristics of a pn-junction.

$$\nabla E = -\frac{d^2V}{dx^2} = \frac{\rho}{\varepsilon_{Si}} \tag{3.41}$$

where the permittivity of silicon is $\varepsilon_{Si} = \varepsilon_r \cdot \varepsilon_0$, being ε_r the silicon dielectric constant and ε_0 is the permitivity of the vacuum. Assuming an abrupt junction and absence of free carriers in the depleted region, the charge density, ρ, is given by the spatial charge that in doped semiconductors, is about equal to the impurity concentration

$$\rho(x) = \begin{cases} -qN_a & -W_p < x < 0 \\ qN_d & 0 < x < W_n \end{cases} \tag{3.42}$$

The width of the depletion zone results in

$$W = W_n + W_p = \sqrt{\frac{2\varepsilon_{Si}}{q \mid N_{eff} \mid}(V_{bi} + V)} \tag{3.43}$$

where W_n and W_p are the width on the n- and p-side respectively. $N_{eff} = N_d - N_a$ is the effective doping concentration. Typically $V \gg V_{bi}$, hence V_{bi} is commonly neglected. The depletion width in terms of the resistivity from the equations 3.32 and 3.33 reads:

$$W = \sqrt{2\varepsilon_{Si}\varrho\mu V} \tag{3.44}$$

where μ indicates the majority carrier mobility.

It is worth to note that the higher the resistivity of the material, the lower bias voltage is necessary to fully deplete a given thickness.

The applied voltage required to extend the depletion region over the complete thickness of the device is called the depletion voltage, V_{fd} and can be calculated using the equation 3.43 for a detector of thickness d

$$V_{fd} \approx \frac{q}{2\varepsilon_{Si}} \mid N_{eff} \mid d^2 \tag{3.45}$$

If the applied bias exceeds the full depletion voltage, the device is said to be overdepleted and a constant field of $(V - V_{fd})/d$ is added at each point in the device. If an external potential with the opposite sign to V_{bi} is applied to the detector, the pn-junction is said to be *forward* biased. The barrier for electrons moving from n- to p-side is decreased. The current flow in this direction increases exponentially (see Fig. 3.10), not being suitable for particle detection. Detector behaviour in forward bias is not discussed here.

Capacitance

Since a reverse biased pn-junction consists of an insulating layer between 2 conducting regions, it acts as a capacitor. The space charge region has a charge proportional to the detector active area (A), the detector thickness and the effective doping concentration. Equation 3.46 provides an expression for the capacitance of the detector [52] which is calculated from the charge carriers accumulated in the depleted zone as the applied voltage changes.

$$C(V) = \frac{dQ}{dV} = \varepsilon_{Si}\frac{A}{W(V)} = A\sqrt{\frac{\varepsilon_{Si} q \mid N_{eff} \mid}{2\,V}} \quad for \quad W \leq d \tag{3.46}$$

Therefore as the applied bias voltage increases, the effective carrier concentration decreases since the region is becoming depleted of free charge carriers. The capacitance of the detector decreases as the bias voltage applied is increased. When the depletion region extends across the whole thickness of the detector at the full depletion voltage ($W(V_{fd}) = d$), the capacitance of the detector saturates at the value calculated by the geometrical capacitance being

$$C_{geom} = \frac{\varepsilon_{Si} A}{d} \tag{3.47}$$

Detector Currents

When a silicon detector operates under reverse bias conditions, the resulting current is called the *leakage current*. The current that flows through a pn-junction has several components, namely; the diffusion current through the barrier (reverse current), generation currents in the space charge region, surface current, and currents associated with the edge of the device. For an ideal device at low bias voltages the reverse current, described before, will dominate. However, for real devices this is rarely the case. The generation current arises from electron-hole pair generation in the space charge region of the device due to thermal excitation of electrons from the valence band to the conduction band. It is due to recombination-generation midgap

states within the depletion region induced by crystal defects and impurities presented at silicon. Since the charge carrier density is low, the recombination processes are improbable and generation dominates. Thermally generated electron-hole pairs in the undepleted region of the device do not contribute to the current as in the lack of electric field they simply recombine. The generation current (J_g) is given by [49]

$$J_g = \frac{qn_iW}{2\tau_g} \propto \sqrt{V} \tag{3.48}$$

where τ_g is the carrier generation time in the space charge region. Also, generation current is proportional to the square root of the applied bias from the equation 3.43. The generated charge carriers are to be considered as a noise source for semiconductor sensors. Due to the temperature dependence of n_i and τ_g the generation current has a temperature dependence given by

$$J_g(T) \propto \frac{n_i}{\tau_g} \propto T^2 exp\left(-\frac{E_g}{2\kappa_B T}\right) \tag{3.49}$$

Typically at operational bias voltage the generation current dominates the reverse current in the device with a strong dependence on the temperature. The *leakage current* measured may be corrected to a reference temperature using the following correction:

$$I(T) = \left(\frac{T}{T_{ref}}\right)^2 exp\left(-\frac{E_g}{2\kappa_B}[\frac{1}{T} - \frac{1}{T_{ref}}]\right) I(T_{ref}) \tag{3.50}$$

where E_g is the silicon bandgap (1.12 eV), κ_B the Boltzman constant and T the absolute temperature.

The currents through the surface and the edges of the detector can be eliminated by the use of an implant surrounding the junction region, known as the guard ring structure that will be explained later. The currents then flow through the guard ring rather than the sensor reducing the sensor leakage current to a negligible level. Therefore, the leakage current can be controlled to a certain extent by proper design and careful manufacturing process.

Breakdown Voltage

If the reverse bias is increased to very high values, electrical breakdown occurs at the junction which is the region of the maximum electric field. An avalanche breakdown occurs as the free charges acquire enough energy from the high electric field and moving through the medium produce new electron-hole pairs by ionization. These can gain enough energy to create further microdischarges. The voltage at which the electrical breakdown occurs is called the breakdown voltage, V_{bd}.

3.3 Silicon detectors

The symmetrical abrupt pn-junctions as decribed in previous section is a simplified version of the most common type of junction used in HEP (High Energy Physics) detector applications.

From the condition of charge neutrality of the system (equation 3.31), it follows that the total positive and negative charge in the space charge region have to be equal. It gives

$$N_a W_p = N_d W_n \tag{3.51}$$

Basically, a silicon detector consists to one side of the junction has a large doping concentration, for example a heavily doped n-type material (denoted by n^+), compared to the other side which is lightly doped, for example, a p-type region (p^-, shortened simply to p). It has been realized a n^+p junction. In that case the depth of the depleted region on the n^+side is small compared to the depth on the weakly doped p-side. The electric field always grows from the n^+ implant and can be extended far into the p bulk silicon with increasing reverse bias. Hence the n^+ implant maybe made only microns wide and the depletion region in the p bulk silicon can be a few hundred microns wide.

Microstrip detectors are a very common type of silicon detectors used in tracking systems of HEP experiments. To achieve a precise position measurement, the n-side of the junction is divided into many parallel strips. Each strip-bulk junction acts as an individual silicon detector.

3.3.1 Structure features

n^+-on-p

In a typical n^+-on-p silicon detector (see Figure 3.11), the bulk of the detector is usually p-type silicon with a doping concentration of 10^{12} atoms/cm^3. This should be compared to the intrinsic carrier concentration which is of the order of 10^{10} cm^{-3}. The microstrips corresponds to the n^+ implants on the top of p-type silicon surface, typically 10-20 μm wide, 1-3 μm deep. Each of the n^+ implanted strips is bonded to the front-end readout electronics, which amplifies the signal produced by ionizing radiation. An advantage of using n^+ implants as readout electrodes is that the signal is basically provided by the movement of electrons that have three times higher mobility than holes. It results in a much shorter collection times and therefore higher charge collection efficiencies [53]. In addition, other elements are necessary to form a proper silicon detector.

- An oxide layer (approximately 1-4 μm thick) lies on top of the implanted strips, known as the AC oxide, which prevents the leakage current flowing directly to the readout electronics.
- The signal from each of the strips is AC coupled to a metal(Al) strip lying directly above the n^+ strip implants, and the charge is read out through this ohmic contact.
- As a bias is applied across the device, a DC path is required between the back and front contacts. The DC path will carry the leakage current of the device, dominated by thermally generated carriers in the bulk. The DC path on the strip side of the device is realized via a common bias line. It is a n^+ implant running across all strips and connected to each strip via a polysilicon bias resistor and returned to the backplane.
- The front segmented face of the detector must have *p-stop* or *p-spray* [54] to maintain isolation between the n^+ implants as explained in the section 3.3.3.

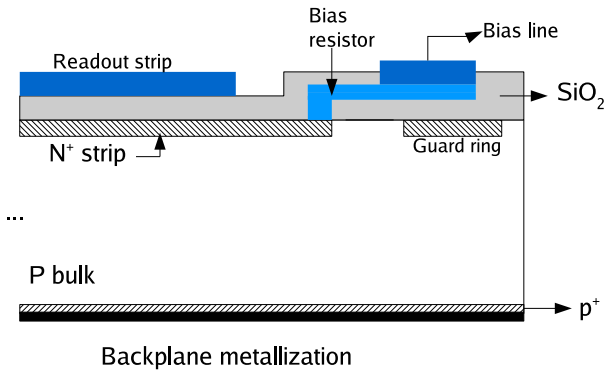

Figure 3.11: Schematic transversal view of a n^+p silicon detector. The bulk type is p-type silicon and the electrodes are n^+ implants. An insulator (SiO_2) is used to protect the silicon of the wafer. The strips are connected to the readout electronics through an aluminum layer.

- A low resistance ohmic contact to the back of the device is required for applying the high voltage and is obtained through a p^+ implant with a layer of metal in direct contact which covers the entire backside of the device. The p^+ implant is required to prevent the depletion region reaching the metallisation.

- The guard ring structure is a feature specially made to minimise the leakage current at the detector edges and avoid possible electrical breakdown. Outside the sentitive region of the device the situation is a bit more complex as not the whole surface is at the same potential. The cutting edge is conductive due to mechanical damage caused by the cutting procedure and will be at the backplane potential, which is the bias voltage. Due to the lateral extension of the depletion, when the space charge reaches the cutting edge the strong crystal damage which is present there acts as a very effective generation center and causes a dramatic increase of the leakage current. Additionally, the always present positive charge in the $Si0_2$ causes electrons to accumulate at the top edge of the bulk. As the electron accumulation is conductive, it will adjust to the backplane potential and the full bias voltage drops over a very short distance, leading to high electric fields and a low breakdown voltage. The purpose of the guard ring (or multiguard rings) is to stablish a smooth voltage drop toward the cutting edge and to assure that the outermost ring is on the backplane potential. No space charge region can then stablish outside the outermost ring.

These features can be observed in the photograph of a silicon microstrip detector which is represented in Fig. 3.12. This arrangement is called n^+-on-p detector. However, this is not the only possible arrangement.

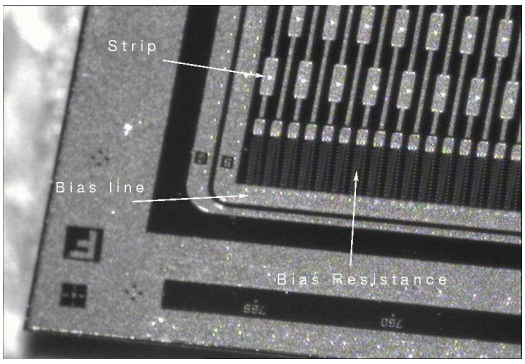

Figure 3.12: Microscope view of a silicon microstrip detector. The R_{bias}, the bias line and the strips are pointed. The outer ring corresponds to the guard ring.

n$^+$-on-n

The bulk is lightly n-type doped silicon and the segmented strips are n^+ implants. The backplane has a p^+ implant and the abrupt junction is the p^+n junction created at the backplane. The depletion zone grows from the backplane to the front n^+ strip implants. While the sensor remains under-depleted, the strips are shorted and this results in higher noise levels [55] so that, the device must be fully depleted to yield good charge collection efficiencies. Nevertheless, by choosing n^+ readout as in the previous structure, the signal is provided by electrons moving towards the n^+ electrodes yielding a higher signal pulses. In addition, these detectors have advantages in performance after radiation damage as will be explained in Chapter 4. Radiation damage causes the silicon to undergo type-inversion which results in the bulk silicon becoming lightly p-doped. Hence, the higher electric field is in the strip side of the device and they will be able to work under-depleted.

This kind of detector also needs isolation structures in both sides. For this reason, the fabrication of n^+-on-n detectors requires aligned double sided processing which increases the complexity and cost of such devices. The double sided processing is necessary for the inclusion of guard ring structures near the junction before irradiation.

p$^+$-on-n

The bulk is lightly n-type doped silicon and the segmented strips are p^+ implants. The back implant is n^+. The abrupt junctions are between the strips and the bulk silicon. The depletion zone grows from the strips to the backplane so that, the device can operate partially depleted and the signal is formed by the movement of holes. Under radiation they will suffer type-version as will be explained in Chapter 4 and the junction will migrate to the backplane.

3.3.2 Substrate types

Silicon detectors are processed on high resistivity monocrystalline silicon. In this section, the silicon growth processes will be briefly described. These different techniques are described in details in [46].

- *Float Zone Silicon* (FZ)
  The FZ method is a high-purity silicon growth method. It has been the exclusive growth method used in the manufacture of detectors until only a few years ago. The monocrystalline FZ silicon is grown in an environment without any physical contact, which leads to the possibility of high resistivity silicon growth ($\geq 1\ K\Omega m$) [56]. For radiation detector applications, it is preferred a high resistivity in order to reach a full depletion at low voltage. The main impurities (carbon and oxygen) have concentration levels not exceeding $5\times10^{15}cm^{-3}$.

- *Diffusion Oxygenated FZ Silicon* (DOFZ)
  It has been proved that the oxygen atoms improve the silicon characteristics under irradiation [57]. The oxygen concentration in FZ Silicon can be increased by diffusing oxygen into a FZ silicon wafers at high temperature ($\sim 1000°C$). The resultant silicon is called DOFZ. An oxygen concentration of the order $10^{17}cm^{-3}$ is reached[1].

- *Magnetic Czochralski Silicon* (MCz)
  Czochralski silicon (Cz) is the growth method of choice for microelectronics applications [58] but its low resistivity makes it unsuitable for particle detectors. This material is characterized by oxygen is always the dominant impurity compared to FZ silicon with typical concentrations of $5\times10^{17}cm^{-3}$. The MCz silicon is produced as Cz silicon but in the presence of a magnetic field reducing the concentration of impurities and allowing higher resistivites [59].

3.3.3 Isolation methods

In contrast to the p^+-on-n case, where the isolation of the adjacent p^+ implants is provided by the omnipresent electron accumulation layer in the oxide, this same layer would shorten the n^+ implants without further precautions. Isolation is usually provided by a p-type boron implants. Depending on the dose of this isolation implant the method is called either p-stop or p-spray.

- p-Stop
  A common technique is to introduce a high dose of p^+ boron implant sorrounding the strips [60, 61] as shown in Figure 3.13(a). An advantage of this technique is that a typical dose of about 10^{14} boron ions cm^{-2} will in any case guarantee a good isolation also after the radiation-induced surface positive charge.

  The potential of the p-stop depends on the implant geometry, the backplane bias, and the substrate effective doping. As the latter two quantities are also very high in a highly irradiated sensor, the potential difference between n^+ strips and p-stops increases with

[1] The saturation concentration of oxygen in silicon is $\sim 10^{18}cm^{-3}$

ongoing irradiation, leading to an additional increase of the electrical field. This means that the breakdown voltage of devices featuring p-stops decreases with irradiation.

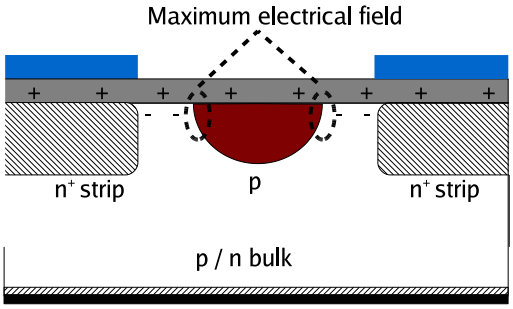

(a) p-stop

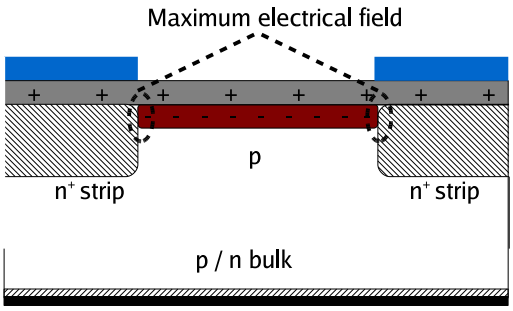

(b) p-spray

Figure 3.13: Isolation techniques for adjacent n^+ implants. (a) p-Stop isolation. (b) p-Spray isolation. The maximum field regions are located at the lateral pn-junctions.

- p-Spray
  If the dose of the isolation implant is matched to the saturation value of the oxide charge which is in the order of $3 \times 10^{12}\ cm^{-2}$, the boron concentration is small enough that an overlap of the boron implant with the n^+ strip implant does not lead to breakdown. The whole surface is then covered by the medium-dose boron implant [62]. As in the p-stop case, the point of maximal electrical field is at the lateral pn-junction between the isolation boron implant and the n^+ strips as indicated in Figure 3.13(b).

  The unirradiated device displays the highest electric field and therefore the lowest breakdown voltage in its lifetime. With the increase of the oxide charge to its saturation value the shallow p-spray layer moves into the depleted and the electric field decreases. The lowest electric field is reached when the boron implant matches exactly the saturation value of the oxide charge. However, if the implantation dose is too low, the isolation

might not be sufficient. Therefore, one usually chooses an implant dose which is slightly higher than the necessary one to prevent failure in the case of fluctuations in the production process. In this case, the device has a better high voltage performance after irradiation than before.

- Moderated p-spray: p-Stop + p-Spray
  In order to improve the pre-irradiation high voltage stability of p-spray devices while keeping their good post-irradiation behaviour, the called moderated p-spray technique has been developed [54](Figure 3.14).

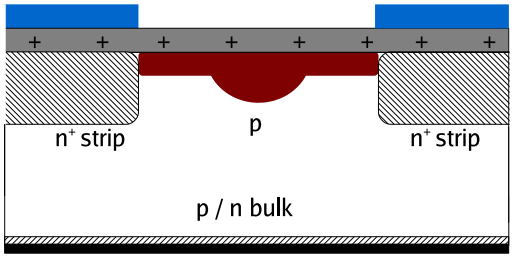

(c) moderated p-spray

Figure 3.14: Schematic cross section of a device with moderated p-spray isolation.

The boron dose in the middle of the gap between two strips can be chosen high enough to ensure interstrip isolation, e.g. twice the expected saturation value of the surface charge. At the same time, the boron dose in the sorrounding of the lateral pn-junction can be optimized for best high voltage performance which is reached if the dose is close to the expected saturation value of the surface charge.

3.3.4 Signal formation

3.3.4.1 Interaction between radiation and silicon

A minimum ionising particle (*mip*) that traverses a silicon detector, loses energy mainly by ionization. An average energy of 3.6 eV is required to produce a single electron-hole pair in silicon. The mean number of electron-hole pairs created by the passage of a *mip* through a silicon detector is 80 electron-hole pairs per micron [63]. In a thin detector, the total energy loss will be small compared to the total particle energy, typically $\geq$ 100 MeV. In practical terms, this means that the high energy particles produced in colliders as the LHC will only lose a small fraction of their energy as they pass through a silicon detector, and will produce nearly uniform carrier generation along their path. For a *mip* traversing a 300 μm thick silicon sensor (as the silicon sensors at ATLAS) the most probable energy loss is 81 KeV [64]. Hence the mean charge deposited by a *mip* amounts to 24000 electron-hole pairs corresponding to 3.6 fC.

The quantity and distribution of the electron-hole pairs generated by ionization will depend on the type of radiation. Neutral particles, such photons and neutrons are transformed in detectable

charged particles by processes as the photoelectric effect in the case of photons, where the neutral particle is absorbed in a single interaction and an electron gains its energy. The energy must exceed the bandgap energy. Additionally, at higher energies other interactions such as Compton scattering or pair production will occur. The neutron interactions are dominated by collisions with the atomic nuclei, leading to elastic scattering, radiative capture or fission. In this processes, charge particles or nuclear fragments are liberated that can directly cause excitation or ionization. Charged particles will suffer direct collisions with the atomic electrons transferring their energy or less frequent with the nucleous of the silicon atoms. The two main processes are ionization and coulomb scattering with the atomic nucleous. Additionally, the charged particles can transfer their energy to the crystal lattice itself, potentially displacing atoms from their lattice sites.

Since these interactions between charged particles and the semiconductors are statistical in nature, the total energy deposited by each particle will vary. However, the energy distribution produced over a large number of events is predictable and follows a Landau distribution [64] as shown in Figure 3.15(a).

This has a long high-energy tail, since collisions can occasionally result in a very large energy transfer to the detector. As a result, the most probable energy loss is different from the mean energy loss. The Landau theory assumes a free charge electron cross section neglecting the atomic bonds. So, a gaussian distribution convoluted with a Landau curve is used to reproduce the experimental energy distribution as shown in Fig. 3.15(b).

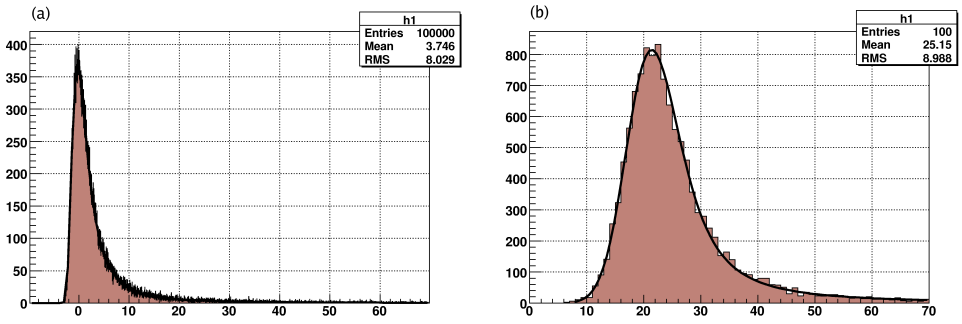

Figure 3.15: Examples of a (a) Landau distribution, and a (b) Landau convoluted with a gaussian distribution.

3.3.4.2 Charge collection

In the following it is assumed a n^+ strips on p-type bulk sensor reverse biased by the backplane so the higher electric field is on the readout strip side. After creation of electron-hole pairs, these charge carriers are in the conduction band and are free to move. Under an applied electric field the charge carriers are accelerated to the electrodes of the device. This electric current produces a measurable signal. A signal is already detectable when the charge starts to move and not only when it arrives at the collecting electrode. During drift, the carriers also diffuse by multiple

collisions (this effect will be discussed in the section 3.3.5).

As the carriers move through the medium they scatter (ballistic motion). Since the characteristic times of the crystal lattice excitations (phonons) are much smaller (of order *ps* in Si) than the transport times, the carrier is always in equilibrium with the lattice. The carrier transport thus becomes non-ballistic and the velocity does not depend on the time during which the charge carrier is accelerated, but only on the magnitude of the local electric field. Thus, the velocity of carriers at position x depends only on the local electric field, $E(x)$, regardless of where they originated and how long they have moved. This leads to the equation 3.52

$$v_{drift}(x) = \mu E(x) \tag{3.52}$$

The instantaneous current induced on a electrode by the movement of a charge q with a drift velocity, v_{drift}, is given by the Shockley-Ramo theorem [65]

$$i = -qv_{drift}(x)E_w(x) = -q\mu E(x)E_w(x) \tag{3.53}$$

$E_w(x)$ is the *weighting field* in units of m^{-1} according to [65] and corresponds to the gradient of a *weighting potential*, ϕ_w. The charge produced by a *mip* is *observed* through the current induced by the charge movement within the electric field. Integrating the induced current over the time as the charge, q, trasverses from position 1 to position 2, yields the difference in induced charge on a considered electrode:

$$\triangle Q = q(\phi(2)_w - \phi(1)_w) \tag{3.54}$$

The electric field, $E(x)$, on all the detector and the weighting field, $E_w(x)$, are distinctly different (for any configuration with more than two electrodes). The electric field determines the charge trajectory and velocity, whereas the weighting field characterizes how charge motion couples to a specific electrode depending only on the geometry of the detector. The equation 3.53 is the solution of the Poisson equation, $\nabla^2\phi_w = 0$, assuming an unit potential on the considered electrode, and 0 on all others [66]. Because the weighting potential is strongly peaked near the signal electrode, most of charge is induced when the moving charge is near the signal electrode, i.e. most of the signal charge is due to the charge terminating on the signal electrode.

Electrons and holes have different mobilities, 1350 and 480 cm^2/s in Si, respectively. Thus, in a field of 10^3 V/cm the electron velocity is 13.5 $\mu m/ns$. For comparison the thermal velocity of an electron in Si at room temperature is about 100 $\mu m/ns$, so the carrier motion is the superposition of a substantial random thermal motion and the drift due to the electric field. Although electrons and holes move in opposite directions, their contribution to the signal current is of the same polarity since they have opposite charge. The total induced charge, that is the signal charge, Q, will be therefore the sum of the induced currents by the moving electrons and holes:

$$Q = \int_0^{t_c(e)} i(t)dt + \int_0^{t_c(h)} i(t)dt \tag{3.55}$$

where $t_c(e)$ and $t_c(h)$ are respectively the collection times for electrons and holes. The collection time is the time required for a charge carrier to trasverse the sensitive volume and is given

by the equation 3.56 [49]. Integration times larger than the collection time of all charge carriers yield the full charge. A shorter integration time yields a fractional charge.

$$t_c = \frac{d^2}{2\mu V_{dep}} ln(\frac{V_{bias} + V_{dep}}{V_{bias} - V_{dep} + 2V_{dep}(1 - x/d)}) \tag{3.56}$$

where V_{dep} is the depletion voltage, V_{bias} is the bias voltage, d is the detector thickness, and x is the distance where the carrier was created with respect to the readout side. Due to their different mobility values, the collection of electrons is much faster than that of holes (roughly a factor ~ 3) and basically the signal current corresponds to the electron current. The resulting distribution for electrons as function of bias voltage and the position of creation of the charge carriers are shown in Fig. 3.16. It is minimum at $x = 0$ (carriers created in the junction), since here the electric field is maximum, whereas a maximum time is reached when the carrier has to trasverse the full detector thickness. If the applied voltage is not enough to fully deplete the detector, $t_c \to \infty$, resulting in long tails in the induced signals. For silicon detectors operating in a high density particles environment, very fast response times are required, so it is desirable to keep the collection time as low as possible. In the case of $V_{bias} > V_{dep}$, the collection time reduces to:

$$t_c = \frac{d^2}{2\mu V_{dep}} ln(1 + \frac{2V_{dep}}{V_{bias} - V_{dep}}) \simeq \frac{d^2}{\mu(V_{bias} - V_{dep})} \tag{3.57}$$

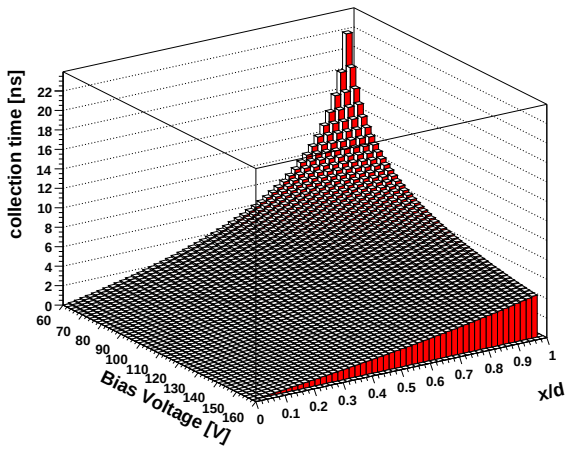

Figure 3.16: Collection time for electrons as a function of bias voltage and the ratio x/d, where d is the sensor thickness and x the position of the creation of charge carriers with respect to the readout electrode. The plot has been obtained assuming a silicon sensor of width 300 μm with a depletion voltage of 60 V in equation 3.56. A value of 1350 cm^2/Vs for the electron mobility has been taken.

A high electric field in the detection volume is desirable for fast response but also for improved

charge collection efficiency. Crystal lattices are not perfect; irregularities in the crystal structure and impurities can form trapping sites for the charge carriers. This is discussed in more detail in Chapter 4. One result is that trapping leads to a carrier lifetime before trapping occurs, so if the carriers are swept more rapidly from the crystal, the trapping probability is reduced. An illustrative view of the movement of a charge carrier under diffusion processes within a low electric field compared to within a high electric field can be seen in Fig. 3.17. The charge carrier movement by diffusion is random due to thermal excitation and it is the electric field that provides a charge carrier net flow. In Fig. 3.17(a) the low electric field makes diffusion more dominant and increases the probability of charge trapping. In Fig. 3.17(b) with higher electric field, the charge carrier drift dominates the way to the electrode and the charge carrier will be collected within a shorter collection time. The charge collection efficiency can be speed up by increasing the voltage to overdepletion, i.e. the bias voltage exceeding the value of the full depletion voltage of the device. Some care must be taken in this case, as if the voltage is raised up enough (electric fields $> 10^5$ V/cm), the avalanching process may lead to breakdown of the junction as explained in section 3.2.

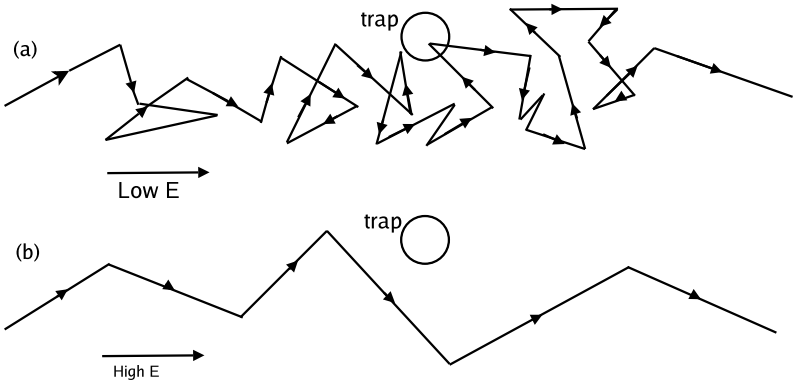

Figure 3.17: Illustrative view of the movement of a charge carrier under diffusion processes within a low electric field (a) compared to within a high electric field (b). The scattering occurs with the crystal atoms. When the electric field is higher, so that, the drift velocity is, the carrier spends less time in the vecinity of the traps.

3.3.5 Spatial resolution and noise

The signal pulse at the strips is amplified and integrated by the readout chip to measure the total charge deposited into the microstrip detector. Since all the strips are readout, the strip to which the signal arrives gives information about one coordinate of position of the traversing particle. So, a microstrip detector is a sensitive position system and can be used as a tracker.

The spatial resolution of microstrip detectors depends on both physical and external parameters:

- The physical parameters are the statistical fluctuations of the energy loss and the diffusion

of carriers during the drift.

- External parameters include the strip pitch and the noise of the readout electronics.

The average drift movement of the charge carriers is along the electric field lines towards the electrodes. But also electrons and holes diffuse during the drift due to the random multiple scattering and originating the spread of the charge cloud mainly in the transversal direction to the drift path. The distribution of the charge carriers around the track may be described by a Gaussian function [67]:

$$\frac{dN}{N} = \frac{1}{\sqrt{4\pi Dt}} exp(-\frac{x^2}{4Dt})dx \tag{3.58}$$

In the above equation, dN/N indicates the fraction of carriers that can be found in a length element dx at a distance x from the track after a time t after the charge creation. D is the diffusion coeficient, proportional to the mobility (see equation 3.35) and hence different for electrons and holes. The standard deviation of the distribution is

$$\sigma = \sqrt{2Dt} \tag{3.59}$$

and is equal for both carriers since the drift time is inversely proportional to the mobility (see equation 3.27).

The position resolution of a silicon detector is determined at first order by geometrical factors, as the width of the electrodes and the pitch. In practice, it is the size of the readout electronics that imposes constraints on the size of the detecting device. The broadening of the charge distribution can be used to improve the instrinsic resolution of the detector, as the charge is shared between more readout electrodes. In a detector characterised by a strip pitch larger than the diffusion width, as it is in ATLAS with a pitch, $p = 80\ \mu m$, the differences between the measured and the true positions have a Gaussian distribution with the standard deviation:

$$\sigma^2 = \frac{p^2}{12} \tag{3.60}$$

so the resolution is the strip pitch divided by $\sqrt{12}$. For the ATLAS strip pitch of 80 μm, the σ corresponds to 23 μm. The centre of gravity of the resulting signal can be calculated, increasing the accuracy of the measurement compared to the case where just the information of which electrode collected the charge is used.

3.3.6 Sources of noise

The signal generated in silicon detectors is generally of small amplitude (24000 electrons) and hence an amplification and shaping stages are required for its further processing. A charge-sensitive preamplifier is typically used, avoiding any dependence on the change of the detector capacitance with temperature. Noise will be introduced by the readout electronics affecting the charge measurement. Consequently, the signal-to-noise ratio, SNR, gets degraded. Some general considerations regarding the noise of an AC coupled detector are described in the following.

1. Thermal noise (or Johnson noise)
   Thermal variations in the temperature of the detector produce fluctuations in the energy of the charge carriers present in the bulk. This term is proportional to $\sqrt{\frac{4kT}{R_{bias}}}$. Hence, the sensor should have high values of the bias resistor.

2. Shot noise (or Parallel noise)
   Due to the quantization of the electric charge, fluctuations in the number of charge carriers occur in the current flow. This is called shot noise and is measured as the variance of the fluctuations about the mean constant current. In this case, the noise is proportional to $\sqrt{2qI_{leakage}}$.

3. Serial noise
   Serial noise finds its source in the readout amplifier. The amplifier noise is described by a combination of voltage (e_{na}) and current noise source (i_{na}) at its input. Other contribution comes from the resistance, R_s, which represents the sum of all resistances present in the input path (the electrode resistance, any protection networks and parasitic resistances in the input transistor).

The electronic noise can be described in terms of either voltage or current noise sources. The thermal and shot noise of the detector are represented by current noise generators. On the other hand, the series resistor, R_s acts as a voltage generator.

A convenient way to express the total noise is in terms of the equivalent noise charge (ENC) corresponding to a signal which would generate an output voltage of the same magnitude as the r.m.s. noise in the system, e.g. a signal-to-noise ratio equal to one. The ENC is usually expressed in Coulombs or the corresponding number of electrons. The total noise is given by

$$(ENC)^2 = a(2qI_{leakage} + \frac{4qT}{R_{bias}} + i_{na}^2)\tau_s + b(4kTR_s + e_{na}^2)\frac{C_d^2}{\tau_s} + c \tag{3.61}$$

where a, b, and c depend on the shape of the pulse determined by the pulse shaper and τ_s is its characteristic time. C_d is the capacitance of the detector. At short shaping times, the voltage noise dominates, whereas, the contribution from noise currents increases with shaping times, i.e. with pulse duration. The total noise is minimum when the current and voltage noise sources are equal.

Chapter 4

Radiation Damage in Silicon

The ATLAS silicon tracker system for the HL-LHC will be immersed in a harsh radiation environment. The expected radiation doses in the innermost region (r ~ 5 *cm*) of the ATLAS experiment are up to 10^{16} particles per square centimeter after 10 years of operation. Therefore, the detectors will suffer serious damage from these high radiation doses. So, it is important to know the effects of the radiation on the detectors.

The radiation induced defects suppose microscopic damage to the silicon crystal structure. The consequences of these defects are shown through macroscopic effects which have to be carefully evaluated to ensure proper operation over the full length of an experiment expected lifetime. Even today, most effects are only partly understood. One has to rely on a careful evaluation of radiation experiments and parametrization of the resulting effects, maybe with a partial understanding about the physical background.

4.1 Microscopic effects

Radiation induced effects are usually divided into bulk and surface defects. The former are caused by the displacement of crystal atoms while the latter include all effects in the covering dielectric and the interface region.

4.1.1 Bulk damage

When silicon sensors are exposed to radiation, the latter interacts with both: the silicon atomic electrons and with the nuclei in the lattice. While the interaction with the atomic electrons is a transient effect that is indeed used for the particle detection, the interaction with the lattice may lead to permanent material changes.

The dominant mechanism of primary defect formation in silicon is the elastic collision of an incoming high energy particle with an atom of the crystal lattice. The primary knocked atom (PKA), that has obtained an excess momentum, starts moving but is exposed to the stopping influence of neighbouring atoms. If the momentum transfer is enough, it may depart from its

site over a distance of several lattice constants. The particle requires on average an energy of 25 eV to displace a silicon atom to intersticial position [68]. In this case a Frenkel pair [47] is created, corresponding to an intersticial, an atom between regular lattice sites, and a vacancy, at the empty lattice site.

The diffusion gives rise to an intersticial and vacancy migration process. Most of the vacancies and interstitials recombine, some vacancies may interact to form stable divacancies V_2, a complex formed by two neighbouring vacancies [69], or higher vacancy complexes while the rest diffuses away. Those can react with other radiation induced defects, forming defect complexes, or react with impurity atoms such as carbon, oxygen and phosphorus, those being among the most common impurities in silicon bulk as it is represented in Figure 4.1.

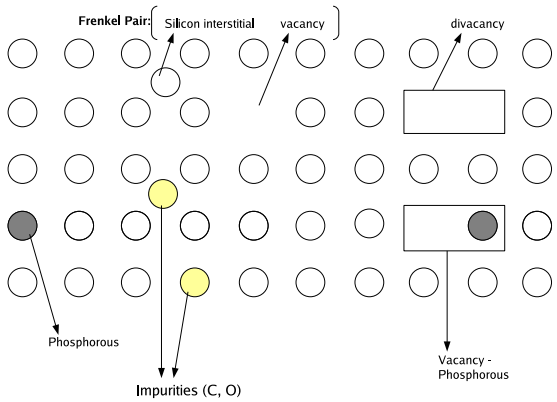

Figure 4.1: Schematic diagram of some defects in a n-type silicon crystal lattice.

Interstitials and vacancies form defect complexes which can establish energy levels (traps) in the band gap. These traps, spatially well localised inside the semiconductor lattice are called ”points defects”.

In the case of heavy incident particles, like neutrons or protons, sufficient energy can be transferred to the PKA so that a multiplicity of secondary displacements occurs in a region with a radius of a few hundred angstrom (Å). Isolated interstitial atoms and vacancies are then formed along the PKA trajectory. As the kinetic energy of the individual atoms decreases during the collisions, the distance between the collisions also decreases. This leads to the formation of random and irregular clusters of points defects.

Due to thermal motion, point defects and clusters interact during and after irradiation. The mobility of the defects is strongly temperature-dependent. Thus, a complex annealing behaviour will occur. In addition, these kinds of defects may be electrically active and they introduce energy levels in the band gap whose position can be measured by different spectroscopic methods [70]. Most of these energy levels are situated near to the middle of the band gap and then called *deep energy levels*. *Shallow levels* are just acceptors and donors lying very close to the valence and conduction bands, which commonly ionize at room temperature. In general, the defects may be electrically active and hence change the electric properties of the material.

Even though it is not possible to correlate all the changes in the macroscopic operation parameters of the sensors with specific microscopic defects, the changes have been studied and paramatrized in detail [71].

NIEL hypothesis

The radiation damage has a dependence on the type and energy of the incident radiation. Therefore, it is useful to scale measurements on radiation damage for different kinds of radiation. As charged particles scatter via electromagnetic interaction with the silicon atom that are partially screened by its electron cloud, they produce more point defects and less clusters than neutrons which only feel the nuclear but not the electromagnetic interaction. However, the differences between the types of interactions are leveled out by the secondary interactions of knocked out silicon atoms.

As the interaction of radiation with electrons produces ionisation but not crystal deffects, the quantity used for scaling is the *non ionising energy loss*, NIEL [72]. This quantity summarizes all energy deposited in the crystal which has not been used for the fully reversible process of ionization and allows to compare the damage caused by the different types of particles with different energies. It is expressed in units of $keV \cdot cm^2/g$.

The *displacement damage cross section*, D(E), also called *damage function* is the average value of the recoil energy released to the silicon in the form of displacement damage by the incoming particle depending on its incident energy (E). It is expressed in units of $MeV \cdot mb$. The relationship between the NIEL and the displacement damage cross section is given by Equation 4.1 [72]

$$D(E) = \frac{A}{N_A}\frac{dE}{dx}(E)|_{\,non-ionizing} \tag{4.1}$$

where A is the atomic weight of silicon and N_A is Avogadro's number. For silicon with $A = 28.086\ g/mol$ the relation between D(E) and NIEL is:

$$100\ MeVmb = 2.144\ KeVcm^2/g \tag{4.2}$$

The displacement damage cross section is shown in Figure 4.2 as a function of incoming particle energy for neutrons, protons, pions and electrons. The displacement damage cross section for 1 MeV neutrons is set as a standard for normalisation, where $D_n(1\ MeV) = 95\ MeVmb$. It is common to use neutrons of 1 MeV as reference particles.
The proton damage cross section is larger than neutrons, especially at low energies, due to additional (and dominating) electrostatic interactions between the particle and the silicon. At higher energies, the electrostatic interactions no longer dominate and the damage cross sections almost reach a common constant value for neutron and proton radiation exposure.

The hardness factor, κ, for a given incident particle, is defined from the displacement damage cross section, $D(E)$, as given in equation 4.3 and normalized to 1 MeV neutrons.

$$\kappa(E) = \frac{\int D(E)\phi(E)dE}{D_n(1\ MeV)\int \phi(E)dE} \tag{4.3}$$

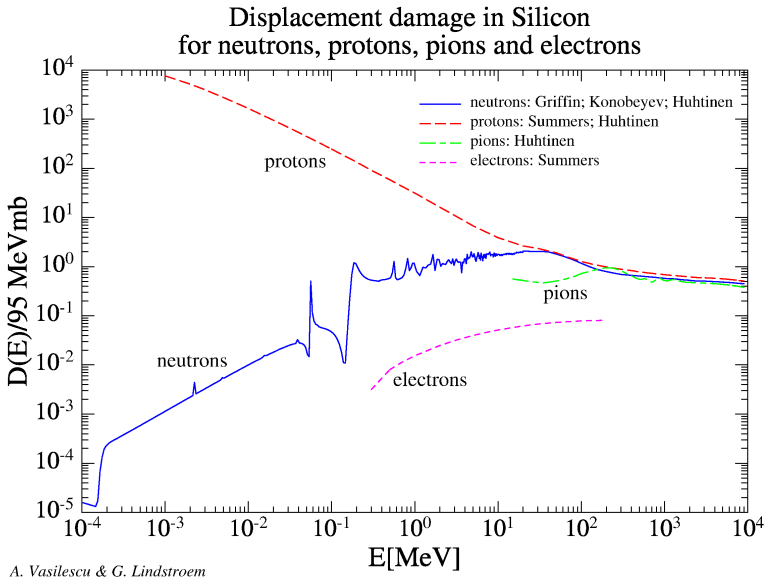

Figure 4.2: The scaling of the displacement damage in silicon with energy for neutrons, protons, pions and electrons. Diagram from [73].

The energy spectrum of the radiation is represented by the function ϕ(E). The fluence of an arbitrary type of particle, Φ_{phys}, is scaled to a fluence of 1 *MeV* neutrons, Φ_{eq}. The energy-dependent *hardness factor*, κ, of a certain type of particle converts the "physical" fluence, Φ_{phys} into the neutron equivalent fluence, Φ_{eq} [74]. Table 4.1 presents the hardness factor as measured for different particle and incident energy types.

Irradiation Facility	Energy and Particle	Hardness Factor κ
Proton Synchroton (CERN)	24 *GeV* protons	0.62
TRIGA Mark II Research Reactor (JSI-Ljubljana)	3 *MeV* neutrons	0.88
Cyclotron and Radioisotope Center, CYRIC (Tohoku University, Japan)	70 *MeV* protons	1.4

Table 4.1: Some examples of the hardness factor, κ depending on the particle type and its energy in different irradiation facilities [57, 75–77].

The equivalent fluence can then be calculated from

$$\Phi_{eq} = \kappa \int \phi(E) dE = \kappa \Phi_{phys}. \tag{4.4}$$

The NIEL scaling hypothesis does not provide a perfect theory to fit all experimentally mea-

sured data. The damage may also depend on the specific modes of energy transfer between the radiation and the silicon lattice, which are not included in the NIEL scaling hypothesis. The main observed deviation from the NIEL scaling values was discovered by the CERN-RD48 (ROSE) collaboration [78] and concerns the radiation damage by charged hadrons. Detectors fabricated with silicon with high oxygen concentrations show increased resistance to charged hadron radiation damage as compared to non-oxygenated silicon [57, 79]. However this effect is not observed for neutron irradiation. Despite this discrepancy between the NIEL hypothesis and the measured data, the NIEL scaling manages to successfully account for most of the particle and energy dependences of the observed damage in silicon and it is widely used.

4.1.2 Surface damage

As already pointed out in the previous chapter, the Si-SiO_2 interface in silicon detectors is in fact characterised by the presence of a net density of positive charges in the SiO_2. The oxide charge consists of this fixed positive charge and additional interface states that are created at the Si-Si0_2 border. This charge increases with the irradiation but it is present even in non-irradiated oxides since it depends on the fabrication process [80].
As the crystal structure of silicon oxide is highly irregular, displacements of single atoms due to irradiation do not lead to macroscopic changes in the silicon oxide properly. However, ionization in the oxide, is not fully reversible and may cause steady changes of the interface properties.

Ionising radiation creates electron-hole pairs in the oxide. In the silicon lattice the pair creation is a completely reversible process with no damaging effects. But this is not true in the surface oxide. Depending on the electric field, a part of the pairs fails to recombine. As the mobility of the electrons is higher than the mobility for holes ($\sim 20\ cm^2/V \cdot s$ for electrons and $2 \times 10^{-5}\ cm^2/Vs$) in oxide, electrons are swept out from the oxide faster than holes which are eventully captured at the oxide-silicon interface leading to a positive charge buildup in the oxide. In addition, the electric field directed away sweeps the holes created elsewhere towards the oxide [81], thereby increasing the oxide charge. As the number of interface states is limited, saturation of positive oxide charge buildup is reached when all are occupied by holes. For high-quality thermally grown oxide a typical value of about $3 \times 10^{12}\ cm^{-2}$ is reached [82].

This charge induces the creation of an electron layer, called the electron inversion layer which is settled at the silicon side of the Si-SiO_2 interface. This layer will affect the electrical behaviour in this region. In a detector with n-type readout electrodes, the electron layer will short the n-type strips together, leading to unwanted signal sharing. To counteract this, these devices use additional p-type implants to compensate the electron accumulation layer. This strip isolation techniques have been explained in the chapter 3. In a detector with p-type readout electrodes, a higher field region will be created where each p-type implant meets the electron layer.

4.2 Macroscopic effects

The radiation leads to a distorsion of lattice symmetry introduced by point defects, clusters and impurities complexes. This reflects in the emergence of discrete energy levels inside the silicon energy gap. These energy levels may act as generation-recombination centers or as

trapping ones, affecting the electrical operation of the device. As the mobility of the defects is strongly temperature-dependent, it is clear that radiation-induced changes of sensor properties show a complex annealing behaviour due to the many possible secondary defects.

Especially, the lattice defects have three consequences on the main detector properties:

- As they are able to capture and emit electrons and holes in the depleted region. It leads to an increase of the leakage current with a consequent increase of the noise. The effects in the detector performance are a decrease of the signal to noise ratio and an increase of power consumption.
- When signal charge is trapped in the depletion zone by defects, it may be released too late causing a signal loss. Therefore, a decreasing of the charge collection efficiency occurs.
- The charge density in the space-charge region can be changed, thus requiring an increased bias voltage to make the detector fully sensitive.

In the following, these radiation induced macroscopic effects will be discussed in detail.

4.2.1 Leakage current

The leakage current of an irradiated detector increases mainly because of the rise of the generation current. This is caused by the creation of traps with deep energy levels situated in the middle of the forbidden gap. Figure 4.3 illustrates the valence and conduction bands with a deep defect. The electron-hole generation can be viewed as the defect promoting an electron to the conduction band and a hole falling to the valence band, or as an electron from the valence band using a defect level as a step in its promotion to the conduction band.

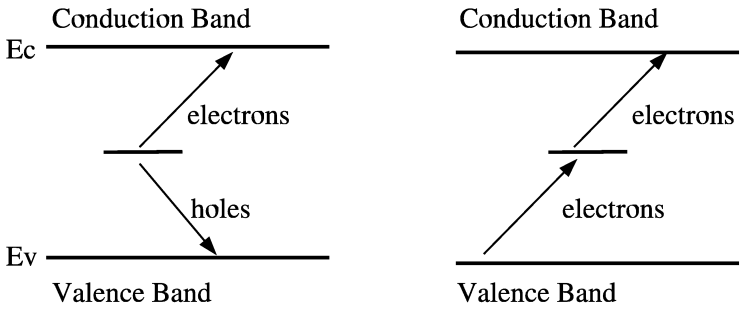

Figure 4.3: Deep defect levels acting as generation centres. On the left the defect level generates a electron-hole pair. On the right the electron in the valence band is promoted to the conduction band by a deep level.

The generation of electron-hole pairs within the space charge region of a silicon detector gives rise to a leakage current in the device. This increase in the leakage current generated in the bulk volume due to radiation damage has a linear dependence on the equivalent fluence received by the silicon detector by means of equation 4.5. Some previous measurements of this dependence with silicon microstrip detectors are shown in [46, 57, 83].

$$\triangle I_{vol} = \alpha\Phi \tag{4.5}$$

The proportionality constant, α, is the current related damage rate. It depends on the intrinsic charge carrier concentration and therefore on the temperature at which the measurement was performed. However, α is independent of the initial resistivity of the silicon, the concentration of other dopants like oxygen or carbon, and the fabrication process of the sensor [84].

4.2.2 Effective doping concentration and depletion voltage

In a non irradiated detector, the effective doping concentration, N_{eff}, is determined by shallow dopants in the material. Under irradiation, the energy levels created in the band gap induced by radiation will change the doping concentration. Only electrically active defects contribute towards N_{eff}. These defect levels are mainly of the acceptor type which become negative charged when occupied by an electron. Then, negative charge accumulates in the depletion region and causes n-type silicon become less n-type with increasing fluence. At some point, the negative charge compensates the positive charge of the donor impurities. With further increasing fluence the material behaves more and more as p-type. This inversion is not the physical removal of the donors in the *n*-type silicon, but rather an increase of acceptor states.

Fig 4.4 shows the change in the effective doping concentration for n-type silicon and the depletion voltage (recalling $V_{dep} \propto \mid N_{eff} \mid$ from Equation 3.45) as a function of the dose. At a certain point, called the *Space Charge Sign Inversion* (SCSI) or *type inversion* point at an irradiation fluence of a few times $10^{12}\ cm^{-2}$, the space charge region is neutral (intrinsic silicon). With increasing radiation the space charge gains a net negative charge. Above this value, the doping concentration increases dominated by acceptor-like defects with a negative space charge. The silicon bulk becomes effectively p-type. The pn-junction moves from the p^+-side of the sensor to the n^+-side and the space charge region grows from there. It is worth to note that the sensor remains operational even after inversion but the detector will not be fully depleted. This can lead to a defect of the collected signal since the charge carriers produced in the undepleted region is affected by diffusion process and are not collected by the electrodes. For initial p-type silicon, the material does not suffer type inversion but an increasing of acceptor-like defects.

Annealing process

As mentioned before, defects migrate through the silicon lattice due to thermal process, the doping concentration changes after the end of the irradiation. Therefore, the detector properties can be subjected to change. The evolution on time of the detector characteristics is denoted *annealing*.

The time evolution of the effective space charge at an environment temperature of $60^{\circ}C$ is

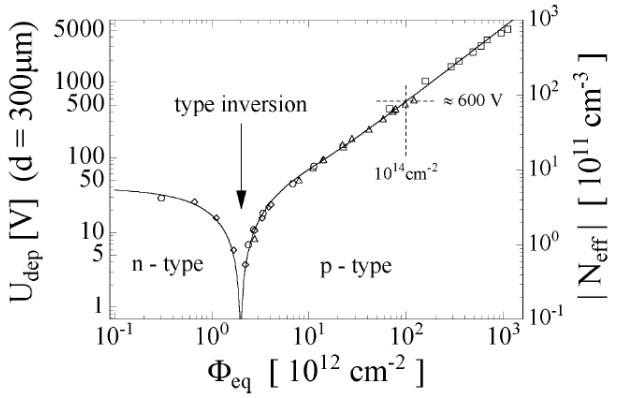

Figure 4.4: Change of the full depletion voltage of a 300 μm thick n-type silicon sensor and its absolute effective doping concentration versus the normalized fluence, immediately after the irradiation [85].

shown in Fig 4.5. As the defects and their reactions are not yet understood in detail, a phenomenological parametrization has been performed. The most accepted description of this behaviour is the so-called *Hamburg model* [46] using the following three components, also illustrated in Fig 4.5.

$$\triangle N_{eff}(\Phi_{eq}, t(T)) = N_a(\Phi_{eq}, t(T)) + N_C(\Phi_{eq}) + N_Y(\Phi_{eq}, t(T)) \tag{4.6}$$

where N_a is the *beneficial* annealing component, N_C is the *stable* annealing component and N_Y is the *reverse* annealing component. They depend on the fluence Φ_{eq} and the annealing time, t, at a certain temperature, T.

Each term is described in detail below:

- **Beneficial Annealing**
  The first term in equation 4.6, N_a, specifies the *short term* or *beneficial* annealing. The term *beneficial* originates from type inverted silicon, where the initial section of the annealing curve leads to a reduction in the depletion voltage. Short annealing times (of the order of hours or less)[1] described in [85] are not relevant for the operation of the sensors. Therefore, all but the longest decay times can be neglected and N_a can be empirically expressed as

  $$N_a \sim \Phi g_a \, e^{-\frac{t}{\tau_a(T_a)}} \tag{4.7}$$

  The introduction rate, g_a, was experimentally determined to be $g_a = (1.81 \pm 0.14) \times 10^{-2}\, cm^{-1}$. The temperature-dependent decay time, $\tau_a(T_a)$, can be expressed by the Arrhenius relation

[1] The beneficial time constant, τ_a, at 60° C has been measured to be around 24 minutes for FZ silicon [46] and around 10 days at room temperature [87]

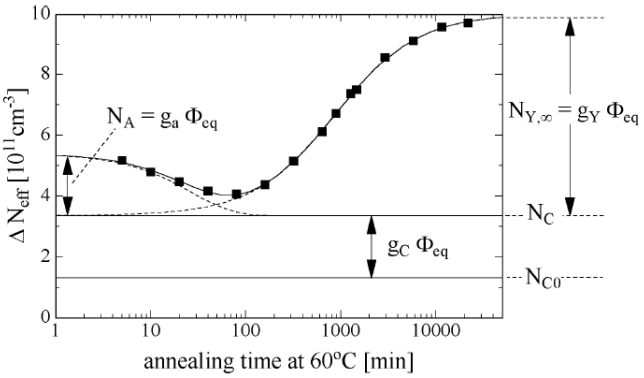

Figure 4.5: Typical annealing behaviour of the irradiation-induced changes of the effective doping concentration $\triangle N_{eff}$ at a temperature of $60°C$ after irradiation with a fluence of $1.4 \times 10^{13}\ cm^{-2}$ [86].The effective doping is parametrised by the beneficial (N_a), stable (N_C), and reverse (N_Y) annealing components.

$$\frac{1}{\tau_a(T_a)} = \kappa_{a,0}\, e^{-E_a/\kappa\, T_a} \tag{4.8}$$

with $\kappa_{a,0} = 2.4^{+1.2}_{-0.8} \times 10^{13}\ s^{-1}$ and the activation energy of the beneficial annealing process, $E_a = (1.09 \pm 0.03)\ eV$ [46].

- **Stable Annealing**
  The expression in 4.6 denotes the *stable damage* as the term $N_C(\Phi_{eq})$, which depends only on the fluence. The paremetrisation of N_C is shown in Equation 4.9.

$$N_C(\Phi) = N_{C,0}(1 - e^{-c\Phi}) + g_c\Phi \tag{4.9}$$

  The first term in 4.9 charecterizes the deactivation of the initial donor states. The initial concentration of removable donors, $N_{C,0}$, differs from the effective doping concentration $N_{eff,\Phi=0}$ measured before irradiation. This is interpreted as a partial donor removal, while part of the initial donors stay electrically active even after very high fluences. The parameter c is the material dependent constant relating donor removal to fluence (values for the donor removal rate of phosphorous in FZ silicon wafers can be found at [88]). This parametrization given for the stable damage assumes that a prioriy no acceptor states are contained in the silicon materials, which is true for most materials used.

  The second term in 4.9, $g_c\Phi$, describes the creation of acceptor-like defects proportional to the fluence. For example for neutron irradiation, the introduction rate is $g_c = 1.5 \times 10^{-2}\ cm^{-1}$ for standard silicon and $g_c = 2.0 \times 10^{-2}\ cm^{-1}$ for oxygenated silicon [89]. These defects are acceptor-like in a sense that they lead to a negative space charge and

hence to an increase of the full depletion. However, they do not lead to an increase of the conductivity of the material, because the levels caused by these defects are deep in the band gap.

The stable damage component is the most critical for the operation of silicon detectors in HEP experiments, since the beneficial component has a short time constant so it will occur during maintenance periods and the reverse annealing component is suppressed by low temperature operation. This results in N_C being the most significant damage component, which can not be controlled by temperature.

- **Reverse Annealing**
  The last contribution, N_Y, in 4.6 is the so-called *reverse annealing* term which describes the increase of the full depletion voltage with time at room temperature as can be seen in Fig 4.5. It is due to the increase in the negative space charge in the silicon detector. This process is described in terms of the buildup of acceptor states, but it could equally be due to the removal of donors. The time constant for this component of the damage is of the order of months at room temperature [46]. Here several parametrizations are possible depending on the underlying model. Although it is commonly agreed that the reverse annealing is a first order process [46], the experimental data are best fit by

$$N_Y(t) = N_{Y,\infty}(1 - \frac{1}{1 + t/\tau_Y}) \tag{4.10}$$

with $N_{Y,\infty} = g_Y\Phi$ being the reverse annealing amplitude. g_Y is the reverse annealing rate and was determined to be $g_Y = (5.16 \pm 0.09) \times 10^{-2}\ cm^{-1}$ [46]. The temperature dependence of the reverse annealing process can be expressed by a standard Arrhenius relation of the time constant, τ_Y

$$\frac{1}{\tau_Y} = \kappa_{Y,0} e^{-\frac{E_Y}{kT}} \tag{4.11}$$

containing the parameters $\kappa_{Y,0} = 1.5^{+3.4}_{-1.1} \times 10^{15}\ s^{-1}$ and the activation energy of the reverse annealing process, $E_Y = (1.33 \pm 0.03)\ eV$ [46].

4.2.3 Charge collection with trapping

The electrons and holes created by the radiation drift to the electrodes under the presence of an applied electric field. Fixed deep defect levels may trap the drifting charge. These *traps* are mostly unoccupied in the depletion region due to the lack of free charge carriers and can hold parts of the signal charge. If the time elapsed before the charge is released from the trap is more than the shaping time of the electronics, then the charge collection efficiency decreases. Shallow traps do not contribute significantly to charge trapping due to the fast detrapping time.

When extra free electrons due to an ionising radiation are generated, they can lose energy and fall into the unoccupied traps, as illustrated in Figure 4.6. This will happen at a rate given by:

$$\frac{\partial n}{\partial t} = -n\upsilon^e_{th}\sigma_e N_{traps} \tag{4.12}$$

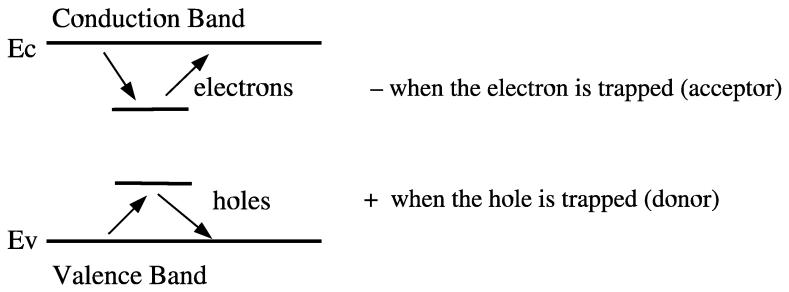

Figure 4.6: Deep defect levels acting as traps for charge carriers. When the charge carrier is held is not mobile and stayed trapped. At some later time the electron (hole) is released to the conduction (valence) band.

for electrons and similarly, free holes will be trapped by energy states below the midgap (to be specific, electrons in this defect states will drop to the valence band and fill these holes) with a rate given by:

$$\frac{\partial p}{\partial t} = -p\upsilon_{th}^{h}\sigma_h N_{traps} \tag{4.13}$$

where υ_{th} is the thermal velocity of electrons/holes, $\sigma_{e/h}$ is the electron/hole capture cross section of the traps and N_{traps} is the number of traps. This will mean that the number of free carriers will decay exponentially over time. Experimentally, this exponential decay in the number of free electrons can be parametrised using the effective electron lifetime, $\tau_{eff,e}$, as follows:

$$\frac{\partial n}{\partial t} = -\frac{n}{\tau_{eff,e}} \tag{4.14}$$

An equivalent expression may be derived for holes. At fluences approaching 10^{16} $1MeV\ n_{eq}/cm^2$, the $\tau_{eff,e}$ will be much lower than the collection time, and trapping will dominate the CCE performance. Furthermore, up to fluences of 10^{15} $1MeV\ n_{eq}/cm^2$, these effective lifetimes have been shown to vary inversely with the radiation fluence Φ_{eq} [90]. This can be parametrised by

$$\frac{1}{\tau_{eff,e}} = \beta_e \Phi_{eq} \tag{4.15}$$

Then, since the defect concentrations should increase linearly with the radiation fluence, we can relate the parameter β_e to the trap parameters by

$$\beta_e = \sum \upsilon_{th}^{e}\sigma_e \eta \tag{4.16}$$

η is the trap introduction rate. The summation is done over all the traps above the midgap. Similar equations apply to hole trapping by states below the midgap [91]. Therefore, the number of traps, N_{traps} is defined by

$$N_{traps} = \eta \Phi_{eq} \tag{4.17}$$

Experimentally, in silicon the trapping parameters β_e and β_h are fairly similar [90]. However, since electrons have about three times the mobility of holes, they can travel much further in a given time and so are less susceptible to trapping effects. Due to the weighting fields, the carriers drifting to the segmented electrodes on the front surface of a planar detector make a much larger contribution to the total signal than the carriers drifting to the back surface. So, by using n-type readout, the electrons will contribute more to the total signal, the effects of trapping will be reduced, and the signal will be improved.

4.2.4 Limit of radiation hardness

One of the limits of radiation hardness is given by the tolerable reduction of the height of the signal. As this degradation is a steady process it is not possible to give a strict rule when a sensor can be considered unusable. For the readout electronics used in ATLAS typically a signal of about 5000 e^- per *mip* is required to ensure the particle detection with an efficiency larger than 95% [25].

The reduction of the signal charge is caused by the increase of the effective space charge and by charge trapping. The former can be compensated up to a certain level by an increase of the operation voltage. Trapping can be reduced by collecting electrons which are less prone to trapping than holes as explained in the previous section and by high bias voltages, resulting in short collection times.

However, an increase on the bias voltage leads to an increased power dissipation and warms the sensor. Higher temperature implies higher leakage current and therefore larger dissipated power. This is a positive feedback system that may quickly diverge (*thermal runaway*) unless prevented by proper cooling. The volume generation current as well as the full depletion voltage can be predicted for a given fluence through the equations presented above.

If the sensors are irradiated above the level of type inversion, the increase of the effective doping concentration proportional to the fluence leads to an increase of the full depletion voltage, which can, in some cases, exceed thousand volts after some years of operation. As it is unpractical to increase the operation voltage into this range, one might choose to work partially depleted sensors. However, for a given maximum operation voltage the depth of the depletion zone and therefore the electrical signal will decrease. The detector system has therefore to be designed in such a way that it still can work with the reduced signals, or the maximal operation voltage is still high enough to provide a sufficient signal.

For the LHC experiments a radiation hardness up to a fluence of 10^{15} $1MeV\ n_{eq}/cm^2$ has been targeted and reached. Nevertheless, the Super-LHC will require a radiation hardness of the tracking devices located closest to the beampipe up to 10^{16} $1MeV\ n_{eq}/cm^2$. Intense research is working to improve radiation hardness of silicon devices as for example the RD50 collaboration where most part of this thesis is framed.

In n-type readout sensors, the collection of the faster electrons (with a three times higher mobilities than holes) on the high electric field side contributes to a significant reduction of t_c, with a very significant improvement on the charge collection efficiency compared to the

traditional p-type readout. A step futher in the implementation of the n-type readout was the use of high resistivity, detector grade p-type substrates, instead of n-type ones. This was motivated by the lower processing cost and by the preference of keeping the high electric field side always near to the segmented electrodes. In fact, in n^+n devices, the junction side is on the backplane of the detectors, before type inversion. In this case, the high electric field side is opposite to the read-out and overdepletion is needed for optimum operation. Also, to avoid high currents due to short between the backplane bias and the readout strips through the detector edges, the implantation of guard rings on the backside is required. This double-side processing can impact the cost of the device up to $40-50\%$ and it can be avoided with n^+p devices.

Research has started into the properties of n^+-strips on p-type bulk detectors for the application to radiation hard particle detector [92–94]. Their higher radiation tolerance comparing to p^+n detectors is shown in Fig. 4.7.

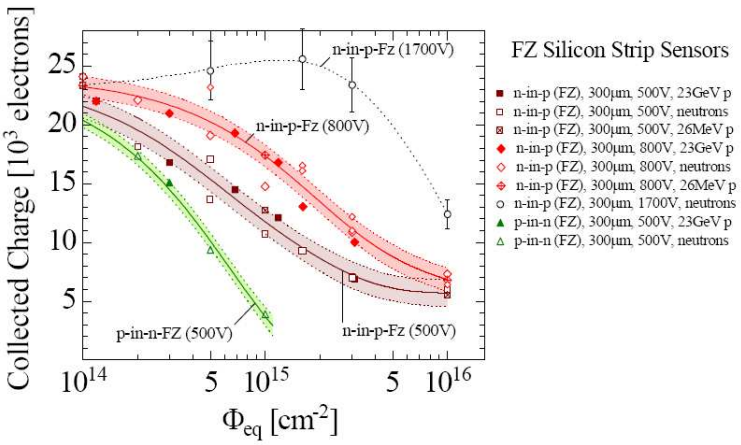

Figure 4.7: Collected charge as function of 1 MeV neutron equivalent fluence of 23GeV protons, 26MeV protons and reactor neutrons for irradiated silicon ministrip sensors [95]. It can be seen the high radiation toleranceof p-type sensors at high bias voltages.

Chapter 5

ISE-TCAD simulation package

The simulation studies in this thesis were done with "Synopsys ISE-TCAD" version X-2005.10 [96], a finite-element semiconductor package. ISE-TCAD uses our knowledge of the partial differential equations describing charge carrier's motions and interactions with the crystal lattice in semiconductors, coupled to finite element method to simulate the electrical parameters of the device.

5.1 Transport equations of semiconductor devices

The dynamics of charge carriers in semiconductors like silicon is well described by the Poisson equation (eq.5.1) coupled to the electron and hole continuity equations (eq.5.2 and eq. 5.3):

$$\varepsilon \bigtriangledown^2 \psi = -q\,(p - n + N_{D^+} - N_{A^-}) \tag{5.1}$$

where ε is the electrical permitivity, ψ is the electrostatic potential, q is the elementary electronic charge, n and p are the electron and hole concentrations, and N_{D^+} is the number of ionized donors, and N_{A^-} is the number of ionized acceptors. The movement of the charge carriers gives a current density:

$$\bigtriangledown \cdot \overrightarrow{J_n} = q\,R_{net} + q\,\frac{\partial n}{\partial t} \tag{5.2}$$

$$-\bigtriangledown \cdot \overrightarrow{J_p} = q\,R_{net} + q\,\frac{\partial p}{\partial t} \tag{5.3}$$

where $\overrightarrow{J_n}$ is the electron current density, and $\overrightarrow{J_p}$ is the hole current density, R_{net} is the electron-hole recombination rate. The electron and hole current densities are given by,

$$\overrightarrow{J_n} = -nq\,\mu_n \cdot \bigtriangledown \phi_n + q\,D_n \frac{dn}{dx} \tag{5.4}$$

and

$$\overrightarrow{J_p} = -pq\,\mu_p \cdot \nabla\,\phi_p - q\,D_p\frac{dp}{dx} \tag{5.5}$$

with μ_n and μ_p, the electron and hole mobilities and ϕ_n and ϕ_p, the electron and hole quasi-Fermi potentials due to the device is displaced from equilibrium. Finally, D_n and D_p are the diffusion coefficients for electrons and holes respectively. Electron and hole concentrations can be recomputed from the electron and hole quasi-Fermi potentials, and vice versa, using well-known formulas 3.14, 3.19. The system of equations is an approximation of the Boltzmann transport equation system that completely describe carrier statistics in the effective mass approximation.

By solving these basic equations of semiconductor devices with appropiate boundary conditions, the behaviour of a semiconductor device can, in principle, be found analytically. However, in practice, this can only be done for relatively simple devices and conditions. The alternative approach involves representing the device structure by a mesh of discrete nodes, and applying the semiconductor equations to each point in an approximate form. Instead of partial differential equations, we now have a large system of equations, written in terms of electrostatic potential and carrier concentrations at each node. These can be solved to an acceptable level of accuracy by iterating [97].

5.2 TCAD - Technology Computer Assisted Design

This section describes a complete TCAD simulation project, starting with the device generation, device simulation and analysis of the results obteined by TCAD tools.

In this project, a semiconductor device is approximated by a 2D mesh of connected nodes which may form a regular grid. Firstly, we need to be able to represent the state of a semiconductor using the mesh. MESH is a meshing tool that provides an automatic generation of meshes. It is used to create the basic geometry of the detector, the boundaries, electrical contacts, and the various doping profiles within the semiconductor material. The meshes are adapted to the doping concentration in order to capture steep gradients.

From the semiconductor equations in section 5.1, there are three important variables that describe the state of the device at any moment: the electrostatic potential, the electron and hole concentrations. Other quantities, such as the carrier currents and electric field, are simply functions of these three variables. During the simulation, each node will have its own electrostatic potential and charge carrier concentrations. The volume between the nodes is split up into a series of elements. The values of the three variables are defined throughout each element by taking the values at the surrounding nodes and applying a linear interpolation process [98].

The resulting system of equations (plus boundary conditions) can be solved by a variety of iterative methods. In *Synopsys* TCAD, a global approximate Newton method is used. The problem can be expressed in the form $g(\mathbf{z}) = 0$, where $\mathbf{z}$ is a vector representing a possible solution and g the system of equations. Suppose we start with a guess solution $\mathbf{z}_n$, giving us a system of equations $g(\mathbf{z}_n)$ whose value is nonzero. If we know the gradient $(\nabla g)_{\mathbf{z}=\mathbf{z}_n}$, then this allows us to generate a new solution that should be closer to the correct one:

$$\mathbf{z}_{n+1} = \mathbf{z}_n - \lambda \frac{(\nabla g)_{\mathbf{z}=\mathbf{z}_n}}{g(\mathbf{z}_n)} \tag{5.6}$$

This iterative process can be repeated until the correction term is sufficiently small. The main challenge of using this method is that since $(\nabla g)_{\mathbf{z}=\mathbf{z}_n}$ is not known precisely, a suitable approximation needs to be found. This is discussed in Ref. [99].

5.2.1 Device generator: *MESH*

The first step in the simulation process is to build a grid of nodes that approximates the structure of the device. In *Synopsys*, this is done using the program MESH. The input to MESH is a set of text files[1] which specify the following:

- The basic device structure.
  The dimensions of the different materials in the device, such as the silicon substrate and dielectric layers, and also the contacts.
- Doping distributions within the device.
  Defined using analytical functions. For example, a doped strip will be defined by the surface region where the doping takes place, and a Gaussian profile describing how the doping concentration varies with depth in the silicon.
- The mesh spacing in the different regions of the device.
  For example, maximum and minimum allowed spacings, conditions to adapt the mesh spacing to the doping profiles accurately.

The simulation process assumes that, between nodes, the electrostatic potential and quasi-Fermi potentials vary linearly. So, if the value of some variables changes rapidly across a region containing few nodes, the accuracy of the simulation will be reduced. However, as the number of nodes increases, the resulting system of equations gets larger and the solving process becomes slower and more difficult. The solution is to use a high mesh density only in the regions where the doping concentration changes rapidly, the electric field is high, high levels of carrier generation will occur or interfaces between different materials. Fig. 5.1 shows an example of a mesh used to simulate a planar silicon detector. The basic structure is a p-type silicon substrate with frontside contacts for the n-doped strips and a backside contact for the p^+ electrode defined as ohmic contacts. The top of the semiconductor structure were passivated using 0.5 μm thick oxide layers. The effects of the oxide layer were taken into account by a surface recombination. Also it has p-spray between the strips.

Within the strips, the doping concentration is high and takes a fixed value, and at the edges of the strips the doping concentration falls off with distance with an error function. The mesh spacing density is highest around the strips (see Fig 5.2), where the doping concentration varies rapidly with position, and also at the back surface, where the p/p^+ interface affects the device behaviour.

[1] These files can be generated by a graphical geometry design and doping profiling tool called MDRAW. It is also linked to the mesh generator

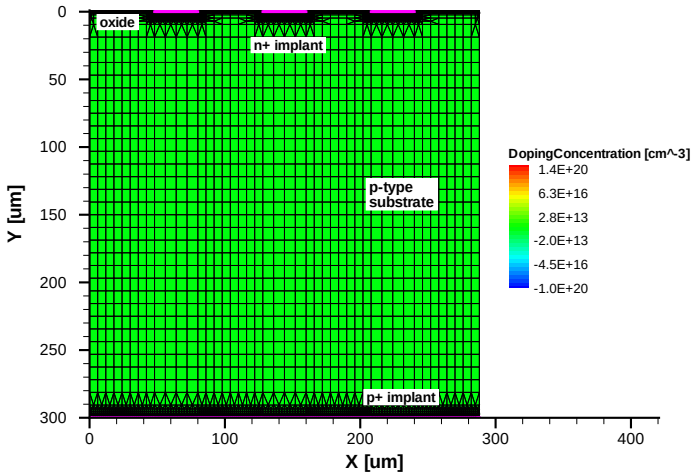

Figure 5.1: Structure of a 2D mesh used in the planar silicon detector simulation.

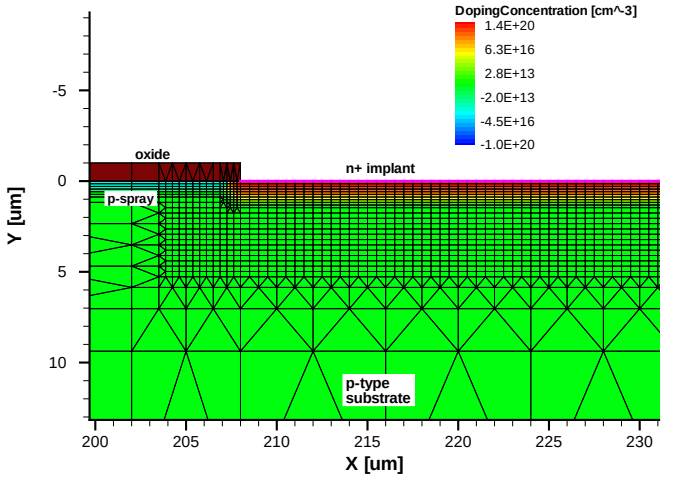

Figure 5.2: Zoom of the 2D mesh simulation. It can be seen the higher node density near the strip.

At the contacts (considering ohmic contacts, i.e. metal-semiconductor surfaces), the boundary conditions generally consist of a fixed electrostatic potential, and charge neutrality, the current is allowed to flow through them. At the boundaries of the device mesh, the default conditions are that the electric field and current density normal to the boundary are zero. These are referred to as Neumann boundary conditions:

$$\vec{E} \cdot \vec{N} = 0 \tag{5.7}$$

$$\vec{J_n} \cdot \vec{N} = 0 \qquad \vec{J_p} \cdot \vec{N} = 0 \tag{5.8}$$

The effect of the contact work function is considered negligible as highly doped regions are located below the electrodes.

In a real detector in a steady state, these conditions will naturally occur along planes of symmetry in the device. This means that basic steady-state simulations can be done using just the simplest repeating unit of the detector. A larger volume would increase the complexity of the mesh. Generally, a detector has a repetitive structure, with many strips or pixels, and in a steady state it will have a repetitive field pattern, carrier densities, etc. In a planar microstrip detector, this will be a strip. However, in order to simulate weigthing fields or charge sharing for example, a larger region must be simulated as shown in Fig. 5.1.

5.2.2 Device simulation: *SENTAURUS DEVICE*

SENTAURUS DEVICE program is used to run the simulation. This is controlled by a text file. It contains a comprehensive set of physical models, manages the device geometry, performs the simulation process and conditions that need to be simulated. It also permits mixed-mode circuit simulations with compact models, and numeric devices. These can be altered by the user from the *sentaurus* text file. These issues will be discussed in detail for a n^+p silicon sensor in the next sections.

Physics Models

Effective Intrinsic Density

The band gap and band density of states are crucial parameters of a semiconductor material. They are summarized in the intrinsic density $n_i(T)$ (equation 3.23) for undoped semiconductors and the effective doping density by means of doping-dependent band-gap narrowing for doped semiconductors through the equation 5.9.

$$n_{i,eff} = n_i exp(\frac{\triangle E_g}{2\kappa_B T}) \tag{5.9}$$

For the simulation of a n^+p silicon sensor, the *Slotboom* model has been chosen [100]. The lattice temperature dependence of the band gap is modelled by

parameter	value	units
α	4.73×10^{-4}	eV/K
β	636	K
E_{bgn}	6.92×10^{-3}	eV
N_{ref}	3.162×10^{18}	cm^{-3}

Table 5.1: Default parameters for silicon at *Slotboom* model.

$$E_g(T) = E_g(0) - \frac{\alpha T^2}{T+\beta} \tag{5.10}$$

where T is the lattice temperature (defined in the simulation file), $E_g(0)$ is the band gap energy at 0 K, and α and β are material parameters defined at the table 5.1 for this model.

The effective band gap results from the band gap reduced by band-gap narrowing ($\triangle E_g$):

$$E_{g,eff}(T) = E_g(T) - \triangle E_g \tag{5.11}$$

Band-gap narrowing for the *Slotboom* model in *Sentaurus Device* is computed from equation 5.12.

$$\triangle E_g = E_{bgn}\left(ln(\frac{N_i}{N_{ref}}) + \sqrt{(ln(\frac{N_i}{N_{ref}}))^2 + 0.5}\right) \tag{5.12}$$

where $N_i = N_A + N_D$ is the total doping concentration. E_{bgn} and N_{ref} are accesible in the *Slotboom* parameter set (see Table 5.1).

Recombination

Generation/recombination terms are important to describe the behaviour of silicon sensors. Generation is responsible for leakage current presented in reverse-biased sensors. Recombination is important to describe the transient behaviour of the device after perturbation by a charged particle crossing the depleted bulk. In a simple simulation (without radiation damage) the carrier generation and recombination rates are based on *Shockley-Read-Hall* (SRH) model. It depends on the electron and hole concentrations and the effective doping density. The model assumes that the transition of carriers between bands occurs through a single trap energy level located deeply in the gap. In *Sentaurus Device*, the following form is implemented for Silicon:

$$R_{net}^{SHR} = \frac{np - n_{i,eff}^2}{\tau_p(n+n_1) + \tau_n(p+p_1)} \tag{5.13}$$

	electrons	holes	units
τ_{min}	0	0	s
τ_{max}	1×10^{-5}	3×10^{-6}	s
N_{ref}	1×10^{16}	1×10^{16}	cm^{-3}
γ	1	1	1

Table 5.2: Default parameters for doping-dependent SRH lifetime.

with

$$n_1 = n_{i,eff}\, exp\left(\frac{E_{trap}}{\kappa T}\right) \tag{5.14}$$

$$p_1 = n_{i,eff}\, exp\left(-\frac{E_{trap}}{\kappa T}\right) \tag{5.15}$$

where E_{trap} is the difference between the defect level and intrinsic Fermi level. The silicon default value is $E_{trap} = 0$.

The minority lifetimes τ_n and τ_p are modelled as doping-dependent factors [101] with the *Scherfetter* relation given by the equation 5.16 and with the default parameter values listed in Table 5.2.

$$\tau_{n,p} = \tau_{min} + \frac{\tau_{max} - \tau_{min}}{1 + (\frac{N_A+N_D}{N_{ref}})^{\gamma}} \tag{5.16}$$

It is also possible to choose an avalanche multiplication model, where the generation rate increases in high-field regions. Electron-hole pair production due to avalanche generation (impact ionization) requires a certain threshold field strength and the possibility of acceleration, that is, wide space charge regions. If the width of space charge region is greater than the mean free path between two ionizing impacts, charge multiplication occurs, which can cause electrical breakdown. The reciprocal of the mean free path is called the ionization coefficient, α.Various expressions exists for the $\alpha_{n,p}$ term [102]. These coefficients depend on the temperature of the phonon gas against which carriers are accelerated and the electric field. With these coefficients for electron and holes, the generation rate can be expressed as:

$$G = \alpha_n n \nu_n + \alpha_p p \nu_p \tag{5.17}$$

where $\nu_{n,p}$ denotes the drift velocity. *Sentaurus Device* allows users to select the appropiate driving force for the simulation, that is, the method used to accelerating field.

The *SRH* recombination model can be included locally at the interface between two different regions as the oxide-silicon interface typical in silicon detectors.

	electrons	holes	units
μ_{min1}	52.2	44.9	cm^2/Vs
μ_{min2}	52.2	0	cm^2/Vs
μ_1	43.4	29.0	cm^2/Vs
P_c	0	9.23×10^{16}	cm^{-3}
C_r	9.68×10^{16}	2.23×10^{17}	cm^{-3}
C_s	3.43×10^{20}	6.10×10^{20}	cm^{-3}
α	0.68	0.719	1
β	2.0	2.0	1

Table 5.3: Default coefficients for the *Masseti* model for silicon.

Mobility

Sentaurus Device uses a modular approach for the description of the carrier mobilities. In the simplest case, the mobility is a function of the lattice temperature. In the so-called constant mobility model, the mobility is only affected by phonon scattering, and, therefore, dependent only on the lattice temperature:

$$\mu_{const} = \mu_b \, (\frac{T}{T_0})^{-\zeta} \tag{5.18}$$

where the μ_b is the mobility due to bulk phonon scattering (see values in the Table 3.1), T is the lattice temperature, and $T_0 = 300\ K$. The default value of the exponent ζ is 2.5 for electrons and 2.7 for holes [49]. This model should be only used for undoped materials. For doped materials, the carriers scatter with the impurities. This leads to a degradation of the mobility.

The model for the mobility degradation due to impurity scattering is a material-dependent one. For silicon, it is the *Masseti* model [103]:

$$\mu_b = \mu_{min1}\ exp\left(-\frac{P_c}{N_A+N_D}\right) + \frac{\mu_{const}-\mu_{min2}}{1+((N_A+N_D)/C_r)^{\alpha}} - \frac{\mu_1}{1+(C_s/(N_A+N_D))^{\beta}} \tag{5.19}$$

The reference mobilities μ_{min1}, μ_{min2}, and μ_1, the reference doping concentrations P_c, C_r, and C_s, and the exponents α and β for silicon are given in Table 5.3.

To activate mobility degradation at interfaces, it is computed the transverse field $E_\perp$. Then, it is used to calculate the surface contribution to the mobility. The surface contribution due to acoustic phonon scattering (μ_{ac}) and to surface roughness scattering (μ_{sr}) are given by the *Lombardi* model [104]. These surface mobilities are then combined with the bulk mobility, μ_b, according to

$$\frac{1}{\mu} = \frac{1}{\mu_b} + \frac{D}{\mu_{ac}} + \frac{D}{\mu_{sr}} \tag{5.20}$$

where $D = exp(-x/l_{crit})$ with x being the distance from the interface and l_{crit} a fit parameter which takes the value of 1×10^{-6} cm for silicon. The coefficient D is a damping that switches off the inversion layer terms far away from the interface.

In high electric fields, the carrier drift velocity is no longer proportional to the electric field strength, instead, the velocity saturates to a finite speed, v_{sat}. This effect is included in the simulation through the *Canali* model [105]:

$$\mu(F) = \frac{(\alpha + 1)\,\mu_{low}}{\alpha + \left[1 + \left(\frac{(\alpha+1)\,\mu_{low} F_{hfs}}{v_{sat}}\right)^{\beta}\right]^{1/\beta}} \tag{5.21}$$

where μ_{low} denotes the low-field mobility defined by the previously described mobility model. The exponent β is temperature dependent according to:

$$\beta = \beta_0 \left(\frac{T}{300\ K}\right)^{\beta_{exp}} \tag{5.22}$$

where T denotes the lattice temperature. F_{hfs} is the driving force given by the value of the gradient of the quasi-Fermi level:

$$F_{hfs} = |\ \nabla\ \Phi_{n,p}| \tag{5.23}$$

Finally, the saturation velocity is given by:

$$v_{sat} = v_{sat,0} \left(\frac{300\ K}{T}\right)^{v_{sat,exp}} \tag{5.24}$$

where T denotes the lattice temperature. This model is recommended for silicon. Table 5.4 lists the silicon default values.

	electrons	holes	units
$v_{sat,0}$	1.07×10^7	8.37×10^6	cm/s
$v_{sat,exp}$	0.87	0.52	1
β_0	1.109	1.213	1
β_{exp}	0.66	0.17	1
α	0	0	1

Table 5.4: Default parameters for silicon at *Canali* model.

Ionizing Radiation Simulation

Beside the device, a called ”heavy ion” model will generate extra electron-hole pairs in some region of the device, to simulate the effects of ionizing radiation. Important factors are:

- The space-time location of the ion at entering the device.
- The shape for the spatial distribution of the ionization (*Gaussian* has been chosen for our simulations).
- The relation between the energy loss and the numbers of pairs created.

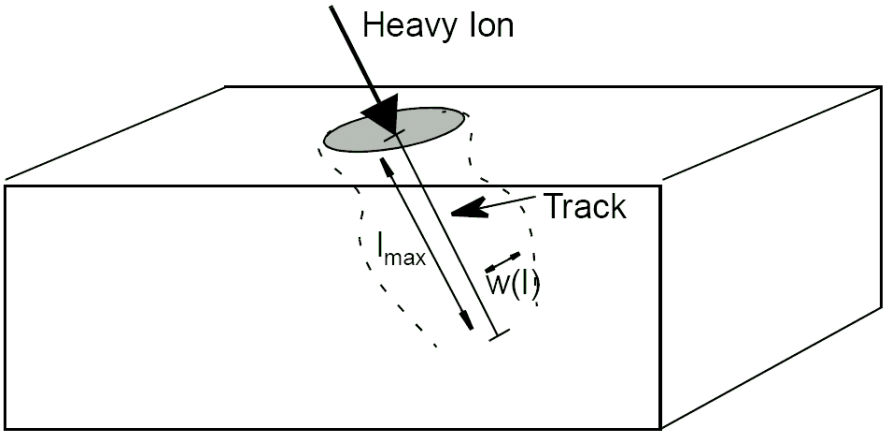

Figure 5.3: A heavy ion penetrating into semiconductor; its track is defined by a length and the transverse spatial influence is assumed to be symmetric about the track axis.

A simple model for the heavy ion impinging process is shown in Fig. 5.3. In this model the generation rate caused by a heavy ion is computed by:

$$G(l,w,t) = LET(l) \times R(w) \times T(t) \quad [cm^{-3}s^{-1}] \tag{5.25}$$

where l is the penetration length of the particle, w is the width of the generation cylinder and t is the time. If $l > l_{max}$ (l_{max} is the length of the track),

$$G(l,w,t) = 0 \tag{5.26}$$

$R(w)$ and $T(t)$ are functions describing the spatial and temporal variations of the generation rate. $LET(l)$ is the linear energy transfer generation density ($pairs/cm^3$) and is the fundamental parameter to define how many pairs/micrometer the heavy ion generates. The functions used for this model are given in reference [106].

Radiation Model

A more complicated issue is the simulation of the effects of radiation-induced defects to match with real data. It is intend by including carrier motion between the conduction and valence bands and a series of extra trap levels within the bandgap. *Sentaurus Device* provides

several trap types (acceptor, donor), types of energy distribution and various models for capture and emission rates. Traps are available for both bulk semiconductors and interfaces. More sophisticated simulations of irradiated bulk properties would require a more complex description of generation-recombination mechanisms that is not included in our simulation. Bulk material is simply represented by its resistivity and generation-recombination processes are parametrized by radiation induced traps and standard *Shockley-Read-Hall* recombination. The amount of ionized traps is determined using Boltzmann statistics.

Simulation Process

The most basic form of simulation simply applies a set of boundary conditions, typically a set of electrode voltages, and finds the solution for a device in a steady state. Under these conditions, the time-dependent terms in the semiconductor equations are zero. These simulations can, for example, be used to find the electric field pattern in the device.

The next variety is ”quasi-stationary”. The device is first solved in a stationary state, as described above. Then, some of the boundary conditions such as the electrode voltages are changed by a small amount, and the device is re-solved in a steady state. This is repeated over a series of steps, in order to find how the device behaviour varies with a determined parameter. This can be used to find the current-voltage characteristics of the device. At each step, an initial solution is found by extrapolation from the previous solutions, speeding up the process.

Also, there are ”transient” simulations, where the device is simulated in the time domain. The initial state of the detector is found in a steady-state, as above, and then the simulation proceeds in a series of small time steps. At each step, the rates of change in carrier concentrations and potential are found for each node, and these are then used to find the state of the device at the next step. This can be used to find the current signal produced by a particle interacting with a detector. To ensure that the process is accurate, the step sizes must be small compared to the time scales of the processes occurring during the simulation (the collection time).

Lastly, in ”mixed-mode” simulations several simulated devices can be connected in a circuit together with elements that have a compact model as for example, resistors and capacitors. This kind of simulations will be used in the chapter 8.

In the following simulations, unless otherwise stated, the effective intrinsic density includes doping-dependent band-gap narrowing. The mobility of the carrier was taken into account using doping concentration-dependent and high field saturation-dependent physical model. This means that the electron and hole velocities can not increases without limit as the electric field gets stronger, but will instead reach a saturation velocity.

The simulations were done at a temperature of 300 K, and it is used the Shockley-Read-Hall recombination model. Specific physics models can be applied in different regions of the device. Examples of simulation command files are added to the appendix B.

5.2.3 *TECPLOT*

It is a compact visualization tool that allows an exploration of meshes and detector characteristics created by MESH and the electrical characteristics obtained by SENTAURUS DEVICE as

results of the simulation. The created figures can be viewed and manipulated and finally printed out in a encapsulated postscript (eps) form.

5.2.4 *INSPECT*

It permits the analysis of the simulated *x*-*y* data, the extraction of characteristic data from TecPlot and provides a programmability using TCL (Tool Command Language) scripting. The final plots can be printed in eps form.

5.3 Basic simulations

This section details the different characteristics of the sensor we want to simulate and the data extracted from the simulation results to obtain information on the possible behaviour of real sensors.

The goal of these simulations is to look inside a simplified two dimensional silicon microstrip sensor. Electric field and depletion behaviour are analised in order to find a model that describes a real silicon sensor as accurate as possible. Macroscopic characteristics as depletion voltage, collected charge... allow to compare them between simulated and real data. A three defect level model is used in the simulations to study the behaviour of such sensors under different level of irradiation.

A 2D basic structure of a silicon sensor (Fig. 5.1) has been used as a simplified model of an unirradiated n^+p microstrip silicon sensor. By reducing the size of our sensor comparatively to the real sensor geometry, the simulations are easily solved in a short computing time and allows us to explore the main parameters that can be extrapolated to a complete sensor geometry. The simulation domain consists of a 3-strip subset of a larger detector array. A 40 μm strip width and 80 μm pitch are assumed, respectively. Single sided detectors have been considered of 300 μm thick.

The doping concentration used for our sensor model is taken from the characteristics of unirradiated n^+p microstrip silicon sensors produced at CNM which also have been studied at the laboratory in order to compare the simulated and the real data. The bulk is p-type silicon. The strip implant is highly doped n-type and are insulated from each other by low dose of p-type implant (p-spray). Back side electrode is highly doped p-type. Figure 5.4 shows the geometrical distribution of the device and Table 5.5 summarizes the numerical values for doping used in the simulation. Doped regions are 1 μm deep and decay exponetially over the doped zone.

The main additional model used here was the introduction of a fixed positive charge of 4×10^{11} cm^{-2} at the interface between the silicon substrate and the oxide layer. This is due to the presence of trapped holes within the oxide layer, as discussed in section 3.3. The outer surfaces of the oxide layers used Neumann boundary conditions, which is a good approximation to the oxide behaviour in a ”clean” wafer.

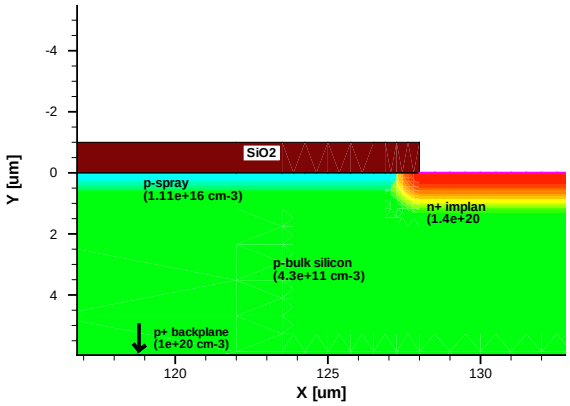

Figure 5.4: Doping profiles used in our simulation.

	concentration $[cm^{-3}]$
p-bulk	4.3×10^{11}
n^+-implant	1.4×10^{20}
p^+-backplane	1.0×10^{20}
p-spray	1.11×10^{16}
Q_{oxide}	4×10^{11}

Table 5.5: Parameter set for doping concentrations used for the simulation of a microstrip silicon sensor. These values have been taken from the characteristics of real microstrip silicon sensor produced by CNM.

5.3.1 IV and CV characteristics

The bulk current of a silicon sensor under reverse bias (the leakage current) is strongly dependent on the generation rate in the drift-diffusion process. This current is given by the applied bias on the sensors, and hence, described as proportional to the depletion width. Also it adds up to the signal pulse when a particle is detected, increasing the noise. It is important to keep its value as low as possible.

Fig. 5.5 shows the I-V curve of the simulated n^+p sensor by a solid line. The simulation data is compared to real data corresponding a n^+p FZ sensor with the same doping profile represented by circles. The differences between real data and simulations are mainly due to the imperfections and surface effects of the real detector as well as to the simplifications of the simulated model. The simulated leakage current data has been scaled to a sensor with 130 strips in order to compare with the real detector data. However, the different level of current is related to the sensor is simulated two-dimensionally and the lenght of the strip is not taken into account. In addition, the simulation does not take into account the edge effects. Respect to the real sensor,

the lateral border of the device presents a high density of defects that increases the generation rate and hence, the leakage current, even after full depletion. However, it is noted that the ink point in the curve at which the leakage current begins ideally to be constant due to full depletion is for both data at an approximately reverse bias of 30 V.

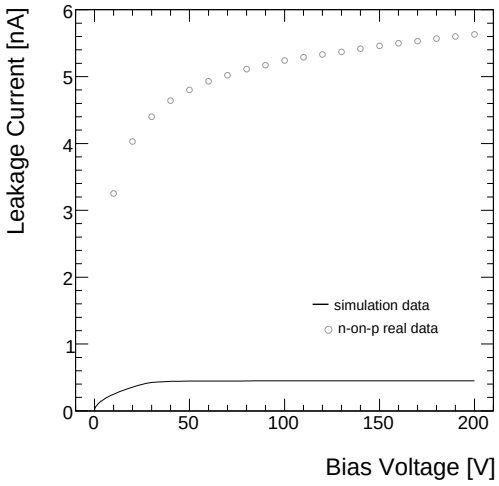

Figure 5.5: Leakage current-bias voltage characteristic for the simulated sensor (solid line) and a real n^+p FZ detector (circles).

Apart from this, as the bias voltage on the sensor electrode increases, the amount of free charge carriers in the sensor bulk is reduced, up to the point where all the charge carriers are gone and the depletion region extends to all the sensor thickness. The bias voltage where this condition is reached (V_{fd}) can be computed through the simulation of the capacitance-bias voltage curve (Fig. 5.6). From this curve the full depletion voltage corresponds to $V_{fd} \sim 30\ V$.

The comparison between simulated and real data is shown in figure 5.7. The simulated data has been scaled to a real sensor area. Nevertheless, the real data includes effects as lateral depletion that is not taken into account in the simulated data.

The simulation model describes the electrical behaviour of a n-on-p FZ sensor in a general way. Despite some effects are not taking into account in the simulation and the simulated geometry does not correspond to a complete sensor, it is possible to extract basic parameters of its performance.

5.3.2 Electric field

The electric field shape inside the bulk of the sensor is an important parameter to determine its charge carrier behaviour and its typical pulse shape. The free charge carriers move in the electric field and its magnitude influences the speed at which the charge is collected and the probability of breakdown due to avanlanche formation. Breakdown electric field in silicon is in average

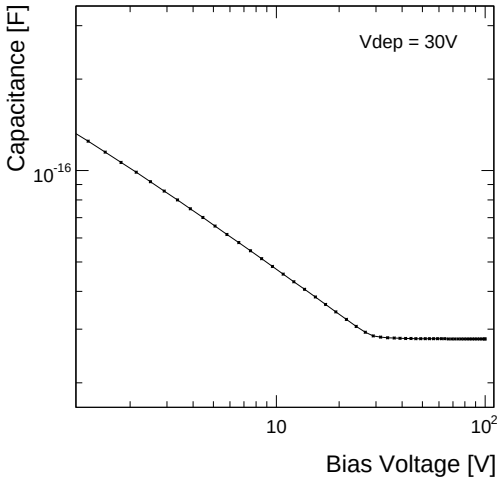

Figure 5.6: Simulated capacitance-bias voltage characteristic for a n^+p FZ sensor. The curve shows a full depletion voltage at 30 V. It is noted the logarithmic scale.

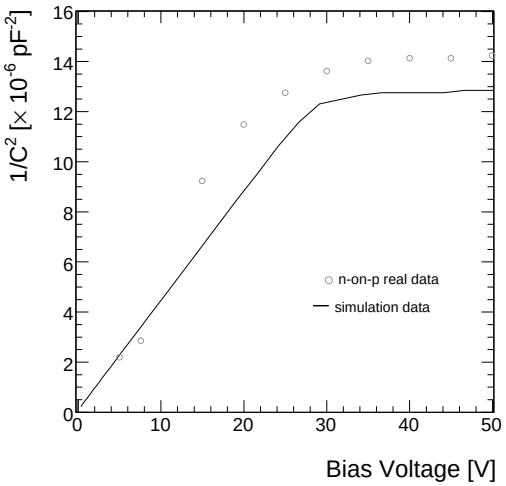

Figure 5.7: $1/C^2$ as a function of the bias voltage for a simulated sensor (solid line) and a real n^+p FZ detector (circles).

close to $|E_{break}| \sim 3 \times 10^5 V/cm$. Figure 5.8 represents the maximum electric field reached during the bias voltage ramp-up time simulation for different voltages. The increasing of the electric field is linear and its magnitude is under the breakdown limit ever for the highest bias voltage of 1000 V. For a safe operation of the sensor, a field magnitude over this limit should not be presented.

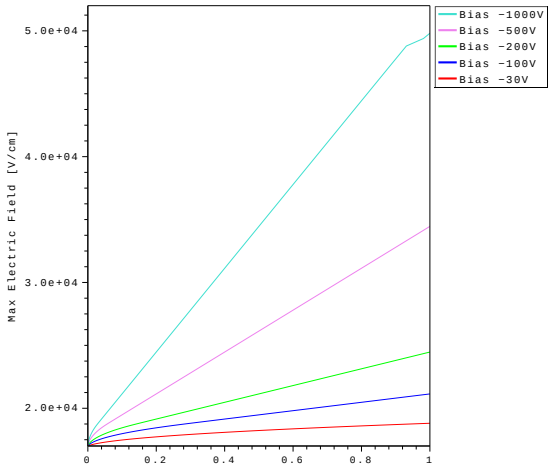

Figure 5.8: Maximum electric field at the simulated n^+p sensor for several bias voltage. The x axis indicates the simulation stages on voltage up to the applied bias voltage.

Figures 5.9 and 5.10 show a zoom of the electric field distribution near the central strip corner. They show the region where higher electric field occurs. Figure 5.9 represents the electric field for low bias voltage considering before (bias at 10 V) and after depletion stages (with bias at 100 and 200 V). Also it is showing the electric field at full depletion voltage (30 V). The region with the highest electric field is defined by the SiO_2-Si interface where the p-spray layer is situated due to doping gradients among the differents regions.

Figure 5.10 shows the electric field pattern for highly biased sensor. Right-handed figure represents a reverse biased sensor at 500 V and left-handed figure is obtained for 1000 V. The electric field magnitude remains under breakdown limit. Nevertheless, at 1000 V a high electric field zone is observed at the strip corner. It is produced due to the contact between the n^+ strip and the p-spray layer at a such applied high potential. It represents a possible microdischarge mechanism on sensors and as consequence not an appropiate performance. The p-spray dose is a crucial parameter to take into account in the design of n^+p sensors in which strip isolation is mandatory.

5.3.3 Strip isolation

For this simulation study, the strip isolation with p-spray is explored. Figure 5.11 shows the electric field distribution through the sensor at a reverse bias of 100 V. It is compared the sensor with p-spray (fig. 5.11(a)) and the same sensor without the p-spray layer (fig. 5.11(b)). Regions

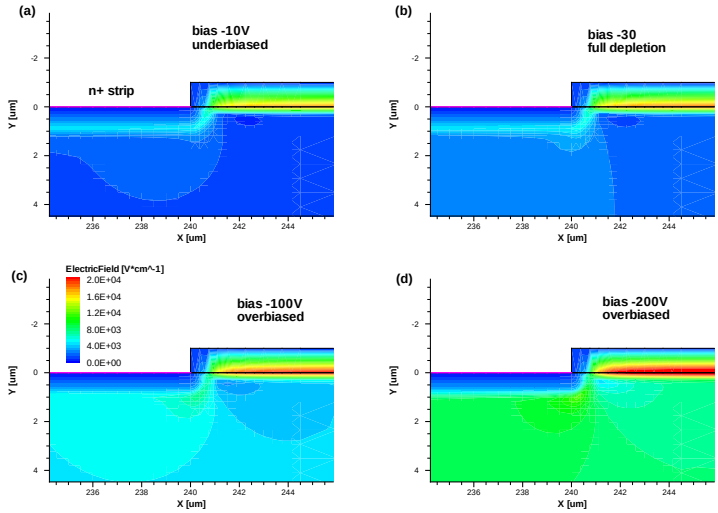

Figure 5.9: 2D electric field distribution for the simulated n^+p sensor for a (a) under depletion bias (10V), (b) full depletion voltage (30V), (c) over depletion bias (100V), and (d) higher bias (200V).

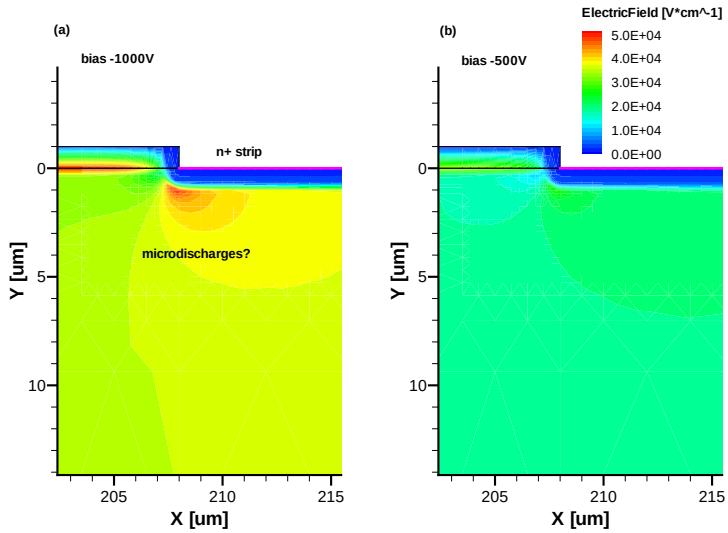

Figure 5.10: 2D electric field distribution for the simulated n^+p sensor for highly reverse bias voltages (a) 1000V, and (b) 500V.

with equal electric field are defined by solid lines. It is important to note that with p-spray the electric field region around every strip is not shared with the neighbouring strip. Not in the case which p-spray is not presented and then, it is increased the charge sharing between the strip, hence, decreasing the spatial resolution of the detector.

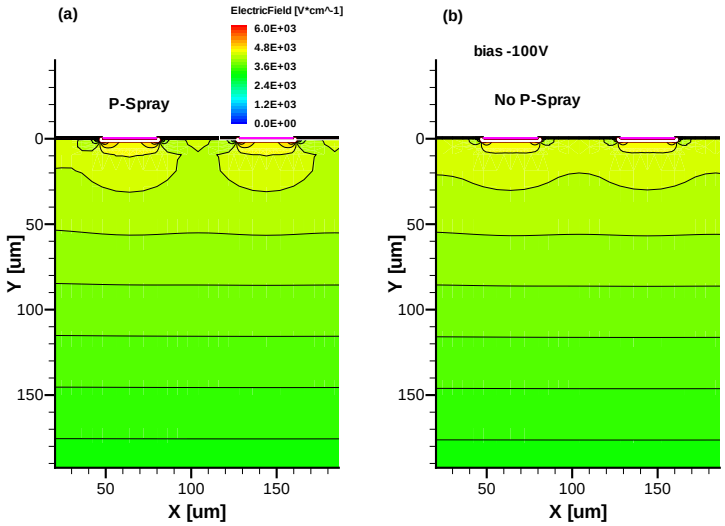

Figure 5.11: 2D electric field distribution of the simulated n^+p sensor at a bias of 100 V (a) with p-spray isolation, and (b) without p-spray isolation.

Fig. 5.12 shows the electron density in the sensor with and without p-spray isolation. The lack of strip isolation has for effect the so-called electron inversion layer as explained in chapter 3. High electron concentration is accumulated in the SiO_2-Si interface attracted by the positive charge trapped at the oxide by the amorphous character of the oxide. This layer makes the strip isolation mandatory in order to avoid shorted strips.

For the time being, a non-irradiated sensor is considered. Even in this case, a low concentration of charge is presented at oxide-silicon interface, such as $4\times10^{11}\ cm^{-2}$. Nevertheless, the most critical situation concerning strip isolation is in the first stages of irradiation where the charge oxide is saturated. It could happen in a very short time after irradiation, after $\sim 1\ Mrad$ of absorbed dose [82]. Fig. 5.13 shows the simulated electric field at a reverse bias of 100 V. After oxide charge saturation with a typical value of $Q_{oxide} = 3\times10^{12}\ cm^{-2}$ and p-spray is represented in the fig. 5.13(a). It is compared with the non-irradiated case with (fig. 5.13(b)) and without (fig. 5.13(c)) p-spray. The presence of a p-spray layer in contact with the substrate originates the higher electric field region that is not seen in fig. 5.13(c).

Concerning oxide saturation, the electric field magnitude decreases lightly and with it, the probability to breakdown. The p-spray layer guarantees a complete strip isolation when the oxide charge saturation occurs as in the case with no saturation as seen the resulting electron density in Fig. 5.14.

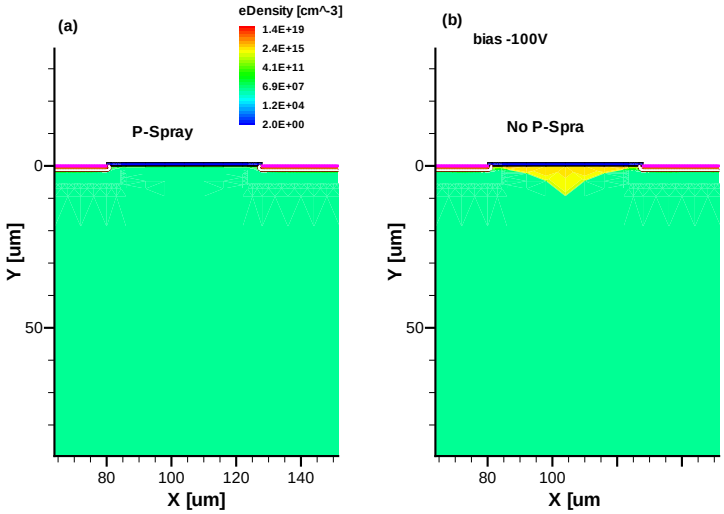

Figure 5.12: 2D electron density on the simulated n^+p sensor at a bias of 100 V (a) with p-spray isolation, and (b) without p-spray isolation.

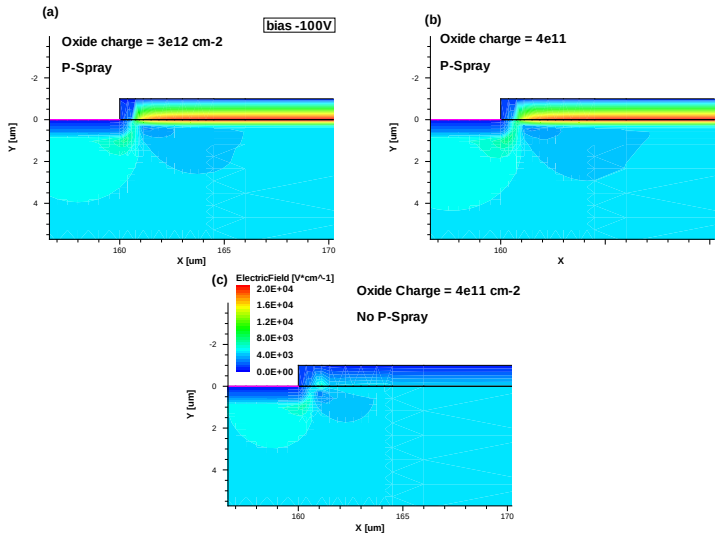

Figure 5.13: 2D electric field distribution on the simulated n^+p sensor at a bias of 100 V with (a) p-spray isolation and oxide charge saturation, compared with the case (b) with p-spray and not oxide charge saturation. (c) shows the case with no p-spray isolation and not oxide charge saturation.

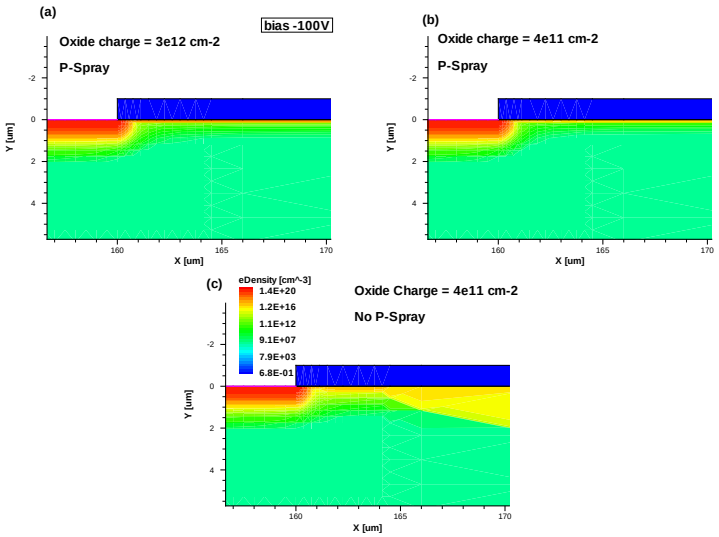

Figure 5.14: 2D electron density distribution on the simulated n^+p sensor at a bias of 100 V with (a) p-spray isolation and oxide charge saturation, compared with the case (b) with p-spray and not oxide charge saturation. (c) shows the case with no p-spray isolation and not oxide charge saturation.

5.3.4 Mobility

Without electric field, in the sensor, the charge carriers (electrons and holes) move around randomly due to their thermal excitation. Therefore, on average there will be no overall motion of charge carriers in any particular direction over time.

When an electric field is applied, each charge carrier is accelerated by the electric field. However, the charge carrier repeatedly scatters off crystal defects, phonons, impurities, etc. Therefore, it does not accelerate indefinitely; instead, it moves with a finite average velocity, that is the drift velocity. This net carrier motion is usually much slower than the normally occurring random motion.

As the electric field increases, the electron mobility starts degrading as shown in the left graph in Fig. 5.15 due to the impurity scattering effects can not be ignored whereas the drift velocity remains finite. In addition, the mobility dependence on the doping concentration contributes to its degradation as the increasing electric field alters the doping at each node. In the simulation, it is also taken into account the scattering with surface phonons and surface roughness.

The mobility model takes into account the drift velocity saturation at high fields. From the right above figure in Fig. 5.15 it observed the carrier drift velocity saturation as the bias voltage increases reaching a saturation velocity of 100-120 $\mu m/ns$ at about 600 V. The right below figure in Fig. 5.15 shows that the simulation are found at the linear regime of the electric field.

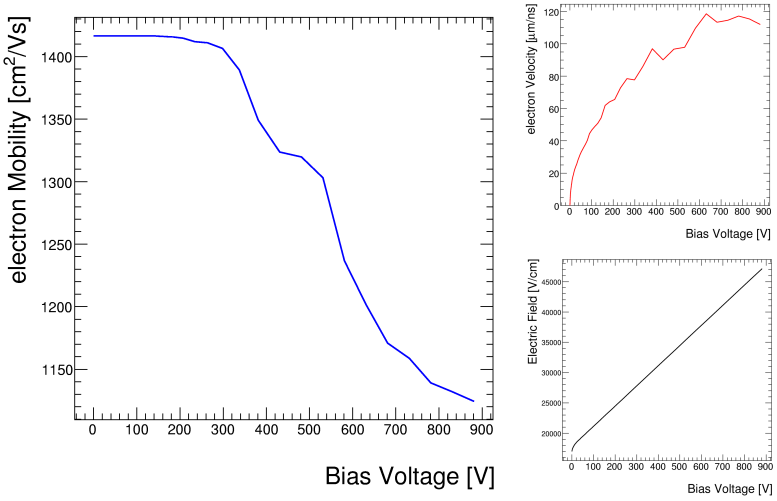

Figure 5.15: Left figure shows the change in the electron mobility as a function of the bias voltage applied to the simulated p-type sensor. Right above figure represents the electron velocity as a function of the bias voltage reaching saturation at high voltages. Right below figure shows the electric field linearity as the bias voltage increases.

5.3.5 Charge collection efficiency

For this study, it is simulated and explored the time-varying current response of the sensor to an ionizing particle across it. A given amount of charge carrier pairs is initially distributed along an arbitrary path, and subsequently moves across the bulk under the influence of electrostatic and diffusion forces.

First, it is considered a non-irradiated sensor to stablish correctly the simulated charge collection processes and then radiation effects are accounted for by introducing suitable terms into the transport equations solved by the program.

Non-irradiated sensor

Simulation of a non-irradiated microstrip sensor was performed up to 1000 V. A fixed trajectory has been assumed, impinging at ($y = 0,\ x = 100\ \mu m$). It is placed between the two first strips, nearer to the first strip than the second one and normal to the detector surface. It crosses full sensor width with a charge density of $1.282 \times 10^{-5} pC/\mu m$ (i.e 80 $e^-/\mu m$ that corresponds to 24000 e^- in the detector volume) which corresponds to the charge density generated by a *mip* traversing a silicon microstrip device of 300 μm thick.

Current pulses at the strips can thus eventually be predicted, allowing to evaluate the sharing of the generated charge among the collecting strips. A 500 V reverse bias has been considered, so that the bulk is fully depleted. The strip to which the generated charge drifts is determined by the electric field strenght and at $V = 500\ V >> V_{fd}$, the influence of diffusion on induced charge

becomes small. Fig. 5.16(a) shows the predicted currents induced at any strips after a $\sim 4\ fC$ charge has been uniformly distributed along the 300 μm trajectory. It is obtained a higher signal response read out by the first strip since it is the strip nearest to the trajectory of the particle. The charge drift induces a current pulse also in the neigbouring strips. Only the two nearest neighbours strips on one side have been considered in the simulation. The 1^{st} neighbour strip gives a considerable signal meanwhile the signal induced on the 2^{nd} neighbour strip is negligible. At this 2^{nd} neighbour it is induced a negative pulse due to this electrode *see* the electron motion to the rest of electrodes in the opposite direction as they were collecting carriers with opposite charge.
By integrating such pulses over a 25 *ns* time interval after subtracting the leakage current, the charge collected at each strip has been stimated as seen in Fig. 5.16(b). The resulting collected charge is shared by the two first microstrips : 1^{st} strip ~ 58 % and its 1^{st} neighbour ~ 42% of the total charge. The influence of the third strip on charge collection is ignored.

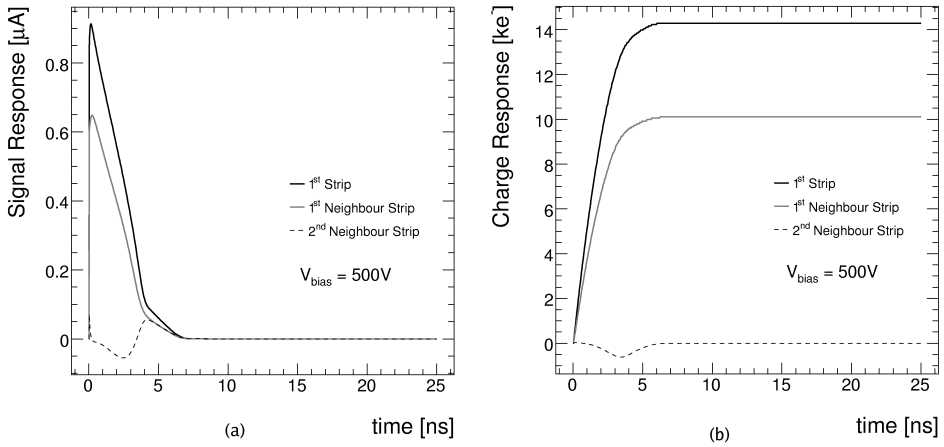

Figure 5.16: Left plot. (a) An example of induced current of a *mip* track of normal incident angle on the simulated non-irradiated p-type sensor operated at 500 *V*. Right plot (b) The signal integral to get the charge collected by every strip of the simulated non-irradiated p-type sensor operated at 500 *V*. It is noted that the total charge collection is accumulated by the two first strips between which the *mip* crosses.

Therefore, the collected charge (CC) is defined as the sum of the signals on the two first strips. Fig. 5.17 shows the dependence of charge collection on the applied bias voltage. It is shown the total charge collected by the sensor up to a bias voltage of 200 *V*. It is compared real data (by grey points) corresponding to a non-irradiated p-type FZ microstrip sensor with simulation data (solid line). The maximum bias voltage is stablished by the upper bias voltage in real data. The CC voltage dependence can be explained by the increase of drift velocity at higher bias voltages, and the consequent reduction of ballistic deficit till the full depletion is reached. Both data sets correspond to a 300 μm thick sensor. This way, after full depletion, a maximum collected charge of 24000 electrons is shown.

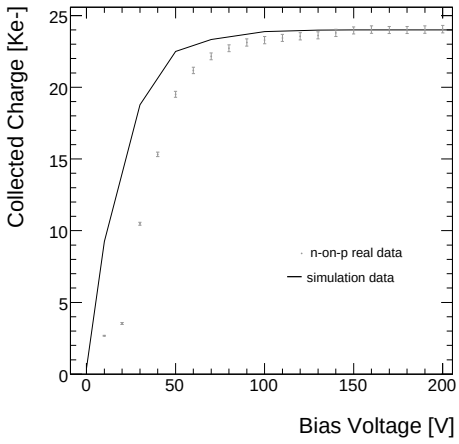

Figure 5.17: Collected charge as a function of bias voltage for a non-irradiated p-type 300 μm thick detector. It is compared the collected charge obtained from a real detector (gray points) and simulated data of a sensor with the same characteristics (solid line).

Illustratively, a self-consistent picture of charge motion is recovered at Fig. 5.18 and at Fig. 5.19. They are showing the electron density (Fig. 5.18) and the hole density (Fig. 5.19) at the particle crossing through the sensor reverse biased at 500 V. Every image corresponds to a determined simulation time. It was considered a total simulation time of 25 ns and it was stored the sensor properties at different stages of the simulation. These are listed in Table 5.6. As well as the alteration of the electric field due to the particle crossing through the sensor is shown in Fig. 5.20.

image	simulation time [ns]
(a)	0.03
(b)	0.2
(c)	0.5
(d)	1.0
(e)	2.0
(f)	5.0
(g)	10.0
(h)	25.0

Table 5.6: Legend to consider to figures 5.18, 5.19, and 5.20. Every subimage corresponds to a different stage of time in the transient simulation of the particle crossing a sensor.

In Fig. 5.18, it is observed the position at which the particle starts crossing the sensor and the electrons are attracted to the frontside of the sensor where the n-type electrodes are. While the Fig. 5.19 shows the hole moviment to the backside of the sensor due to they are attracted to the

p-type electrode. The motion of these charge carriers leads to the signal pulse read out from those electrodes. With the readout on the n-type electrodes the signal pulse is mainly due to the electrons moving to the electrodes.

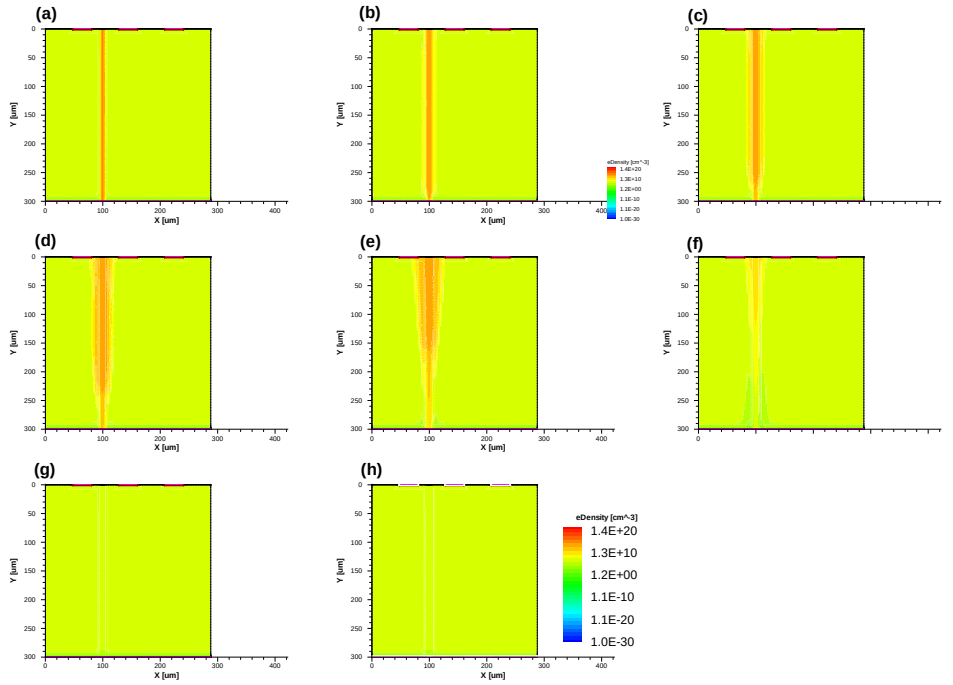

Figure 5.18: Electron density pattern of a simulated p-type sensor biased at 500 V. Every image corresponds to a different stage of the transient simulation of a particle crossing the sensor. The legend of the images is shown in Table 5.6. Every image corresponds to a different simulation time, that is, (a) 0.03 *ns*, (b) 0.2 *ns*, (c) 0.5 *ns*, (d) 1 *ns*, (e) 2 *ns*, (f) 5 *ns*, (g) 10 *ns*, and (h) 25 *ns*.

Irradiated sensor

Radiation damage introduces defects in the bulk of the silicon that modify its behaviour as explained at Chapter 4. These defects may recombine, or they can form complexes with each other, or with existing impurities in the bulk introducing extra energy levels within the silicon bandgap. *Synopsys* simulates this bulk radiation damage modelling the dynamics of these traps. It is necessary to select the parameters of a set of defects reasonably consistent with experimental measurements of trap types and concentrations in order to reproduce the correct macroscopic behaviour.

The trap levels used here correspond to the modified p-type model from the work done at the University of Glasgow [107] that is, in turn, based on the model cited at [108]. It is used to

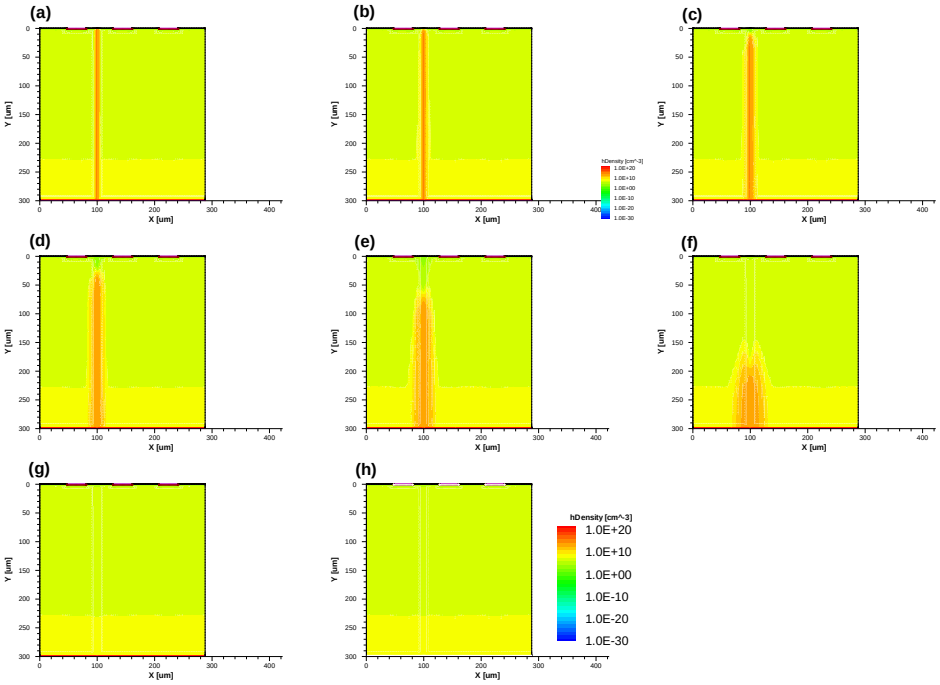

Figure 5.19: Hole density pattern of a simulated p-type sensor biased at 500 V. Every image corresponds to a different stage of the transient simulation of a particle crossing the sensor. The legend of the images is Table 5.6. Every image corresponds to a different simulation time, that is, (a) 0.03 *ns*, (b) 0.2 *ns*, (c) 0.5 *ns*, (d) 1 *ns*, (e) 2 *ns*, (f) 5 *ns*, (g) 10 *ns*, and (h) 25 *ns*.

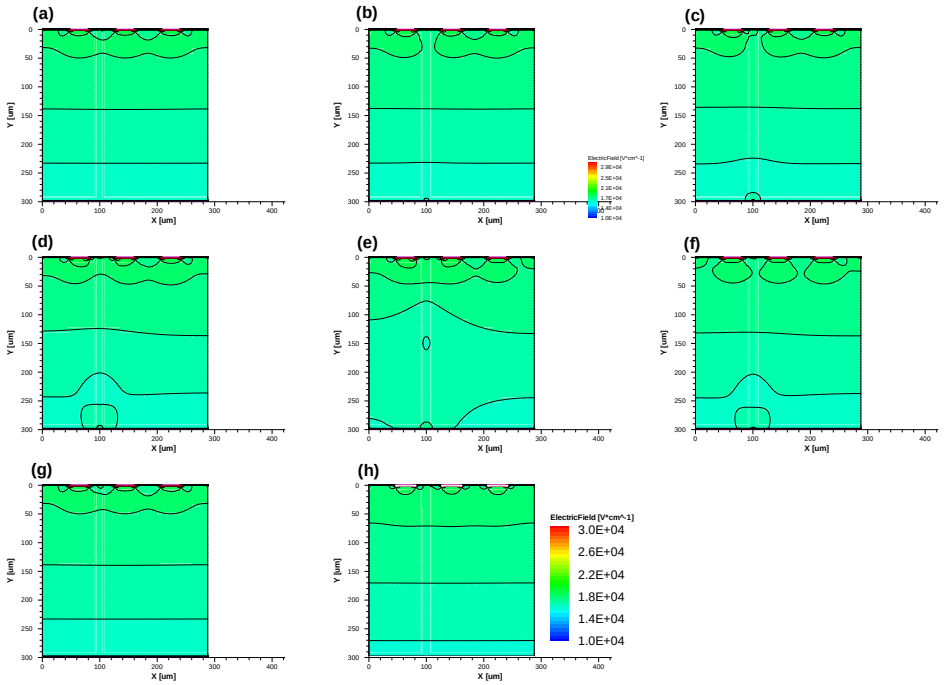

Figure 5.20: Electric field pattern of a simulated p-type sensor biased at 500 V. Every image corresponds to a different stage of the transient simulation of a particle crossing the sensor. The legend of the images is Table 5.6. Every image corresponds to a different simulation time, that is, (a) 0.03 *ns*, (b) 0.2 *ns*, (c) 0.5 *ns*, (d) 1 *ns*, (e) 2 *ns*, (f) 5 *ns*, (g) 10 *ns*, and (h) 25 *ns*. Iso-electric field regions are marked with solid lines for clearer view of the images.

model p-type float zone silicon. The details of the traps are given in Table 5.7. Each single trap can be independently parametrised [106] in terms of:

- Trap type: acceptor and donor.
- Energetic distribution of traps: level (used), uniform, exponential, and gaussian.
- Trap energy /in eV).
- Trap concentration (in cm^{-3} for bulk and cm^{-2} for interfaces):

$$Conc = \Phi \cdot \eta \tag{5.27}$$

  where Φ is the fluence in cm^{-2} and η is the introduction rate. By default, trap concentrations are uniform over the domain for which they are specified.
- The electron and hole capture cross sections, σ_e and σ_h in cm^2 which reflect the probability of trapping.

Type	Energy (eV)	Defect	σ_e (cm^2)	σ_h (cm^2)	η (cm^{-1})
Acceptor	$E_C - 0.42$	VV	9.5×10^{-15}	9.5×10^{-14}	1.613
Acceptor	$E_C - 0.46$	VVV	5×10^{-15}	5×10^{-14}	0.9
Donor	$E_V + 0.36$	$C_i\,O_i$	3.23×10^{-13}	3.23×10^{-14}	0.9

Table 5.7: Modified p-type float zone silicon trap model used in the following simulations.

The two acceptor levels are slightly above the midgap, and so will generate electron-hole pairs increasing the leakage current. Although most of the acceptors will be empty, a small proportion will be occupied by electrons and become negatively charged, increasing the effective p-type doping. Finally, the unoccupied acceptors will trap excess electrons from the conduction band. The one donor level is significantly below the midgap, and its main effect is trapping excess holes from the valence band and a little contribution to leakage current or effective doping concentration. In addition, the three level are related to dominant defects based on direct measurements of trap properties from techniques as Deep Level Transient Spectroscopy [109]. Then, they can be modified to give a better match to the macroscopic damage effects seen in detectors. What really make an irradiated sensor simulation complicate is to know exactly the defect concentration and their energy levels. The model uses isolated defect levels. Nevertheless, it is not understood the influence of defect clusters on the electrical properties.

Simulation of irradiated sensors was limited to a fluence of 10^{15} n_{eq}/cm^2 as this is the maximum fluence at which the radiation damage model has proven to be quite accurate. Experimentally, the electron and hole trapping rates have been shown to be linear with fluence up to 1×10^{15} n_{eq}/cm^2 [110], as parametrised by $\beta_{e/h}$. These have been measured as β_e = 4.0×10^{-7} cm^2s^{-1} and 4.4×10^{-7} cm^2s^{-1}. This limitation is because the method used to measure the lifetimes will only work with fully depleted detectors, and the depletion voltage of a heavily irradited sensor may become very high, being experimentally very difficult to reach full

depletion. So, these simulations only consider fluences up to $1 \times 10^{15}\ n_{eq}/cm^2$. Finally, surface damage was modeled by means of an amount of charge trapped within the oxide of $1 \times 10^{12}\ cm^{-2}$ being $4 \times 10^{11}\ cm^{-2}$ before irradiation.

The charge collection behaviour of the strip detector was simulated at different levels of damage as shown in Fig. 5.21. It is represented the predicted CCE, for three fluences, depending on the applied reverse bias. The effect of trapping can be clearly seen. Above V_{fd}, a substantial part of the charge is trapped due to the slow drift. Due to the detrapping time is long compared to the simulation time used, charge once trapped, does not contribute to the signal. The trapping probability is proportional to the fluence, so, this effect is more pronounced at the higher fluences.

Related to experimental measurements, the prediction of simulations does not match perfectly with measurements as illustrated in Fig. 5.22. It is shown the corresponding decrease in the collection efficiency as function of the fluence at 400 V of applied reverse bias for the simulated sensor and three microstrip n^+p FZ silicon sensors with different silicon bulk (FZ, MCz, and DOFZ) and one microstrip n^+n FZ silicon sensor. The simulated CCE values follow the same trend as the experimental values. However, at the fluence increases, the simulations give substantially higher charge collection except when comparing with the n^+n sensor. In this case, the simulations results are close to the experimental measurements reminding that after irradiation, the n-type silicon bulk is type-inverted becoming effectively p-type. Conclusively, the simulation data result in an overstimation of the charge collection for p-type sensors, with a close approximation at type-inverted n-type sensors due to the better performance of n^+n sensors in terms of charge collection as explained in Chapter 4.

At this point, the next step would be a modification of the model in order to fit the simulation results more closely to the experimental results. However, since the charge collection is dependent on different factors (electron and hole trapping rates, and changes in the effective doping), it is converted in a tedious time-consuming task with likely a partial success. It is likely that there is more charge carrier trapping that this model predicts. So, this model is taken as a optimistic stimation for charge collection measurements of planar microstrip p-type silicon sensors.

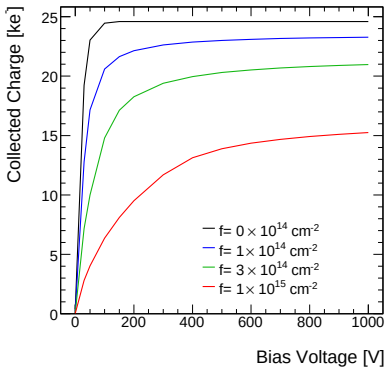

Figure 5.21: Simulated charge collection in n^+p strip detectors at different fluence as function of the applied reverse bias.

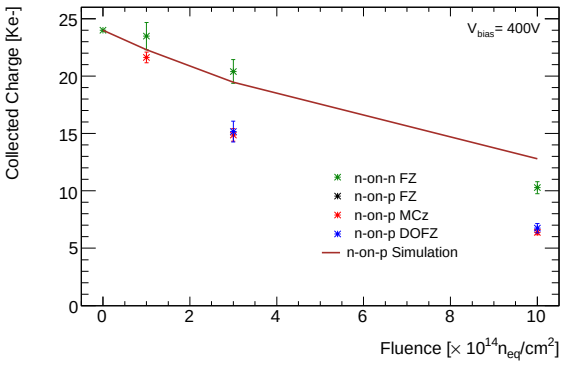

Figure 5.22: Comparison between simulated and experimental charge collection in n^+p strip detectors as function of the fluence. It is also included the experimental measurements obtained from a n^+-n strip sensor. Experimental results are taken from measurements presented in this thesis. Both the simulation and the experimental results used 400 V bias.

Chapter 6

Experimental techniques for the characterization of silicon microstrip detectors

This chapter provides an overview of some of the basic characterization procedures of silicon microstrip detectors, namely the current-voltage (IV) and capacitance-voltage (CV) techniques and the sytems used to evaluate the performance of sensors after irradiation. Also, two different charge collection test setups are discussed. These techniques are then applied to different strip detectors. Details of the irradiation facilities used throughout the studies in this thesis are also provided.

6.1 IV and CV techniques

Measurements of the current-voltage (IV) and the capacitance-voltage (CV) characteristics are made as basic tests for characterizing and evaluating the performance of silicon detectors.

The characterization of such sensible devices as the microstrip detectors must be carried out under controlled environmental conditions. A clean room class 10 000[1] with an area of 80 m^2 is used to that effect. It is located at *IFIC* (Instituto de Física Corpuscular) and shown in the picture 6.1. The clean room system allows to control the temperature and the humidity. The work values were set to $20 \pm 0.5^{\circ}C$ and $45 \pm 5\%$ respectively and they are within the fixed values by the ATLAS Collaboration ($21 \pm 2^{\circ}C$ and $50 \pm 10\%$) for the characterization of detectors.

6.1.1 Current-Voltage (IV) testing

The leakage current can degrade the detector operation contributing to the noise and if the breakdown voltage occurs at a very low voltage, it will prevent any signal from being measured,

[1] Particle count of a size $0.5\mu m$ and larger should not exceed a total of 10 000 particles per cubic foot.

Figure 6.1: Clean room facility at IFIC-Valencia.

and can also damage the readout electronics or the detector itself.

For a silicon sensor, the leakage current is dominated by generation current in the silicon bulk with a temperature dependence given by equation 3.50. For non-irradiated sensors it is generally low. But as seen in section 4.2.1, the current scales with radiation fluences, so for irradiated sensors the leakage current contribution to the noise is higher. In other side, the leakage current determines the power consumption of the detector since the leakage current will lead to power dissipation within the detector, which places greater demands on the power supply and the cooling systems in a experiment.

Due to these considerations, the control of the IV characteristics is mandatory, especially for experiments with high volume of detectors. From a practical point of view, the current flow should ideally be as low as possible. In any case the leakage current will increase with radiation damage. In addition, it will also determine the voltage at which the avalanche breakdown occurs and establish the maximum operation voltage of the detector.

The non-irradiated detectors were mounted in a probe station placed at the temperature-humidity controlled clean room. They were held against a metal chuck of the probe through a vacuum suction system. The chuck was electrically isolated except for an electrical contact to the measurement system. Finely-tipped needles were used to make contact with the metal pads on the front face of the detector, consisting of the strip structure and the guard rings surrounding the device under test.

Fig. 6.2 shows the IV measurement system. A Keithley K237 voltage source is used also as current meter to measure the variation in the current through each needle with the applied voltage. An example of a I-V test on a strip detector can be seen in Fig 7.7 in the chapter 7.

In all measurements presented in this thesis the guard ring was connected unless explicitly mentioned otherwise. So, the contribution of the surface current is collected independtly to the bulk current generated within the depleted region.

Aside from these practical concerns, the IV test also gives some information about the device's internal behaviour. The shape of the IV curve indicates a dependence on the squared root of the applied voltage as seen from the equation 3.48. It denotes a leakage current dominated by the carrier generation in the depleted bulk. From the depletion voltage approximately, the curve linearizes and the value for the generation current remains constant. Then, the current is

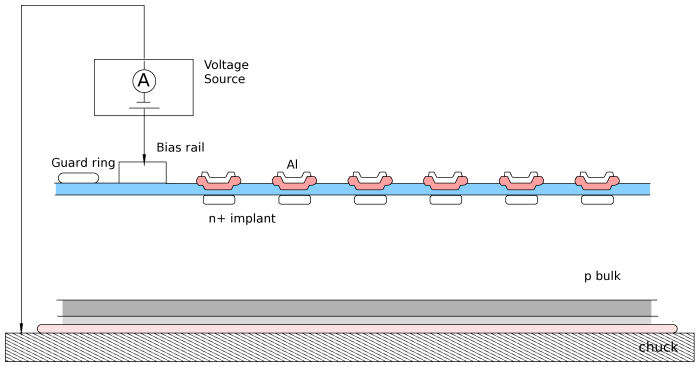

Figure 6.2: IV measurement setup.

dominated by the resistivity of the diode.

6.1.2 Capacitance-Voltage (CV) testing

The CV characteristic of a device was measured in a similar manner as the IV characteristic except for the addition of a LCR meter (Wayne Kerr 6425B). The LCR meter was connected in parallel across the device with the Keithley voltage source as shown in Fig. 6.3 to measure the sensor capacitance as a function of the supplied voltage. The probe needles simultaneously bias the device and apply a small-amplitude AC voltage to the corresponding contacts at a frequency ω. The amplitude of the resulting small-signal AC current flow can be used to calculate the capacitance between the two contacts, given that,

$$I_c = V_c/Z_c = V_c j\omega C \tag{6.1}$$

where V_c is the applied voltage and $Z_c = 1/j\omega C$ is the detector impedance seen by the AC signal.

A frequency of 10 *KHz* was used, to match RD50 recommendations [111] so the measured capacitance is almost independent on the applied voltage. The DC supply voltage was decoupled from the small-amplitude AC voltage of the LCR meter using capacitors. This extra capacitance is accounted for through a trimming calibration of the system capacitance. An example of a CV curve from a strip detector can be seen in Fig 7.7 in the chapter 7.

As the capacitance squared of a diode is proportional to the inverse of the applied bias voltage (as given in equation 3.46), the measured capacitance dependence on the voltage of a device can be used to extract the width of the space charge region. After full depletion, the capacitance of a diode is unchanged with applied bias, therefore the full depletion voltage, V_{fd}, maybe determined from the CV method. In practice, two straight lines were fitted to the *logC* versus *logV* plot, one to the linearly increasing section before full depletion and one to constant capacitance section after full depletion. The point of interception of the two lines corresponds to the point at

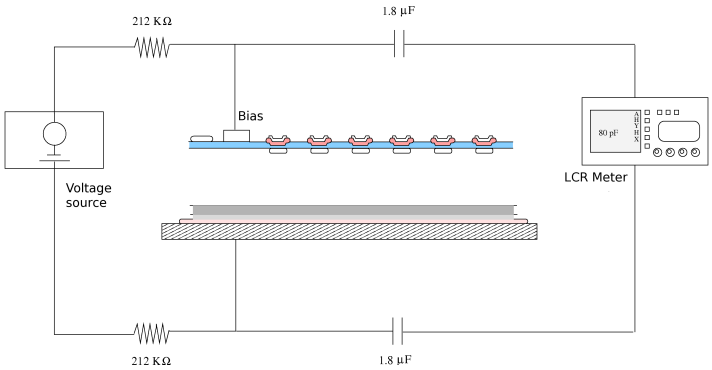

Figure 6.3: CV measurement setup.

which the device is fully depleted and therefore the value of the full depletion voltage may be obtained.

It is also used the $1/C^2$-V curve to determine the full depletion voltage that will also show the characteristic kink at V_{fd}. The systematic errors are mainly due to frequency and temperature and are estimated to be below 10%. It is important to note that the method of determining V_{fd} is not affected in any way by the segmentation of the detector.

The extracted value for V_{fd} is the minimal voltage required to obtain maximal charge collection efficiency, which is ultimately the most significant parameter for detector operation. This simple technique provides reliable results when applied to non-irradiated silicon devices.

In irradiated detectors, the obtained V_{fd} is not 100% correlated to the one obtained by the CV method in a simply way. This is due to the effect of trapping since a number of charge carriers is removed to the signal by trap defects affecting to N_{eff} and therefore to V_{fd}.

6.1.3 Interstrip resistence

The interstrip resistance is an important parameter used to study the sensor surface. One can conclude from the value of the interstrip resistance on the state of its surface, defect content in silicon, etc. Apart from this, the interstrip resistance at the ohmic side of the detector shows the quality of performance of the strip isolation structure. So that, a sufficiently high interstrip resistance can prevent signal sharing between neighbours which could lead to degradation of the position resolution.

While measuring the interstrip resistance, minimum distorsions of electrostatic fields within the interstrip volume should be provided. The pn-junction on p-type sensors extends from the frontside of the sensor, near the n^+ strips to the backside. This guarantees a stable electric field in the interstrip region even if there is no full depletion.

The used method permits to determine the interstrip resistance from strip leakage currents [112]. The essence of the method is in that while the sensor is biased by a voltage source (U_1), an additional voltage source (U_2) is applied between two adjacent strips according to Fig. 6.4. Then,

the resulting current of the U_2 is measured and plotted as a function of its voltage. A equivalent resistance is determined by the slope of the straight line corresponding to the ohmic region according to the equation 6.2.

$$R_{eq} = \left(\frac{dI_{eq}}{dU_2}\right)^{-1} \tag{6.2}$$

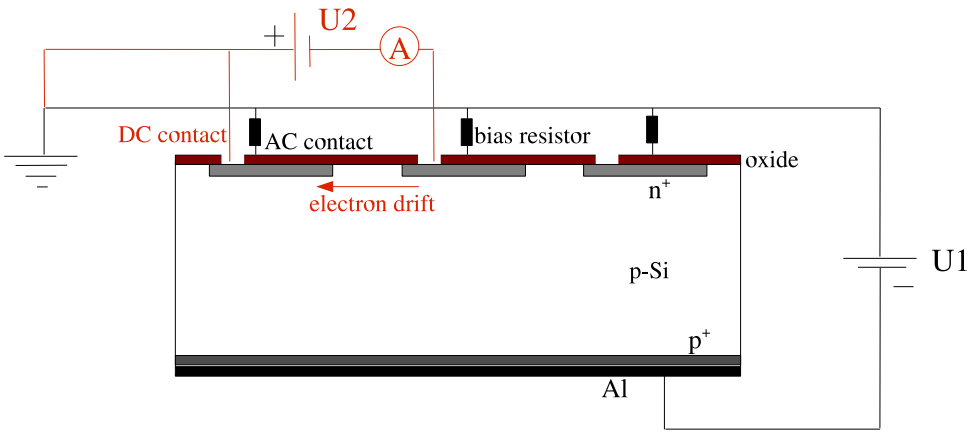

Figure 6.4: Scheme employed for the determination of the interstrip resistance.

The ohmic isolation resistance should be independent on U_1, since that it is related mainly with surface leakage current. The U_2 voltage is applied directly between the strip implants (DC contacts). Fig. 6.5 shows the view of the contacts presented at the surface of a typical microstrip silicon sensor.

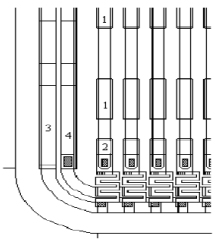

Figure 6.5: Schematic view of a corner of a microstrip detector: 1- AC strip contact, 2- DC strip contac, 3- guard ring pad, and 4- biasing pad of microstrips.

Due to the presence of the bias resistors, the R_{eq} is determined as the equivalent resistance made up by two bias resistors and one interstrip resistors switched in parallel according to equation 6.3.

$$\frac{1}{R_{eff}} = \frac{1}{R_{bias}} + \frac{1}{R_{interstrip}} \tag{6.3}$$

6.2 Charge collection test setup

A very important test of the detector performance is to evaluate its response to incident charged particles. i.e the efficiency on charge collection. By measuring the charge collection efficiency (CCE) of a detector versus the bias voltage, one can also get information about the depletion behaviour, since only the carriers generated in the depletion region will be collected.

In this section, two different charge collection test setups are described. One setup in which a β source is used as source of charged particles and a second setup that tests the detector under a laser source. Apart of this, two acquisition systems have been used throughout these studies and with the two setups mentioned before. Both will be also described in this chapter.

6.2.1 Radioactive source setup

The used source is a ^{90}Sr β source (*Activity:* $0.25\mu Ci$,10 *kBq Ref. date: 1 June 2006*). This emits electrons with a spectrum of energies up to 2.28 MeV. These electrons will pass through the silicon detector. As the energy loss of electrons of this energy is close to minimum ionising particle (*mip*), these electrons generate 80 electron-hole pairs per micron along their path. In that way, these electrons can be referred to as *mips*. The source will also emit low-energy electrons which will be stopped by the detector and generate a larger, and variable quantity of charge carriers.

In this setup (Fig. 6.6), a microstrip silicon detector is placed under the β source. In addition, a collimator is necessary between the β source and the detector under test, to give a narrower beam of electrons. The reverse bias voltage applied to the detector is supplied by an external voltage source. Under the detector, there is a scintillator ($0.5 \times 0.5\ cm^2$), connected to a photomultiplier tube as well.

When the radioactive source emits a high-energy electron, it passes through the detector, resulting in a current signal. At the same time, it is absorbed by the scintillator. The light pulse at the scintillator is detected by the photomultiplier, producing a fast electrical negative analogue pulse. These output signal pulses of the photomultipliers are amplified and discriminated, obtaining digital pulses which are used as trigger signals. The setup includes two photomultipliers. They both can be used together in the setup, taking as trigger the coincidence signal between the two photomultipliers. Nevertheless, it is recommended using an unique photomultiplier previously calibrated since that a low quantity of electrons reachs the below photomultiplier as they are absorbed by the scintillator plastic.

This provide to the system a trigger signal to measure the signal from the detector under test each time a hit occurs. This trigger signal is also used to exclude the lower-energy β because they will not reach the scintillator, as they may be stopped by the silicon sensor.

The detector signal is amplified by a charge sensitivity amplification stage with a gain factor of 1000 and connected to a *HP infinium* 1 GHz bandwidth oscilloscope.

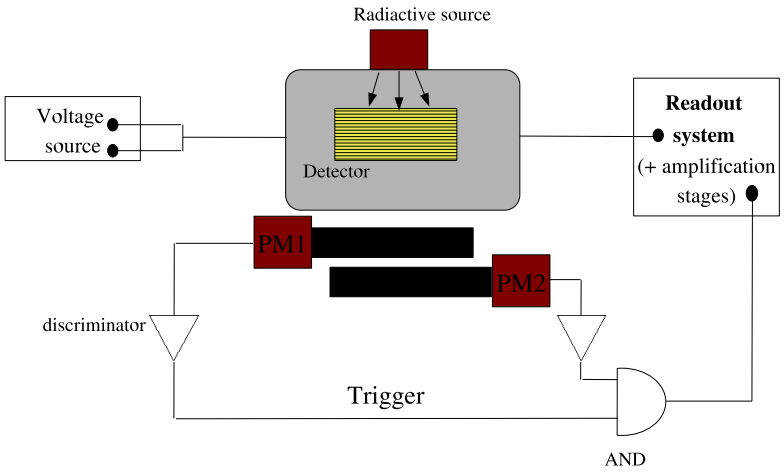

Figure 6.6: Scheme of the radioactive source setup.

Calibration

The photomultipliers were calibrated before mounting the setup in order to estimate the threshold required for an appropiate signal counting. The threshold is set to ensure that only β particles are accepted and are not masked by noise signals.

It was considered two different photomultipliers placed as in Fig. 6.6. Fig. 6.7 shows the counts per second for every photomultiplier as a function of the gain voltage. It is noted a higher signal frequency in PM1 than in PM2 due to PM1 is closer to the radiactive source, only with the silicon sensor between them. From these plots it is stablished a gain voltage of 870 mV for PM1 and 920 mV for PM2.

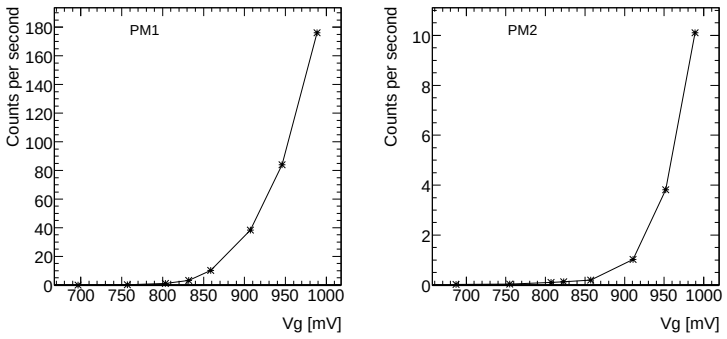

Figure 6.7: Counts per second as a function of the gain voltage applied to two different photomultipliers.

The second step is to evaluate the number of counts as function of the threshold as seen in Fig. 6.8 for every photomultiplier. Trigger signals would be lost if a too high threshold is considered. In the other case, a too low threshold introduces noise counts that would be taken as trigger. An acceptable threshold of 40 mV is considered for both photomultipliers to ensure that the PM signal is due to the passage of a high-energy β particle.

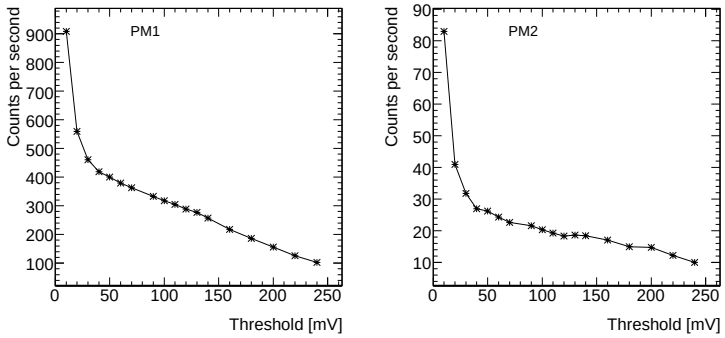

Figure 6.8: Counts per second as a function of the threshold for two different photomultipliers. It is noted that only around ~ 10 % of electrons reachs the PM2.

6.2.2 Laser setup

A laser setup was used for the charge collection measurements in order to get more intensive signals from the detector. Figure 6.9 shows the diagram of the setup.

The laser beam is a beam of photons instead of charged particles. The penetration and interaction mechanisms of photons of laser light differ in several aspects from ionising particles. Since the laser beam energy (1.17 eV) is lower than the energy required for the generation of an electron-hole pair in Silicon (3.6 eV), the ionization is generated by exciting the electrons of the bands ($E_{laser} > E_{GAP} = 1.1\ eV$ in Silicon).

A laser light is generated by exciting a laser source with an external squared pulsed signal of 2 V and 1 MHz rate which comes from a pulse generator *Agilent 81130A*.

The laser light has a wavelength of 1060 nm that corresponds to near infrared. This light penetrates deeply into silicon and the charge generation geometry is therefore more similar to what a *mip* generates. With a laser wavelength less than 800 nm (typically 682 nm), charge generation is produced at an average depth of $\sim 4\ \mu m$ in Silicon. It allows to study surface charge collection if the detector does not have metal coating in its back side. The light is lead through an optical fibre with a focusing lens to the sensor which is situated on a positioning system in three dimensions with micrometer precision. This alternative offers a good spatial resolution with a laser beam well focused. Placing the laser in a position of maximum signal on the detector and moving it perpendicular to the strips in small steps of a few microns, you can get the variation of the signal and do an estimation of the spot size of the laser. The minimal spot size achieved was of $\sim 8\ \mu m$ of radius (see Fig. 6.10).

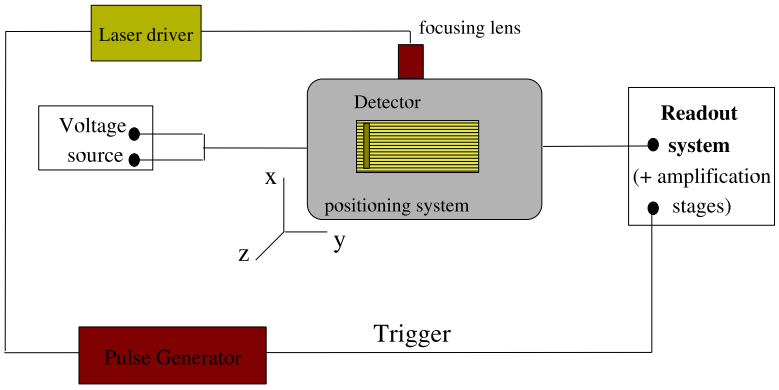

Figure 6.9: Scheme of the laser setup.

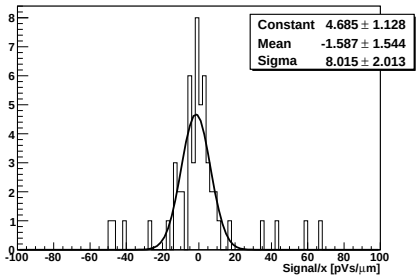

Figure 6.10: laser spot calculated for the setup, $\sigma = 8 \pm 2\mu m$.

The pulse generator also triggers the signal acquisition. The reverse bias voltage applied to the detector is supplied by an external voltage source, as in the case of the β source setup. The output signal of the detector is connected to a charge sensitivity amplifier with a gain factor of 100 and the output (trigger and detector signals) is connected to a *HP Infinium* oscilloscope.

6.3 Single channel acquisition system

The output (trigger and detector signals) is sent to a 1 GHz bandwidth *HP Infinium* oscilloscope, which serves as data acquisition system. This kind of system is called *Single Channel* since it just allows to read one channel of the detector (usually the sum of various channels is acquired). For this system, all the strips of a microstrip silicon detectors are read out together as seen in Fig. 6.11.

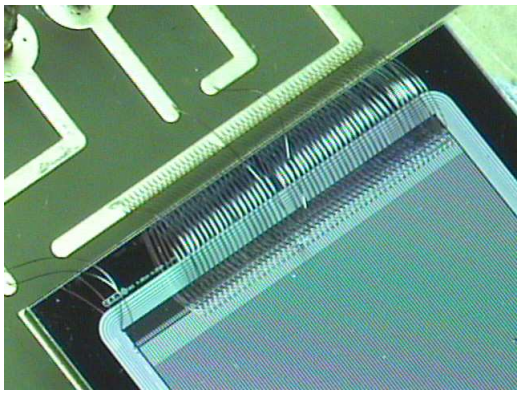

Figure 6.11: View of the strips of a 1 cm^2 p-type sensor connected shorted together to a pad in the detector board of the *Single Channel Acquisition System*.

In order to filter the noise, the sensor signal is averaged over a sufficient large number of triggers. The output signals are monitored at the oscilloscope and stored in output text files for an *offline* analysis. The analysis extracted the pulse shape: signal amplitude, rise time as well as the sensor leakage current. Then, the charge can be computed as the time integral of the average signal amplitude of the signal. In this system, the sensor probe box (where the sensor is mounted) is equipped with a PT100 probe for temperature monitoring.

As example, Fig. 6.12 shows the oscilloscope screen representing an averaged laser signal (in green) read out from a non-irradiated sensor biased at 70 V ($V_{fd} \sim 30$ V). The yellow line corresponds to the laser pulse used as trigger. The pulse signal is acquired in units of $V \cdot s$.

The acquisition of the detector signal through this system is not the most adequate due to different reasons. As explained before, the readout of the sensor signals is for all the strips at the same time. One can not know what channels have been hit, which is the final use of a silicon tracker detector. It is interesting to characterize the sensors with a system as similar as possible to those used at real experiments. Nevertheless it is useful for a general characterization of the sensor properties and behaviour with an appropiate speed of the readout electronics.

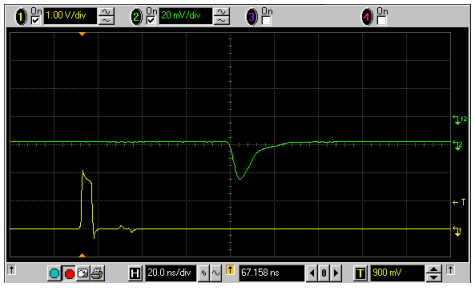

Figure 6.12: Oscilloscope screen showing a laser signal (in green) of a non-irradiated microstrip silicon detector biased at 70 V ($V_{fd} \sim 30\ V$) and the laser pulse used as a trigger (in yellow). Acquired with the *Single Channel Acquisition System*.

Taking into account these considerations, a more sophisticated acquisition system was made necessary. A new acquisition system was developed in order to research the performance of high irradiated microstrip silicon sensors as similar as possible to real experiments. This system will be explained in the next section.

6.4 ALIBAVA system

An analogue signal readout system for microstrip silicon sensors was developed as a result of a collaboration among the University of Liverpool, the CNM (Centro Nacional de Microelectrónica) of Barcelona and the IFIC (Instituto de Física Corpuscular) of Valencia. This system is able to measure the collected charge in microstrip silicon sensors by reading out all the channels of the detector at the same time (2×128).

There is a need of studying the main properties of highly irradiated microstrip silicon sensors since this type of detectors are used at the LHC experiments. Also as a higher luminosity is intended to be achieved at HL-LHC experiments, it would be an advantage to be able to predict the behaviour of this kind of sensors under HL-LHC operating conditions.

This sytem can measure the collected charge per channel in two microstrip silicon sensors by using two front-end readout chips. The system can operate either with non-irradiated and irradiated sensors as well as with n-type and p-type microstrip silicon sensors. In this thesis, this system has been used to research the performance of microstrip silicon sensors irradiated at the expected doses under HL-LHC conditions.

The *ALIBAVA* system is a compact and portable acquisition system. It has been divided into two main parts, a hardware part and a software part (see Fig. 6.13). The hardware part acquires the microstrip silicon sensor signals either from an external trigger input, in case of radiactive source setup is used, or from a synchronised trigger output generated by the system, if a laser setup is used. This acquired data will be roughly processed and sent by the hardware in order to be stored in a PC or laptop for a more detailed processing.

This hardware part is a dual board based system composed by a mother board and a daugther

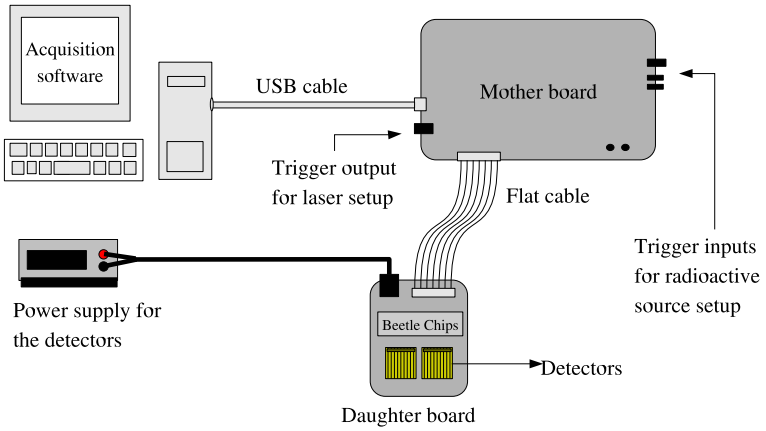

Figure 6.13: Diagram of the ALIBAVA system with its different components.

board. The mother board is intended to process the analogue data that comes from the readout chips, to process the trigger input signal in case of radiactive source setup or to generate a trigger signal if a laser setup is used, to control the whole system and to communicate with a PC via USB port. The daugther board is a small board intended for containing two Beetle readout chips [113], fan-ins and detector support to interface the sensors.

Hence, the most of the hardware required is implemented in the mother board. Particularly, the following hardware blocks are implemented in the mother board: the trigger output generation stage for the laser setup, the trigger input processing stage for the radiactive source setup, the signal conditioning and digitalization of the analogue data coming from the Beetle chips, the control and configuration generation block for the Beetle chips, the USB communication controller, and external memory for temporary storing the acquired data. Also, the FPGA and associated circuits and the power supply generation block for the required voltage levels (analogue and digital supply levels) are integrated in the mother board.

The daugther board contains the hardware required for accommodating the two Beetle readout chips, for buffering the analogue data that is sent to the mother board, for receiving the control and configuration signals for the Beetle chips, for sending to the mother board a temperature signal, for connecting the microstrip silicon sensor(s) to the Beetle chips and for biasing the detector(s) from an external voltage source.

The main reason for dividing the hardware into two boards is to prevent the rest of the hardware from the aggressive environment (radiation or very low temperatures) that will suffer the detectors. Both boards are communicated by flat ribbon cable for the analogue data signals coming form the Beetle chips, slow and fast control digital signals to the Beetle chips and temperature signals as well as the supply level for the Beetle chips and buffers. The high voltage detector power supply will be provided directly to the daugther board. Therefore, the daugther board can be placed close to the radiation source whereas the mother board can be near the controller. The length of the flat cable can be about various metres without any need of signal equalization.

Regarding the software part of the system, its function is to control the hardware part of system and to process the data acquired (temperature data, TDC data and digitalized Beetle chips data output), which is sent in a raw format from the motherboard, in order to obtain data with physical meaning. Also, data introduced by the user is processed by the software to be sent to the FPGA in the correct format and the software also monitors the state of the system and the data acquired for user information. The software is the interface between the system and the user by means of a Graphical User Interface (GUI). This way, the software controls the whole system for configuration, calibration and acquisition.

The acquisition data is stored in adequate output file format. This format file will be compatible with software used for further data analysis.

6.5 Data analysis with ALIBAVA

When a high-energy particle passes through a detector, it deposits energy through a series of collisions with electrons in the material. This is a statistical process, which means that the amount of energy deposited in the detector, and hence the signal generated, will vary from particle to particle. The total number of electron-hole pairs generated is proportional to the deposited energy. Over a large number of hits, the quantity of energy deposited will follow a predictable distribution. In a thick detector, the number of collisions will be large, and so this distribution will be a Gaussian about the mean value. For a typical silicon detector, which is relatively thin, the number of collisions will be smaller. The energy loss will follow a Landau distribution convoluted with a Gaussian distribution to compensate for any broadening of the espectrum due to noise, and non uniformity of the incident particle momentum.

By integrating the signal current induced by the charge motion, the signal charge is obtained. The signal charge is very low (typically to the order of 3.6 fC [63]), and must be amplified. Electrical noise and inherent statistical fluctuations can distort the signal, which leads to an important design requirement. The signal from the preamplifier passes to a shaping amplifier to fit the frequency of the signal, as the signal and noise frequencies vary from each other. By doing this, the signal-to-noise ratio is improved significantly. Then, the pulse returns to a baseline voltage before the next pulse begins. Then, it is obtained a pulse with a specific height which can be measured through analog-to-digital converter (or ADCs), which are proportional to the original charge induced on the strip. Fig. 6.14 shows the reconstruction of the Beetle analogue front-end pulse shape using an electron as incident particle. The averaged collected charge in electrons versus the TDC measurement is plotted. The pulse is negative since electrons are collected with a p-type detector.

The system was calibrated by using a precision pulse generator to inject known charge pulses into the preamplifier, and measuring the signal arriving at the ADC. Due to noise, the recorded ADC values followed a Gaussian distribution, so the peak of the distribution was taken. After repeating this using charge pulses with different magnitudes, a linear fit was made to this data to find the conversion factor from ADC values to charge in electrons. The results are shown in Fig. 6.15. In the upper plot of the Fig. 6.15, the ADC counts/electrons rate as a function of the channel is shown for a non-irradiated p-type detector. This rate is used to calculate the equivalent signal amplitude in electrons from the signal amplitude in ADC counts read out from every channel of the detector. It can be seen that there is a difference between the values of

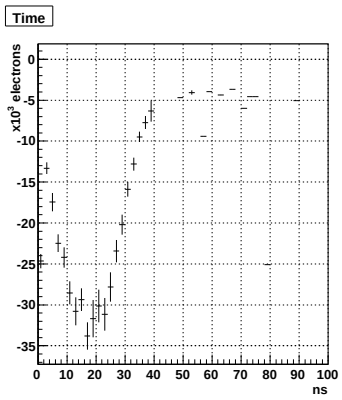

Figure 6.14: A sample signal shape of an electron in a p-type detectors as obtained out of the ALIBAVA system. It is represented the averaged collected charge (in electrons) as a function of the TDC measurement (in *ns*). It is noted a charge peak around 33000 electrons instead the expected 24000 electrons for a 300 μm thick silicon sensor. It is due to gain effects that are explained in chapter 7.

the first 128 channels (which correspond to the Beetle chip not connected) and the second 128 channels (which corresponds to the Beetle chip connected) due to the equivalent capacitance of the detector. The plot shows that the ADC counts/electrons rate does not change in a significant way, which was the expected behaviour. In the lower plot of the Fig. 6.15, the signal in ADC counts is represented as a function of the corresponding injected charge and the channel number.

The standard approach when measuring CCE is to plot the distribution of the remaining charge in electrons (after calibration and pedestal and common mode corrections have been made) of the measured events versus the frequency of them, and then to fit the distribution to find the peak value as seen in Fig. 6.16. It can be seen that the spectrum fits a distribution similar to the *Landau* distribution with a long tail for greater collected charges and convoluted with a gaussian due to noise. This was the expected result for this type of measurement since it would be directly related to the energy loss in the silicon detector with a thickness of 300 μm. The peak of the distribution corresponds to the charge generated for a *mip* in a such silicon detector. In the espectrum shown in Fig. 6.16 the peak value (27.16 ± 0.13 ke^-) does not correspond to the expected maximum collected charge (24 ke^-) due to gain effects that are explained in the chapter 7. In the work presented at this thesis, the measurements carried out with the ALIBAVA system were an early testing of the system and some issues came to the surface (gain effects, temperature dependence...) that were taking into account in the measurements analysis.

In Fig. 6.17, the signal spectrum for the Beetle chip not connected to the detector (upper plot) and the signal spectrum of the Beetle chip connected to the detector (lower plot) are shown. They represent the number of events for every charge collection in electrons. The sigma of the curve fitted in each plot represents the noise in electrons corresponding to each Beetle chip (i.e. detector noise, Beetle chip noise and electronic noise). Therefore, the noise of the detector and the corresponding Beetle chip (lower plot) is 1247 electrons. It shows that a negative spectrum

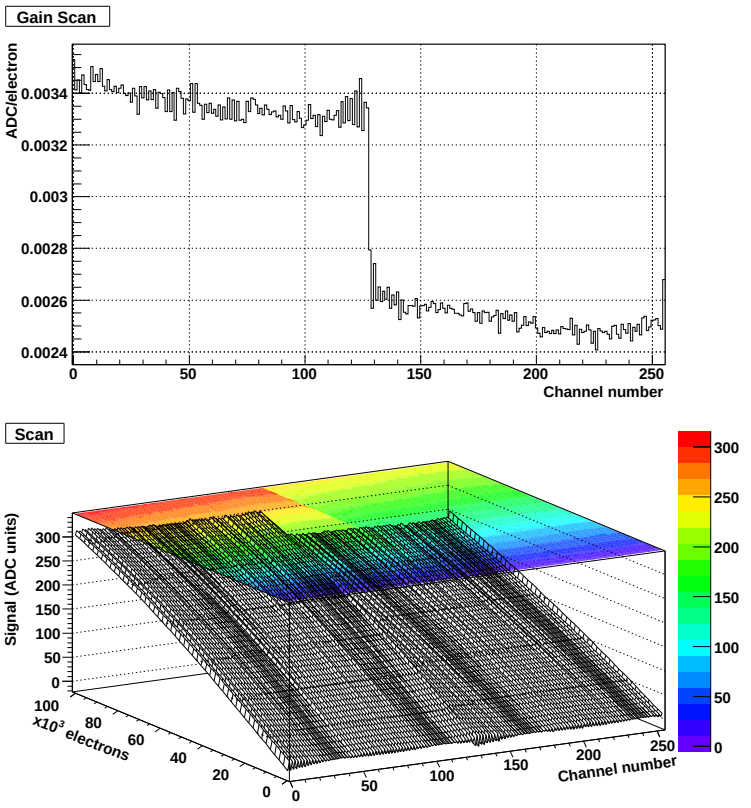

Figure 6.15: System with a non-irradiated p-type detector connected to one Beetle chip (channels 129-256). Upper plot: ADC counts/electrons rate for every channel number. Lower plot: signal in ADC counts versus injected charge in electrons and channel number.

corresponding to the charge collected by a p-type detector are electrons. In addition, it shows also positive spectrum due to noise in posible channels which were not operative because of shorts in the bonding process. The upper plot only has the chip noise spectrum since there is no detector connected to that Beetle chip.

In Fig. 6.18 the spectrum signal is shown for a non-irradiated p-type detector biased at 200 V measured by means of the laser setup. In this case, laser light provides a fairly uniform beam of photons throught the detector volume. Every photon produces a large number electron-hole pairs in a small region where the photon is absorbed primarily by means of photoelectric effect [48]. The absorption of these photons is probabilistic. Due to the large number of collisions, the distribution will be a gaussian about the mean value which is taken as the collected charge. This resulting charge collection is then scaled to find the corresponding signal that would be produced by a minimum ionizing particle.

After the acquisition of the peak value of the collected charge at every bias voltage, it can be

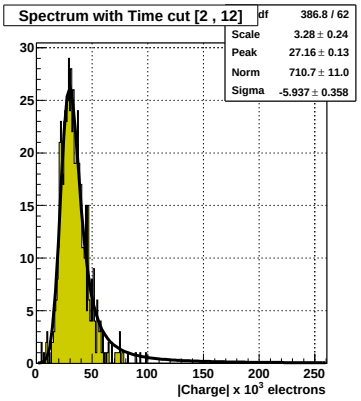

Figure 6.16: System with a non-irradiated p-type detector connected to one Beetle chip (channels 129-256) at a bias voltage of 200 V. Spectrum of the signal acquired with a time cut between 12 *ns* and 22 *ns* with the radioactive source setup. The number of events as a function of the absolute value of the collected charge (electrons) is represented. It is noted that the peak value around 27 ke^- is higher than the expected maximum collected charge (24 ke^-). It is due to gain effects that will be explained in the chapter 7.

represented the collected charge versus the bias voltage for every silicon detector.

6.6 Irradiation facilities

6.6.1 Neutron irradiation facility

The reactor research centre of the Jozef Stefan Institute is the site of a nuclear reactor of type TRIGA [114], constructed to provide neutrons for experimental purposes. The main part of the reactor is its core, consisting of fuel and control rods. It is surrounded by a graphite reflector and placed into a reactor vessel filled with water, all within a thick concrete shield.

Irradiation of a sample is done by placing it into the core through an irradiation tube which occupies a fuel rod position. ATLAS group uses two such irradiation tubes which are located at the edge of the core. The tubes have two different dimensions:

- The small tube has a circular cross section with 2.2 *cm* diameter.
- The large tube has an elliptic cross section with axis lengths 7 and 5 cm.

The irradiation tubes enter the core from above and are about 5 *m* long because the core is covered with 5 *m* of water. The tubes are curved in a chicane just above the core to prevent radiation from the core escaping through the tube. The chicane limits the length of the sample to be irradiated to about 15 *cm*. A closed liquid cooling circuit was designed to ensure their stable temperature during and after the irradiation. The proximity of the core provides high neutron

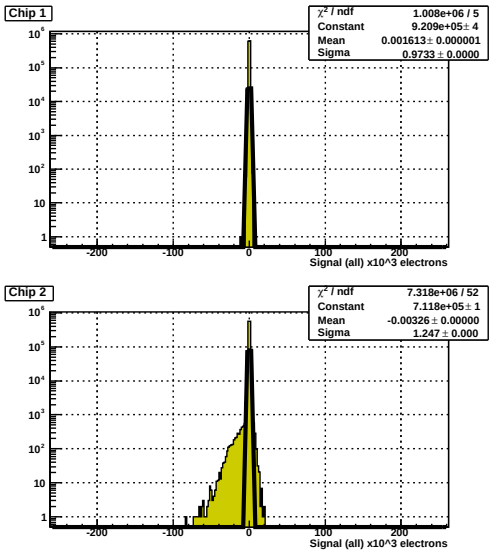

Figure 6.17: System with a non-irradiated p-type detector connected to one Beetle chip (channels 129-256) at a bias voltage of 200 V. Upper plot: number of events for every acquired charge collection (in electrons) for the channels corresponding to the Beetle chip not connected. Lower plot: number of events for every acquired charge collection (in electrons) for the channels corresponding to the Beetle chip connectrd to the detector.

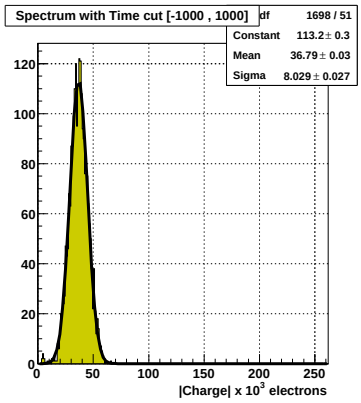

Figure 6.18: Spectrum of the signal acquired with the laser setup. The number of events as a function of the absolute value of the collected charge (electrons) is represented. The peak value corresponds to the charge collection by a photon beam and it has to be scaled to the equivalent signal produced my a minimum ionizing particle. It corresponds to a non-irradiated p-type detector connected to one Beetle chip (channels 129-256) at a bias voltage of 200 V.

fluxes with a relatively high portion of fast neutrons. The neutron energy spectrum in the tube was determined by measuring the activation of foils of different materials. Using the measured energy spectrum and damage functions one can determine the flux of 1 *MeV* NIEL equivalent neutrons [115]. NIEL equivalent flux was also measured using the leakage current method [83]. Since the flux is linearly proportional to the reactor operating power, the flux of 1 *MeV* NIEL equivalent neutrons in the reactor is:

- 8.8×10^9 $n/kW \cdot cm^2 s$ in the small tube
- 18×10^9 $n/kW \cdot cm^2 s$ in the large tube

The reactor can be run with large span of operating powers (few W to 250 kW), enabling irradiations with various neutron fluxes. A reactor power of 25 *kW* means a fluence of 1×10^{13} n/cm^2 reached in 22 seconds.

The hardness factor was calculated to be 0.90 ± 0.05 (0.05 is the statistical error only, describe the reproducibility under the same experimental conditions) [116]. The neutron flux is expected to vary linearly with reactor power. The irradiations were performed at different reactor power, thus varying the neutron flux.

6.6.2 Proton irradiation facility

The proton irradiation was made by a Cyclotron AVF930 at CYRIC [77] in Japan. The protons are accelerated to a kinetic energy of 70 *MeV* with the azimuthally varying field (AVF) cyclotron of a magnet radius of 930 *mm* with the accelerating radio frequency of 11-22 *MHz* and extracted to a beamline. The beamline flange is just an exit made through a shield wall.

The beam profile is measured by using finger aluminum bars (5 $mm \times 40$ $mm \times 20$ *mm* thick). These are scanned and reading the current induced by protons (70 *MeV* protons should stop in 20 *mm* of Aluminum). The maximum beam current of the beamline is 500 *nA* and the maximum FWHM of the beam spot is about 5 *mm*. It is determined the beam current and irradiation time so that the sum fluence should reach the target.

Sample PCBs (Fig 6.19) are stacked and Al foils are attached to allow final proton beam intensity measurements by $Al \rightarrow {}^{24}Na$ spallation process. They are also cooled at - 10° C and biased at 100 *V* during irradiation. The uncertainty of the fluence comes from the cross section uncertainty for this process (10%). Then, it is calculated the scan area about the samples PCBs. Samples are wire bonded to allow for electrical characterization before and after irradiation. The 70 *MeV* proton to 1 *MeV* n_{eq} conversion is assumed to be 1.4.

6.6.3 Other irradiation facilities

The detectors used in this thesis were irradiated in the above described irradiation facilities. Nevertheless, several irradiation facilities are available to irradiation process for research.

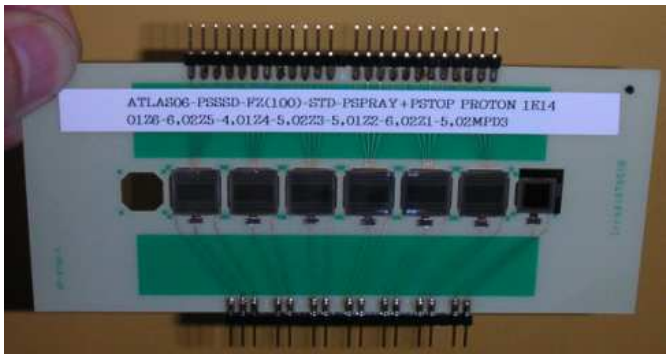

Figure 6.19: Sample PCB. Bias lines and sampled electrodes are wire bonded to allow electrical characterization before and after irradiation.

CERN PS

It is a Proton Synchroton accelerator[1] located at CERN. Two types of irradiations can be performed:

- Protons of 24 GeV/c with fluxes of 1-3$\times 10^{13} p\ h^{-1}\ cm^{-2}$. The dimensions allowed for the samples to irradiate are $2\times 2\ cm^2$.
- Neutrons of 1 MeV with fluxes between 3-10$\times 10^{12} n\ h^{-1}\ cm^{-2}$ and with a maximum sample size of $300\times 300\times 300\ mm^3$.

Proton Irradiation Facility, PIF

It is located at the Paul Scherrer Institut (PSI)[2] at Switzerland. As a prime use, the PIF is available for irradiation experiments connected with the European Spacial Agency (ESA) space program. The facility is also available for other applied research conducted by external laboratories as CERN, universities and industry. It uses protons within an energy range of 6-63 MeV with fluxes of $< 5\times 10^8\ p\ s^{-1}\ cm^{-2}$. The beam spot is a circle of up to 9 cm diameter with an uniformity > 90% over a 5 cm diameter.

Cyclotron Research Centre (CRC) at Louvain-la-Neuve

It is an Isochronous Cyclotron[3] located at the Institut de Physique Nucléaire (UCL-FYNU) in Belgium. It provides:

- Fast neutron beams with energy ranging from 1 MeV to 45 MeV with a maximum neutron flux of $7.3\times 10^{10}\ n\ s^{-1}\ cm^{-2}$, using Deuteron on a Be target.

[1] https://irradiation.web.cern.ch/irradiation
[2] http://pif.web.psi.ch
[3] http://www.cyc.ucl.ac.be

- Monoenergetic neutron beams, using protons on a Li target giving a more energy-peaked beam (25-70 *MeV*), but with lower fluxes of the order of $10^6\ n\ s^{-1}\ cm^{-2}$.
- Light ion beams, protons with energy from 10 to 75 *MeV* and fluxes up to $10^9\ p\ s^{-1}\ cm^{-2}$.
- Heavy ion beams as for example of α particles. Developed in collaboration with ESA to tests electronics components with high linear energy transfer (LET) particles.
- Cobalt irradiator for gamma irradiations, most used for nuclear chemistry purposes.

Chapter 7

Radiation silicon detector characterization

In this chapter, it is presented the characterization of the new technology for radiation detectors that is the n^+p detectors. As explained in chapter 4, n^+ strip readout on a p-type silicon bulk sensors present better performance in terms of radiation hardness than the p^+ strip readout on a n-type silicon bulk sensors. So, n^+p detectors have been proposed, within the RD50 collaboration, as candidates to survive the extreme radiation conditions of the both HL-LHC and sLHC environment.

7.1 CNM microstrip silicon sensors

7.1.1 Prototypes of CNM microtrip silicon sensors

n^+p sensors have been prototyped by the CNM-IMB for these studies. Microstrip sensors have been manufactured on a 10 cm silicon wafer containing 26 microstrip detectors, 20 pad detectors, 12 pixel detectors and 8 different test structures to measure fabrication process parameters as the interstrip resistence and the oxide charge. A view of the wafer is shown in Fig. 7.1. The used mask set was designed by the CERN RD50 Collaboration[1]. Sensors were manufactured with $\langle 100 \rangle$ silicon wafers from Siltronix[2].

The main parameters of the microstrip detectors used for these studies are summarized in table 7.1. They have a structure of multiple guard rings (8) surrounding the 130 strips (solely the central 128 strips are connected to avoid a different underlying electric field for the edge strips). The strips are biased via polysilicon resistors connected to a bias ring. The strips also have an integrated metal capacitor for the capacitive coupling of the signal connected to the electronics by wire bonding.

[1] http://cern.ch/rd50
[2] http://www.siltronix.com

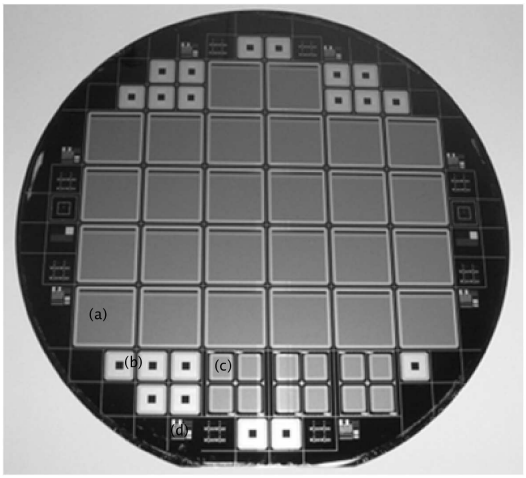

Figure 7.1: Wafer processed at CNM-IMB clean room facilities. The wafer contains (a) strip detectors, (b) pad detectors, (c) ATLAS pixel detectors, and (d) different test structures.

sensor parameter	value
area	$1.06 \times 1.06\ cm^2$
thickness	$285 \pm 15\ \mu m$
# strip channels	128
length	$10472\ \mu m$
strip width	$32\ \mu m$
pitch	$80\ \mu m$
nominal resistivity	$30\ k\Omega \cdot cm$

Table 7.1: Main parameters of CNM microstrip silicon sensors.

Concerning the interstrip isolation, the p-spray isolation is used (see section 3.3.3). The implant conditions for the p-spray are [117] (except for the *early set*):

- Energy, $E = 100\ keV$
- Dose, $dose = 3 \times 10^{12}\ cm^{-2}$

In addition, these studies are for different sort of silicon substrates in order to compare them under irradiation. So, the considered silicon substrates for the CNM sensors are Float Zone (FZ), Diffusion Oxygenated Float Zone (DOFZ) and Magnetic Czochralski (MCz).

The table 7.2 summarizes all tested CNM sensors considered in this studies: the number of the sensors from a numbered wafer, their detector technology, silicon growing method, and the acquisition system used to carry out the measurements. There are three series of CNM sensors that are called *early detector set*, *CNM07*, and *CNM09*. Every serie draws together sensors

measured at a particular period of time under different conditions as for example the signal acquisition system used.

# Wafer	# sensors	Technology	Growing Method	Acquisition System
Early detector set				
1(∗)	5	$n-on-p$	FZ	Single Channel System
CNM07				
5	6(-1)	$n-on-p$	DOFZ	Single Channel System
10	6(-2)	$n-on-p$	MCz	Single Channel System
CNM09				
4	4	$n-on-p$	FZ	ALIBAVA System
17(∗∗)	4	$n-on-n$	FZ	ALIBAVA System

Table 7.2: Summary of the used devices. (∗) Early p-type sensors was used to calibrate the system and other relevant tests. (∗∗) A batch of n^+n sensors was considered to compare with n^+p sensors.

7.1.2 Neutron irradiation

It is important to test prototype silicon detectors after neutron irradiation in order to stablish their radiation hardness properties to survive the expected HL-LHC radiation fluences. The most significant contribution to the radiation damage of the microstrip sensors in the tracker volume is due to backscattered neutrons. Simulations show that the neutron fluence equals the charged particle fluence emerging from the interactions at a radial distance of about 25 cm from the beam axis and is maintained at the same level up to a radial distance of about 100 cm [118].

In order to evaluate the neutron radiation tolerance in terms of charge collection for different silicon bulk materials, detectors have been irradiated with neutrons at TRIGA Mark II Nuclear Reactor (see section 6.6.1) at Jozef Stefan Institute in Ljubljana at several fluences from $10^{14}\ cm^{-2}$ up to about $10^{16}\ cm^{-2}$. These fluences corresponds to the expected doses which the sensors will have to cope with under the conditions of high luminosity.

After irradiation, the sensors were shipped in a cold package and stored at -30° to prevent annealing processes except a period of two hours during the wire bonding.

In table 7.3 it is showed the neutron fluences at which the sensors are irradiated.

7.2 Single channel acquisition system characterization

7.2.1 Weighting potential: Simulation studies

Early measurements were carried out in a Single Channel Acquisition (SCA) system (see section 6.3). The signal data is read out from an oscilloscope and analysed offline. The main singularity of this acquisition system is that all the strips are connected to the same pad. In this way, all the strips are read out together as they are shorted.

CNM Sensor Label	Neutron fluences [n_{eq}/cm^2]
Early detector set	
p-FZ-1	0, 10^{14}, 10^{15}, 2×10^{15}, 10^{16}
CNM07	
p-DOFZ-5	0, ~~10^{14}~~, 3×10^{14}, 10^{15}, 3×10^{15}, 8×10^{15}
p-MCz-10	0, 10^{14}, 3×10^{14}, 10^{15}, ~~3×10^{15}~~, ~~8×10^{15}~~
CNM09	
p-FZ-4	0, 10^{14}, 3×10^{14}, 10^{15}
n-n-FZ-17	0, 10^{14}, 3×10^{14}, 10^{15}

Table 7.3: Neutron Irradiation on CNM sensors. The radiations marked with ~~X~~ corresponds to irradiated sensors which could not be measured because of different reasons as very high level of noise, and thermal runaway.

It was thought if this configuration could affect to the characterization measurements respect to the usual configuration where the signal is read out independently. Firstly, it was considered the simulation of a detector under the two posible configurations. The usual configuration for the experiments will be called *strip configuration* in the following and the single channel configuration used at the testing laboratory will be called *diode configuration* as all the strips were read out as if they were just one strip.

The simulated structure is a 288 μm wide and 300μm thick sensor. It consists in a p-type substrate with a doping concentration of 10^{12} cm^{-3}. It has three 32 μm wide n^+ strips with a pitch of 80 μm and a doping concentration of 10^{19} cm^{-3} each. The p^+ backplane concentration is 10^{20} cm^{-3}. A p-spray isolation layer was added with a peak concentration of 10^{17} cm^{-3} and a SiO_2 layer on the sensor surface with a typical concentration for a non irradiated sensor of 4×10^{11} cm^{-2}. All these parameter values are standard and within the limits for the typical values for silicon detectors [52].

A first simulation consisted of the calculation of the weighting potential [66] for a single strip (*strip configuration*) and for 3 strips together (*diode configuration*). It is known that the contribution of the charge carrier to the induced signal depends on the variation of the weighting potential (ϕ_w) as shown in equation 3.54 [65]. The variation shape in ϕ_w varies for different sensing electrode geometry. The weighting potential for a single strip in the *strip configuration* is shown in red in Fig. 7.2 across the detector depth and it agrees with results reported in [119]. Fig. 7.2 also shows the weighting potential for the shorted strips in black in the *diode configuration*. The computed weighting potential agrees with the weighting potential for a pad sensor found in the literature [119]. Fig. 7.3 represents the weighting potential profiles for both configurations on the sensor area. A strong field in the region close to the considered strip can be observed.

An effect of the difference between the two configurations is on the collection time for the signal. From collected charge simulations it is observed that one needs more integration time to collect all the charge in the *diode configuration* than in the *strip configuration* as shown in Fig. 7.4. It is observed that it is needed approximately 5 ns to collect all the charge for the *strip configuration* whereas about 15 ns are needed to collect all the charge for the *strip configura-*

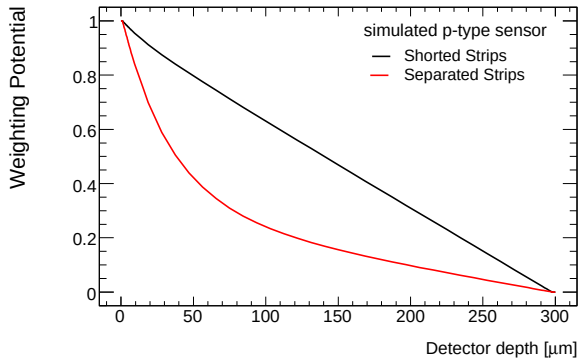

Figure 7.2: Simulated weighting potential variation with detector depth for a single strip (*strip configuration*) represented by a red line and for shorted strips (*diode configuration*) represented by a black line. Both profiles have been taken at a x coordinate of 150 μm on the sensor.

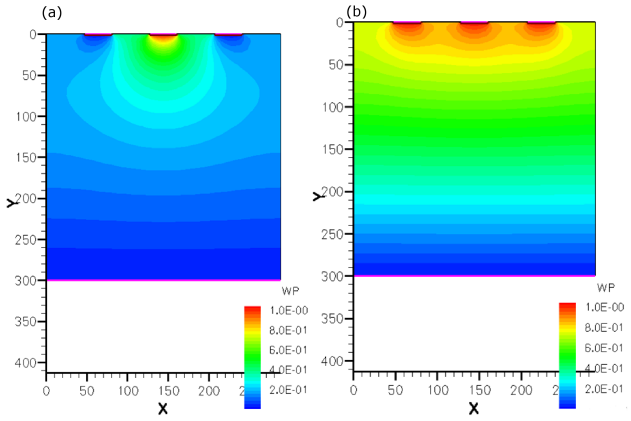

Figure 7.3: Simulated weighting potential distribution in the sensor area for both configurations. (a) *strip configuration*, and (b) *diode configuration*.

tion. In principle, if the signal integration time is larger than the collection time of all charge carriers, the measured charge will be the full charge with no dependence on the configuration. A shorter integration time yields to a fractional charge or ballistic deficit. Finally, representing the simulated collected charge as a function of the bias voltage for both configurations during an enough integration time of 25 ns, the results are identical for both configurations as shown in Fig. 7.5. So that, with a sufficient collection time, this acquisition system can be used.

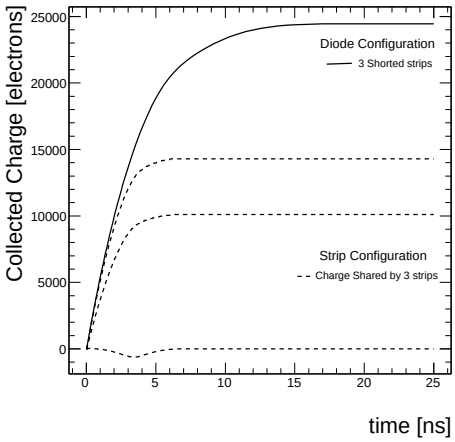

Figure 7.4: Simulated collected charge as function of integration time for a p-type sensor for both configurations. The sensor is reverse biased at 500 V. It is shown the collected charge for the three individual strips (*strip configuration*) with dash lines and for the three strips shorted (*diode configuration*) with a solid line. It is noted that approximately 5 ns is enough to collect all the charge for the *strip configuration* whereas about 15 ns are needed to collect all the charge for the *strip configuration*.

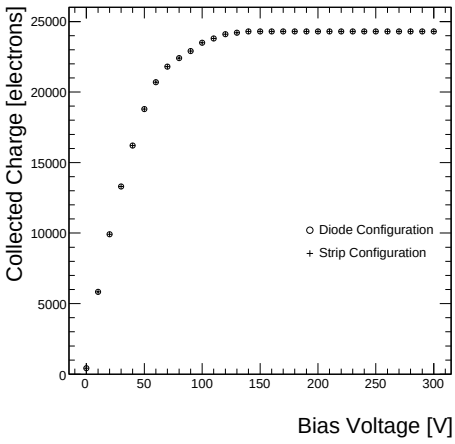

Figure 7.5: Simulated collected charge as a function of the bias voltage for a p-type sensor for both configurations after 25 ns of integration time.

7.3 Characterization of CNM sensors - I

In this section, microstrip p-type silicon sensors produced at CNM are characterized in terms of charge collection performance. Their electrical properties as leakage current and capacitance are also measured for non-irradiated sensors of every set of detectors to stablish their initial parameters. In addition, all the sensors were characterized before irradiation in the *Silicon* laboratory at the PH Department Silicon Facility [3] (DSF) at CERN. The DSF provides services and support to any CERN related experiment or project which use silicon detectors with emphasis on the four LHC experiments. This initial characterization was made in order to check the after-manufacture state previous to the detector delivery to the irradiation facilities and their posterior distribution to the different research centres. All the tested CNM sensors were considered suitable to be used as radiation damage testing sensors.

In the following it must be considered that, for all detectors, the closest guard ring to the sensor active area was grounded as shown in the picture 7.6 unless explicitly mentioned otherwise. This is in order not to include the contribution of the current from the surface. During the tests, the detectors were kept at -30°.

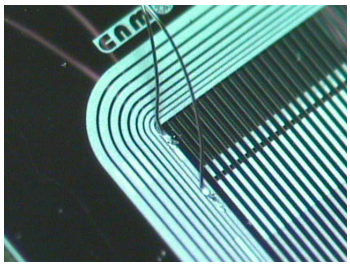

Figure 7.6: Front view of a p-type sensor corner showing the wire bonding to the bias ring (the closest ring to the strip area) and the first closest guard ring.

7.3.1 Early detector set of CNM microstrip silicon sensors

A first set of irradiated microstrip n^{+}p silicon sensors were characterized using the SCA system in order to calibrate the acquisition system. The silicon wafer is FZ. These sensors correspond to the wafer numbered as 1 in table 7.2. They were manufactured at CNM in order to optimize the p-spray implant parameters in p-type microstrip detectors before processing the RD50 wafers [62, 117] that do not constitute part of this work. The sensors, labelled as *p-FZ-1*, were irradiated at the fluences indicated in table 7.3. A non-irradiated sensor was also measured for reference.

As explained in chapter 6, the charge generated across the sensor is due to a laser beam on the sensor. The use of a laser beam provides more intensive signals than with a radiactive source specially with irradiated sensors where the produced signals may be very masked by noise and low due to trapping. However, with a laser beam, there is an uncertainty in the number of

[3] http://ssd-rd.web.cern.ch/ssd-rd/labo28/default.htm

generated electron-hole pairs depending on the pulse intensity, the beam incidence angle, etc. So, the signal produced by this quantity of particles is calibrated with the one produced by the β^- emission of a ^{90}Sr radiactive source. Only a few relevant voltages are considered to measure the signal at the radiactive source setup (as the signal acquisition can be very laborious due to the low activity of the radiactive source or, as mentioned before, very low signals produced in the heavily irradiated sensors).

The non-irradiated sensor was electrically characterized in the probe station at the clean room to stablish the performance of this kind of technology before irradiation. Fig. 7.7 shows the current-bias voltage characteristic and the capacitance-bias voltage by means of the linear relation between the $1/C^2$ with the bias voltage. The latter allows to extract the value of the full depletion voltage at the knee of the curve. For this p-type FZ silicon sensor, a full depletion voltage of 27.6 ± 1.3 V is obtained.

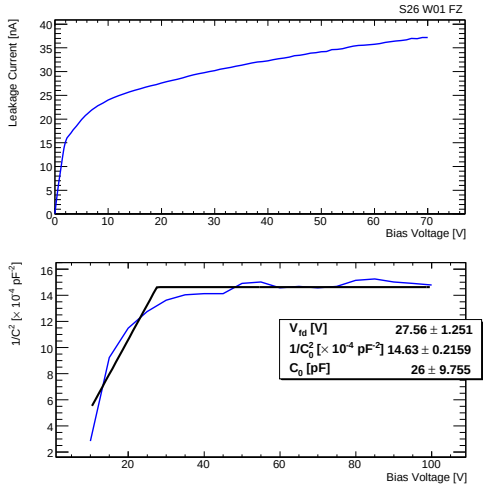

Figure 7.7: Leakage current as a function of the bias voltage (upper plot) and $1/C^2$ as a function of bias voltage for the reference non-irradiated FZ silicon sensor. The fit of the data gives a maximum capacitance of 26.0 ± 9.8 pF and a full depletion voltage of 27.6 ± 1.3 V.

Figure 7.8 shows the current-voltage characteristic measured at the laser setup and the collected charge versus bias voltage for the non-irradiated sensor. The collected charge has been fitted to a function defined as

$$Q(V) = \begin{cases} Q_0 \cdot \sqrt{\frac{V}{V_{fd}}} & V < V_{fd} \\ Q_0 & V \geq V_{fd} \end{cases} \tag{7.1}$$

The full depletion is reached at a bias voltage of $V_{fd} = 30.9 \pm 0.2$ V which is close enough with the value extracted from the $1/C^2$-V curve. No systematic errors were determined. From V_{fd}, the collected charge remains constant and corresponds to the maximum collected charge at the sensor resulting from the fit, $Q_0 = 23.6 \pm 0.1$ ke^- again close enough to the expected

value. The IV characteristic shows a kink point at approximately the full depletion voltage which indicates that the current is dominated by the resistivity of the diode as the bulk is fully depleted. The increasing of the current after full depletion is due to the lateral extension of the junction.

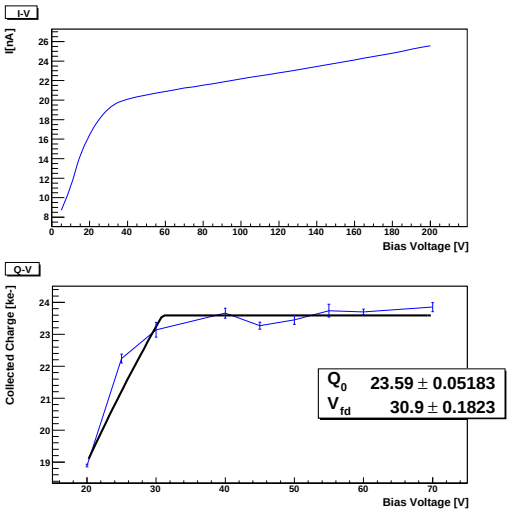

Figure 7.8: Leakage current (upper plot) and collected charge (lower plot) as a function of the bias voltage for a non-irradiated FZ silicon sensor. The fit of the collected charge versus bias voltage characteristic gives a full depletion voltage of $V_{fd} = 30.9 \pm 0.2\ V$.

The current-voltage characteristics for irradiated microstrip detectors are shown in Fig. 7.9 obtained at the laser setup. The level of leakage current increases with higher fluences. However, breaks at earlier voltages are observed on the sensors when irradiated with the lower fluences. Moreover, there was provided one sensor more irradiated with $10^{13}\ n/cm^2$ but it was lost due to an irreversible very early break ($I \sim 1\ mA$ at 150 V).

A possible explanation of the breakdown may be that the direct contact between the n^+ implant and the p-spray layer gives high electric field regions which may cause breakdown. With higher fluences, the p-spray charge is compensated with the oxide charge and the electric field is reduced, decreasing the risk of an early breakdown.

Figure 7.10 shows the collected charge versus bias voltage for each irradiated *p-FZ-1* detector measured with both setups (laser beam and radiactive source). The collected charge for the detector irradiated with $10^{14}\ n_{eq}/cm^2$ was only tested up to a bias voltage of 450 V at the laser setup due to limitations because of a high leakage current (breakdown was observed starting at $\sim 200\ V$).

During the measurements, microdischarges were observed on the tested sensors irradiated at the highest fluences (10^{15}, 2×10^{15}, and $10^{16}\ n_{eq}/cm^2$). These phenomena difficulted the study of charge collection. Microdischarge onset appeared at different voltage for each detector. Table 7.4 presents the applied reverse bias voltage at which microdischarges appear. Through up

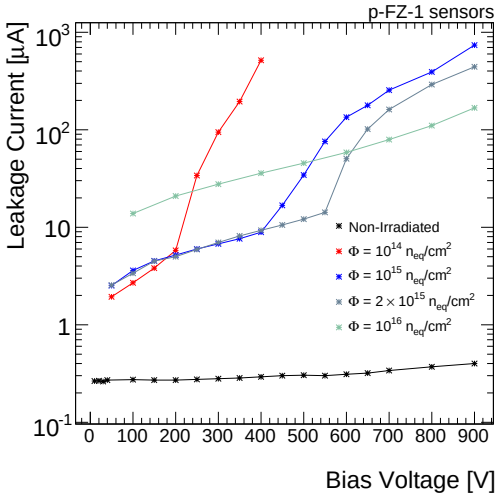

Figure 7.9: Leakage current as a function of the bias voltage for the irradiated sensors *p-FZ-1*. They are microstrip n^+p FZ silicon detectors irradiated with neutrons (measurements at $-30°$C).

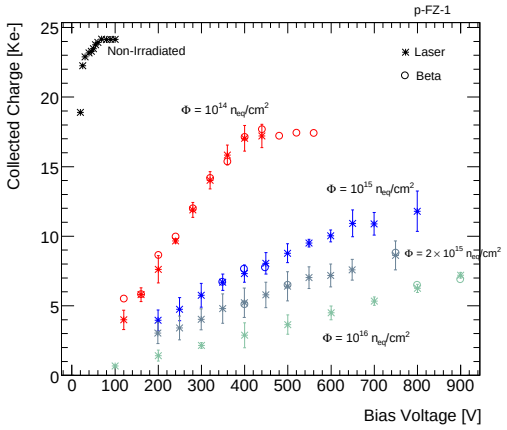

Figure 7.10: Collected charge as a function of the bias voltage for the irradiated sensors *p-FZ-1*. They are microstrip n^+p FZ silicon detectors irradiated with neutrons (measurements at $-30°$C). It is represented measurements with the laser setup ($*$) and the β^- radiactive source setup ($\circ$). The laser measurements are calibrated with the ones obtained from the β^- radiactive source setup.

to $\sim 500\ V$, the microdischarges appear randomly. At a voltage greater than 500 V, they appear with a fixed frequency. The frequency shows a dependency on the leakage current as shown in Fig. 7.11.

Fluence	Microdischarges onset
$10^{14}\ n_{eq}/cm^2$	no microdischarges
$10^{15}\ n_{eq}/cm^2$	420 V
$2\times10^{15}\ n_{eq}/cm^2$	200 V
$10^{16}\ n_{eq}/cm^2$	430 V

Table 7.4: Every sensor irradiated at the fluences above shows microdischarges starting at the different voltages indicated in the table.

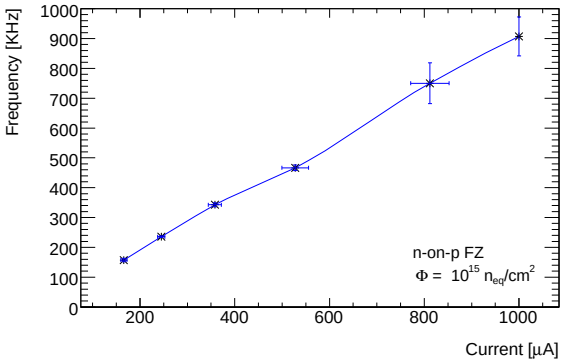

Figure 7.11: Frequency of the microdischarges as a function of the leakage current for the sensor irradiated with $10^{15}\ n_{eq}/cm^2$.

Figure 7.12 shows the microdischarges observed at the sensor irradiated with $10^{15}\ n_{eq}/cm^2$ biased at 700 V.

These microdischarges can be a consequence of high electric field regions inside the silicon bulk likely related to the p-spray dose. Detector performance becomes very sensitive to the p-spray implant parameters as microdischarges can represent the earliest mechanism of failure for microstrip detectors when operated at high voltage. Nevertheless, they were able to be used to test the acquisition system as it is the purpose of this work. Partially depleted operation of the most highly irradiated sensors is satisfactory and for instance, corresponds to a signal of ~ 5000 electrons at a bias of 800 V. Nevertheless, this voltage can be considered as an upper limit for any practical large detector system.

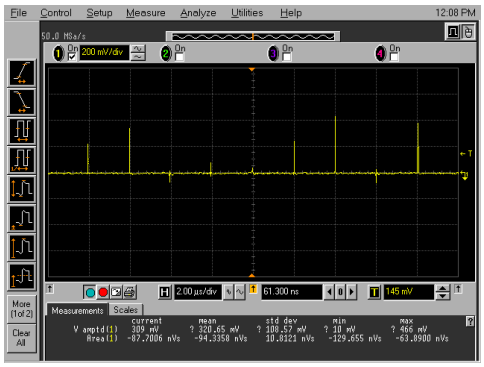

Figure 7.12: View of the oscilloscope screen showing the microdischarges for the sensor irradiated with 10^{15} n_{eq}/cm^2 biased at 700 V. The microdischarges appear at a fixed rate (seen as peaks at a fixed distance), that depends on the leakage current.

Annealing

An annealing process was carried out with a detector irradiated with 10^{15} n_{eq}/cm^2. In order to perform the measurements in an affordable time, the sensor was exposed to a high temperature of 80°C for different times to accelerate the annealing. This high temperature provides an acceleration factor of about 7400 times with respect to room temperature (4 minutes at 80°C is equivalent to 20 days at room temperature). This allows to reach the plateau between the beneficial and the reverse annealing in 4 minutes [120].

In this way, the collected charge dependence on time can be evaluated. The annealing of the device was done in five cumulative steps: 3 min, 10 min, 30 min, 100 min and 300 min at 80°C. The sensor was heated inside an oven in ambient air. The standard procedures were followed to measure the charge collection properties after each annealing step. Fig. 7.13 shows the collected charge as a function of annealing time at different voltages. It is only represented the collected charge up to a bias voltage of 500 V as this detector shows breakdown at 400 V and microdischarges start appearing at 420 V. At these high bias voltages, the self-heating of the device even when kept at a temperature of −30°C made the measurement difficult.

It must be noted that the bias applied is far below the full depletion. The depletion voltage dependence on annealing time is illustrated in Fig. 4.5. As the effective doping and the depletion voltage grow with the annealing time there will be a decrease of the depleted region, which translates to less collected charge at large annealing times.

Collected charge is unaffected by short annealing times. However, it decreases for long annealing times: > 200 days at room temperature. Maintenance periods of several weeks during the experimental lifetime of the detector (with temperatures at or close to room temperature) will certainly not exceed the short annealing times where the radiation damage is lower.

Nevertheless, several measurements of accelerated annealing effects made with irradiated p-type bulk detectors show that changes of charge collection efficiency with annealing time in p-type microstrip detectors are not very dramatic [121–123]. Moreover, one can see that the

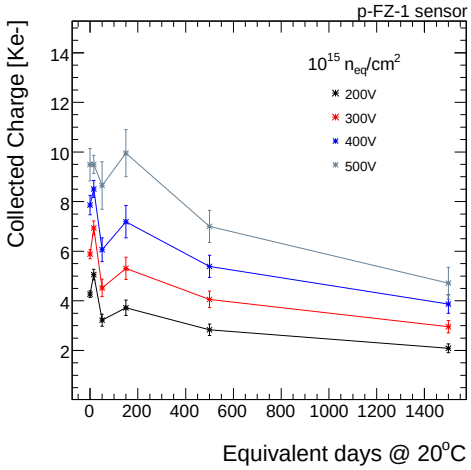

Figure 7.13: Changes of the collected charge as a function of annealing time after irradiation for a microstrip p-type detector irradiated at 10^{15} n_{eq}/cm^2 and biased at different voltages. The measurements were performed at $-30°$C.

charge collection does not deteriorate even after long annealing times, when effects of reverse annealing of space charge concentration are already dominant.

Final note

The difficulties found during these charge collection measurements determined the need of automation in this kind of detector characterization. It was solved by the development of an appropiate software and user interface (thanks to Sergio González Sevilla) that made data taking more efficient. The *C* based software allowed to stablish all the initial parameters of the oscilloscope, voltage source, pulse generator and photomultiplier power supply by means of *GIPB* buses as seen in the scheme 7.14. During the data taking, the selected voltage, the measured current read out from the voltage source and the corresponding scope channel signals are also stored in order to an offline analysis of the detector signals.

In addition, these measurements allowed to stablish the noise environment inside the laboratory determining also the degree of its electric isolation. For example, we realized that a radio frequency slipped in our data taking masking the sensor signals. This was solved by the use of an adequate faraday cage for the measurements.

Finally, the charge collection measurements for the sensor irradiated at 10^{14} n_{eq}/cm^2 showed lower values than expected for that dose (if compared with sensors measured later). The early and irreversible breakdown of the sensor did not allowed to determine the reason of those values (defective sensor, irradiation not corresponding to the labelled one, wrong calibration, signal masking by noise...).

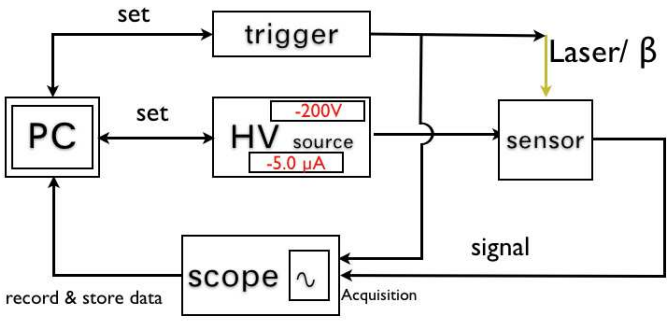

Figure 7.14: Schematic view of how the software performs the charge collection measurements. The measuring instruments are managed through an user interface at the PC by means of GIPB buses.

7.3.2 CNM07 microstrip silicon sensors

Other two sets of microstrip p-type detectors from CNM were tested. The sensors correspond to the series called CNM07. The wafer numbered as 5 is DOFZ and the wafer numbered as 10 is MCz (see table 7.2). They were characterized at the Single Channel Acquisition System (SCA System). Every set was labelled as *p-DOFZ-5* and *p-MCz-10* for the DOFZ silicon sensors and MCz silicon sensors respectively. They were irradiated at the fluences indicated in table 7.3. A non-irradiated sensor of each set was also measured for reference.

7.3.2.1 IV/CV measurements

First of all, the non-irradiated sensors were tested in the probe station at the clean room to evaluate the electrical performance of these technologies. Figures 7.15, and 7.16 shows the leakage current versus bias voltage and the capacitance (plotted as $1/C^2$) versus bias voltage for both sensors prior irradiation.

Concerning the capacitance plots, before depletion, it is expected deviations from the simple linear plot because there are interface charges in the interstrip gaps altering the electrostatics. Nevertheless, it is observed that the plots are still approximately linear. From the knee of the curve it is estimated that the total depletion of the substrate is reached at $V_{fd} = 26.7 \pm 0.9\ V$ on the DOFZ sensor and $V_{fd} = 104.3 \pm 5.7\ V$ on the microstrip sensor produced on MCz silicon. This translates in a doping concentration using the equation 3.45 and a resistivity from the equation 3.32 listed in the table 7.5.

It is obtained a maximum capacitance of $29.1 \pm 6.4\ pF$ and $29 \pm 15\ pF$ for the DOFZ sensor and the MCz sensor respectively. The saturation capacitances are similar for both sensors since the capacitances saturation values are inversely proportional to the thickness of the sensors by means of the equation 3.47.

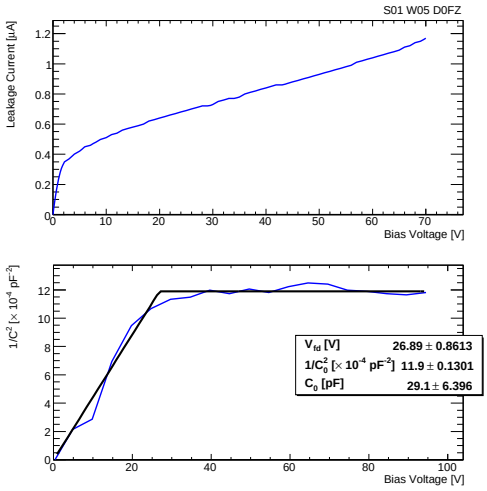

Figure 7.15: Leakage current versus bias voltage and backplane capacitance plotted as $1/C^2$ versus bias voltage for the non-irradiated DOFZ silicon sensor under study. From the fit, it is noted the very low depletion voltage, $V_{fd} = 26.7 \pm 0.9\ V$.

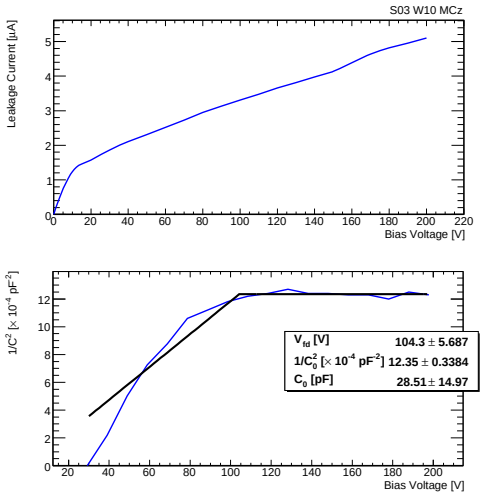

Figure 7.16: Leakage current versus bias voltage and backplane capacitance plotted as $1/C^2$ versus bias voltage for the non-irradiated MCz silicon sensor under study. $V_{fd} = 104.3 \pm 5.7\ V$.

	V_{fd} [V]	N_{eff} [cm^{-3}]	ϱ [k$\Omega \cdot$ cm]
DOFZ	26.7 ± 0.9 V	$(4.34 \pm 0.16) \times 10^{11}$	10.6 ± 0.4
MCz	104.3 ± 5.7 V	$(1.67 \pm 0.90) \times 10^{12}$	2.8 ± 0.6

Table 7.5: The full depletion voltage extracted from the plots is used to estimate doping concentration and the resistivity of the bulk for both non-irradiated p-type sensors with DOFZ and MCz silicon.

7.3.2.2 CNM07 sensors under neutron irradiation

The collected charge is measured as a function of the bias voltage for every of the five irradiated sensors and one non-irradiated for reference. The sensors were irradiated with 1 MeV equivalent neutrons at the fluences 10^{14}, 3×10^{14}, 10^{15}, 3×10^{15}, and 8×10^{15} n_{eq}/cm^2.

Concerning DOFZ sensors, the sensor irradiated at 10^{14} n_{eq}/cm^2 could not be measured because of thermal runaway. Fig. 7.17 shows the collected charge (CC) as a function of the bias voltage for the irradiated DOFZ sensors. The signal in the non-irradiated detector reaches a plateau at around 40 V and it is used to set the scale for full CCE. The V_{fd} of 285 μm thick detectors irradiated with neutrons at 3×10^{14} n_{eq}/cm^2 and higher exceeds the maximum possible applied bias voltage. Nevertheless, even for 8×10^{15} n_{eq}/cm^2 the DOFZ sensors are operational. The charge loss is very acceptable.

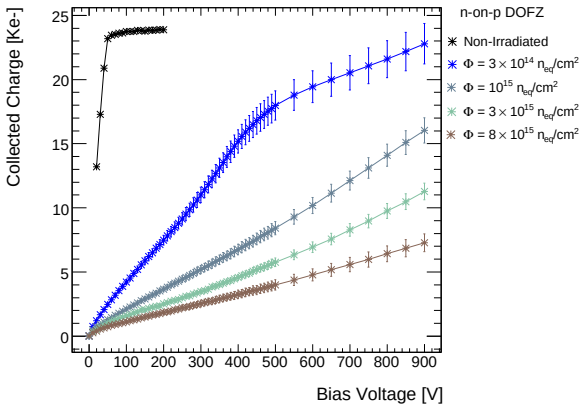

Figure 7.17: Collected charge versus bias voltage for the irradiated n^+p microstrip sensors with DOFZ silicon.

Considering the MCz sensors, Fig. 7.18 is showing the corresponding collected charge versus the bias voltage for the surviving irradiated sensors. The two sensors irradiated at the highest fluences were seriously radiation damaged and any signal could be observed.

The signal in the non-irradiated detector reaches a plateau at around 170 V. As expected, the

irradiated detectors show lower signal than the non-irradiated one at lower bias voltages. Even, for $\phi = 10^{14}\ n_{eq}/cm^2$, it is observed a plateau at around 340 V that represents the maximum collected charge at that fluence due to trapping loss charge. However, the signal keeps on rising with increasing bias voltage. For voltages of 750 V and higher, the signal in the sensors irradiated at the fluences of 10^{14}, and $3\times10^{14}\ n_{eq}/cm^2$ clearly exceeds the one in the non-irradiated reference detector. For the detector irradiated with $10^{15}\ n_{eq}/cm^2$, a charge of around 15000 electrons were measured at 850 V. This is a remarkable signal for a detector irradiated by a such high fluence.

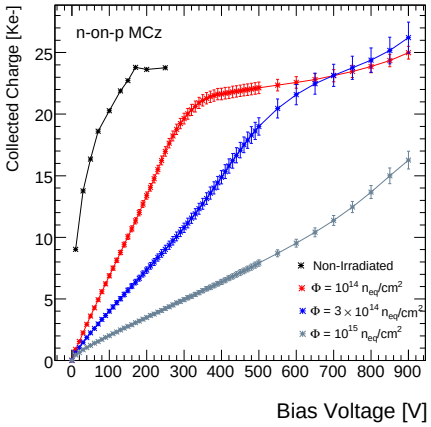

Figure 7.18: Collected charge versus bias voltage for the irradiated n^+p microstrip sensors with MCz silicon.

The effect of more charge being measured than the maximum charge expected can be attributed to charge multiplication [51, 124] occuring due to impact ionization. The multiplication effect is not found in non-irradiated silicon detectors, indicating that the radiation induced defects cause a change in the effective space charge that leads to an increase of the electric field at the junction between the n^+ electrode and the p-type substrate. Drifting charges accelerated in such presumably very high electric field can gain enough energy to create additional electron-hole pairs needing a considerably high bias voltage to see this effect. Similar effects have also been observed in others heavily irradiated planar silicon strip detectors [125–127]. This effect becomes more pronounced with bias voltage above 1000 V as shown in the previous references.

It is also shown the leakage current versus bias voltage measured with the detector mounted on the charge collection setup in Fig.7.19. It represents the total current from the high-voltag power supply including the current through the guard ring. The level of the leakage current remains around the μA order of magnitude except for the DOFZ sensors irradiated at the highest fluences of 3×10^{15}, and $8\times10^{15}\ n/cm^2$ which reachs tenths of μA.

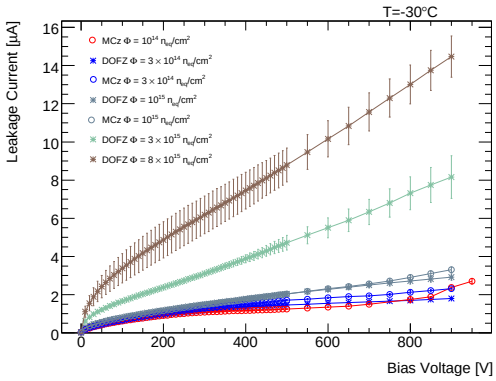

Figure 7.19: Leakage current as a function of the bias voltage for the irradiated n^+ microstrip sensors with DOFZ silicon (with $*$) and MCz silicon (with $\circ$) measured with the Single Channel Acquisition System.

Discussion

Surprisingly high values of collected charge were measured with detectors irradiated with neutron fluences. Measurements of collected charge versus bias voltages for the considered sensors with DOFZ and MCz silicon material are compared in Fig 7.20. Charges as high as those measured for non-irradiated sensors were observed under the uncertainties for a fluence of 10^{14} n_{eq}/cm^2 for MCz sensors and 3×10^{14} n_{eq}/cm^2 for both sensors. This charge multiplication effect is more prominent for MCz sensors at least for 3×10^{14} n_{eq}/cm^2, being the charge collection perfomance similar for 10^{15} n_{eq}/cm^2.

Every edge of the strip implants supposes a stronger electric field in this region compared to pad detectors for the same space charge concentration. In addition, trapping alters the space charge. Therefore, one could expect that conditions give higher probabilities for charge multiplication in the detector volume near the strips, highly irradiated at high bias voltages. Nevertheless, the measured collected charge does exceed significantly the 100 % and this effect is not observed at the leakage current measurements which are within reasonable levels.

It has been proved that the addition of oxygen to high purity and high resistivity FZ silicon, resulting in DOFZ silicon, was more resistent against charged hadron irradiation [78, 89]. The high purity FZ method can yield wafers with low concentration of O ($\sim10^{16}$ cm^{-3}), reaching till $\sim10^{17}$ cm^{-3} with oxygen diffusion technique. A much higher oxygen concentration and naturally presented is found in wafers produced with MCz silicon [59]. The oxygen concentration in MCz silicon is about 5×10^{17} cm^{-3}. Both kinds of oxygen enriched substrate technologies (DOFZ, MCz) are compared in this study under neutron irradiation. In Fig. 7.21 the collected charge at a representative bias voltage of 500 V (the maximal voltage at which silicon detectors can be biased in the SCT of ATLAS [128]) is shown for different neutron fluences. It shows that under neutron irradiation, the total collected charge, therefore the trapping, is unaffected by the silicon substrate type.

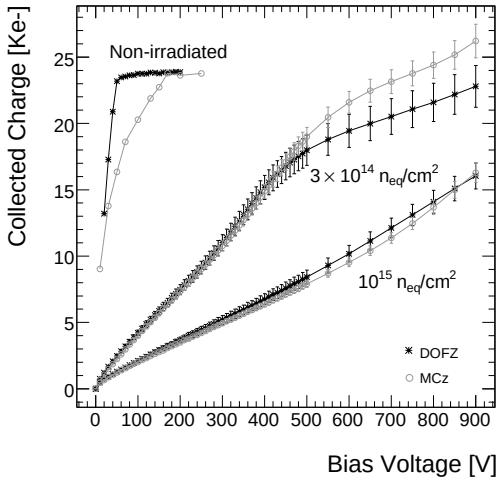

Figure 7.20: Comparison of charge collection as function of bias voltage for the sensors with DOFZ ($*$) and MCz ($\circ$) silicon substrates. It is shown the data for the non-irradiated, and the fluences 3×10^{15}, and 10^{15} n_{eq}/cm^2.

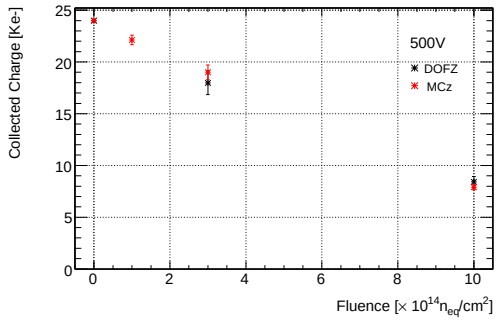

Figure 7.21: Comparison of the charge collection as function of neutron fluence for DOFZ (in red) and MCz (in black) silicon sensors. The data corresponds to a reverse bias voltage of 500 V.

7.3.2.3 Noise of CNM07 sensors

In order to determine the signal as a consequence of a particle crossing through the detector, the strip signal must substantially exceed the noise. Therefore it is essential to determine the noise that affects the search of the signal in the SCA system.

Over a sufficiently large number of events ($N \sim 2048$), the channel mean signal-pedestal ($\overline{P}$) and noise (σ^2) were calculated as

$$\overline{P} = \frac{1}{N}\sum_{j}^{N} P_j \tag{7.2}$$

$$\sigma^2 = \frac{1}{N}\sum_{j}^{N} P_j^2 - \overline{P}^2 \tag{7.3}$$

where P_j is the raw signal (voltage level) for the j-th event for the single channel. Then, to calculate the signal within this acquisition system, the extracted signal should be redefined as $S_j = P_j - \overline{P}$ to substracte the pedestal.

The pedestal distributions were obtained from special data-taking runs using CNM sensors with off-beam data or with the detector signal delayed out of the trigger gate. The noise is measured as the r.m.s. of the pedestal distribution fitted to a Gaussian function. It was used a range-scale of 200 mV/div at the oscilloscope enough to record the points properly.

Firstly, the pedestal distributions were measured for several non-irradiated detectors at room temperature. In Fig. 7.22 is shown the pedestal distribution for a DOFZ silicon detector at 150 V as example. All these points are fitted to a gaussian to extract the mean signal-pedestal and the noise (σ).

The noise measured at room temperature with a non-irradiated CNM detectors is reported in Fig. 7.23 as a function of the voltage. The noise is extracted from the linear fit of the data. The data show that the noise is practically constant due to the noise is dominated by the serial noise for a non-irradiated sensor [129]. This value corresponds to the minimum level of noise due to the readout electronics.

The noise is also evaluated for three detectors irradiated with increasing neutron fluences: 10^{14}, 3×10^{14}, and 10^{15} n_{eq}/cm^2. The measurements were done at -30°C, in the same conditions that in irradiated detector characterization. Fig. 7.24 shows the pedestal distributions for the three irradiated sensors. The reported data correspond to a bias voltage of 600 V. As shown, the level of noise are pretty similar for all cases.

In Fig. 7.25, the noise as a function of the bias voltage is plotted which is showing a constant level of noise when increasing bias. It is noted that the noise measured for irradiated detectors is not so different from the one measured for non-irradiated detectors and with no dependence on the irradiation fluence.

For irradiated sensors, the noise is mainly affected by the reverse current (parallel noise). Nevertheless, this limiting factor is reduced by operating the irradiated detectors at low temperature (~ -30°C). This is the consequence that the noise of non-irradiated and irradiated detectors is dominated by the serial noise whose main source is the readout amplifier. However, the size

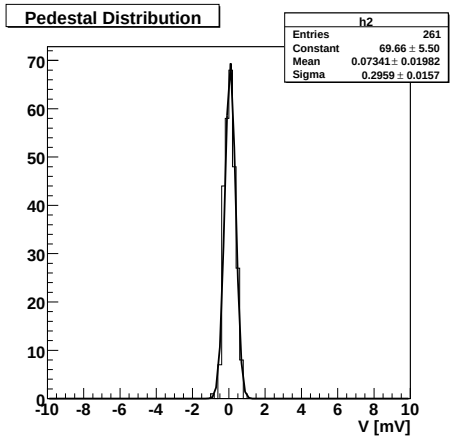

Figure 7.22: Pedestal distribution for a non-irradiated DOFZ p-type sensor biased at 150V. The pedestal value corresponds to the mean and the noise value corresponds to the sigma of the gaussian fit for this bias voltage.

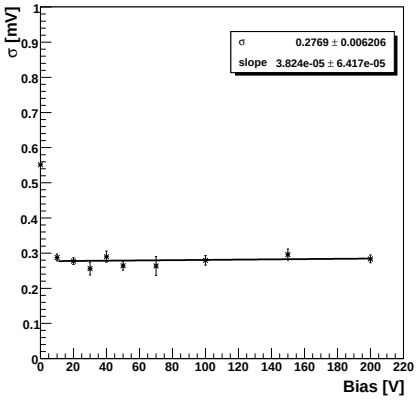

Figure 7.23: Measured noise as a function of the bias voltage for a non-irradiated DOFZ silicon sensor. The measurements were done at room temperature. It is noted that the noise is independent of the bias voltage.

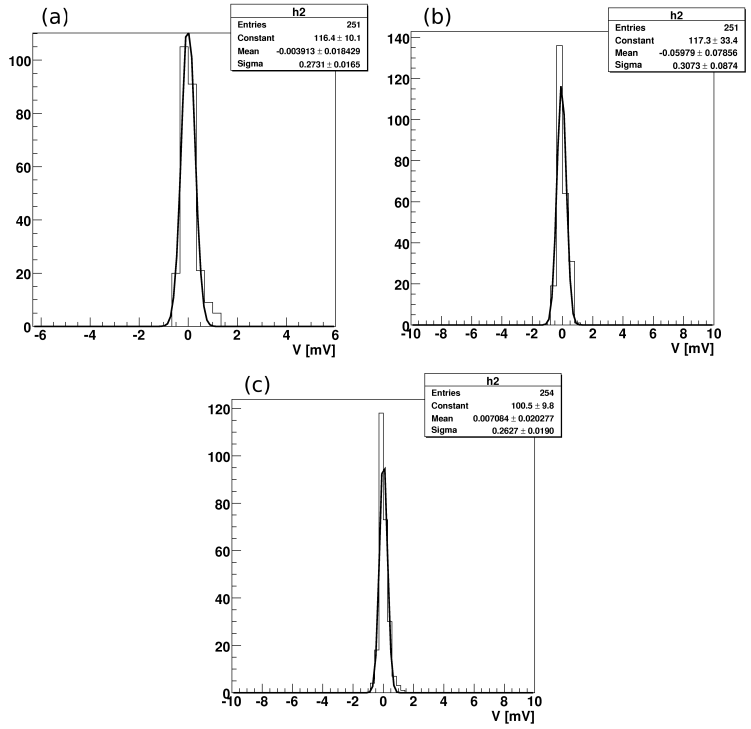

Figure 7.24: Pedestal distributions for silicon sensors irradiated at (a) 10^{14}, (b) 3×10^{14}, and (c) 10^{15} n_{eq}/cm^2 at a temperature of -30°C. The bias voltage corresponds to 600 V. From these plots are extracted the mean (pedestal, $\overline{P}$) and the σ (noise level) values at this bias.

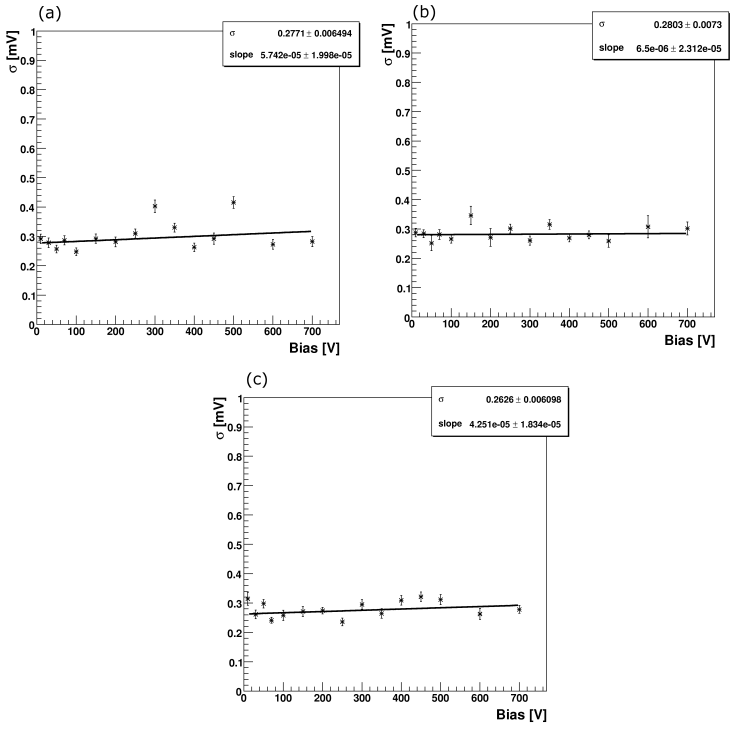

Figure 7.25: Measured noise as a function of bias voltage for silicon sensors irradiated at (a) 10^{14}, (b) 3×10^{14}, and (c) 10^{15} n_{eq}/cm^2 at a temperature of $-30°$C.

of the serial noise could be reduced by using improved electronics which is showed with the ALIBAVA system (see results in section 7.7) and with it, an increased signal-to-noise ratio is expected.

Table 7.6 summarizes the noise values for the considered fluences and shows a no dependence on radiation working at low temperature.

Fluence [n_{eq}/cm^2]	σ [mV]	$I_{leakage}$ [μA] at $-30°$	
		200 V	700 V
Non Irradiated	0.277 ± 0.006	$25.5 \pm 0.04\ nA$	-
10^{14}	0.277 ± 0.007	0.900 ± 0.003	1.500 ± 0.004
3×10^{14}	0.280 ± 0.007	0.920 ± 0.006	1.620 ± 0.003
10^{15}	0.263 ± 0.006	1.18 ± 0.08	2.50 ± 0.02

Table 7.6: Level of noise for p-type silicon detectors measured at SCA system. It is shown the leakage current level at theses fluences.

7.3.2.4 Signal-to-noise ratio

Another figure of merit to characterize the detector performance is the ratio of the signal of incident particle to the system noise,

$$SNR = S/N \tag{7.4}$$

S is the corresponding signal generated by an incident particle on the sensor and N is the σ noise of the system under test. The signal-to-noise performance for CNM07 sensors irradiated at several neutron fluences has been estimated and plotted in Fig 7.26 for a bias voltage of 600 V. S was obtained as the amplitude peak of the averaged signal registered at 600 V in units of mV. N corresponds to the σ of the pedestal distribution and its values are summarized at the table 7.6 for every fluence.

For the fluence $10^{14}\ n_{eq}/cm^2$ it is achieved a SNR ~ 14 and for a fluence of $3 \times 10^{14}\ n_{eq}/cm^2$ the observed SNR is ~ 11 at a typical bias voltage of 600 V. For both cases, it is observed a SNR above than the required SNR of 10 for the microstrip region in the ATLAS tracker upgrade. It is important to note that the SNR is overestimated due to the noise dependence on the strip length (these test detectors have a smaller interstrip capacitance). These test sensors have a strip length of less than 1 cm whereas the anticipated geometry for the Short Strip Detector region considers 2.4 cm long strips. However, for the highest expected fluence in the innermost microstrip region that is $10^{15}\ n_{eq}/cm^2$, it is achieved a SNR very lower than 10 in our sytem. The measured signal-to-noise ratio of the silicon detector means that the signal decreases with increasing fluence mainly due to trapping effects.

Before irradiation, it is obtained a SNR of ~ 12 at a bias voltage of 350 V for the MCz sensor and ~ 11 at a bias voltage of 200 V for the DOFZ sensor (not plotted in 7.26).

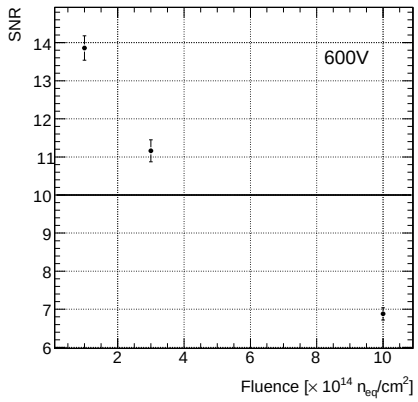

Figure 7.26: Signal-to-noise ratio (SNR) for different fluences for the CNM07 microtrip silicon sensors. The signal data correspond to a bias voltage of 600 V for the MCz sensor irradiated at $10^{14}\ n_{eq}/cm^2$ and DOFZ sensors for the fluences $3\times10^{14}\ n_{eq}/cm^2$ and $10^{15}\ n_{eq}/cm^2$.

7.4 ALIBAVA acquisition system characterization

The limitations of the single channel acquisition system together with the need to carry out the sensor measurements as similar as they performs in real experiments became decisive to the development of a new data acquisition system. It should allow to study the main properties of highly irradiated microstrip silicon sensors in research laboratories.

The ALIBAVA system complies with the requisites given above. All concerning this new acquisition system is explained in details in section 6.4. In this thesis, the early measurements made with ALIBAVA system are presented. These measurements also served as a batch test for the new acquisition system. These first tests allowed to debug the system and its software. Thus, the system performance could be improved.

The charge collection measurements should be carried out at low temperature in order to evaluate the proper radiation damage avoiding reverse annealing. All the irradiated sensors presented in this thesis are tested inside a freezer at -30°C where the measurements are done. Working with the ALIBAVA system, only the daughter board with the sensor is introduced to the freezer. The Beetle chip has also to operate inside the freezer. It was observed a gain dependence on the temperature as shown in Fig. 7.27. Operating the Beetle chip at $-30^{\circ}C$ inside the freezer affects its calibration. Specifically, the low temperature affects the common mode, which may shift outside the calibration range.

To overcome this limitation the calibration data at 20°C must be used. In addition, it is necessary to compute a gain correction factor with a non-irradiated sensor and the β^- setup to apply to the irradiated sensors in this way:

$$R_{cal} = Q_{RT}/Q_{-30^{\circ}C} \tag{7.5}$$

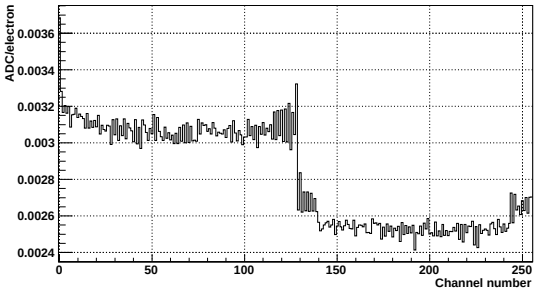

(a) $20°C$

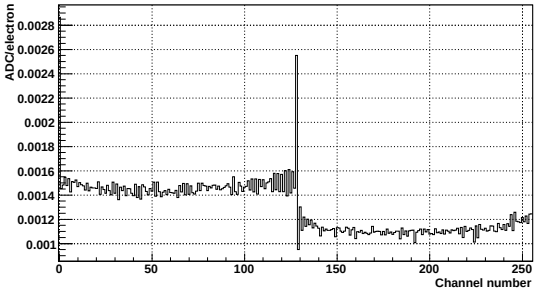

(b) $-30°C$

Figure 7.27: The ADC/electron ratio as a function of the channel number obtained at different temperatures. It is shown the channels for both Beetle chips presented at the daughter board. Only a sensor is connected to the second chip that corresponds to the channel numbers 128-255. The observed difference between the channels connected to every chip (with and without detector) is due to the change in the gain induced by the detector.

where Q_{RT} is the charge collected by the non-irradiated sensor in the β^- setup at room temperature and $Q_{-30^\circ C}$ is the collected charge by the same non-irradiated sensor in the the β^- setup at -30°C. It is used for both cases the calibration data for the corresponding Beetle chip at room temperature.

Thanks to the knowlegde improvement on the operation of the ALIBAVA system, this limitation was tackled directly increasing the common mode limit of the daughter board buffer by changing the buffer supply level from 3.3 V to 5 V. This modification (not applied to these measurements) allowed a right calibration data at -30°C and gain changes with temperature were accurately tracked by calibration. Thus, there was no need to use a gain correction factor.

How to perform with the ALIBAVA system at this early stage of this design is summarized as following. The measuring process involves five run modes:

- Calibration. ADC counts/electron rate for each input channel by means of calibration pulse injected to the Beetle chips. The calibration data is obtained for each Beetle chip considered at room temperature.
- Pedestal run. The pedestals are saved and substracted at the offline data analysis.
- Laser synchronization for scanning the time delay between the laser pulse and the acquisition.
- Laser run for each bias voltage.
- β^- radiactive source run (^{90}Sr) for each bias voltage.

For the laser and radiactive source runs, the signal is computed as the sum of strips in a cluster with a SNR > 6 and for the neighbours, a SNR > 2.5. The signal is measured in units of ADCs and the calibration data is used to obtain the charge in electrons (Q_e). The charge collected with the laser illumination is normalized to that collected with a β^- source at the same bias voltage. It is only needed for a few voltages in order to get the normalization factor:

$$R_{norm} = Q_{source\ setup}/Q_{laser\ setup} \tag{7.6}$$

In addition, the peak of the charge spectrum for a non-irradiated in the Q-V plateau at the β^- setup sensor is normalized to the theoretical value of 24000 electrons in order to compare all the measurements by means of the factor R_{24ke}.

Finally, the collected charge at a specific bias voltage measured at the laser setup for irradiated sensors is recomputed as:

$$Q = R_{24ke} \times R_{norm} \times R_{cal} \times Q_e \tag{7.7}$$

For every set of sensors, R_{24ke} and R_{cal} are computed with the corresponding non-irradiated sensor whereas R_{norm} is computed for every specific sensor. The collected charge for a non-irradiated sensor is computed in this way except for the factor R_{cal}.

7.5 Characterization of CNM sensors - II

7.5.1 CNM09 microstrip silicon sensors

The next sets of microstrip silicon sensors were tested by means of the ALIBAVA acquisition system (more details in section 6.4). The p-type sensors corresponds to the series *CNM09*. The wafers were manufactured with FZ silicon. The wafer 4 contains n^+p sensors and the wafer 17 contains n^+n sensors (see table 7.2). For identification, every set was labelled as *p-FZ-4* and *n-n-FZ-17*. They were irradiated at the fluences indicated in table 7.3. One non-irradiated of each set was also measured for reference.

7.5.1.1 IV/CV measurements

The first step is the electrical characterization of the non-irradiated FZ sensors in the probe station at the clean room to evaluate the electrical performance of these technologies. Figures 7.28, and 7.29 shows the leakage current versus bias voltage and the capacitance (plotted as $1/C^2$) versus bias voltage for both non-irradiated sensors.

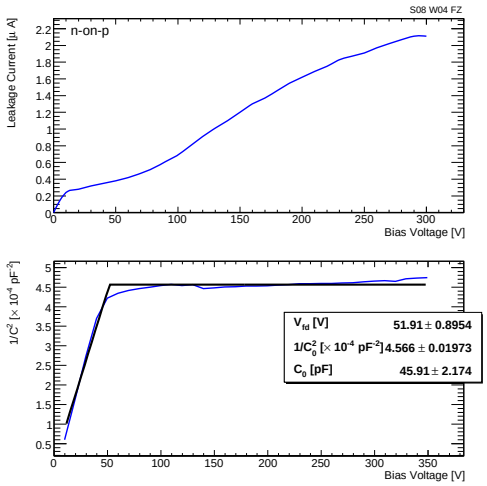

Figure 7.28: Leakage current versus bias voltage and backplane capacitance plotted as $1/C^2$ versus bias voltage for the non-irradiated n^+p FZ silicon sensor under study.

For the p-type sensor, the I-V plot does not show a stabilization of the leakage current as seen for the n-type sensor. Nevertheless, the n-type sensor shows a level of current around 55 μA, higher than the p-type sensor that is around 1-2 μA. Concerning capacitance plots, the behaviour is as expected. From the knee of the curve it is estimated that the full depletion of the substrate is reached at $V_{fd} = 51.9 \pm 0.9$ V on the p-type FZ sensor and $V_{fd} = 51.2 \pm 1.9$ V on the microstrip FZ sensor with the n^+n technology. Both non-irradiated sensors reach full depletion at similar bias voltages which indicates that the full depletion voltage does not depend

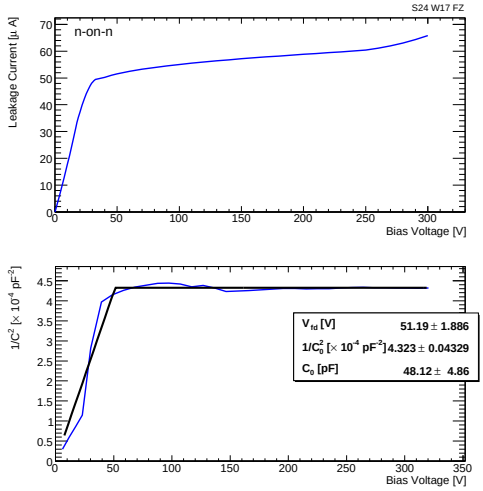

Figure 7.29: Leakage current versus bias voltage and backplane capacitance plotted as $1/C^2$ versus bias voltage for the non-irradiated n^+n FZ silicon sensor under study.

on the sensor technology. Taking the DOFZ sensor V_{fd} aforementioned, oxygen enrichment of the silicon bulk which is achieved within the manufacturing process, results in a substantial lower depletion voltage compared to FZ standard devices [89]. In the same way as in previous section, it can be estimated the doping concentration using the equation 3.45 and the resistivity from the equation 3.32. They are listed in the table 7.7.

It is obtained a maximum capacitance of 46 ± 2 pF and 48 ± 5 pF for the p-type sensor and the n-type sensor respectively. The saturation capacitances are similar for both sensors since the capacitances saturation values are inversely proportional to the thickness of the sensors by means of the equation 3.47.

	V_{fd} [V]	N_{eff} [cm^{-3}]	ϱ [k$\Omega \cdot$cm]
n^+-p FZ	51.9 ± 0.9 V	$(8.36 \pm 0.16) \times 10^{11}$	5.51 ± 0.11
n^+-n FZ	51.2 ± 1.9 V	$(8.37 \pm 0.32) \times 10^{11}$	5.51 ± 0.21

Table 7.7: The full depletion voltage extracted from the plots is used to estimate doping concentration and the resistivity of the bulk for both non-irradiated FZ sensors with p-type and n-type silicon substrate.

Finally, Fig. 7.30 represents the collected charge as function of the applied bias voltage is represented for the non-irradiated CNM sensors given in table 7.2. It shows the data for sensors with different kind of substrates (FZ, DOFZ and MCz) and for the technologies n^+p and n^+n. In addition, it is including measures from the two different acquisition systems (single channel and ALIBAVA system). And as expected, no discrepancy is observed.

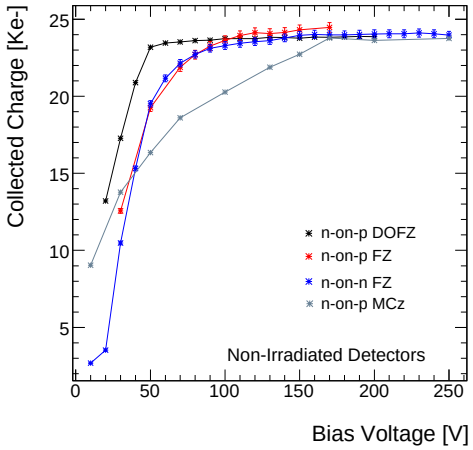

Figure 7.30: Collected charge as function of the bias voltage for the non-irradiated CNM sensors considered. It is noted that the DOFZ sensors obtains the lower depletion voltage.

7.5.1.2 CNM09 sensors under neutron irradiation

Going on to the irradiated FZ sensors, Fig. 7.31 shows the collected charge as a function of the bias voltage for the *p-FZ-4* sensors. During measurements the sensors were kept in a freezer at a temperature of $\sim -30°C$. For the n^+p FZ sensors, the charge collection was limited by microdischarges. For example, the sensor irradiated at 10^{14} n_{eq}/cm^2 could only be measured at a bias voltage of 150 V. Even more, strong microdischarges were observed when measuring the sensor irradiated at 3×10^{14} n_{eq}/cm^2. The attempt to evaluate them made microdischarges affected to the electronics and the daughter board chip stopped working properly.

In the laser setup the microdischarges and the signals can be separated clearly since the microdischarges are located in certain channels. Therefore, they can be masked for the offline analysis of the data. In other hand, when using the β^- setup, it makes necessary measure at bias voltages without microdischarges. The random nature of the radiactive source implies possible overlaps between β^- signals and microdischarges. In addition, working with microdischarges implies a limitation of the bias voltage in order to avoid damaging the sensor and the electronics. A more detailed study of the observed microdischarges can be found in the section 7.5.2.

In Fig. 7.32 it is shown the collected charge versus bias voltage for FZ n^+n sensors. This sensor technology shows the best charge collection efficiency. At a fluence of 10^{14} n_{eq}/cm^2 all deposited charge is collected at around 200 V. Even at 3×10^{14} n_{eq}/cm^2 the charge is fully collected reaching the maximum at ~450 V. Microdischarges were also observed for this set of sensors. Nevertheless, their effect was more easily masked as they appeared at a lower rate.

The leakage current versus bias voltage is shown in Fig. 7.33 for all the irradiated FZ sensors. At a fluence of 10^{14} n_{eq}/cm^2 the irradiated n^+n sensor does not break down up to 700 V, whereas the n^+p sensor shows a breakdown at an early bias voltage of 230 V. At the highest dose (10^{15} n_{eq}/cm^2), no breakdown is seen for both types of sensors. However, the leakage current

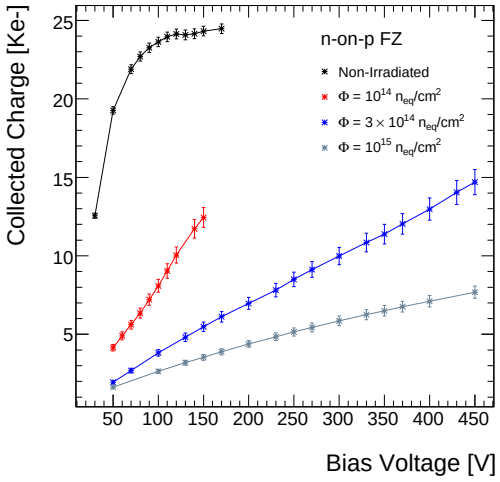

Figure 7.31: Collected charge as function of the bias voltage for the *p-FZ-4* sensors. It is noted that the sensor irradiated with 10^{14} n_{eq}/cm^2 could solely measured untill a bias voltage of 150 V due to microdicharges.

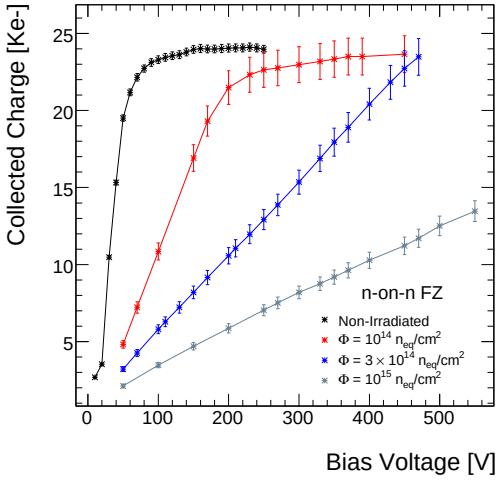

Figure 7.32: Collected charge as function of the bias voltage for the *n-n-FZ-17* sensors.

gets increased continuously which is likely caused by thermal runaway phenomena.

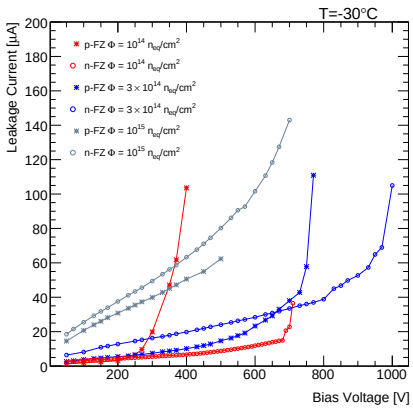

Figure 7.33: Leakage current as a function of the bias voltage for the irradiated FZ sensors with p-type silicon substrate (in $*$) and with n-type silicon substrate (in $\circ$).

7.5.1.3 Noise and signal-to-noise ratio

The signal-to-noise ratio (SNR) has been calculated for this sensor series *CNM09*. Fig. 7.34 plots the SNR for sensors irradiated at several neutron fluences for a bias voltage of 450 V. In black points, it is shown the SNR for the n^+p FZ sensors and in red, the SNR for the n^+n FZ sensors. For every fluence, the signal is extracted as the peak from the charge spectrum at the corresponding bias voltage in units of electrons. The noise is extracted as the σ from the pedestal distribution in units of electrons and its values are summarized in table 7.8. The pedestal distributions are measured from specific data taking runs without laser or β^- signals.

	p-FZ-4	*n-n-FZ-17*
Fluence [n_{eq}/cm^2]	σ [ke^-]	σ [ke^-]
Non Irradiated	1.26	1.38
1×10^{14}	1.47	1.30
3×10^{14}	1.23	1.32
1×10^{15}	1.40	1.40

Table 7.8: Level of noise for n^+p (*p-FZ-4*) and n^+-on-n silicon (*n-n-FZ-17*) detectors at 450 V measured at the ALIBAVA system, given in electrons.

The SNR for the two lowest fluences (1, and 3×10^{14} n_{eq}/cm^2) remains in a high level, around 19 for the n^+n sensors whereas it gets decreased for a fluence of 10^{15} n_{eq}/cm^2 till a value of ~ 8. In other hand, n^+p sensors show a higher degradation in terms of SNR. It is obtained a $SNR \sim 12$ for a fluence of 3×10^{14} n_{eq}/cm^2 and very lower SNR of almost 6 for the highest fluence of

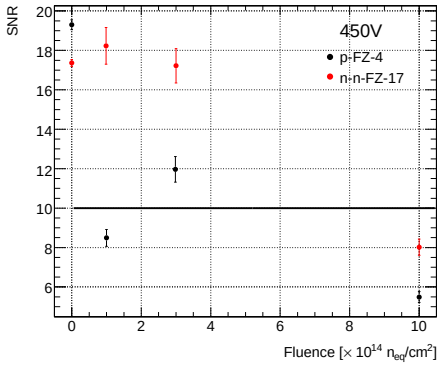

Figure 7.34: Signal-to-noise ratio (SNR) for different fluences for the CNM09 microstrip sensors. The signal data correspond to *p-FZ-4* sensors in black points and in red for the *n-n-FZ-17*. They were biased at 450 V.

10^{15} n_{eq}/cm^2. The SNR of the n^+p sensor irradiated at 10^{14} n_{eq}/cm^2 was very affected by microdischarges and its charge collection measurements were limited to 150 V. Before irradiation, it is obtained a SNR of $\sim$19 for the n^+p sensor and $\sim$17 for the n^+n sensor at a bias voltage of 150 V.

7.5.1.4 Comparing with CNM07 sensors

The comparison of all CNM sensors can be seen in Fig. 7.35. It is shown the collected charge as a function of the neutron fluence at a bias voltage of 400 V. n^+p sensors on FZ, DOFZ, and MCz silicon substrate have very similar performance under neutron irradiation whereas the n^+n sensors show an improved charge collection performance requiring lower bias voltages to fully collect the deposited charge. They are less affected by trapping. Nevertheless, n^+p sensors have sufficient charge collection efficiency for the envisaged semiconductor tracker layers under high luminosity conditions. Even, at the highest radiation dose of 8×10^{15} n_{eq}/cm^2, the size of the output signal is still considerable.

7.5.2 Sensor microdischarges measured by the Alibava acquisition system

For CNM09 sensors, microdischarges were observed during charge collection measurements. They appear as high signal peaks and they can show both polarities, positive and negative. Fig. 7.36 corresponds to two images of the oscilloscope screen during measurements. The yellow line represents the analogue readout corresponding to one Beetle chip connected to a sensor, where *16 bits* header and the multiplexed 128 channels can be seen. The figure to the left shows two microdischarges with different amplitudes and the figure to the right shows a microdischarge in coincidence with a signal produced in the laser setup.

Microdischarges do not occur in all detectors and are located in certain channels which can be

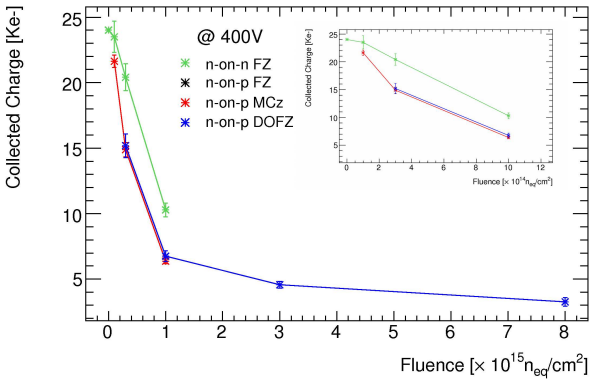

Figure 7.35: Collected charge as a function of neutron fluences for different kinds of substrates of n^+p sensors and FZ n^+n sensors produced at CNM. The data corresponds to a bias voltage of 400 V. The inserted plot shows a zoomed view of the graph up to a fluence of 10^{15} n_{eq}/cm^2.

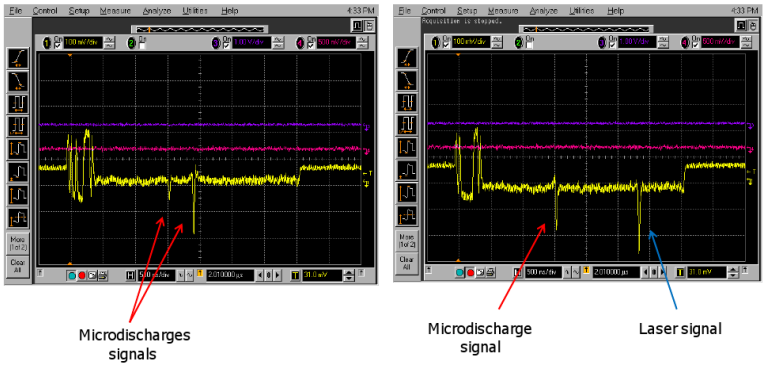

Figure 7.36: Oscilloscope screen views of microdischarge signals (left) and in coincidence with a laser signal (right). The yellow channel is the analogue readout corresponding to one Beetle chip where the 16 bits header and the 128 channels are showed.

masked in order not to affect the data. However, they become more frequent at higher voltages and the amplitude of the microdischarges can become significant contributing to the spectrum considerably as it is shown in Fig. 7.37.

Microdischarges appear at a higher bias voltage with increasing fluence as seen in table 7.9 for the *p-FZ-4* and *n-n-FZ-17* sensors.

In the other hand, its frequency increases with the voltage applied. The hit map for several FZ sensors is studied. It is plotted the frequency of registered signals as a function of the channel. These plots are showing untill 256 channels which correspond to the two Beetle chips presented in a daugther board. Only a sensor is measured at a time that is connected to the second Beetle

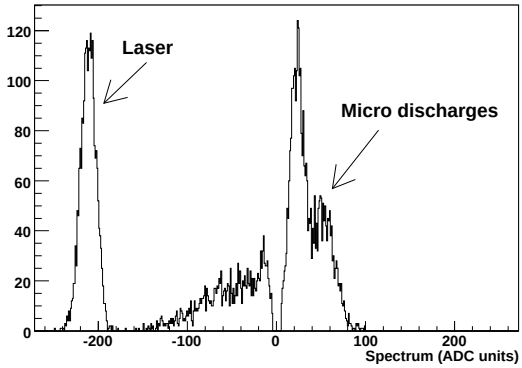

Figure 7.37: Spectrum of the laser signal in ADC units corresponding to an irradiated sensor showing microdischarges. The amplitude of the microdischarge is estimated to be approximately the corresponding to a 1.5 *mip*. These microdischarges were recorded in coincidence with the laser trigger.

	p-FZ-4	*n-n-FZ-17*
Fluence [n_{eq}/cm^2]	onset voltage [V]	onset voltage [V]
0	160	230
1×10^{14}	150	390
3×10^{14}	270	400
1×10^{15}	330	400

Table 7.9: The microdischarge onset voltage for every irradiated CNM09 sensor.

chip (channels 128-255). The microdischarges are random but only those in coincidence with the laser trigger are registered.

Firstly, it is considered a *better* case in which the microdischarges appear at a higher bias voltage. Let consider the sensor *p-FZ-4* irradiated at 3×10^{14} n_{eq}/cm^2 where the microdischarges appear at 270 V. Fig. 7.38 shows its hit map for several voltages. At 220 and 250 V it is only registered the hits produced by the laser beam located at a specific channel around 213 with a frequency of approximately 2500 hits/run. At the onset voltage, microdischarges start appearing also in certain channels. Even at higher voltages the number of channels with microdischarges increases and less laser hits are observed. During data-taking more high intensity microdischarges in coincidence with trigger are registered and the laser signals are masked.

Fig. 7.39 shows the hit map for a worse case with a non-irradiated sensor. The sensor in this case corresponds to the *n-n-FZ-17* non-irradiated sensor. At 240 V microdischarges are already observed at around channel 255 but not affecting too much to the laser hits. However, at 270 V the frequency of the microdischarges increases to 4900 hits/run whereas laser hits decreases to around 2000 hits/run and microdischarges in other channels begin to be registered. At 280 V,

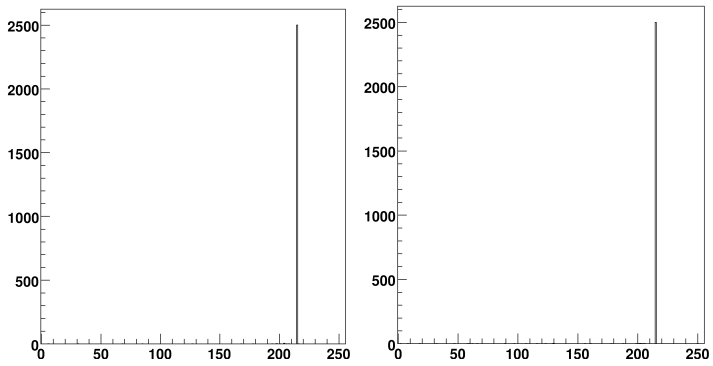

(a) 220 V (b) 250 V

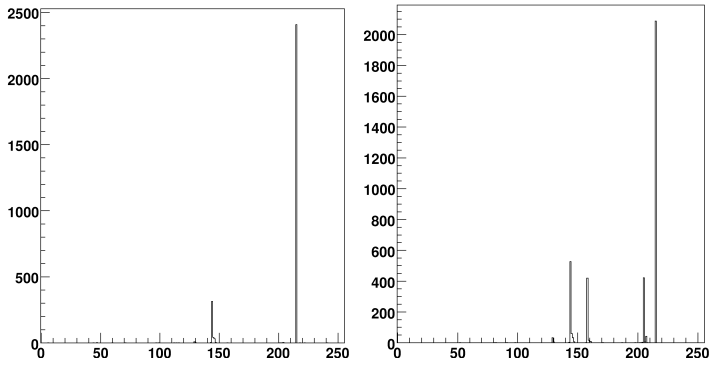

(c) 270 V (d) 300 V

Figure 7.38: Hit Map for the sensor *p-FZ-4* irradiated at 3×10^{14} n_{eq}/cm^2. It is plotted the frequency of the signal hits (laser and microdischarges hits) registered in coincidence with the laser trigger as function of the sensor channel for several voltages using the laser setup. The laser hits are located around channel 213. The ALIBAVA acquisition system is used. It is noted that the plots includes the channels for the two Beetle chips presented in the ALIBAVA system. Only a sensor is connected to the second chip which corresponds to 128-255 channels.

the frequency of the microdischarges continues increasing. It is also shown the hit map at 300 V where the frequency of microdischarges exceeds to the laser one and therefore making the charge collection measurement nosense.

Finally, it is plotted the hit map for another non-irradiated sensor (p-FZ-4) whose microdischarge onset voltage is 160 V. As seen in Fig. 7.40 at 150 V there are no microdischages, and at 160 V, they start appearing. However, the frequency of the microdischarges increases abruptly untill 3500 hits/run whereas the registered laser hits decrease from 2000 hits/run at 160 V to 1000 hits/run at 170 V. As seen in the plot *(d)*, the hits are dominated by microdischarges and no laser hits are registered.

The causes of the microdischarges were difficult to determine. The microdischarges may be

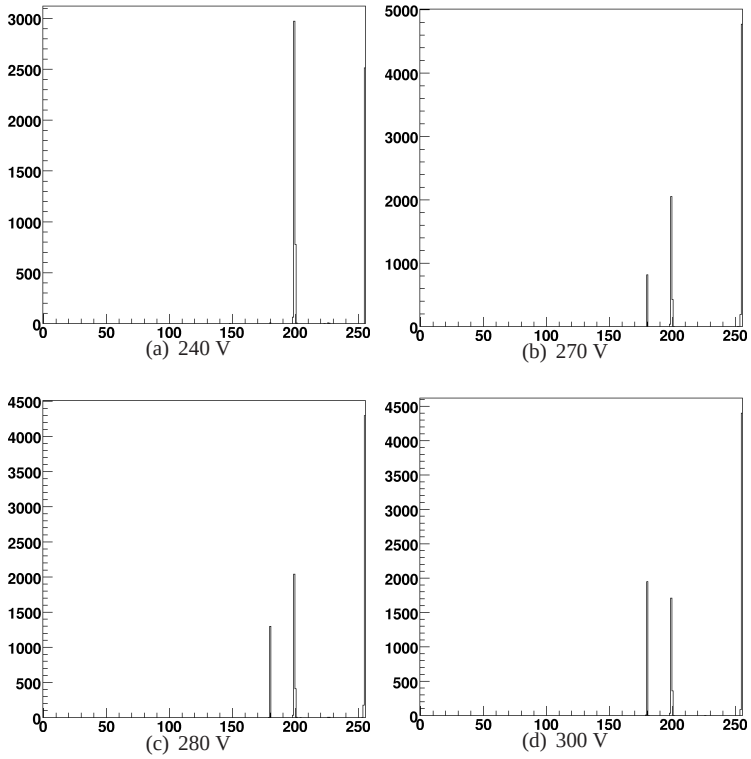

Figure 7.39: Hit Map for the sensor *n-n-FZ-17* non-irradiated. It is plotted the frequency of the signal hits (laser and microdischarges) registered in coincidence with the laser trigger as function of the sensor channel for several voltages using the laser setup. The laser hits are located around channel 213. The ALIBAVA acquisition system is used. It is noted that the plots includes the channels for the two Beetle chips presented in the ALIBAVA system. Only a sensor is connected to the second chip which corresponds to 128-255 channels.

due to high electric fields induced by high doping gradient regions as for example, in the contact between the n^+ implant and the p-spray layer. Other reasons may be electric field distorsions caused by fabrication process defects or pin-holes during bonding. In addition, it has been observed that the p-spray isolation has a better performance after irradiation than before and as seen, the microdischarge onset voltage gets increased with irradiation. Thus, microdischarges may be related to p-spray dose.

7.6 Study of the interstrip resistance

The technique to performance interstrip resistance (R_{int}) measurements was already explained in section 6.1.3. The value of R_{int} determines for the strip how the charge produced by an ionizing particle is distributed (cluster) and, consequently affects the spatial resolution of the

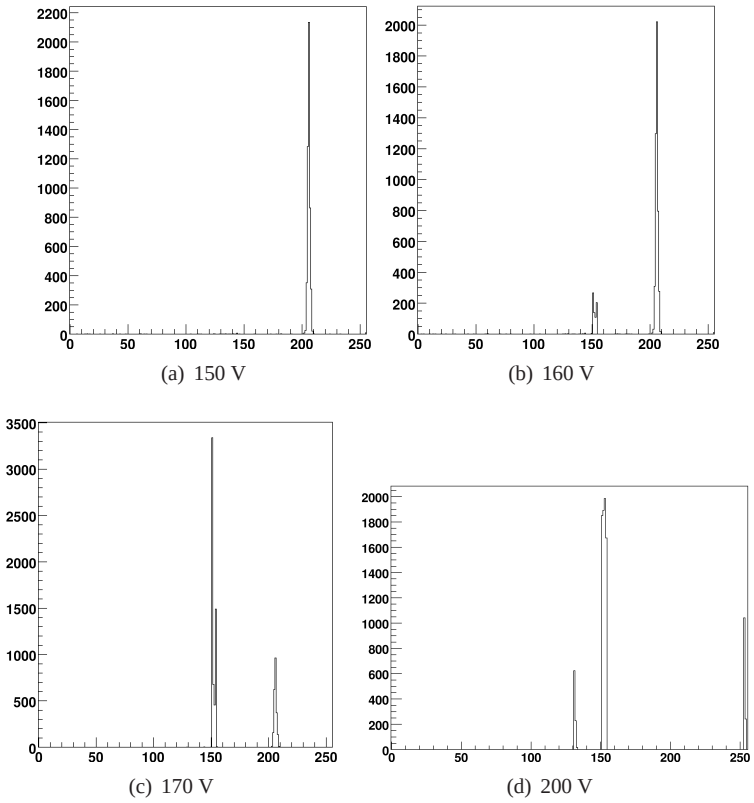

(a) 150 V (b) 160 V

(c) 170 V (d) 200 V

Figure 7.40: Hit Map for the sensor *p-FZ-4* on-irradiated. It is plotted the frequency of the signal hits (laser and microdischarges) registered in coincidence with the laser trigger as function of the sensor channel for several voltages using the laser setup. The laser hits are located around channel 213. The ALIBAVA acquisition system is used. It is noted that the plots includes the channels for the two Beetle chips presented in the ALIBAVA system. Only a sensor is connected to the second chip which corresponds to 128-255 channels.

detector. Apart from this, studying the behaviour of R_{int} one can reveal the yield of good strips or possible technological defects.

Non-irradiated p-type CNM sensors were used for these tests. The studies were performed in a probe station in the clean room facility. Both sensors differ in the kind of silicon substrate as shown in table 7.10.

Fig. 7.42(a) and (c) show the equivalent resistance measurement of both considered detectors by means of the linear fit of the ohmic region. It is represented the leakage current versus bias voltage applied between two adjacent strips (U_2) through the DC contacts for several bias voltage applied to the sensors (U_1) (see Fig. 6.4). Fig. 7.41 shows the leakage current as a function of the bias voltage applied to the whole sensor (U_1) for the two considered detectors.

Fig. 7.42(b) and (d) show a zoom of the previous leakage current versus bias voltage plots in

Label	technology	silicon substrate
s08-w04	n^+-on-p	FZ
s21-w10	n^+-on-p	MCz

Table 7.10: Sensor used for interstrip resistance studies.

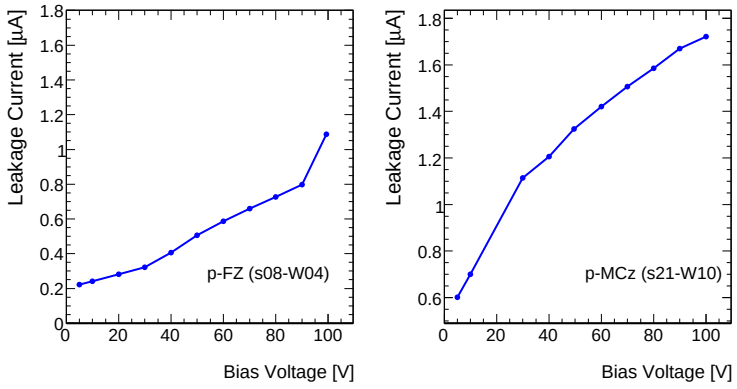

Figure 7.41: Leakage current as a function of the bias voltage applied by the sensor backplane (U_1). The upper plot corresponds to the p-Fz sensor labelled *s08-w04* and the lower plot is for the p-MCz sensor labelled *s21-w10*.

the ohmic region in order to extract the interstrip resistance value by means of:

$$\frac{1}{R_{eq}} = \frac{1}{R_{int}} + \frac{1}{2R_{bias}} \tag{7.8}$$

For the estimation of R_{int}, the nominal value for R_{bias} has been considered [128].

$$R_{bias} = 1.25 \pm 0.75\ M\Omega \tag{7.9}$$

It is obtained as expected similar values of R_{int} for both sensors (see table 7.11). These interstrip resistances are close to ATLAS specifications ($R_{int} > 2 \times R_{bias}$) and in the order of magnitude as R_{bias}. So it can be considered an interstrip isolation of the same level of R_{bias}.

Label	R_{eq} [MΩ]	R_{int} [MΩ]
s08-w04	1.01 ± 0.01	1.69 ± 0.69
s21-w10	0.964 ± 0.001	1.57 ± 0.59

Table 7.11: measured R_{eq} and estimated R_{int} for non-irradiated p-type sensors.

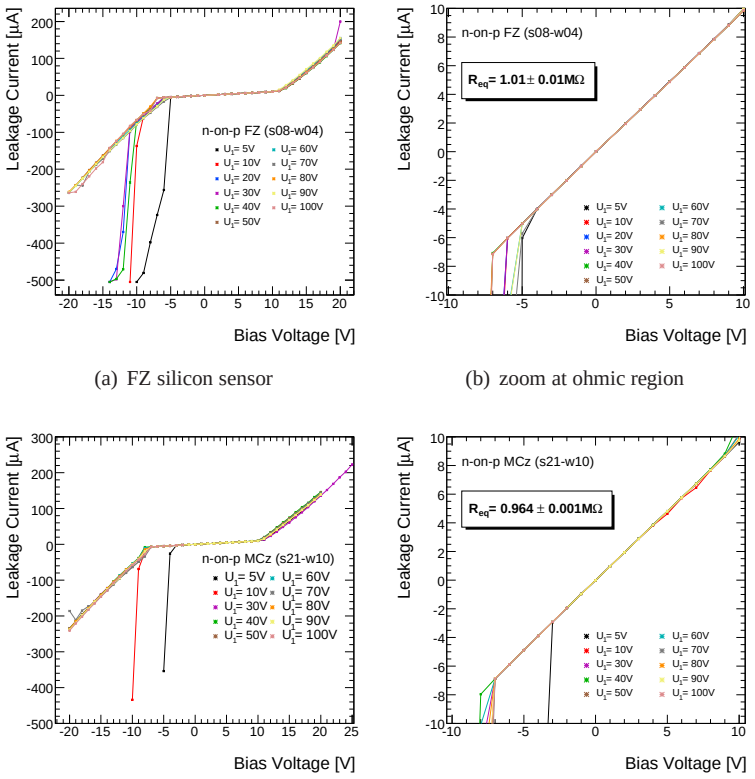

(a) FZ silicon sensor (b) zoom at ohmic region

(c) MCz silicon sensor (d) zoom at ohmic region

Figure 7.42: The leakage current measured between two adjacent strips as a function of the bias voltage applied between the strips for a FZ sensor (a) and a MCz (c). Figures (b) and (d) corresponds to a zoom of the previous figures in the ohmic region in order to extract the equivalent resistance. U_1 corresponds to the bias voltage applied to the whole sensor.

7.7 HAMAMATSU microstrip silicon sensors

7.7.1 Prototypes of HAMAMATSU microstrip silicon sensors

n^+p sensors were prototyped by HAMAMATSU Photonics[4] on 6 inch (150 mm) wafers for the HL-LHC [130]. These sensor series are called *ATLAS07*. The silicon material is float-zone (FZ) and the wafer orientation is <100>. The mask layout for the wafer is shown in Fig. 7.43. The layout contains a large-area main sensor of dimensions 9.75×9.75 cm^2, which is the maximum size square possible in the usable area defined by HAMAMATSU Photonics. In addition, miniature 1×1 cm^2 sensors with varius strip and isolation structures are included in the layout, as well as 4×4 mm^2 miniature diodes, which are fit into the space remaining on

[4]Hamamatsu Photonics K.K., 1126-1 Ichino-cho, Hamamatsu-shi 435-8558, Japan

the wafer. For this study the miniature sensors have been used. The main parameters of the miniature strip detectors are summarized in table 7.12.

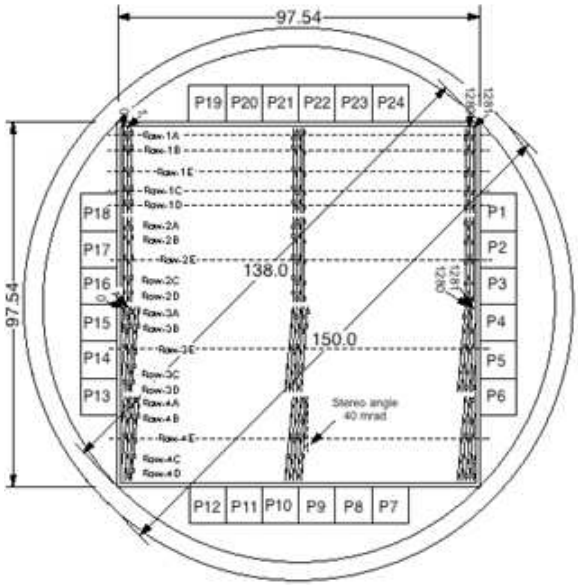

Figure 7.43: The mask layout for the ATLAS07 sensors for a 150 mm wafer. The central piece is a $9.75 \times 9.75\ cm^2$ main sensor and the positions P1-P24 correspond to the miniature sensors of $1 \times 1\ cm^2$ [131].

Sensor parameter	value
area	$1\ cm^2$
thickness	$320\ \mu m$
number of strips, Z1-Z5 (Z6)	104 (77)
strip length	0.80 cm
strip width Z1-Z6 (Z5)	16 (22) μm
strip pitch, Z1-Z5 (Z6)	74.5 (100) μm
nominal resistivity	$\sim 6.7\ k\Omega cm$

Table 7.12: Main parameters of HAMAMATSU microstrip silicon sensors.

Each miniature sensor has one out of six different surface structures for strip isolation. The cross sections of the surface structures, Zone 1- Zone 6 (Z1-Z6), are shown in Fig. 7.44. Z1 has no p-stop structure, Z2 has individual p-stops independently encircling each n-strip and Z3-Z6 have one continuous, common p-stop in between n-strips that are 6 μm wide. The sensors are made with an integrated AC-coupling structure consisting of a sandwich of an insulating layer with aluminum-metal and implant strips. For all the zones except Z5, metal is wider than the n-

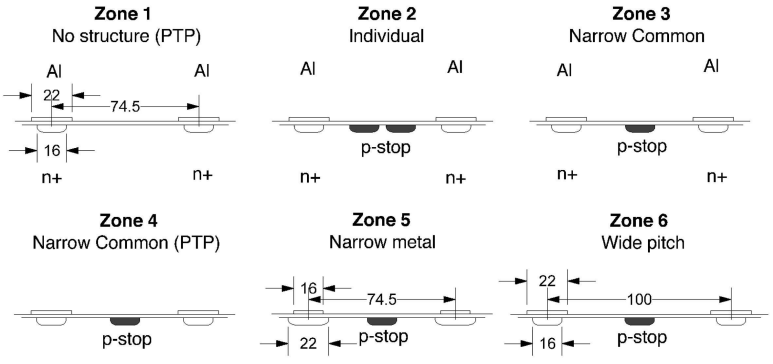

Figure 7.44: Cross-sections of the strip (n^+) and the isolation structures (p-stop) in the surface of the miniature sensors. Six structures, named Zone 1- Zone 6, are implented- One structure per miniature sensor. The dimensions are in μm.

strip implant to reduce the electric field strength at the n-strip implant edge when the potential of the metal and the n-strip implant is the same. The Z4 miniature sensors include a structure for the AC coupling insulator to protect against accidents such as a beam splash into the sensors [132]. The protection structure, already considered at current SCT microstrip sensors (see chapter 8), is called the punch-through protection structure (PTP). The Z6 miniature sensors have a wider pitch (100 μm).

There were several batches trying p-stop and p-stop combined with a p^+ surface-density concentration (p-stop + p-spray). The surface concentrations for the n^+-strip isolation methods are:

- p-Stop Dose = 2×10^{12} $ions/cm^2$
- p-Stop + p-Spray Dose = $2 \times 10^{12} + 2 \times 10^{12}$ $ions/cm^2$

7.7.2 Proton and neutron irradiations

A large number of miniature *ATLAS07* sensors have been irradiated with both protons and neutrons to evaluate the bulk damage produced at the particle fluences expected in the upgrade strip tracker.

Proton irradiation was made with 70 MeV protons at the Cyclotron and Radioisotope Center (CYRIC) of Tohoku University in Japan (see section 6.6.2). The proton fluences were $2.3\times$, $6.0\times$, and 13×10^{14} n_{eq}/cm^2. The fluences are scaled to units of 1 MeV equivalent neutrons per cm^2 taking into account the NIEL correction factor of 1.4 with a fluence uncertainty no more than 10%. The irradiation took typically tens of minutes to a few hours depending on the fluence. The sensors were kept cold at $-7°C$ during irradiation and the irradiated samples were inmediately stored in a refrigerator to prevent any post-irradiation annealing. The samples were irradiated as bare chips with no bias applied.

Neutron irradiation was carried out at the TRIGA nuclear reactor, at the Jozef Stefan Institute in Slovenia (see section 6.6.1) and with energies below approximately 3 MeV. The NIEL cor-

rection factor is 0.88 with the overall fluence uncertainty of 10%. The doses were $2\times$, $5\times$, and 10×10^{14} $1-MeVn_{eq}/cm^2$. The irradiation was made at a rate of 1.9×10^{12} n_{eq}/cm^2s^{-1} with no bias to the sensors. The irradiation to 10^{15} n_{eq}/cm^2 is thus completed in 9 minutes and annealing effects during irradiations can be ignored. The irradiated samples were stored in a refrigerator.

7.8 Characterization of HAMAMATSU sensors

7.8.1 IV/CV measurements

The pre-irradiation characterization consisted of their electrical characteristics: the leakage current and the sensor capacitance as a function of the reverse bias voltage. These measurements were carried out at room temperature in the clean room facility at IFIC. The hamamatsu sensors available for this study are listed in table 7.14.

The leakage currents of sensors with p-stop isolation are plotted in Fig. 7.45(a) as a function of the bias voltage. Some sensors were only measured up to a bias voltage of 600 V how it was stablished at first. In a second performance of the measurements reaching a bias voltage of 1000 V, thoses sensors had been sent to irradiate as they do not show breakdown below 500 V. Only one sensor showed breakdown at a bias voltage of 490 V. Other three sensors showed breakdown at a voltage range between 850 and 950 V. The rest of the sensors did not show breakdown up to 1000 V.

The sensor capacitance is represented by means of $1/C^2$ as a function of the bias voltage in Fig. 7.45(b). From this plot, the full depletion voltage, V_{fd}, can be extracted by the intersection of the two linear functions fitted to two different slopes of the curve (see section 6.1.2). The obtained full depletion voltages are in the range [170-190] V.

Just as example, the effective doping concentration and resistivity of the bulk have been calculated. It has been taken the sensor *W27-BZ6-P12*. The fit of the $1/C^2$ vs. bias voltage gives a $V_{fd} = 183.3\pm1.1$ V and the corresponding values of N_{eff} and ϱ are listed in the table 7.13.

	V_{fd} [V]	N_{eff} [cm^{-3}]	ϱ [k$\Omega\cdot$cm]
n^+-p FZ	183.3 ± 1.1 V	$(2.94\pm0.02)\times10^{12}$	4.4 ± 0.03

Table 7.13: The full depletion voltage extracted from the plots is used to estimate doping concentration and the resistivity of the bulk for a non-irradiated FZ sensor from Hamamatsu (*W27-BZ6-P12*).

In the same way, the leakage currents of sensors with p-stop+p-spray isolation are plotted in Fig. 7.45(c) as a function of the bias voltage. These sensors showed breakdown voltages from 390 V up to 1000 V. The contact between the p-spray layer with the n^+ implant may give rise high electric field regions which may produce earlier breakdowns than without p-spray (compared with figure 7.45(a)). Nevertheless, the p-spray isolation improves with irradiation because the p-spray layer is compensated by the electron inversion layer induced by radiation. In order that, high electric fields regions can be reduced.

The sensor capacitance by means of $1/C^2$ as a function of the bias is shown in Fig. 7.45(d).

ID label	isolation method	Wafer No.	Zone No.	Position No.	V_{BD} [V]	V_{fd} [V]
W23-BZ6-P12	p-Stop	23	6	12	>1000	165
W24-BZ6-P12	p-Stop	24	6	12	850	160
W26-BZ6-P12	p-Stop	26	6	12	850	160
W27-BZ6-P12	p-Stop	27	6	12	950	170
W24-BZ4-P22	p-Stop	24	4	22	>600	
W27-BZ4-P22	p-Stop	27	4	22	>600	
W28-BZ4-P10	p-Stop	28	4	10	>600	
W29-BZ3-P3	p-Stop	29	3	3	>1000	155
W23-BZ3-P6	p-Stop	23	3	6	>600	
W24-BZ3-P3	p-Stop	24	3	3	>1000	155
W24-BZ3-P18	p-Stop	24	3	18	>600	
W26-BZ3-P18	p-Stop	26	3	18	>1000	160
W27-BZ3-P6	p-Stop	27	3	6	>600	
W28-BZ3-P3	p-Stop	28	3	3	490	160
W4-BZ6-P12	p-Stop + p-Spray	4	6	12	550	190
W7-BZ6-P12	p-Stop + p-Spray	7	6	12	390	180
W11-BZ6-P12	p-Stop + p-Spray	11	6	12	630	180
W13-BZ6-P24	p-Stop + p-Spray	13	6	24	700	190
W14-BZ4-P10	p-Stop + p-Spray	14	4	10	530	180
W4-BZ4-P4	p-Stop + p-Spray	4	4	4	>600	
W7-BZ4-P10	p-Stop + p-Spray	7	4	10	390	
W11-BZ4-P10	p-Stop + p-Spray	11	4	10	>600	
W1-BZ3-P15	p-Stop + p-Spray	1	3	15	950	
W4-BZ3-P9	p-Stop + p-Spray	4	3	9	>600	170
W6-BZ3-P9	p-Stop + p-Spray	6	3	9	>600	
W7-BZ3-P9	p-Stop + p-Spray	7	3	9	600	170
W9-BZ3-P6	p-Stop + p-Spray	9	3	6	>600	
W11-BZ3-P1	p-Stop + p-Spray	11	3	1	850	170
W13-BZ3-P9	p-Stop + p-Spray	13	3	9	930	170
W13-BZ3-P15	p-Stop + p-Spray	13	3	15	970	170

Table 7.14: HAMAMATSU microstrip silicon sensors used for these studies. The ID label for every sensor refers to the wafer number, the zone, and the position number in the wafer. The table includes the breakdown and full depletion voltages for the tested sensors prior to irradiation.

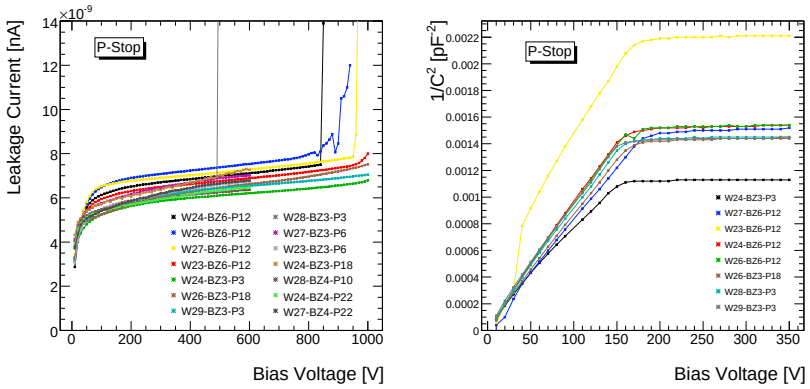

(a) Leakage current-bias voltage (p-stop isolation)

(b) $1/C^2$-bias voltage (p-stop isolation)

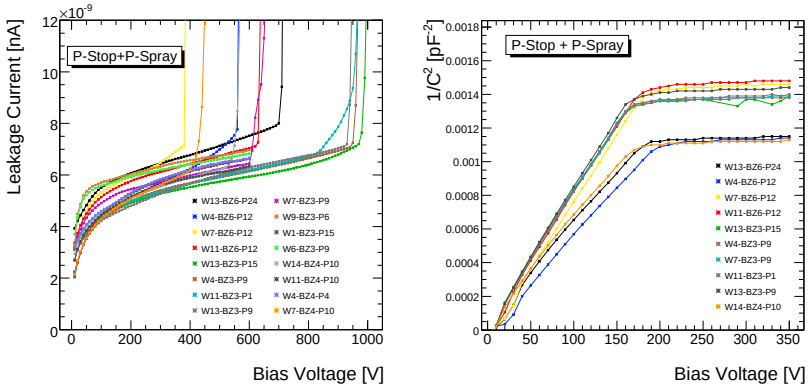

(c) Leakage current-bias voltage (p-stop+p-spray) isolation)

(d) $1/C^2$-bias voltage (p-stop+p-spray)

Figure 7.45: Electrical characteristics: Leakage current (a)-(c) and $1/C^2$ (b)-(d) as a function of the bias voltage for the p-type sensors.

The full depletion voltages extracted from the plot are between 170 and 190 V. As expected, they are similar to those with p-stop isolation.

Finally, in the figure 7.46 is showing the breakdown voltages for the *ATLAS07* sensors. They are plotted in groups for every sensor zone and isolation method. The zone 3 sensors have a common narrow p-stop. The zone 4 sensors have a punch-through protection. And the zone 6 sensors have a wider pitch (100 μm) than the common line (74.5 μm). The technical specifications [133] set a limit for the breakdown voltage of 600 V. This limit corresponds to the maximum operating voltage as the onset voltage for breakdown should exceed the operation bias voltage. The zone 3 shows a good behaviour and with p-spray is acceptable.

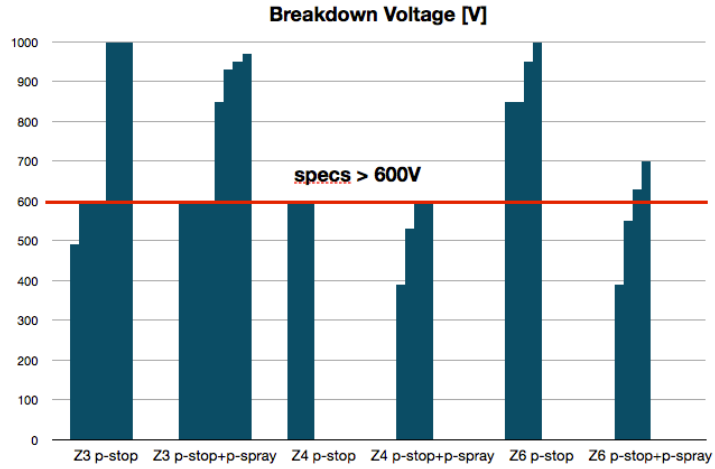

Figure 7.46: Breakdown voltages for the *ATLAS07* sensors. They are shown for every zone (Z3, Z4, and Z6) and every isolation method (p-stop and p-stop+p-spray) of the considered sensors. The technical specification is set at 600 V.

7.8.2 ATLAS07 sensors under irradiation

The *ATLAS07* sensors which were irradiated are listed in table 7.15.

The collected charge as a function of the bias voltage was measured for every sensor after proton irradiation as shown in Figure 7.47 .

The figure 7.48 shows the charge collection measured as a function of the bias voltage for neutron irradiated sensors.

The performance for both set of irradiated p-type sensors is showing a good n^+ isolation and compatible for both kinds of isolation method. Fig. 7.49. The radiation damage apparent from the charge collection seems worse for neutrons than for protons for the fluence scaled by the corresponding NIEL factor. Nevertheless the sensors have a good operation at such high radiation fluences. For instance, at the highest fluence of 1×10^{15} n_{eq}/cm^2 , and 600 V, the collected charge is estimated to be 14000 and 10000 e^- with protons and neutrons respectively. Measurements with similar sensors *ATLAS07* have been carried out in other laboratories with different acquisition systems showing an agreement between the data from different sites. Data compilation is showed in [134].

The evaluation of the *ATLAS07* miniature sensors revealed the presence of microdischarges which was a limiting factor in the sensor performance. The table 7.16 displays the microdischarge onset voltage for every measured sensor. However, the microdischarges could be masked in the offline analysis as explained in the section 7.5.2. This method can be only used while the microdischarges are located in known channels and do not mask the *mip* signal. Measuring with microdischarges can damage the sensor performance and the chip.

ID label	isolation method	Irradiation type	Fluence [$\times 10^{14}$ n_{eq}/cm^2]
W27-BZ6-P12	p-Stop	n	0
W23-BZ6-P12	p-Stop	n	2
W24-BZ6-P12	p-Stop	n	5
W26-BZ6-P12	p-Stop	n	10
W13-BZ6-P24	p-Stop + p-Spray	n	0
W4-BZ6-P12	p-Stop + p-Spray	n	2
W7-BZ6-P12	p-Stop + p-Spray	n	5
W11-BZ6-P12	p-Stop + p-Spray	n	10
W29-BZ3-P3	p-Stop	p	0
W24-BZ4-P22	p-Stop	p	2.3
W27-BZ4-P22	p-Stop	p	6
W28-BZ4-P10	p-Stop	p	13
W13-BZ3-P9	p-Stop + p-Spray	p	0
W1-BZ3-P15	p-Stop + p-Spray	p	2.3
W6-BZ3-P9	p-Stop + p-Spray	p	6
W9-BZ3-P6	p-Stop + p-Spray	p	13

Table 7.15: HAMAMATSU microstrip silicon sensors used for irradiation studies.

ID label	isolation method	Irradiation type	Fluence [$\times 10^{14}$ n_{eq}/cm^2]	$V_{\mu dis}$ [V]
W29-BZ3-P3	p-Stop	p	0	290
W24-BZ4-P22	p-Stop	p	2.3	600
W27-BZ4-P22	p-Stop	p	6	750
W28-BZ4-P10	p-Stop	p	13	450
W13-BZ3-P9	p-Stop + p-Spray	p	0	270
W1-BZ3-P15	p-Stop + p-Spray	p	2.3	600
W6-BZ3-P9	p-Stop + p-Spray	p	6	650
W9-BZ3-P6	p-Stop + p-Spray	p	13	500
W27-BZ6-P12	p-Stop	n	0	270
W23-BZ6-P12	p-Stop	n	2	550
W24-BZ6-P12	p-Stop	n	5	400
W26-BZ6-P12	p-Stop	n	10	400
W13-BZ6-P24	p-Stop + p-Spray	n	0	160
W4-BZ6-P12	p-Stop + p-Spray	n	2	300
W7-BZ6-P12	p-Stop + p-Spray	n	5	400
W11-BZ6-P12	p-Stop + p-Spray	n	10	400

Table 7.16: The microdischarge onset voltage, $V_{\mu dis}$, for every irradiated *ATLAS07* sensor.

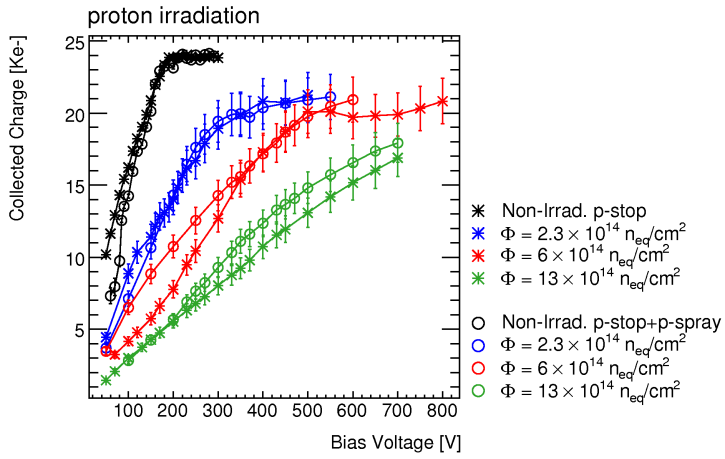

Figure 7.47: Collected charge versus bias voltage for Hamamatsu p-type sensors irradiated with protons. The sensors with p-stop isolation and p-stop+p-spray isolation are compared. Similar non-irradiated sensors were measured as reference.

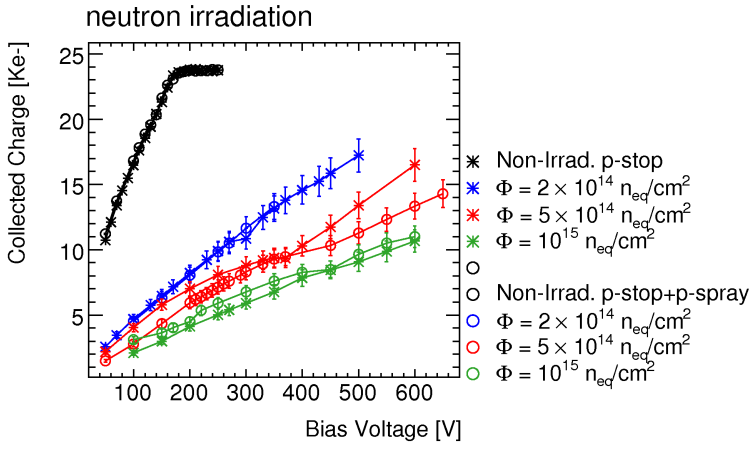

Figure 7.48: Collected charge versus bias voltage for Hamamatsu p-type sensors irradiated with neutrons. The sensors with p-stop isolation and p-stop+p-spray isolation are compared. Similar non-irradiated sensors were measured as reference.

Investigations from *Hamamatsu Photonics* identified several weak spots on the sensors as the potential causes associated with an asymmetric p-stop design [131]. The mask was modified accordingly and improved sensors, *ATLAS07-II* (no tested in this thesis) were subsequently fabricated. A p-stop concentration of 4×10^{12} $ions/cm^2$ showed an onset voltage of microdischarge

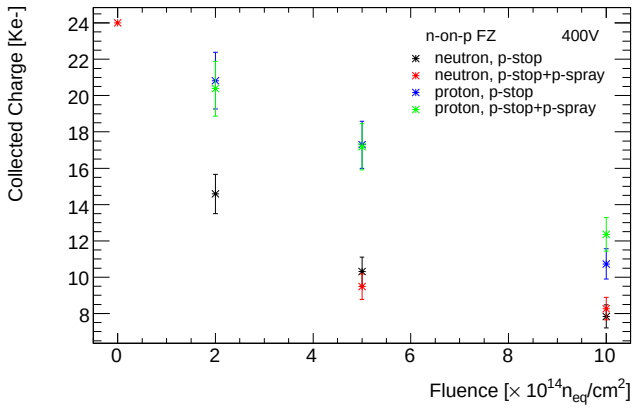

Figure 7.49: Collected charge versus fluence for Hamamatsu p-type sensors irradiated with neutrons and protons. The sensors with p-stop isolation and p-stop+p-spray isolation are compared. The measurements correspond to a bias voltage of 400 V.

increased to over 1000 V [61, 130].

7.8.3 Noise and signal-to-noise ratio

The signal-to-noise (SNR) ratio has been calculated for the *ATLAS07* sensors. Fig. 7.50 shows the SNR for the sensors irradiated at several proton fluences for a bias voltage of 500 V. It has been represented separately the data for the sensors with p-stop isolation (black points) and with p-stop+p-spray isolation (red points). For every sensor, the signal is extracted as the peak of the charge spectrum in units of electrons at the corresponding bias voltage (500 V) from charge collection measurements. The σ is obtained from the peak of the pedestal distribution in units of electrons and they are summarized in table 7.17.

	p-stop sensors	p-stop+p-spray sensors
Fluence $[n_{eq}/cm^2]$	σ $[ke^-]$	σ $[ke^-]$
Non Irradiated	1.24	1.24
2.3×10^{14}	1.26	1.28
6×10^{14}	1.30	1.34
13×10^{14}	1.34	1.42

Table 7.17: Level of noise in electrons corresponding to the Beetle chip (i.e. detector noise, Beetle chip noise and electronics noise) for the *ATLAS07* sensors at 500 V. The ALIBAVA acquisition system has been used.

In the same way, it is calculated the SNR for the sensors irradiated at several neutron fluences for a bias voltage of 500 V shown in Fig. 7.51. It has been represented separately the data for

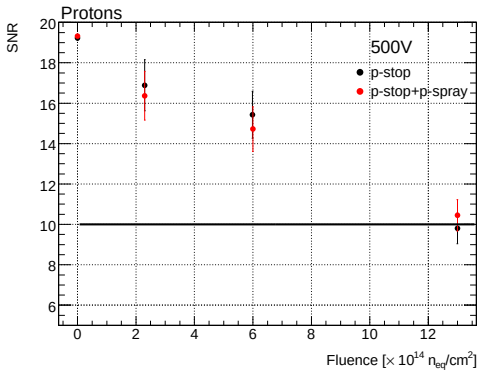

Figure 7.50: Signal-to-noise ration (SNR) for different proton fluences for the *ATLAS07* microstrip sensors. The signal data correspond to sensors with p-stop isolation in black points and with p-stop+p-spray isolation in red points. The sensors were biased at 500V. The technical specifications set a minimum SNR of 10.

the sensors with p-stop isolation (black points) and with p-stop+p-spray isolation (red points). The noise level obtained for every detector at the different neutron fluences are summarized at table 7.18.

	p-stop sensors	p-stop+p-spray sensors
Fluence [n_{eq}/cm^2]	σ [ke^-]	σ [ke^-]
Non Irradiated	1.20	1.30
2×10^{14}	1.31	1.43
5×10^{14}	1.35	1.31
10×10^{14}	1.40	1.56

Table 7.18: Level of noise in electrons corresponding to the Beetle chip (i.e. detector noise, Beetle chip noise and electronics noise) for the *ATLAS07* sensors at 500 V. The ALIBAVA acquisition system has been used.

The specifications set a reasonable signal-to-noise ratio (SNR > 10) to be achieved at maximum rated voltage of 500 V bias. Before irradiation the SNR is estimated to be around 20 with no dependence on the interstrip isolation method. The same occurs for every fluence. At a fluence of 2.3×10^{14} n_{eq}/cm^2 it is estimated a SNR around 17 and at 6×10^{14} n_{eq}/cm^2 it is obtained a SNR of around 15. At the highest fluence (13×10^{14} n_{eq}/cm^2) the SNR is reduced to around the specification limit of 10 at 500 V.

Going to sensors irradiated with neutrons, the more severe neutron radiation damage is clearly exhibited. For the sensors with p-stop isolation, it is estimated a SNR of around 13 for 2×10^{14} n_{eq}/cm^2 and 10 for 5×10^{14} n_{eq}/cm^2. The SNR drops to nearly 7 for 10×10^{14} n_{eq}/cm^2. Before irradiation, the SNR it is stimated to be around 20 at a bias voltage of 500 V.

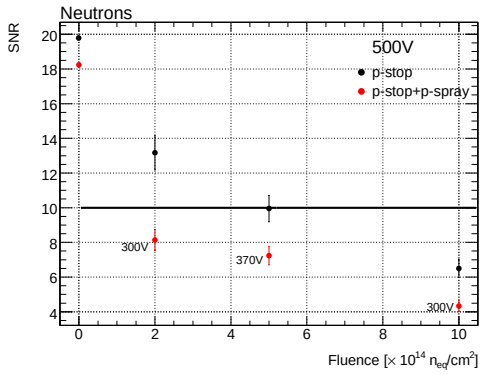

Figure 7.51: Signal-to-Noise ration (SNR) for different neutron fluences for the *ATLAS07* microstrip sensors. The signal data correspond to sensors with p-stop isolation in black points and with p-stop+p-spray isolation in red points. The sensors were biased at 500V. The technical specifications set a minimum SNR of 10. It is noted that for the p-stop+p-spray sensors, the SNR is measured for a different bias voltage (written down beside the measure) not affected by microdischarges.

The p-stop+p-spray sensors are considered apart because they could not be meaured up to 500 V due to microdischarges. The SNR is calculated at a possible bias voltage at which the microdischarges can be masked without affecting the signal and noise measurements. In the figure 7.51 is written down the bias voltage beside the obtained SNR. For a fluence of 2×10^{14} n_{eq}/cm^2, the SNR results around 8 at 300 V whereas a SNR of around 7 is obtained with a fluence of 5×10^{14} n_{eq}/cm^2 at 370 V. Finally, at the highest fluence (10×10^{14} n_{eq}/cm^2), the SNR is estimated to be by 4 at 300 V. Before irradiation, it is obtained a SNR of 18 at 150 V.

7.9 CNM and Hamamatsu sensors under neutron irradiation

In this section, microstrip silicon sensors from two different suppliers (CNM and Hamamatsu) have been characterized before and after irradiation. In particular, they both have been irradiated with neutrons at the expected fluences under HL-LHC conditions. Then they were characterized in terms of their charge collection performance. In Fig. 7.52, the charge collection curves of the CNM detectors are observed to nicely straddle the Hamamatsu detectors curves, clearly indicating a consistency in the charge collection behaviour of strip detectors from different manufacturers.

Both p-type sensors (CNM and Hamamatsu) have shown sufficient charge collection for use in those conditions. The n^+p FZ is set as the baseline technology choice for the ATLAS upgrade. It is shown a better charge collection with FZ silicon than with DOFZ and MCz silicon at the highest fluence ($\sim10^{15}$ n_{eq}/cm^2) expected in the inner part of the strip region (short strip region). Therefore, the collected charge is required to be larger than 6000 electrons at 10^{15} n_{eq}/cm^2 (expected noise at this fluence 600 electrons) at 500 V bias in order to get a minimum SNR

= 10. For instance, the collected charge is about 9700 electrons for the *ATLAS07* FZ sensor and about 8000 electrons for the CNM MCz sensor that is adequate.

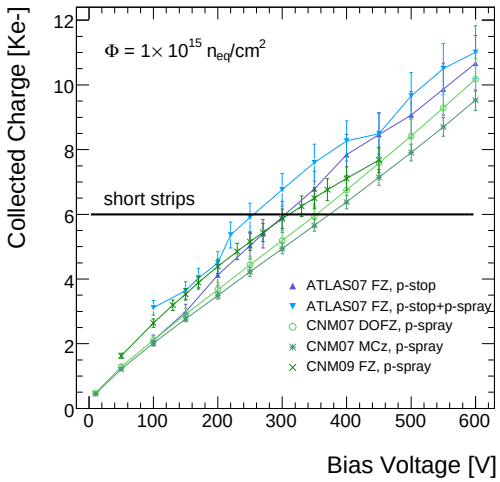

Figure 7.52: Collected charge as a function of the bias voltage for p-type silicon detectors. *ATLAS07* sensors from Hamamatsu (in blue) and CNM sensors (in green) are compared. The short strip limit (6000 electrons at 500 V) is marked as reference.

Chapter 8

High ionisation studies

Apart from the studies on radiation damage in microstrip silicon detectors, it will be studied the possible damage from the effects of a large instantaneous ionization in microstrip silicon detectors. In this case, there have been considered n-type silicon sensors instead p-type ones. It corresponds to the current detector technology for the ATLAS SCT. The final objective is to apply the results to a possible beam loss scenario, impacting directly on the detectors for the current operating conditions at LHC.

8.1 Introduction

As already explained in chapter 2, in the LHC, 2808 counter-rotating bunches of $\approx 10^{11}$ protons per bunch will collide at a frequency of 40 MHz. The products of the collisions will be registered by the experiments situated sorrounding the four collision points. The ATLAS experiment is located at the so-called Point 1 (IR1) of the accelerator. The ATLAS Inner Detector (ID), whose function is to track charged particles coming from the beam interaction point is located the closest to this interaction point.

As the central beam can deviate from its trajectory, stray protons can continually impact the beam containment structure, or in the worst case directly the detectors and its electronics. Multiple beam loss scenarios could occur:

- Single-turn losses: likely to occur during injection or beam dump processes. IR1 (ATLAS) can be considered safe in this sense because it is situated far away from injection and dump. In addition, the experiments are in safe mode operation during these LHC phases.
- Multi-turn losses: because of beam degradation (equipment failure, wrong magnet settings,...).

Considering multi-turn losses, beam failures leading to serious detector damage are related to the scrapping or the hit on collimators, beam apertures, vacuum valves and the beampipe it-

Table 8.1: Doping concentrations for the simulated sensor

	Doping concetration (cm^{-3})
p^+ implant	3×10^{17}
n substrate	1×10^{12}
n^+ backplane	1×10^{19}

self, resulting in uncontrolled *beam splash* events. The ID could be damaged from secondary radiation showers as it is located close to the beam line.

These simulations are focused on the microstrip silicon detectors of the ID subsystem, the Semiconductor Tracker (SCT). The SCT as explained in the chapter 2 consists of 4 barrel layers at radius of $30-51$ cm from the beam axis and 9 discs in each of the two end caps at each side of the barrel, with every layer able to read out a position in two dimensions. The modules mounted on barrels and endcaps are built on four single-sided sensors. The silicon sensors [128, 135] are glued back to back around a high thermal conductivity substrate. They are p^+ strips on a n-type bulk, AC coupled and biased through polysilicon resistors [136].

The strip detectors are designed to be robust and durable to the long term effects of the radi in which they will operate [137]. However, it is not clear their behaviour in the extreme cases in which an intensive number of charged particles cross the sensor in a very short time, that is, a beam loss scenario. No integral radiation effects are expected other than electrical stresses on the bulk and their effect in the oxide of the AC coupled devices.

8.2 High ionisation simulations

In order to study if the ATLAS SCT detector can survive LHC beam losses, a basic unit of a microstrip detector was simulated and its response inspected when exposed to comparable beam intensities. The simulation of a silicon sensor has been carried out using a SCT sensor based model implemented in the *Synopsys* ISE-TCAD software [96]. The behaviour of a semiconductor sensor is described by a series of differential equations, such as the Poisson and carrier continuity equations. In this package, a "mesh" of discrete elements is defined to approximate the structure of the device. The differential equations are applied to each element in the mesh, resulting in a system of equations that will be solved numerically to determine the device's behaviour.

The simulated structure corresponds to a two dimensional simple diode (equivalent to one strip). All parameters have been established from the requirements for the SCT silicon microstrip sensors [128] and annotated in Table 8.1. It consists of a 1 μm deep, 60 μm wide p^+ implant on a 285 μm thick and 100 μm wide n substrate. It is AC-coupled by means of a 0.5 μm thick SiO_2 layer between the strip implant and the metallised (Al) strip contact as in Figure 8.1. The effect of charge build up at the Si/SiO_2 interface in a sensor is taken into account by defining a low charge oxide concentration ($4\times10^{11}\ cm^{-2}$) into it.

The device is biased via a metallised n^+ implant on the rear of the device and the strip implant is grounded by a resistor of 1.4 $M\Omega$ representing the bias polysilicon resistor in the silicon sen-

sor [138]. Finally, the strip contact is connected to an approximation of the chip input impedance of 100 Ω [139].

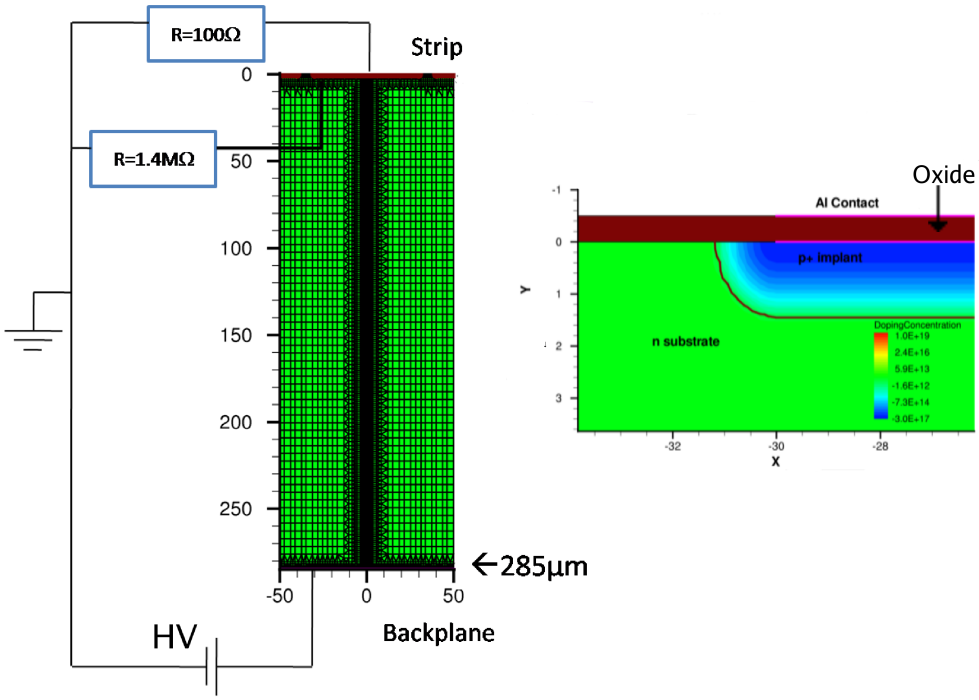

Figure 8.1: Simulated sensor schematics with electrical setup together with a zoom of the p-n junction (right figure). The sensor shows the mesh considered for the simulation, denser in the central part where the ionization is produced.

In a scenario where a large number of charged particles are crossing simultaneously the sensor, a copious number of free carriers will be created and then drifted towards the electrodes: backplane and p^+ implant. **The electric field accross the detector will be temporarily modified due to the high concentration of free carriers and will evolve as the carriers drift.**

The aim of the simulation is to investigate if the voltage at the p^+ implant is modified temporarily as a consequence of the electric field variation and therefore the voltage across the oxide layer. Several charge densities are created along a central and uniform 285 μm-long track through the full thickness of the substrate. They are carried out at 500 V bias[1] and let evolve during 15 ns. From these simulations, the device mesh is altered to create a region of high mesh density around the starting position of the charge cloud, to ensure the total charge deposited is calculated accurately. The simulation then calculates the resulting potential in all parts of the device.

[1]Before irradiation the SCT is biased at 150 V for operation. 500 V is the maximum bias when the sensors are irradiated as a higher bias is needed to reach full depletion. It is studied the worst case scenario.

Firstly, considering a charge density of 1 $pC/\mu m$, the voltages reached at the implant and at the *Al* strip contacts as a function of time are shown in Fig. 8.2(a) This charge density corresponds to 74000 *mips* per strip. With such charge density, the implant voltage saturates to 500 V very fast at approximately 0.3 ns as shown in the Fig. 8.2(b). At the *Al* contact, a small voltage pulse is induced over the coupling capacitance, which is read out by the front-end electronic. The highest voltage reached at the *Al* strip contact is about 3.1 V as shown in Fig. 8.2(c). It is far below the voltage reached at the p^+ implant. So, these electrostatic simulations show that the potential across the oxide will be basically the voltage reached in the implant.

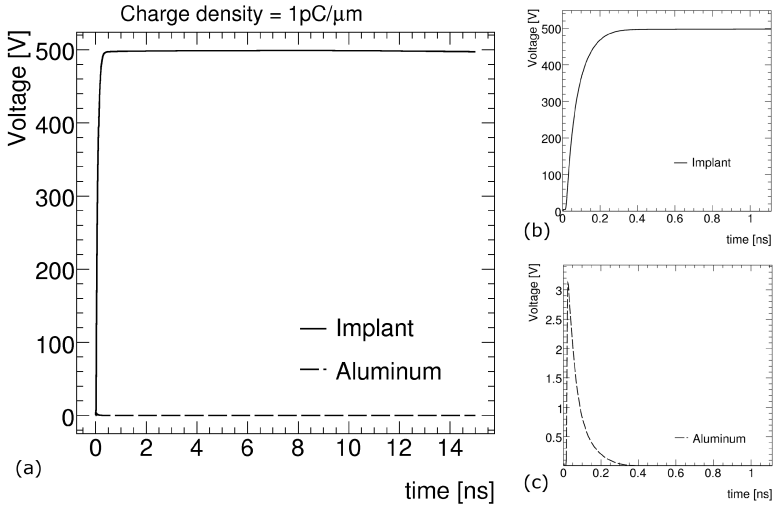

Figure 8.2: Voltage reached at the implant and the aluminum contacts as a function of the simulation time with 74000 *mips* per strip (a). A zoom of the voltage within 1 ns at the implant (b) and the aluminum (c) contacts. Bias voltage = 500 V, saturation.

Simulations with lower charge densities are carried out in order to check non-saturated cases. As an example, it is shown the voltage reached at the p^+ implant (Fig. 8.3(a)) and the *Al* strip contact for a charge density of 0.2 $pC/\mu m$ (Fig. 8.3(b)). This charge density corresponds to 15000 *mips* per strip. The highest voltage in the implant is 441 V at 2.3 ns and then it decreases slowly as the charge carriers are collected. For the *Al* strip contact it is found the highest peak voltage at about 1.4 V. The voltage at the *Al* strip is consequence of the induced charge due to the movement of the free carriers along the bulk. Obviously, the same voltage is also induced on the p^+ implant. However, the arrival of a huge quantity of free charge carriers modifies the voltage at the p^+ implant, because there is an accumulation effect. The time constant of the charge draining out of the p^+ implant is dominated by the bulk capacitance and the polysilicon resistor.

As a last example it is interesting to show the electrostatic potential across the sensor bulk (see Fig. 8.4). It has been done for a charge density of 0.01 $pC/\mu m$. This charge density corresponds to 740 *mips* per strip. The high ionisation modifies the electric potential in the sensor as the charge carriers are swept towards the electrodes and the potential recovers the linearity as the

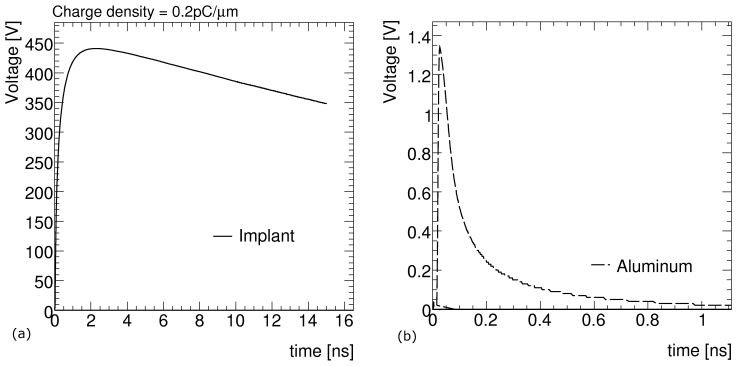

Figure 8.3: Voltage reached at the implant (a) and the aluminum (b) contacts as function of simulation time with 15000 *mips* per strip. Bias voltage = 500 *V*, no saturation is reached.

Table 8.2: *mips* vs. Implant Voltage

Charge Density ($pC/\mu m$)	# *mips* (per strip)	Max. Implant Voltage(V)
8×10^{-4}	60	27.4
0.01	740	125.3
0.015	1110	158.5
0.02	1500	185.0
0.1	7400	367.7
0.2	15 000	441.0
1	74 000	498.5
2	148 000	499.1
10	740 000	499.7
850	63*M*	500.0

charge carriers are drained. Every line refers to a different time. The solid black line corresponds to the case with no charge density and the dashed line for a time of 25 *ns*.

The reached p^+ implant voltages for all the simulated charge densities and their correspondence in number of *mips* are shown in the Table 8.2. Above 10^5 *mips* in one strip, the voltage at the implant reachs full HV (500V) and above 10^3 *mips* per strip there is more than 160 *V* across the oxide.

In real detectors, if HV(500 *V*) is reached across the oxide, the 768 strips per side resistences that act as a resistance of 1100 Ω/module would let flow a current of approximately 0.5 *A*. It is obvious that the power supply system cannot provide the currents which are requested and the current limit will stop powering the sensors.

If a potential difference across the oxide is higher than 160 *V*, the oxide will breakdown according to ref. [140]. So, **from simulations, it is concluded that there is a risk to break**

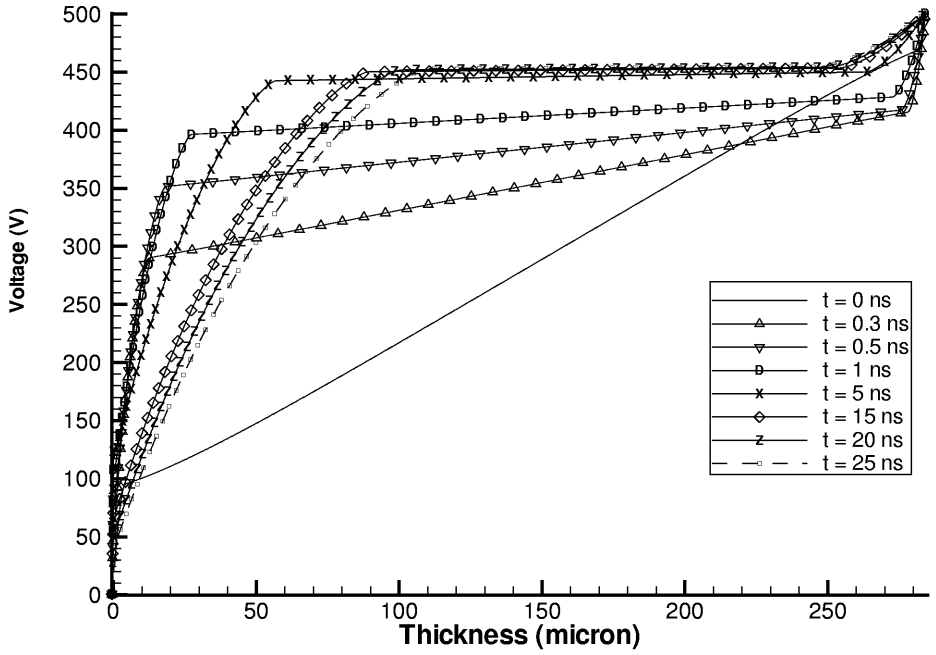

Figure 8.4: Voltage distribution across the sensor thickness with a charge density of $0.01 pC/\mu m$ (740 *mips* per strip).

the oxide in a possible beam loss incident with an operational bias voltage of 500 V. In real detectors, apart from a non-operational sensor, this would cause a fatal charge deposition on the electronic readout which is even more sensitive [141]. However, the sensors were designed to take this issue into account. There is a punch-through protection structure [142] for the coupling dielectric in order to prevent any damage. This punch-through fuse acts as a variable resistance depending on the voltage applied between its terminals.

8.3 Punch-through fuse performance

In order to verify the behaviour of the punch-through fuse, several SCT sensors (6×6 cm^2) have been tested at the IFIC-Valencia clean room [143]. The sensors are spare samples from the SCT production. Two or three random strips have been tested in every sensor. The testing procedure has been the following: Firstly, the proper state of the strips is verified by means of the measurements of the RC bias components. And secondly, the behaviour of the fuse is studied. The setup configuration is shown in Fig. 8.5. The sensor is biased at 500 V for full depletion operation (*K237* voltage source). A separated voltage source (*K2410*) is applied between the strip implant (DC contact) and the *Al* (AC contact) for the strip. Then, the resulting current of the *K2410* is measured as a function of its voltage. The measurement of the RC ($R_{polysilicon}$, $C_{coupling}$) bias components is done also after the test in order to check the integrity of the oxide. It is expected that during normal operation, the current flows through the polysilicon resistor. When the fuse is activated as the voltage increases, the current will be diverted through the fuse resistor (its resistance is smaller than the polysilicon resistance). In the worst case, the oxide could break and the current would flow through the oxide increasing considerably the current at the *K2410* source.

The strip current is shown as a function of the voltage applied across the oxide up to 50 V (Fig. 8.6(a)). At low voltages, an ohmic behaviour is observed whose slope corresponds to the bias polysilicon resistor (this region is observed in Fig. 8.6(b) that is a zoom from the corresponding figure on the left).

Differential resistance, dV/dI, is calculated from the I-V curves as shown in Fig 8.7. A similar shape is visible for all 4 sensors. Table 8.3 shows some relevant results for the sensors:

1. The RC bias components after the test in order to check the integrity of the oxide. All the measured strips give the expected values [138].

2. The value of the resistance in the ohmic region. It comes from the linear fit in Fig 8.7. All the fit results are in agreement with the value of the polysilicon bias resistor to be around 1.4 $M\Omega$ [138].

3. The voltage at which finishes the ohmic region that lies between $13 - 16$ V and are in agreement with previous measurements [140].

The conclusion is that the punch-through fuse is working properly for the SCT sensors. The resistance of the fuse lowers dramatically to ~ 5 $K\Omega$. Thus, in the case of high ionisation, it will help to discharge the p^+ implant when its voltage is above ~ 16 V. Hence, it will protect as well the coupling capacitor because it will reduce the voltage across.

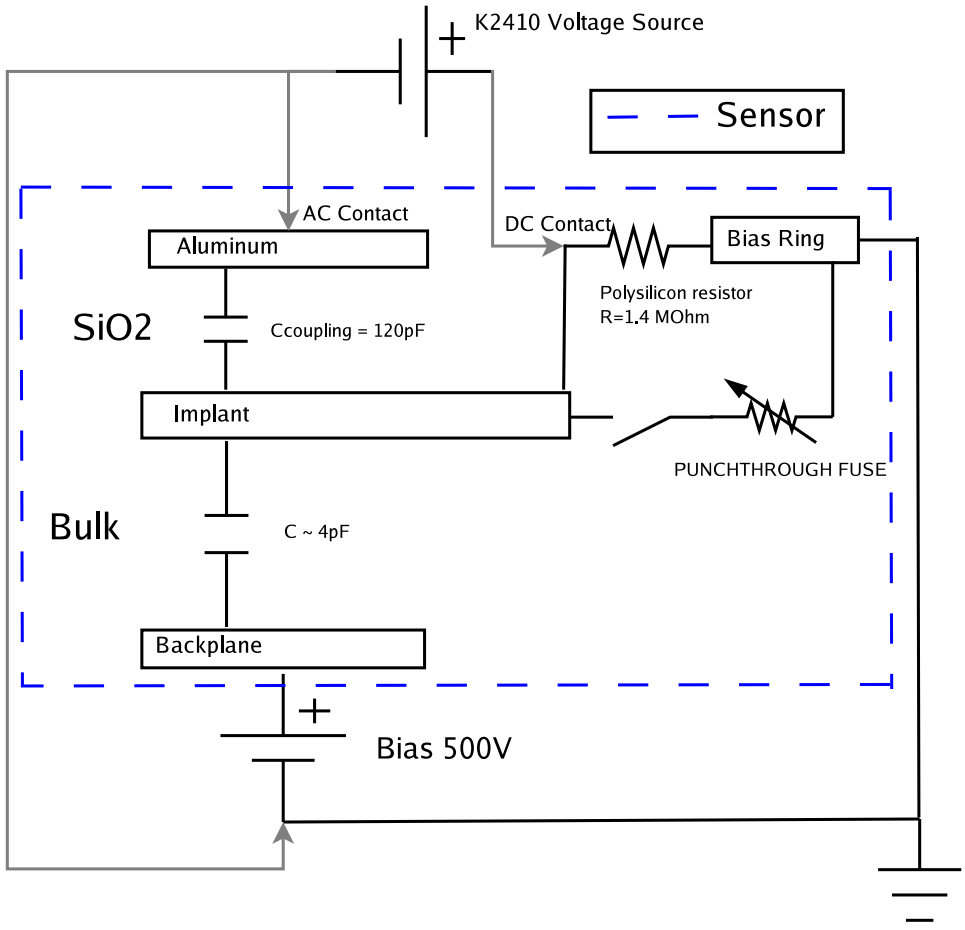

Figure 8.5: Configuration Scheme for sensor measurements in order to test the punch-through fuse performance.

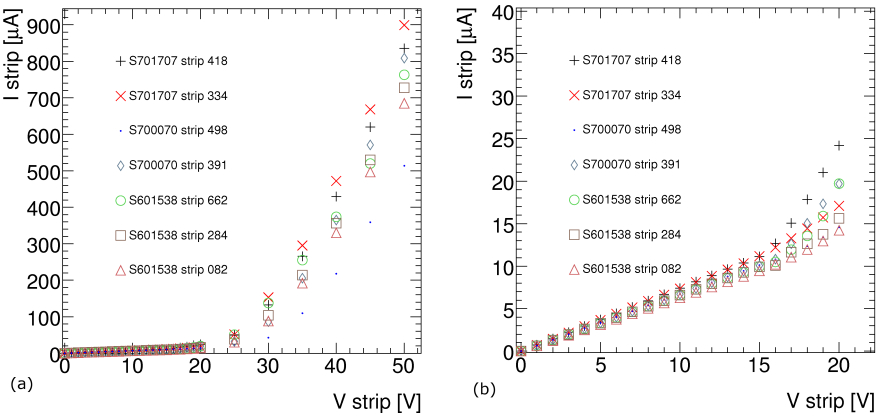

Figure 8.6: Total strip current vs. strip potential (a) and a zoom of the voltage within 25 *V* on the ohmic region (b). Measurements performed on different sensors and on various strips per sensor.

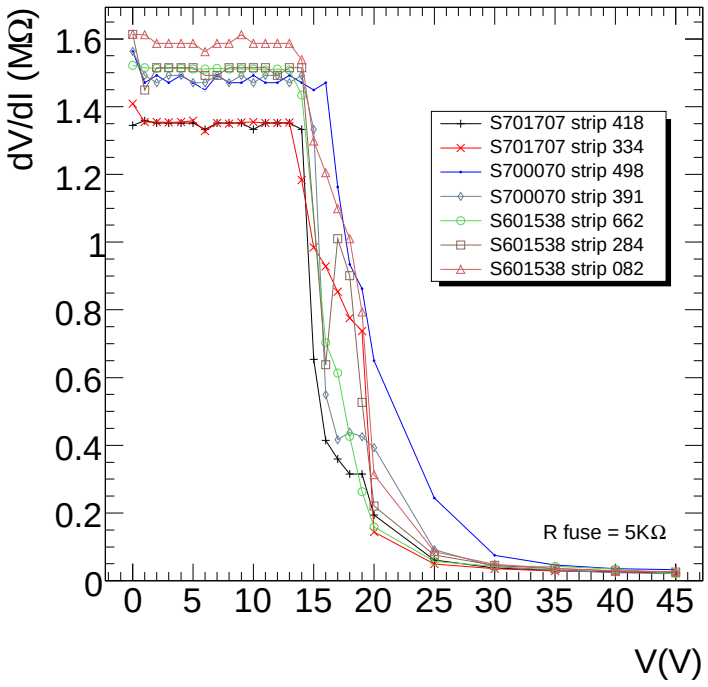

Figure 8.7: Dynamic resistance vs. strip potential. Measurements performed on different sensors and on various strips per sensor.

Table 8.3: SCT sensor parameters after the oxide test

		RC components	Rfit ($M\Omega$)	kink voltage (V)
Sensor number:	S701707			
# strip	418	R=1.29$M\Omega$ C=129pF	1.35 ± 0.30	14
	334	R=1.25$M\Omega$ C=128pF	1.35 ± 0.30	13
Sensor number:	S700070			
# strip	498	R=1.36$M\Omega$ C=120pF	1.48 ± 0.30	14
	391	R=1.34$M\Omega$ C=124pF	1.48 ± 0.30	16
Sensor number:	S601538			
# strip	662	R=1.40$M\Omega$ C=129pF	1.59 ± 0.30	14
	284	R=1.40$M\Omega$ C=137pF	1.51 ± 0.30	14
	82	R=1.49$M\Omega$ C=130pF	1.51 ± 0.30	14

Fig. 8.8 shows the I-V curves obtained for one strip of the sensor labelled 701484. In this case, the strip current is taken increasing the voltage from 0 V up to 60 V. After this, the current measurements are repeated decreasing the voltage from 60 V to 0 V. A lower fuse onset voltage is observed when the measurements are taken decreasing the voltage (8 V) than when the applied voltage is increasing (13 V). This is most likely due to temperature effects [49].

One sensor labelled 700043 was tested for higher voltages. Only, it was possible up to 170 V due to the voltage source limitations. In Fig. 8.9 it is shown the current for three strips as a function of the voltage applied across the oxide at 500 V bias voltage. For this case, at every voltage, the test was stopped to verify the bias resistor and coupling capacitance components and check the oxide.

In Fig. 8.9, after the linear part of the graph, the fuse is activated and then, the current is diverted. Under 160 V the oxide looks well but for larger voltages, the RC measurements give different values compares to those shown in Table 8.4 suggesting some kind of break. However, these tests were repeated on the same strips some days later and it was proved that the strips recovered their expected values. So that, the oxide did not break at least up to a voltage of 160 V.

From these measurements, it is demostrated that the fuse activates when the p^+ implant reaches the range of $13 - 16$ V. This will protect the oxide of higher electric fields up to 160 V supporting ref. [140]. Nevertheless, it could not be proven the oxide breakdown at higher bias voltages although some troubling effects started to appear at 160 V.

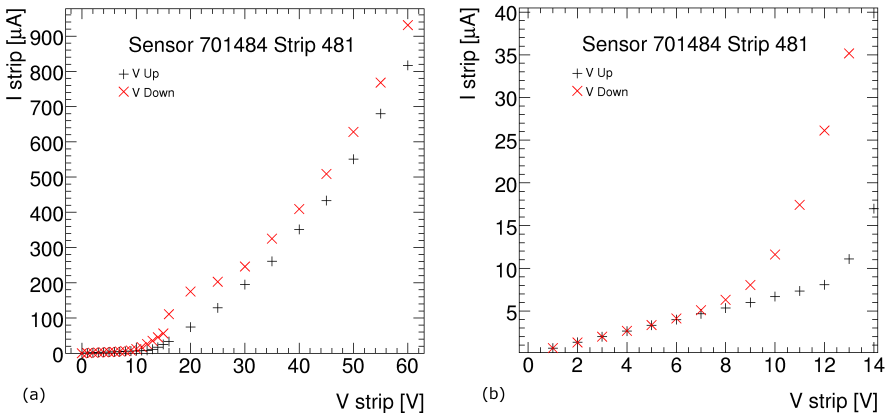

Figure 8.8: Total strip current vs.strip potential for only a strip, increasing the voltage across the oxide up to 60 *V* in black and repeating the test decreasing the voltage from 60 *V* to 0 *V* in red (a) and a zoom within 14 *V* on the ohmic region (b).

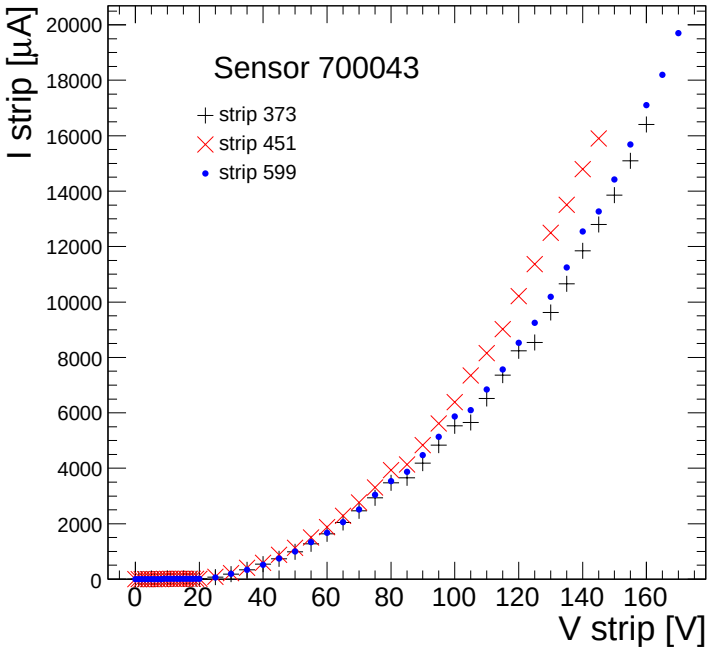

Figure 8.9: Total strip current vs.strip potential for 3 strips of the sensor S700043 up to a voltage of 170 *V*.

Table 8.4: Oxide test: RC Components. Sensor number:700043

Strip:	373	451	599
Init	R=1.39$M\Omega$ C=121.4pF	R=1.42$M\Omega$ C=120.4pF	R=1.43$M\Omega$ C=121.1pF
80 V	R=1.48$M\Omega$ C=125.7pF	- -	R=1.43$M\Omega$ C=124pF
100 V	R=1.42$M\Omega$ C=122.9pF	- -	R=1.47$M\Omega$ C=122.2pF
120 V	R=1.42$M\Omega$ C=124.6pF	- -	R=1.44$M\Omega$ C=122pF
140 V	R=1.43$M\Omega$ C=121.5pF	- -	R=1.44$M\Omega$ C=123.3pF
160 V	R=688.2$K\Omega$ C=135.4pF	R=784.7$K\Omega$ C=133.3pF	R=672.4$K\Omega$ C=136.44pF
After a couple of days:			
	R=1.44$M\Omega$ C=118.2pF	R=1.39$M\Omega$ C=120.5pF	R=1.42$M\Omega$ C=121.0pF

8.4 Punch-through fuse simulations

In high ionisation scenarios, the fuse will help to drain carriers from the p^+ implant, reducing the accumulation of charge and its voltage. The simulations showed in the first part of this chapter were done for a resistance of 1.4 $M\Omega$. It was observed that above 10^3 *mips* per strip, the voltage at the implant reached 160 V. The measurements with real sensors showed no oxide breakdown at least up to approximately 170 V. At this point the question to answer is: which is the dose at which the implant voltage will reach more than 160 – 170 V with the fuse activated. This test was done with ISE-TCAD simulations as explained in section 8.2.

In the Current-Voltage Figure 8.7, the fuse region is fitted to extract the resistance of the fuse. It is obtained to be about 5 $K\Omega$. This value is used for the simulations in order to study its effect on the detector. Despite that in a real detector, the fuse resistor is in parallel to the polysilicon resistor, in our simulation, and for practical purposes, the bias resistor is replaced by the fuse resistor. Then several charge densities are simulated on a device in the same way that in the previous simulations (section 8.2).

Table 8.5 shows the maximum implant voltage comparing both simulations (with the polysilicon and the fuse resistor) for the simulated doses. In Fig. 8.10, the voltages reached at the implant are shown as a function of time for different numbers of *mips* hitting the simulated device. The potential difference across the oxide is basically determined by the voltage at the implant. As the number of *mips* crossing the sensor increases, the implant gets a higher voltage. Nevertheless, the implant voltages are lower than with the polysilicon resistor for the same dose. With the highest charge density, no saturation is visible but more than 25 *ns* are necessary to drain all the charge. It is not possible to simulate an oxide breakdown, but taking into account the results with real sensors (previous section and [140]), it is possible to stablish a limit for the

Table 8.5: Maximum Implant Voltage with the polysilicon resistor and the fuse resistor for different charge densities. Bias voltage = 500 V.

Charge Density($pC/\mu m$)	# *mips* (per strip)	Max. Implant Voltage (V) R_{bias}=1.4 $M\Omega$	Max. Implant Voltage (V) R_{fuse}=5 $K\Omega$
8×10^{-4}	60	27.4	3.5
0.01	740	125.3	5.7
0.1	7400	367.7	35
0.2	15 000	441.0	54
1	74 000	498.5	121
2	148 000	499.1	159
3	222 000	499.5	179
5	370 000	499.5	207
7	520 000	499.7	226
10	740 000	499.7	244
20	1.5M	500.0	274
100	7.4M	500.0	354
850	63M	500.0	437
1000	74M	500.0	442

oxide breakdown at 160 V. So, the punch-through fuse avoids the charge accumulation at the implant untill a dose above 150 000 *mips* per strip that is when the p^+ implant reaches a voltage of $\sim$160 V.

8.5 High ionisation at lower voltage operation

In previous sections, a high voltage operation of 500 V has been considered. In that case, the simulations show the dose at which the implant voltage exceeds 160 V, the voltage at which the oxide break could occur. It has been shown that with a high voltage of 150 V the oxide will not break yet. However, the sensor behaviour at low voltage operation has been drawn from simulations. Fig 8.11 shows the configuration scheme considering a resistence of 100 Ω as approximation of the chip impedance and a resistance of 5 $K\Omega$ for the punch-through fuse. As the voltage at the p^+ implant reach 16 – 20 V, the fuse is activated and a resistance of 5 $K\Omega$ is used.

This configuration has been simulated and Fig. 8.12 shows the voltage reached at the implant as function of the time with a bias of 50 V and the fuse activated. In the same way, Fig. 8.13 is reporting the voltage reached at the implant as function of the time with a bias of 150 V and the fuse activated. Three different doses has been simulated as 74 000 *mips*, 7.4 M *mips*, and 74 M *mips* per strip. For the highest dose the saturation is observed even within a simulation time of 25 ns. In general, it is observed a similar behaviour if compared with the device biased at 500 V.

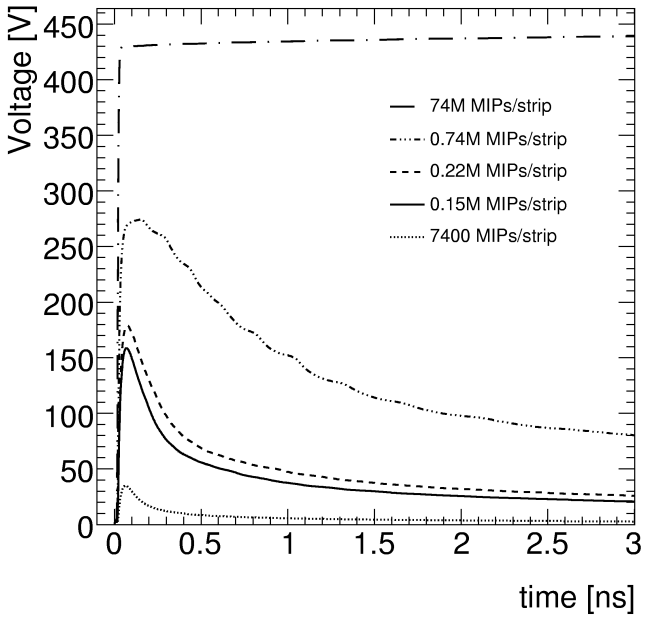

Figure 8.10: Voltage reached at the p^+ implant as a function of time for different number of mips per strip. An approximation of the fuse resitance(R=5 $K\Omega$) has been used for the simulations.

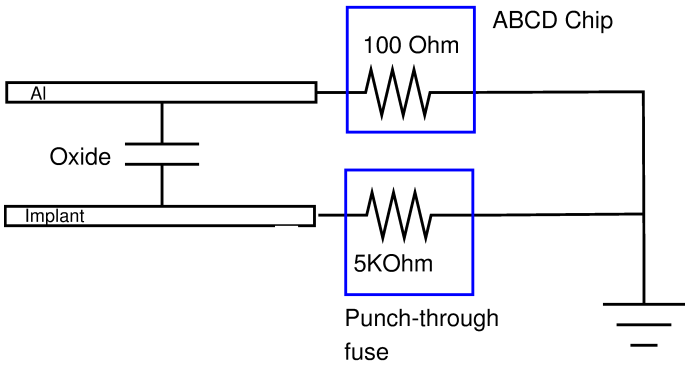

Figure 8.11: Resistor configuration for a strip. 100 Ω as approximation of the chip input impendance and a resistence of 5 $K\Omega$ for the punch-through protection.

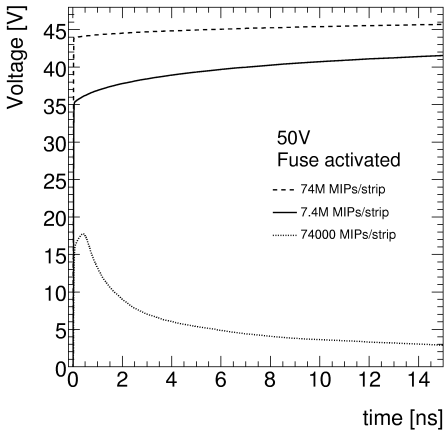

Figure 8.12: Voltage reached at the p^+ implant as function of time of different number of *mips* per strip. Bias = 50 V and an approximation of the fuse resistance = 5 $K\Omega$.

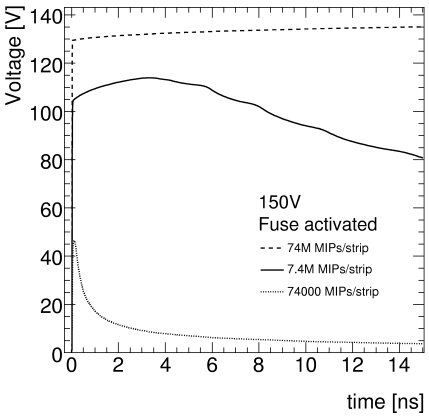

Figure 8.13: Voltage reached at the p^+ implant as function of time of different number of *mips* per strip. Bias = 150 V and an approximation of the fuse resistance = 5 $K\Omega$.

8.6 High ionisation on a broken oxide strip

If an oxide break is considered, this does not inmediately suppose a non-operational channel or module. Actually, in the current SCT detector there are a few channels ($\leq$ 1%) with broken oxides. Nevertheless, it is important to know how the channel behaves and its effects on the electronics in case of high ionisation at low voltage operation (50, 150 V). In this case, the configuration scheme shown in Fig.8.14 considers there is no dielectric between the p^+ implant and the Al contact. A those low voltages, the fuse is not activated and a resistance of 1.4 $M\Omega$ is used. The voltage at the implant is directly read from the Al contact.

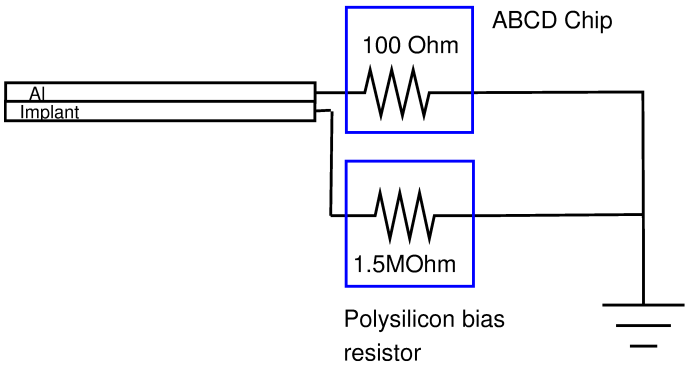

Figure 8.14: Resistor configuration for a strip without oxide. 100 Ω as approximation of the chip impendance and a resistence of 1.4 $M\Omega$ for the polysilicon bias resistor.

This configuration has been simulated and Fig. 8.15 and 8.16 show the voltage reached at the p^+ implant as function of the time for three different doses at which no saturation occurs. Fig.8.15 is done for 50 V and Fig. 8.16 for 150 V. The maximum voltage that reaches the implant is not as high as with oxide as the current flows through the low chip input impedance. It has been considered as approximation of the chip input impedance 100 Ω that is the minimum for the chip dynamic resistance. One must add that according to literature [141] the experiments and tests performed on the chips show that these voltages are safe for the chips.

8.7 Conclusions

With this work, it has been studied the effects of very high instantaneous ionisation in a silicon microstrip detector. For this purpose, one strip wide region has been simulated and exposed to high beam intensities. It has been demonstrated that the electric field in the detector bulk and the voltage are modified under an intensive charge density. This modification supposes a high charge accumulation at the p^+ implant and therefore a considerable risk to break the oxide. However, the SCT sensors have a punch-through protection fuse for the coupling dielectric. For a better understanding of this structure, several real SCT spare sensors were tested. These tests showed a properly working of the protection fuse which switched on about 14 – 16 V. The fuse permits

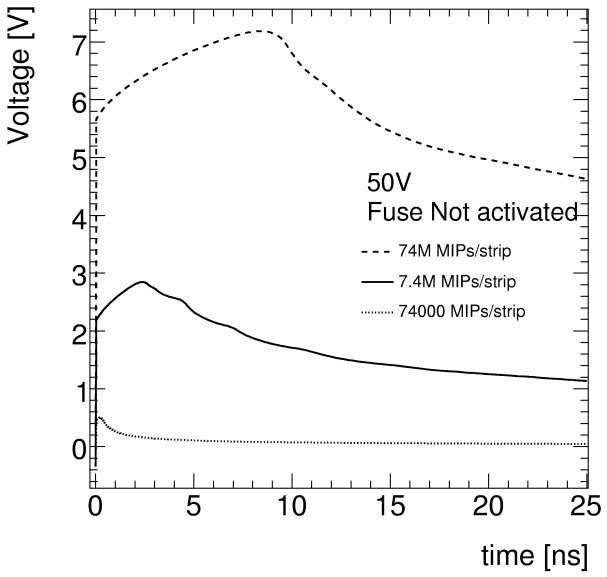

Figure 8.15: Voltage reached at the p^+ implant as function of time of different number of *mips* per strip. Bias = 50 V and the polysilicon bias resistor = 1.4 $M\Omega$.

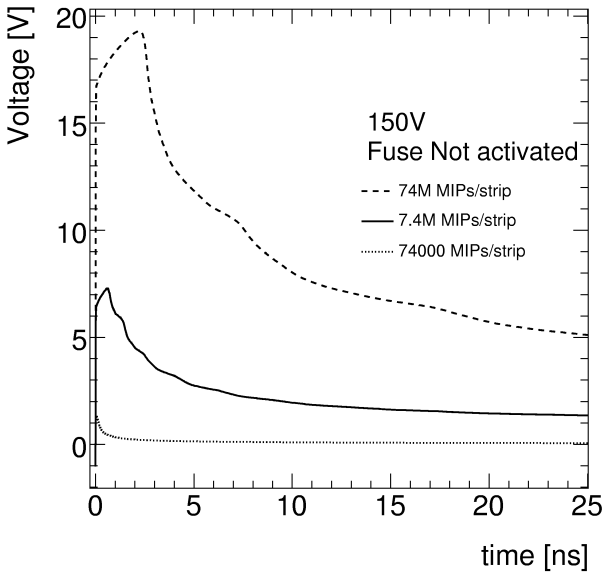

Figure 8.16: Voltage reached at the p^+ implant as function of time of different number of *mips* per strip. Bias = 150 V and the polysilicon bias resistor = 1.5 $M\Omega$.

a faster discharging of the sensor. Simulations taking into account this structure permitted to establish the limits not to break the oxide with a dose above 150 000 *mips* per strip. In addition, the sensor behaviour at low voltage operation also has been reported and compared with high voltage operation. The simulations show that with 50 *V* and 150 *V*, a similar behaviour under high ionisation is observed.

Apart from this, an oxide break does not suppose a non-operational sensor. The detector continues working. Actually, in the current SCT detector there are a few channels ($\leq$ 1%) with broken oxides. The fundamental problem is in the effects on a detector affected by a considerable number of broken oxides and on its electronics since that the chips are the most sensitive components to high ionisation [141]. On the basis of this, an oxide break on a strip were simulated at 50 and 150 *V*. When the oxide is broken, the *Al* strip and the p^+ implant strip are shorted and the current flows through the chip input impedance. High charge accumulation is not observed at the implant and the reached voltages look safe for the module operation [141].

Chapter 9

Conclusions

This thesis is framed in the ATLAS experiment at CERN LHC accelerator. Specifically, for phase II of the accelerator upgrade operation. It has been studied the physics potential of an increase of almost an order of magnitude in luminosity from the current instantaneous value of $10^{34} cm^{-2} s^{-1}$ to a value of $5 \times 10^{34} cm^{-2} s^{-1}$. This project is known as HL-LHC (High Luminosity LHC). Operation in such conditions involves pile-up processes due to increased interaction rate, from the order of 20 collisions to 200 collisions per beam crossing. Furthermore, it is also assumed very high radiation doses reaching particle fluences of 10^{16} $n_{eq} cm^{-2}$ on the closest detectors to the particle collision point. Current technology presented in the LHC experiments could not stand such conditions. Therefore, for the ATLAS inner detector (ID), it is strongly required further research in the field of silicon detectors. The anticipated ID for this Phase II is intended to be completely of silicon and with an increase over the number of channel to avoid effects of pile-up events. This thesis is focused on the strip region of the ID located at distances of 38-100 cm from the collision point of the beams.

In the last few years, a silicon detector technology resistant to higher radiation doses as expected in the HL-LHC was being developed. The excellent properties showed by the n^+p detectors with respect to current p^+n technology make them very suitable choice for these large experiments. In fact, this technology is the baseline chosen for these detectors, while an optimization of the detector structure is needed.

In the first part of this work, it is studied different types of n^+p silicon detectors processed by different centers (CNM-Barcelona and Hamamatsu Photonics, Japan). These detectors were irradiated with particles fluences at the expected doses for HL-LHC. The radiation effects on the detectors were analyzed mainly in terms of charge collection efficiency and signal-to-noise ratio, which decrease the longer the detector is irradiated. Therefore, the detector design must be such that it can operate with reduced signals and operating voltages required to provide a sufficient signal.

The CNM detectors were irradiated with neutrons at fluences up to $8 \times 10^{15} cm^{-2}$. Detectors were tested with different types of silicon substrates (FZ, DOFZ and MCZ). These three types of silicon are based on different processing methods of silicon crystal and they differ in the oxygen concentration therein. As it was already known, the oxygen in the crystal silicon improves the

resistance of the detectors to the charged hadron irradiation. However, the results in this thesis reflect that the charge collected by the detectors is not affected by the type of substrate and therefore the oxygen concentration.

Collected charge as function of the applied voltage measurements showed almost the first time values as high as those measured for a similar detector unirradiated within the uncertainties at a fluence of $10^{14} cm^{-2}$ for MCZ silicon and $3 \times 10^{14} cm^{-2}$ for MCZ silicon and DOFZ. Charge multiplication effects are taking place during the charge collection. This effect has been seen in numerous similar measurements being more evident at higher voltages. The study of this mechanism in steady state opens new possibilities for highly irradiated detector operation.

It was also compared n^+p silicon detectors with n^+n detectors (both FZ silicon) in terms of charge collection. n^+n detectors showed better charge collection efficiency, although n^+p detectors have sufficient charge collection required for silicon microstrip detectors for high luminosity conditions. n^+n detectors behave very well under irradiation, but this technology requires double-sided processing because the pn junction begins to grow from the back, making it more expensive. This is why it is preferred n^+p technology for the ATLAS strip region. FZ silicon detectors showed microdischarges during charge collection measurements as a function of the applied voltage. This effect represents a major failure mechanisms in the detector operation. It is a limiting factor at data taking and can damage the detector and its associated electronics since its intensity increases with the applied voltage. The most likely cause for this effect has to do with the interstrip isolation. Detectors with n^+ implants require isolation techniques to prevent shorted channels. These techniques require p-type implants. The characterized CNM detectors have a p-spray isolation. The high doping gradient between these implants can result in intense electric field region and consequently located microdischarges. Furthermore it has been observed that these microdischarges appear at lower voltages for non-irradiated detectors and this onset voltage increases with higher irradiation. It is shown that the dose of p-spray is moderated by the radiation effect.

The following detectors considered are those provided by Hamamatsu Photonics. In this case, it was assessed the effects of both radiation (protons and neutrons) at different fluence rates up to 10^{15} cm^{-2}. Detectors with p-stop and p-stop + p-spray isolation methods were available. These detectors showed excellent performance in terms of charge collection and isolation between the strips. However, these FZ silicon detectors also showed microdischarges. Research carried out by Hamamatsu Photonics led to these microdischarges were due to the asymmetrical design of the p-stop used to isolate the strips, which was conveniently corrected in later processed detectors.

Comparing both types of detectors irradiated at the expected dose for the ID strip region shows that both types of detectors have sufficient charge collection efficiency. Therefore, this detector technology meets the requirements for the new ATLAS ID can operate at luminosity conditions of the HL-LHC. It is also observed that silicon FZ is slightly higher in these terms, however, the presence of microdischarges with this type of detectors calls for further research on the detector design parameters. This thesis demonstrates a proper choice of design parameters is essential for an effective detector operation: A suitable p-spray dose or a correct geometry of p-stop.

Finally this thesis has contributed to the current operation of the ATLAS SCT. It has been studied a possible beam loss scenario that is, an beam impact directly on the SCT p^+n silicon

detectors. A silicon device with the same characteristics has been edited and has been exposed to high charge densities by means of simulations. It is shown that the electric field alters and this change leads to a high accumulation of charge in the p^+ implant and therefore a considerable risk of oxide breaking. In order to protect the oxide, these detectors incorporate in its design a punch-through structure (PTP) that prevents these accumulations enabling quick discharge of the sensor. These studies allowed to establish a limit in order not to break the oxide with a dose up to 150000 per strip.

Resumen

10.1 Introducción

Los detectores de silicio son dispositivos que se usan en la reconstrucción de las trazas de las partículas que los atraviesan en experimentos de colisiones de partículas elementales. Los experimentos del gran colisionador hadrónico del CERN[1] (LHC) son una buena muestra de ello.

El LHC, funcionando desde noviembre de 2010, es actualmente el mayor colisionador construido. En él, se aceleran y se hacen colisionar protones con una energía nominal de 14 TeV (actualmente a 7 TeV) y una luminosidad instantánea nominal de $10^{34}\ cm^{-2}\ s^{-1}$ (actualmente a $3.65 \times 10^{33}\ cm^{-2}\ s^{-1}$). Además también puede colisionar iones pesados de plomo con una energía de 2.8 TeV por nucleón y hasta una luminosidad instantánea de $10^{27}\ cm^{-2}\ s^{-1}$.

La alta luminosidad del LHC da lugar a una tasa de interacción del orden de 10^9 colisiones por segundo. Esta tasa de interacción es necesaria debido a las pequeñas secciones eficaces de producción de procesos físicos relevantes que se pretenden estudiar. El número de eventos por segundo generados en una colisión del LHC viene dada por la ecuación 10.1.

$$N_{event} = L\sigma_{event} \tag{10.1}$$

σ_{event} es la sección eficaz del evento considerado y L es la luminosidad integrada, la cual es definida como la luminosidad instantánea, $\mathcal{L}$ integrada en un intervalo de tiempo dt determinado. A su vez, $\mathcal{L}$ depende básicamente de los parámetros del haz.

El propósito del acelarador LHC es básicamente dar respuesta a las limitaciones que presenta el Modelo Estándar [1] y revelar la física más allá del mismo. Además, también está proporcionando medidas más precisas de los parámetros ya conocidos del Modelo Estándar. Uno de sus objetivos fundamentales es la búsqueda del bosón de Higgs, partícula predicha por el Modelo. Sin embargo, la teoría no predice su masa por lo que dependerá del canal de desintegración. Los experimentos del LHC tienen la tarea de explorar todo el rango posible de masa del bosón de Higgs en función de su canal de desintegración hasta una escala de energía de 1 TeV. Resultados de finales del año 2011 han mostrado evidencias que, si el Higgs existe, su masa se encontraría en el rango [114-141] GeV (ver figura 1.3).

[1] www.cern.ch

Experimentos del LHC

Para cumplir sus objetivos el LHC cuenta con cuatro experimentos, los cuales se muestran gráficamente en la figura 10.1.

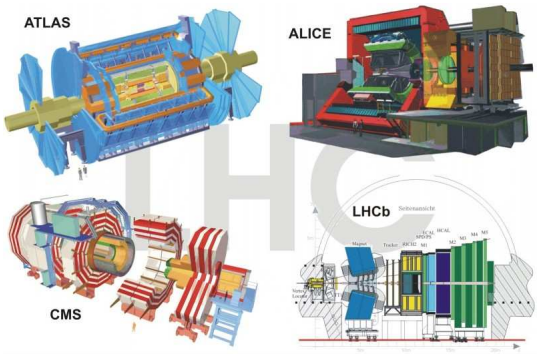

Figure 10.1: Simulación gráfica de los 4 experimentos del LHC (imagen no a escala).

El LHC tiene dos experimentos de propósito general, ATLAS [20] y CMS [21], ambos operarán a la máxima luminosidad instantánea de $10^{34}\ cm^{-2}s^{-1}$. También, tiene dos experimentos de baja luminosidad: LHCb [22] para estudios del física del quark *b* con una luminosidad instantánea de $10^{32}\ cm^{-2}s^{-1}$, y TOTEM [23](integrado en CMS) para el estudio de protones procedentes de interacciones elásticas a pequeños ángulos, a una luminosidad instantánea de $2\times10^{29}\ cm^{-2}s^{-1}$. Finalmente, para las colisiones con haces de iones de plomo, el LHC cuenta con ALICE [24] con una luminosidad de $10^{27}\ cm^{-2}s^{-1}$ y dedicado al estudio del plasma quark-gluón a altas temperaturas.

ATLAS

Esta tesis está enmarcada dentro del experimento ATLAS, por lo que será el único que se explique con más detalle.

El experimento ATLAS está básicamente compuesto por tres subsistemas, los cuales son, de mayor a menor proximidad al punto de interacción:

- El **Detector Interno** (ID), el cual combina detectores de silicio de alta resolución espacial (detectores pixel y microstrip) con un detector de tubos de deriva en su parte más externa. Está inmerso en un solenoide que proporciona un campo magnético de 2 T. Su alta granularidad permite una eficiente reconstrucción de trazas, medida de vértices secundarios y determinación de momentos.

- El **calorímetro electromagnético** (ECAL), para la identificación y medida de energía de electrones y fotones. Combina cámaras de LAr (Argón líquido) como medio ionizante con absorbentes de plomo en una geometría de acordeón. Todo rodeado por un criostato ya que necesita operar a muy baja temperatura.

- El **calorímetro hadrónico** (HCAL), para la identificación y medida de jets hadrónicos y energía perdida (E_T^{miss}). Se basa en absorbentes de hierro y plástico centelleador como medio ionizante.
- El **espectrómetro de muones**, para la reconstrucción de trazas de los muones. Está compuesto por diferentes tipos de tecnologías que combinan cámaras para la reconstrucción de trazas de alta precisión y cámaras de respuesta muy rápida para trigger.
- Un **sistema magnético toroidal** con una importante potencia de curvatura. Su parte barril proporciona un campo magnético de 3 Tm y sus dos tapas a cada lado del experimento proporciona un campo magnético de 6 Tm.

HL-LHC

Una mejora del LHC en términos de un aumento en su luminosidad ha sido considerado como una extensión en su programa de física [36]. Un aumento de casi un orden de magnitud en su luminosidad incrementará la tasa de interacción extendiendo entre 20-30% el alcance en masa de nueva física y permitiendo mediciones mucho más precisas. Se ha establecido una luminosidad máxima de operación de $5 \times 10^{34}\ cm^{-2}s^{-1}$. Este nuevo proyecto para el LHC se denomina *High Luminosity LHC* (HL-LHC) y se llevará a cabo en dos fases:

- **Fase I**. Después de alrededor de 4 años de operación con los valores nominales de luminosidad y energía para el LHC, se espera una parada técnica de la máquina de alrededor de 9 meses. En este tiempo, se realizarán tareas de consolidación de la colimación o el reemplazo de cuadrupolos magnéticos para el enfoque de los haces cerca de las regiones de interacción de los mismos donde sufren un mayor daño por la radiación. También se actulizarán el sistema de cruce de haces para una mayor efectividad. Con estas mejoras, se espera alcanzar una luminosidad de 2-$3 \times 10^{34}\ cm^{-2}s^{-1}$ y un total de 300 fb^{-1} de luminosidad integrada al final de esta fase.
- **Fase II**. Actualmente los planes situan esta fase alrededor 2022-2023, con un cierre previo de la máquina de $\sim$18 meses para preparar principalmente los experimentos para las condiciones de alta luminosidad prevista de $5 \times 10^{34}\ cm^{-2}s^{-1}$. Se espera llegar a acumular hasta 3000 fb^{-1} de luminosidad integrada.

El incremento en luminosidad supone mayores tasas de colisiones y niveles de radiación que tendrán que soportar los detectores que conforman los experimentos alrededor del acelerador, sobre todo, los detectores situados más próximos al punto de interacción, como es el detector interno. Esta tesis está centrada en la fase II del proyecto de alta luminosidad de LHC y más concretamente, en los detectores de microstrip del detector interno de ATLAS, por lo que a partir de ahora, se hará referencia a esta esta región. Más detalles de la actualización requerida en ATLAS para su operación a alta luminosidad se pueden encontrar en [40].

Dos son, por tanto, los factores que principalmente afectan al funcionamiento del detector interno:

- Un incremento de eventos de alrededor de 20 hasta 200 colisiones por cruce de haces. Esto puede suponer problemas de apilamiento en los detectores, lo que implica la necesidad de

una mayor granularidad de los mismos para mantener la ocupancia a los mismos niveles de operación de los actuales detectores.

- Un incremento del flujo total de partículas que atraviesan los detectores. Este hecho da lugar a la degradación tanto de los detectores como de su electrónica e implica el desarrollo de nuevos detectores más resistentes a la radiación.

Estos factores determinan cómo llevar a cabo la mejoras necesarias en los detectores para una operación adecuada bajo las condiciones del HL-LHC. Para la preparación de los detectores, varios programas *I+D* ya están trabajando para proporcionar las pautas para nuevas tecnologías de detectores resistentes a los niveles de radiación anticipados, como también, posibles diseños en la distribución de los detectores.

Los estudios realizados en esta tesis se enmarcan en la Colaboración *RD50*[2] del CERN. Es uno de los programas *I+D* cuyo principal objetivo es el desarrollo de dispositivos semiconductores resistentes a niveles radiación más allá de los límites de dispositivos actualmente en uso. Esta colaboración está participando activamente para el desarrollo de nuevas y más resistentes tecnologías de detectores para el detector interno de los experimentos que operarán en el HL-LHC.

La mejora prevista para el Detector Interno

El actual detector interno de ATLAS combina detectores pixel de silicio (PIXEL) en sus capas más próximas al punto de interacción de los haces, detectores microstrip de silicio (SCT, de SemiConductor Tracker) en sus capas intermedias y detectores de tubos de deriva TRT por Transition Radiation Tracker) en su parte más exterior. Los detectores basados en silicio (PIXEL y SCT) son capaces de reconstruir las trazas de las partículas con una resulición muy elevadak, imprescindible para distinguir vértices secundarios. Los tubos de deriva del TRT permiten realizar el seguimiento continuo de las partículas (con 36 puntos por traza), aunque con una menor resolución espacial.

Las condiciones de luminosidad del HL-LHC implicarían grandes niveles de ocupancia en el TRT. Además el Detector Interno ha sido disenãdo para operar hasta unos niveles de radiación correspondientes a 500 fb^{-1}. Su funcionamiento por encima de estas condiciones daría lugar a una degradación seria de los detectores, limitando, por tanto, los datos de física. Por lo que el detector interno será totalmente reemplazado para la fase II con un sistema basado todo en detectores de silicio, con más granularidad y resistentes a las dosis esperadas en el HL-LHC.

La parte barril del SCT se extenderá a 5 capas de detectores de microstrip a unas distancias entre 38-95 cm del punto de interacción de los haces (en vez de las actuales 4 capas entre 30-51 cm). Las 3 capas más externas del SCT reemplazarán al TRT. De las 5 capas, las tres más internas estarán formadas de detectores de microstrips con strips de longitud 2.4 cm (capas *short strips*) y las dos más externas de detectores de microstrip con strips de longitud de 4.8 cm (capas *long strips*), en vez de los actuales strips de 9 cm y por tanto, proporcionando mayor granularidad. El detector PIXEL estará compuesto por 4 capas entre los radios 3.7-20.9 cm, en vez de las actuales tres capas entre 5.1-12.3 cm. Las regiones a cada lado de la parte barril consistirán en 6 discos de detectores pixel y 5 discos de detectores microstrip.

[2] www.cern.ch/rd50

La tabla 10.1 muestra de los niveles de radiación esperados para la fase II en comparación con los niveles de radiación que tiene que soportar el detector interno actualmente en funcionamiento. La contribución de la radiación a los detectores viene dada por aproximadamente un 50% de neutrones y un 50% de hadrones cargados para las capas de strips más internas, mientras que para las capas más externas domina la contribución de neutrones debido a procesos secundarios que tienen lugar en el calorímetro electromagnético.

Detector	f_{max} [10^{15} n_{eq} cm^{-2}] (HL-LHC)	f_{max} [10^{15} n_{eq} cm^{-2}] (LHC)
Pixel	22 a 3.7 cm	1 a 5.1 cm
Short Strip (38-62 cm)	1.2	0.2 (SCT)
Long Strip (74-100 cm)	0.56	0.03 (TRT)

Table 10.1: Flujos máximos de partículas estimados para el detector interno de ATLAS bajo las condiciones de luminosidad del HL-LHC y del LHC.

10.2 Detectores de Silicio

Teoría de semiconductores

El paso de una partícula por un sensor de silicio se detecta a partir de la interacción de esta partícula con los átomos de la red cristalina de silicio que constituye el sensor. El modelo de bandas de energía en un sólido cristalino establece una banda de valencia que contiene los electrones ligados al átomo. Mientras que la banda de conducción contiene los electrones libres que contribuyen a la conductividad eléctrica del material. Ambas bandas están separadas por una banda prohibida o *gap*. Para un material como el silicio, el cual es semiconductor, la anchura de esta banda es de 1.12 eV. A 0K, todos los electrones ocuparán la banda de valencia y no hay flujo de corriente. A temperatura ambiente (300 K), los electrones pueden ser excitados térmicamente y adquirir la suficiente energía para pasar a la banda de conducción, dejando un hueco positivo en la banda de valencia que actúa como portador de carga positivo. En los semiconductores se produce corrientes producidas tanto por el movimiento de electrones como del desplazamiento de los huecos (cuando un hueco se va llenando con electrones de átomos vecinos).

Un semiconductor es intrínseco cuando no contiene impurezas en la red cristalina. La conductividad se debe únicamente a los portadores de carga excitados térmicamente. La introducción deliberada de impurezas en pequeñas cantidades en un material semiconductor para aumentar su concentración de electrones o huecos se llaman dopaje. El material resultante es un semiconductor extrínseco.

Cuando el silicio se dopa con átomos con átomos pentavalentes (P), con cinco electrones de valencia, cuatro de los cuales participan en enlaces covalente con los átomos de silicio vecinos. El electrón restante, débilmente ligado a su núcleo, por lo que casi con toda probabilidad estará ionizado positivamente a temperatura ambiente. A este tipo de semiconductor extrínseco se le denomina de tipo N.

Por el contrario, si dopamos el silicio con átomos trivalentes (B), con tres electrones de va-

lencia, se introducen huecos en la red que son fáciles de excitar a la banda de valencia a temperatura ambiente, dejando atrás un átomo ionizado negativamente. A este tipo de semiconductor extrínseco se le denomina de tipo P.

La estructura fundamental de la mayoría de los detectores de silicio es la unión PN. Estas uniones se forman al combinar en un material una región tipo P con otra tipo N, cuyas propiedades dependen principalmente de los niveles de dopaje. La fuerte diferencia de concentraciones de portadores de carga da lugar a procesos de difusión de electrones a la región de tipo P y huecos a la región de tipo N, ya que las concentraciones tienden a igualarse y da lugar a una corriente. Por otro lado, a ambos lados de la unión existe una región de cargas fijas (iones positivos en la región N y negativos en la región P) dando lugar a una diferencia de potencial. Aparecerá, por tanto, una campo eléctrico a través de la unión, causando una corriente de deriva que se opone a la corriente por difusión.

El dispositivo alcanzará un estado de equilibrio cuando el flujo de corriente neto sea cero:

$$J_{deriva} + J_{dif} = 0 \tag{10.2}$$

Un región desierta, es decir, libre de portadores de carga, es creada a ambos lados de la unión. Esta región es la base para la detección de radiación en los detectores de silicio. La radiación incidente en esta región ioniza los átomos de silicio y los pares electrón-hueco resultantes son acelerados en en el campo eléctrico generado por la unión. Los portadores de carga derivan en direcciones opuestas dando lugar a una señal de corriente medible del paso de la radiación. La carga generada en las zonas no desiertas se recombinan inmediatamente y no contribuyen a la señal. Lo que se suele hacer es extender la región libre de carga a todo el área sensible del detector aplicando un voltaje del mismo signo que la diferencia de potencial en la unión (voltaje en inversa) y la corriente por difusión disminuye.

Operación de un detector de silicio

Se ha descrito la estructura básica de un detector de silicio. Un detector de silicio aplicado a experimentos de física de altas energías consiste, básicamente, en una cara de la unión con un alto dopaje (expresado como n^+ para silicio tipo n) comparado con el otro lado de la unión ligeramente dopado, por ejemplo de tipo p. Se denomina una unión n^+p. En toda unión p-n se cumple la ecuación 10.3 [51],

$$N_a W_p = N_d W_n \tag{10.3}$$

siendo N_a y N_d las concentraciones de dopaje y W_p y W_n las anchuras de las zonas desertizadas en las regiones p y n respectivamente. De la cual se deduce que la anchura de la región con mayor dopaje (n^+) es pequeña comparada con la región débilmente dopada, p. El campo eléctrico siempre crecerá de la zona n^+ hacia la zona p y se extenderá a lo largo de toda su anchura.

Los detectores de microstrips de silicio que se usan como sistemas de reconstrucción de trazas se basan en dividir la región fuertemente dopada, que puede ser de unas pocas micras, en bandas paralelas sobre el volumen menos dopado de silicio. Cada unión actua como un detector de silicio individual para medidas precisas de posición.

Los principales detectores de microstrips de silicio estudiados en esta tesis son del tipo n^+p, como el que se representa en la figura 10.2. Existen también otras estructuras como p^+n, la cual corresponde a los actuales detectores de microstrips del SCT o n^+n. Hay numerosos estudios que demuestran una mayor tolerancia a altas dosis de radiación de la tecnología n^+p sobre p^+n [92, 93] y por ello, es la tecnolgía considerada para los detectores de silicio previstos para el detector interno de ATLAS en el HL-LHC.

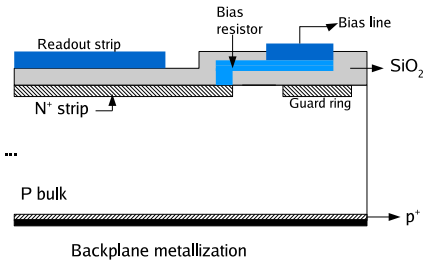

Figure 10.2: Vista transversal de un detector de silicio n^+p. La capa aislante de SiO_2 sirve como acoplamiento capacitivo. Las bandas n^+ actuan como electrodos y están conectados a la electrónica de lectura a través de una capa de aluminio.

Para los detectores de silicio con bandas n^+, es necesario incluir una estructura de aislamiento entre los electrodos. Esto es debido a la capa de acumulación de electrones que se produce en la superficie del sensor al ser atraidos por la carga positiva presente en la interfaz Si-SiO_2. La señal que *ven* los electrodos n^+ se debe principalmente al movimiento de los electrones, por lo que la capa de acumulación de electrones puede cortocircuitar los implantes n^+. Los métodos de aislamiento de strips que se utilizan son:

- p-Stop. Consiste en una implante p^+ de boro rodeando los strips.
- p-Spray. Consiste en la difusión de una capa p^+ de boro sobre los strips.
- p-Spray moderado. Una capa p^+ de boro sobre los strips con una dosis más moderada y un implante p^+ en el centro con una dosis que garantice un correcto aislamiento entre strips.

Cuando una partícula atraviesa un detector de silicio, la cantidad de pares electrón-hueco creados es proporcional a la energía perdida por esa partícula. La energía media necesaria para producir un par electrón hueco en silicio es 3.6 eV. Para una partícula de mínima ionización (*mip*) atravesando un detector de silicio de 300 μm, el valor promedio de energía perdida es de 81 KeV, luego un *mip* creará una carga máxima de unos 22500 pares electrón-hueco. Ya que las interacciones entre las partículas cargadas y el semiconductor son estadísticas, la energía total depositada por cada partícula puede variar. Sin embargo, la distribución de energía y por tanto, de carga generada en el detector, sobre un número grande de eventos sigue la distribución de Landau. En este caso, el valor medio no coincide con el valor más probable, que corresponde a $\sim$24000 electrones para un detector de 300 μm. Para reproducir los resultados experimentales se asume una distribución de Landau convolucionada con una gausiana.

La señal en el detector tiene la forma de pulso de corriente y su integración con el tiempo es la carga total creada por el paso de la partícula. Si el tiempo de integración no es lo bastante largo, no se estará dando cuenta toda la carga depositada y la carga perdida se conoce como déficit balístico del detector. Como éste último viene fijado por las necesidades del experimento, entran en juego los parámetros del detector: su grosor, la carga generada por un *mip* en un detector de 300 μm tiene un tiempo de colección del orden de los 10 ns. Más delgado podría limitar la señal mínima necesaria para una buena relación señal/ruido. O también aumentar su campo eléctrico aumentando el voltaje de operación; Un campo eléctrico muy alto puede dar lugar a fenómenos de ruptura por avalancha del detector. Obviamente, en un detector parcialmente desertizado, sólo la carga depositada en el volumen activo del detector será recogida por los electrodos.

Efectos de la radiación

La radiación que atraviesa los detectores supone daño microscópico a la estructura cristalina del silicio. Ésto da lugar a niveles de energía en la región prohibida de bandas. Estos niveles inducidos por radiación actuan como centros de generación y recombinación afectando a la operación eléctrica del dispositivo. Un buen conocimiento de la física de estos efectos dará lugar al desarrollo de tecnologías que puedan operar bajo condiciones de alta radiación de una manera eficiente. Los efectos en sus propiedades macroscópicas se describirán a continuación.

- Un detector de silicio que opera en inversa tiene un flujo de corriente inherente. A esta corriente se le denomina corriente de fugas y viene dominada por procesos de generación de pares y dependiente de la temperatura. Los estados creados por la radiación cerca del centro de la banda de estados prohibidos actúan como centros de generación por lo que aumentan la corriente de fugas. Esto supone un aumento del ruido electrónico y por tanto de una disminución del la relación señal/ruido.

- Los niveles de energía creados en la banda prohibida y activos eléctricamente afectan de un modo directo a la concentración de dopaje efectiva. Al voltaje al cual la anchura de desertización coincide con el grosor del detector se le denomina *voltage de desertización*, V_{fd}. Éste es directamente proporcional a la concentración de dopantes efectiva (N_{eff}) a partir de la ecuación 10.4.

$$V_{fd} = \frac{q}{2\varepsilon_{Si}} \mid N_{eff} \mid d^2 \tag{10.4}$$

  Por lo que un aumento en N_{eff} implica la necesidad de aplicar un mayor voltaje al detector para su completa desertización. Altas dosis de radiación suponen voltajes no asumibles y por tanto, el detector tendrá que operar por debajo de la desertización completa, disminuyendo la eficiencia de recolección de carga y la relación señal/ruido.

- El mecanismo principal para la degradación de la eficiencia de la colección de carga es el atrapamiento de la carga generada por el paso de partículas por los estados electrónicos en la banda prohibida correspondientes a defectos causados por la radiación. Si la electrónica de lectura lee la carga en un tiempo inferior al tiempo de reemisión del portador de carga de la *trampa*, esta carga se pierde y disminuye la eficiencia de recolección de carga y de la relación señal/ruido.

10.3 Resultados

Caracterización de detectores de silicio

En esta sección se presentará un resumen de la caracterización de detectores de silicio de microstrips llevada a cabo en el laboratorio de Silicio del Instituto de Físca Corpuscular de Valencia. Se han evaluado sensores de microstrips de diferentes fabricantes: del Centro Nacional de Microeléctronica (Barcelona) como de Hamamatsu Photoniks (Tokio, Japón). Se han medido sus características eléctricas (corrientes de fugas, capacidad...) como de operación (carga recogida, relación señal/ruido...).

sensores microstrips del CNM

La tabla 10.2 muestra los principales parámetros de estos sensores.

parámetro del sensor	
área	$1.06 \times 1.06\ cm^2$
grosor	$285 \pm 15\ \mu m$
# strips	128
longitud del strip	$10472\ \mu m$
anchura del strip	$32\ \mu m$
distancia entre strips	$80\ \mu m$
resistividad nominal	$30\ k\Omega \cdot cm$
aislamiento entre strips	p-spray

Table 10.2: Parámetros principales de los detectores de silicio microstrips procesados en el CNM.

Se dispone de varias series de detectores n^+p. Se diferencian en el tipo de sustrato de silicio utilizado para el procesado de los detectores. Éstos son: Silicio crecido mediante la técnica *Float Zone* (FZ), silicio *Diffusion Oxigenated Float Zone* (DOFZ), el cual se obtuvo a partir de una oblea FZ sometiéndola a procesos de difusión de oxígeno y silicio *Magnetic Czochralski* (MCz). También se dispone de una serie de detectores n^+p con silicio FZ para comparar.

Estos detectores fueron irradiados con neutrones en el reactor nuclear TRIGA Mark II del Instituto Jozef Stefan en Liubliana (Eslovenia) con diferentes dosis hasta $8 \times 10^{15}\ n_{eq}\ cm^{-2}$. Estos flujos de partículas corresponden a las dosis que tendrán que soportar los detectores microstrip en condiciones de alta luminosidad. También se midió un detector no irradiado de cada serie como referencia.

Se hicieron medidas pre-irradiación de características eléctricas como la corriente de fugas y la capacidad en función del voltage. Un nivel de corriente de fugas alto degrada el funcionamiento del detector, contribuyendo al ruido. Además, esta medida te permite reconocer procesos de ruptura por avalancha en el sensor. Para estos detectores no irradiados se obtienen corrientes de fugas del orden de unos poco μA, lo que es considerado relativamente bajo. La medida de la capacidad del detector te permite calcular el voltaje de desertización completa,

al cual la capacidad se hace mínima y constante con el voltaje aplicado porque ocupa todo el grosor del detector. La tabla 10.3 muestra los valores de V_{fd} para los detectores medidos.

	V_{fd} [V]	N_{eff} [cm^{-3}]
n^+-p DOFZ	26.7 ± 0.9 V	$(4.34 \pm 0.16) \times 10^{11}$
n^+-p MCz	104.3 ± 5.7 V	$(1.67 \pm 0.90) \times 10^{12}$
n^+-p FZ	51.9 ± 0.9 V	$(8.36 \pm 0.16) \times 10^{11}$
n^+-n FZ	51.2 ± 1.9 V	$(8.37 \pm 0.32) \times 10^{11}$

Table 10.3: Valores de voltaje de desertización completa extraídos de las curvas $1/C^2$ vs. V_{bias} para los detectores no irradiados. A partir de éstos, se puede estimar la concentración de dopantes efectiva con la ecuación 10.4.

Una vez conocido que los parámetros eléctricos de los diferentes detectores son adecuados, se procede a la evaluación de estos tipos de detectores irradiados. Se ha medido la carga recogida en función del voltaje aplicado. La carga recogida se debe al paso de un haz láser a través del detector como se muestra en la figura 10.3.

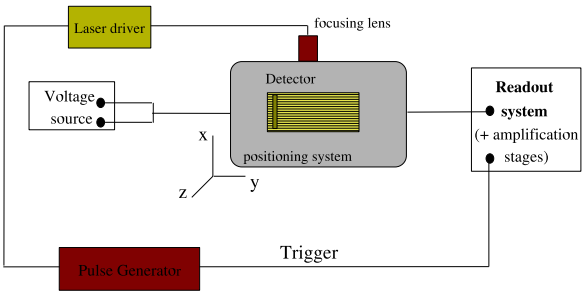

Figure 10.3: El sistema para la medida de recolección de carga a partir de un haz láser.

También se ha hecho uso de un sistema para la medida de la carga recogida a partir de la emisión β^- de una fuente radiactiva (^{90}Sr). El uso de un haz láser proporciona señales más intensas que la fuente radiactiva. Sin embargo, existe una incertidumbre en el número de pares generados por el láser dependiente de cambios en la intensidad del haz o del ángulo de incidencia. Debido a ésto, la medidas realizadas con láser son calibradas con algunas medidas usando la fuente radiactiva para cada detector. El sistema de medida con fuente radiactiva se muestra en la figura 10.4.

Las medidas se llevan a cabo a una temperatura de $-30°$C. Esta baja temperatura se debe a evitar procesos de migración de los defectos inducidos por radiación que ocurren a mayores temperaturas con el tiempo y así evaluar directamente el daño primario producido por la radiación. Este efecto se denomina *annealing* y da lugar a la variación temporal de las propiedades de los detectores.

Los tipos de sustratos DOFZ y MCz se caracterizan por una alta concetración de átomos de oxígeno en la red cristalina como impurezas, hasta 10^{17} cm^{-3} para el silicio DOFZ y $\sim 5 \times 10^{17}$ cm^{-3}

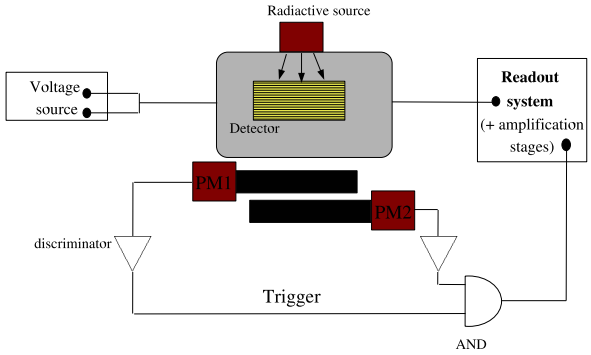

Figure 10.4: El sistema para la medida de recolección de carga a partir de una fuente radiactiva.

para silicio MCz. Por otra parte, se ha comprobado que este tipo de impurezas en el silicio da lugar a una mayor tolerancia a la radiación de hadrones cargados[3]. La figura 10.5 muestra la carga recogida en función del flujo de neutrones a un voltaje representativo de 500 V (el voltaje máximo al cual los detectores de silicio pueden ser alimentados en el SCT). En este caso, se muestra que bajo irradiación de neutrones, la carga recogida total no varía en función del tipo del sustrato del detector.

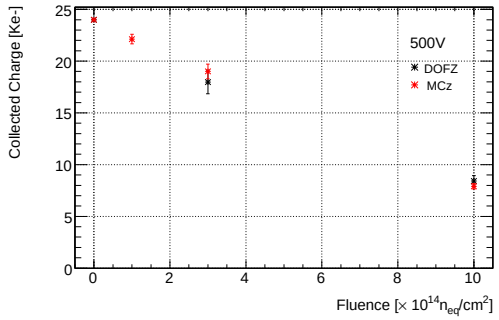

Figure 10.5: Comparación de la carga recogida como función del flujo de neutrones para los detectores de silicio DOFZ (en rojo) y MCz (en negro). Los datos corresponden a un voltaje en inversa de 500 V.

La figura 10.6 muestra la comparación de la carga recogida por los detectores de silicio para los diferentes tipos de sustratos en función del flujo de neutrones recibidos y para un voltaje de 400 V. Los detectores n^+p muestran un comportamiento similar independientemente del tipo de sustrato. Sin embargo, los detectores n^+n muestran mayor carga recogida requiriendo, por tanto, voltajes más bajos para recoger toda la carga depositada.

[3] www.cern.ch/rd48

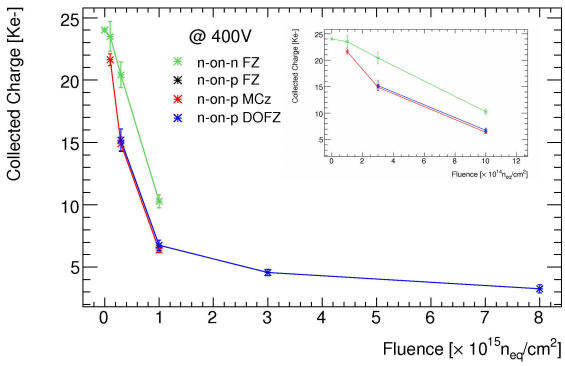

Figure 10.6: Carga recogida en función del flujo de neutrones para diferentes tipos de sustratos de detectores n^+p y n^+n producidos en el CNM. Los datos corresponden a un voltaje en inversa de 400 V. La gráfica inmersa muestra las mismas medidas hasta una dosis de 10^{15} n_{eq}/cm^2.

Se observaron microdescargas durante las medidas de recolección de carga en los detectores de silicio FZ. Las microdescargas se muestran como picos de señal que pueden alcanzar una alta intensidad y pueden tener ambas polaridades, positiva y negativa. Éstas no ocurren en todo el detector si no que están localizadas en ciertos canales. Estos canales pueden ser enmascarados para un correcto análisis de las medidas. Sin embargo, a mayores voltajes, llegan a ser más frecuentes y sus amplitudes significantes, contribuyendo al espectro de carga medida como se observa en la figura 10.7.

La tabla 10.4 muestra el voltaje al cual los detectores comienzan a mostrar microdescargas. El voltaje más bajo lo muestra el detector no irradiado mientra que es mayor a mayor irradiación sobre el detector. Las microdescargas se producen en zonas de alto campo eléctrico que corresponden a zonas con gradientes altos de dopaje. Concretamente en estos detectores con p-spray como método de aislamiento entre strips, las zonas de mayor campo eléctrico se encuentran en la zona de contacto del implante n^+ con la capa de p-spray. Además es conocido que el p-spray tiene un mejor funcionamiento después de irradiado ya que su dosis es compensada con la capa de acumulación de carga que se forma entre los implantes n^+, lo que reduciría la intensidad de esas regiones de alto campo eléctrico. Ésto explicaría que con flujos mayores, las microdescargas aparecieran más tarde.

sensores microstrips de Hamamatsu

detectores n^+p de silicio de microstrips fueron procesado por Hamamatsu Photonics (Tokio, Japón). Estos sensores pertenecen a una serie denominada *ATLAS*07 que se produjo para la colaboración ATLAS que trabaja en el desarrollo de detectores microstrips para el detector interno de ATLAS en el HL-LHC. Los principales parámetros de estos sensores se muestran en la tabla 10.5.

Estos detectores han sido irradiados con protones y con neutrones para evaluar el daño producido por la radiación a las fluencias que se esperan en el sistema de reconstrucción de trazas

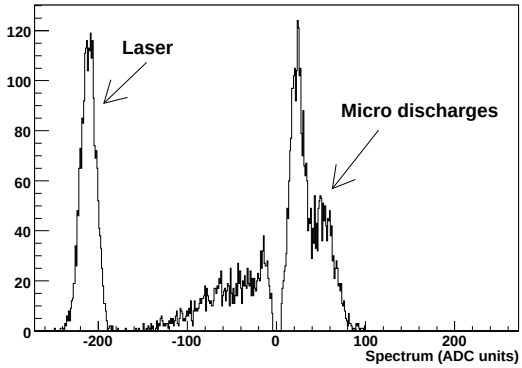

Figure 10.7: Espectro de carga en el sistema láser en unidade de ADCs, correspondiente a un detector irradiado con microdescargas. Se estima la amplitud debida a microdescargas del orden de 1.5 *mip*. Estas microdescargas corresponden a las registradas en coincidencia con la señal trigger del láser.

	n^+p FZ	n^+n FZ
Flujo $[n_{eq}/cm^2]$	V_{md} [V]	V_{md} [V]
0	160	230
1×10^{14}	150	390
3×10^{14}	270	400
1×10^{15}	330	400

Table 10.4: Voltaje al cual comienzan a aparecer microdescargas para los detectores de silicio FZ.

de ATLAS para condiciones de alta luminosidad.

La irradiación con neutrones fue en el reactor nuclear TRIGA Mark II del Instituto Jozef Stefan en Liubliana (Eslovenia) con diferentes dosis hasta 10^{15} n_{eq} cm^{-2}. Y la irradiación con protones fue llevada a cabo en el ciclotrón de CYRIC, centro de investigación de la universidad de Tohoku, en Japón hasta una dosis de 1.3×10^{15} n_{eq} cm^{-2}. Se tomaron detectores no irradiados con las mismas características como referencia.

Antes de enviarlos a irradiar, se evaluaron sus características eléctricas como la corriente de fugas y la capacidad del detector en función del voltage aplicado. Estas medidas se muestran en las figuras 10.8.

De las corrientes de fuga se deduce que los detectores con aislamiento p-stop+p-spray tienen voltajes de ruptura más bajos que los detectores con p-stop únicamente. Puede ser debido al contacto directo de los implantes n^+ con la capa de p-spray. La figura 10.9 se muestran los voltajes de ruptura para los detectores Hamamatsu medidos. Las especificaciones técnicas de ATLAS sitúan un límite de 600 V para el voltaje de ruptura. El 85% de los detectores cumplen

Parámetro del sensor	
área	1 cm^2
grosor	320 μm
número de strips	104
longitud del strip	0.80 cm
anchura del strip	16 μm
distancia entre los strips, Z1-Z5 (Z6)	74.5 (100) μm
aislamiento entre strips	p-stop y p-stop+p-spray
silicio	FZ

Table 10.5: Principales parámetros de los sensores de Hamamatsu.

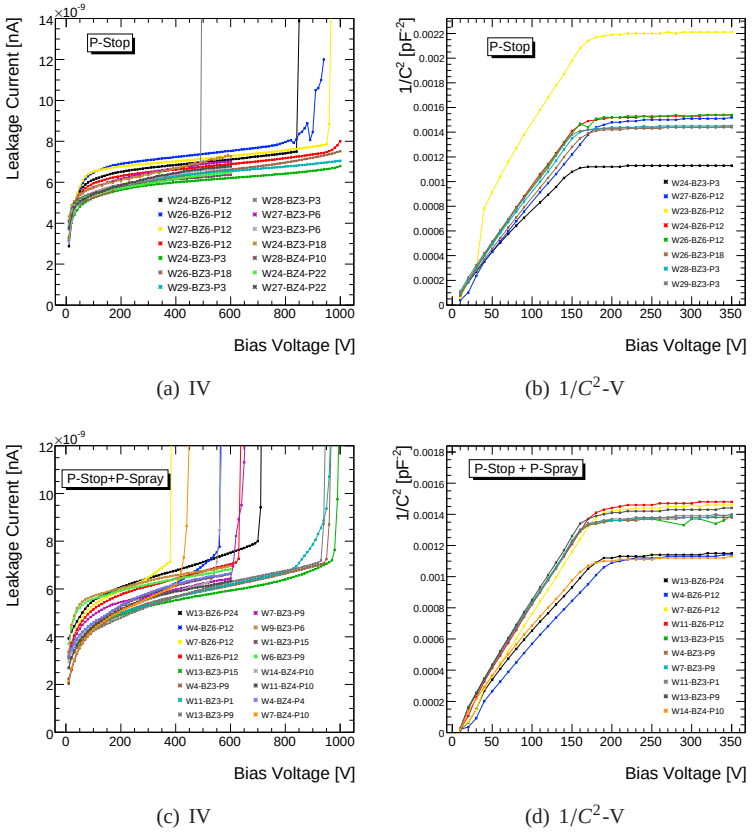

(a) IV (b) $1/C^2$-V

(c) IV (d) $1/C^2$-V

Figure 10.8: Características eléctricas: Corriente de fugas y $1/C^2$ en función del voltaje para los detectores n^+p con aislamiento p-stop (a)-(b) y con aislamiento p-stop+p-spray (c)-(d).

las especificaciones, si bien el resto tienes rupturas muy próximas a los 600 V. De las curvas de las capacidades se extrae un voltaje de desertización completa para todos los detectores medidos

entre 170-190 V.

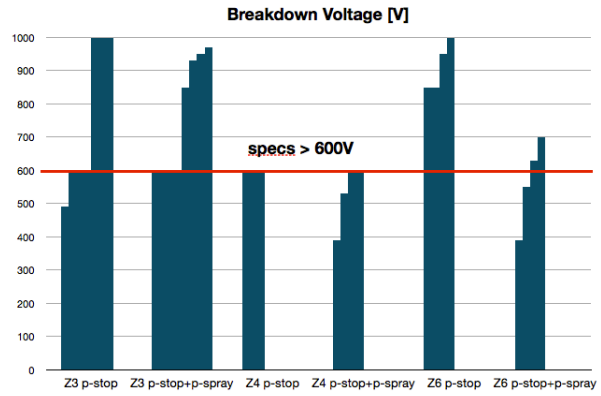

Figure 10.9: Voltajes de ruptura para los detectores *ATLAS07*. Las especificaciones téctnicas establecen un voltaje de ruptura mínimo de 600 V.

De la misma manera que con los detectores del CNM, se ha procedido a evaluar la eficiencia de recolección de carga de los detectores n^+p de microstrips de Hamamatsu debido al paso de un haz láser a través de ellos. También se realizaron a una temperatura de 30°C. La figura 10.10 muestra las medidas de carga recogida en función del voltaje de alimentación para los detectores irradiados con protones y con neutrones respectivamente. En cada gráfica también se especifican los detectores con aislamiento p-stop y p-stop+p-spray.

El funcionamiento de estos detectores muestran un buen aislamiento entre los implantes n^+ y compatible para ambos tipos de aislamiento: p-stop y p-stop+p-spray como se puede ver en la figura 10.11. El efecto de la radiación es más severo con neutrones que con protones. Sin embargo, los detectores muestran una buena operación a estos altas dosis. Por ejemplo, a la más alta dosis de 10^{15} n_{eq} cm^{-2} y 600 V, la carga recogida es de 14 000 y 10 000 electrones con protones y neutrones respectivamente.

La evaluación de estos sensores reveló la presencia de microdescargas. La tabla 10.6 muestra los voltajes a los cuales comienzan a observarse estas microdescargas para cada detector. De igual manera, los canales en los que aparece este efecto se pueden enmascarar para que no afecte a las medidas de señal debida al paso de un *mip*. Esto sólo se puede hacer cuando las microdescargas están localizadas y no enmascaran la señal del *mip* lo que limitó las medidas en términos de voltaje aplicado. Al ir aumentando el voltaje, aumenta la presencia y la intensidad de las microdescargas pudiendo dañar tanto el sensor como la electrónica asociada. También se observan microdescargas a un voltaje más bajo para los detectores no irradiados.

Investigaciones llevadas a cabo por *Hamamatsu Photonics* identificó algunos puntos de alto campo eléctrico asociados con un diseño asimétrico del p-stop [131]. La máscara utilizada para el procesado de las obleas de detectores de silicio fue convenientemente modificada y detectores mejorados (*ATLAS07-II*), no testeados en esta tesis, fueron fabricados.

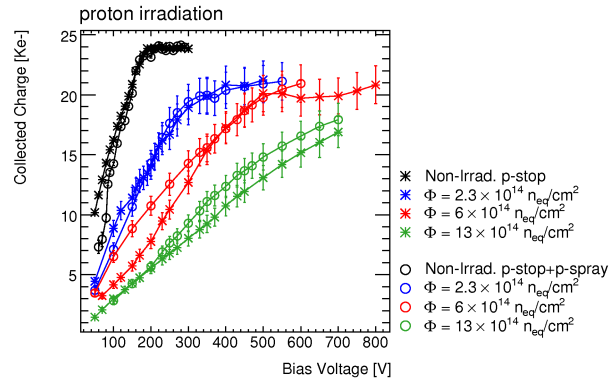

(a) Irradiación de protones

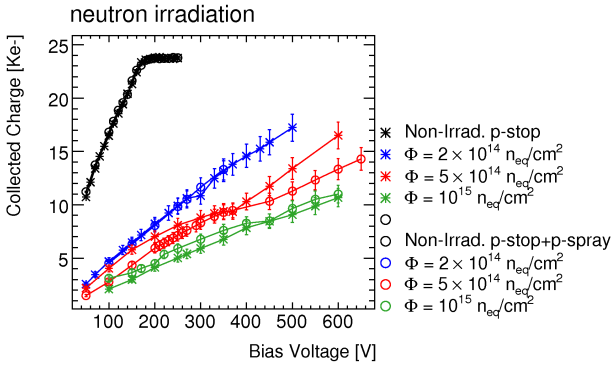

(b) Irradiación de neutrones

Figure 10.10: Carga recogida en función del voltaje de alimentación para los detectores n^+p de Hamamatsu irradiados con protones (a) y con neutrones (b). Detectores similares no irradiados fueron medidos como referencia.

Simulaciones de detectores de silicio con alta ionización

Para las actuales condiciones de operación del LHC, se ha evaluado el daño por alta ionización sobre los detectores de silicio microstrips del actual SCT. Nos referimos a la situación en la que el haz de protones se desviara de su trayectoria. En este caso, los protones dispersos pueden continuamente impactar en la estructura que contiene el haz dando lugar a radiación secundaria denominada eventos *beam splash* sobre los detectores más cercanos al punto de interacción de los haces y en el peor de los casos directamente sobre los detectores y su electrónica. Posibles pérdidas del haz pueden deberse principalmente a fallos en el sistema mágnetico que define la trayectoria de los haces.

Los detectores microstrips del actual sistema de reconstrucción de trazas están específicamente diseñados para resistir los efectos a largo plazo a la distancia a la que se encuentra del punto de

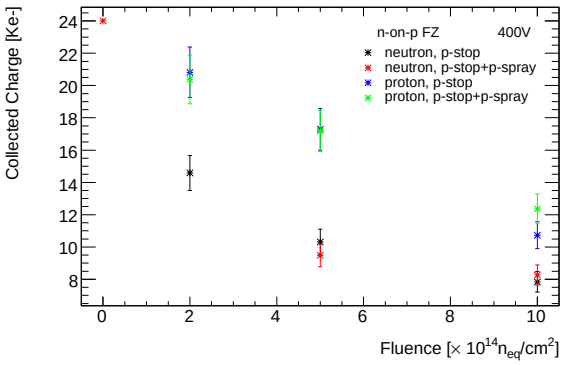

Figure 10.11: Carga recogida en función del flujo de partículas para los detectores Hamamatsu irradiados con neutrones y protones. Los sensores con p-stop y p-stop+p-spray son comparados. Las medides corresponden a un voltaje de alimentación de 400 V.

$N°$ de identificación	aislamiento	irradiación	Flujo $[\times 10^{14}\ n_{eq}/cm^2]$	V_{md} [V]
W29-BZ3-P3	p-Stop	p	0	290
W24-BZ4-P22	p-Stop	p	2.3	600
W27-BZ4-P22	p-Stop	p	6	750
W28-BZ4-P10	p-Stop	p	13	450
W13-BZ3-P9	p-Stop + p-Spray	p	0	270
W1-BZ3-P15	p-Stop + p-Spray	p	2.3	600
W6-BZ3-P9	p-Stop + p-Spray	p	6	650
W9-BZ3-P6	p-Stop + p-Spray	p	13	500
W27-BZ6-P12	p-Stop	n	0	270
W23-BZ6-P12	p-Stop	n	2	550
W24-BZ6-P12	p-Stop	n	5	400
W26-BZ6-P12	p-Stop	n	10	400
W13-BZ6-P24	p-Stop + p-Spray	n	0	160
W4-BZ6-P12	p-Stop + p-Spray	n	2	300
W7-BZ6-P12	p-Stop + p-Spray	n	5	400
W11-BZ6-P12	p-Stop + p-Spray	n	10	400

Table 10.6: El voltaje al cual comienzan a aparecer microdescargas, V_{md}, para cada detector Hamamatsu (*ATLAS07*).

interacción de los haces. Sin embargo, no está claro su comportamiento en situaciones extremas en la cual un número muy grande de partículas cargadas atraviesan el detector en un tiempo muy corto, es decir, en un escenario de pérdida de haz que impacta sobre los detectores de silicio. Los siguientes estudios se sitúan en ese escenario y pretenden anticiparse a posibles consideraciones que debieran tomarse en la operación de estos detectores.

Resultados

Para estudiar si los detectores que constituyen el SCT pueden sobrevivir a un escenario de pérdida de haz, se llevaron a cabo simulaciones de un detector microstrip de silicio. Se utilizó el programa de simulación *Synopsys* ISE-TCAD [96]. La estructura simulada corresponde a una unidad básica de un detector, es decir, un strip con los mismos parámetros de diseño que los detectores de silicio del SCT [128] y se puede ver en la figura 10.12. En este caso, corresponde a un detector p^+n.

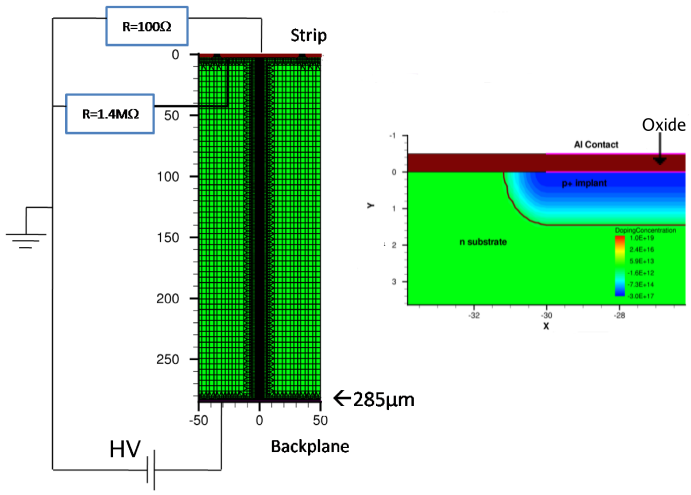

Figure 10.12: Representación de la estructura simulada (izquierda) junto con una imagen más cercana a la unión p-n (derecha).

Del paso de un número muy alto de partículas en un periodo de tiempo muy corto se espera fundamentalmente un estrés eléctrico en el volumen sensible del sensor y su efecto en el óxido (SiO_2) que permite un acoplamiento AC de los dispositivos. En esta situación, un número muy alto de portadores de carga libre en creado y derivan hacia los electrodos p^+ y la cara posterior n^+. El campo eléctrico a través del detector será modificado temporalmente debido a la alta concentración de portadores y evolucionará conforme las cargas deriven. Como consecuencia el voltaje en los implantes p^+ variará y por tanto, el voltage a través del óxido.

Varias densidades de carga altas fueron simuladas a lo largo del grosor del detector y éste fue llevado a 500 V (voltaje máximo posible para los detectores de silicio del SCT). Se observó que a partir del orden de 10^5 *mips* por strip, el voltage en el implante p^+ se satura situándose en 500 V en un tiempo aproximado de 0.3 *ns* y se puede leer en el contacto de aluminio un voltaje inducido del orden de 3 V. Ésto supone una alta diferencia de potencial a través del óxido mientras se van drenando el alto número de portadores de carga que pudiera dar lugar a su ruptura. A través de las resistencias de polisilicio, este drenaje daría lugar a una corriente muy alta del orden de 0.5 *A* que supera los límites de corriente del sistema de alimentación de los detectores. Sin embargo, los detectores fueron diseñados con una estructura de protección para estos casos. Se trata de la estructura PTP (*punch-through protection*) y actúa como una

Table 10.7: Voltaje máximo en el implante con la resistencia de polisilicio y la resistencia de la PTP para diferenctes densidade de carga. Voltaje de alimentación = 500 V.

Densidad de carga ($pC/\mu m$)	# *mips* (por strip)	Voltaje$_{implante}$ Max. (V) R_{polysi}=1.4 $M\Omega$	Voltaje$_{implante}$ Max. (V) R_{PTP}=5 $K\Omega$
8×10^{-4}	60	27.4	3.5
0.01	740	125.3	5.7
0.1	7400	367.7	35
0.2	15 000	441.0	54
1	74 000	498.5	121
2	148 000	499.1	159
3	222 000	499.5	179
5	370 000	499.5	207
7	520 000	499.7	226
10	740 000	499.7	244
20	1.5M	500.0	274
100	7.4M	500.0	354
850	63M	500.0	437
1000	74M	500.0	442

resistencia dinámica dependiendo del voltage aplicado entre los terminales.

El funcionamiento de la estructura PTP fue verificada a partir de medidas con detectores reales. Se usaron muestras de sobra de sensores utilizados para conformar módulos del SCT. A partir de medidas de corriente en función del voltaje aplicado entre el implante p^+ y el contacto de aluminio para strips concretos, se obtuvo lo siguiente:

- La estructura PTP se activa alrededor de 13-16 V.
- La resistencia del PTP cae hasta alrededor de 5 $K\Omega$ permitiendo que el detector se descargue a través de ella.

También se demostró y junto a referencias previas [140] que el óxido permanece protegido hasta al menos 160-170 V. La siguiente pregunta es la dosis a la cual el voltaje en el implante alcanza estos voltajes con la PTP activada. Para responder a esta pregunta, se hicieron simulaciones de altas densidades de carga a través de nuestro detector de silicio con una resistencia de 5 $K\Omega$. A partir de estas simulaciones, se estableció que la estructura PTP evita una acumulación de carga en el implante p^+ hasta una dosis sobre 150 000 *mips* por strip, que es cuando el implante alcanza un voltaje de ~ 160 V. Estos datos se pueden ver en la tabla 10.7.

10.4 Conclusiones

Esta tesis está enmarcada en el experimento ATLAS del acelerador LHC del CERN. Concretamente, para la fase II de operación del acelerador. Se estudió el gran potencial de física que

supone un aumento de casi un orden de magnitud en luminosidad del acelerador, pasando del actual valor instantáneo de $10^{34}\ cm^{-2}\ s^{-1}$ a un valor de $5\times10^{34}\ cm^{-2}\ s^{-1}$. A este proyecto se le conoce con el nombre de HL-LHC (*High Luminosity LHC*). Operar en tales condiciones de luminosidad implica procesos de apilamiento de datos debido al aumento de la tasa de interacción, pasando del orden de 20 colisiones por cruce de haces a 200 colisiones. Por otro lado, también suponen muy altas dosis de radiación sobre los detectores llegando a flujos de $10^{16}\ n_{eq}\ cm^{-2}$ en los más próximos al punto de colisión de las partículas. La tecnología actual presente en los experimentos del LHC no soportaría tales condiciones. Es por ello, que particularmente para el detector interno de ATLAS se hace obligatorio nuevas investigaciones en el campo de los detectores de silicio. El nuevo detector interno de ATLAS previsto para esta fase II pretende ser completamente de silicio y con un aumento de canales respecto al actual para evitar efectos de apilamiento de eventos. Esta tesis está enfocada en la parte del detector interno de ATLAS de detectores de microstrips, situados a una distancia entre 38-100 cm del punto de colisión de los haces.

Desde hace ya unos años se está desarrollando una tecnología de detectores de silicio resistentes a mayores dosis de radiación, como las que se esperan en el HL-LHC. Las excelentes propiedades que vienen mostrando los detectores n^+p con respecto a los actuales p^+n, hacen de ellos una opción muy adecuada para estos grandes experimentos. De hecho, esta tecnología es la línea escogida como base de estos detectores, si bien, se necesita optimizar la estructura del detector.

En la primera parte de esta tesis se ha estudiado diferentes tipos de detectores de silicio n^+p procesados por diferentes centros (CNM-Barcelona y Hamamatsu Photonics-Japón). Estos detectores fueron irradiados con flujos de partículas a las dosis esperadas en HL-LHC. Se estudiaron los efectos de la radiación sobre los detectores principalmente en términos de su eficiencia de recolección de carga, la cual disminuye cuanto más irradiado esté el detector. El diseño de los detectores, por tanto, debe ser tal que puedan funcionar con señales reducidas y operar a los voltajes necesarios que proporcionen una señal suficiente.

Los detectores del CNM fueron irradiados con neutrones hasta un flujo de $8\times10^{15}\ cm^{-2}$. Se evaluaron detectores con diferentes tipos de sustrato de silicio (FZ, DOFZ y MCz). Estos tres tipos de silicio se basan en diferentes métodos de procesado del cristal de silicio y se diferencian en la concentración de oxígeno que contienen. Se ha demostrado que el oxígeno en el cristal de silicio mejora la resistencia de los detectores a la irradiación con hadrones cargados. Sin embargo, aquí se refleja que la carga recogida por los detectores no viene afectada por el tipo de sustrato y por tanto por la concentración de oxígeno.

Las medidas de carga recogida en función del voltaje aplicado mostraron casi por primera vez valores de carga tan altas como las medidas para un detector similar no irradiado dentro de las incertidumbres para un flujo de $10^{14}\ cm^{-2}$ para silicio MCz y $3\times10^{14}\ cm^{-2}$ para silicio MCz y DOFZ. Efectos de multiplicación de carga están teniendo lugar durante la recolección de carga. Este efecto se ha visto en numerosas medidas similares y siendo más evidente a mayores voltajes. El estudio de este mecanismo en régimen estable abre nuevas posibilidades de operación de estos detectores altamente irradiados.

También se compararon medidas de carga recogida por los detectores n^+p con silicio FZ con detectores n^+n también con silicio FZ. Los detectores n^+n mostraron mejores eficiencias de recolección de carga, si bien, detectores n^+p tienen suficiente recolección de carga requeridas

para los detectores de silicio de microstrips para condiciones de alta luminosidad. Los detectores n^+n se comportan muy bien bajo irradiación, pero esta tecnología requiere procesado a doble cara porque la unión p-n comienza a crecer desde la cara posterior, lo que la encarece. Es por ésto por lo que se prefiere la tecnología n^+p para la región de microstrips de ATLAS.

Los detectores con silicio FZ mostraron microdescargas durante las medidas de carga recogida en función del voltaje aplicado. Este efecto representa uno de los principales mecanismos de fallo en la operación de los detectores. Limita la toma de medidas y pueden llegar a dañar el detector e incluso su electrónica asociada ya que su intensidad aumenta con el voltaje aplicado. La causa más probable para este efecto tiene que ver el aislamiento entre strips. Los detectores con implantes n^+ requieren técnicas de aislamiento entre ellos para evitar que los canales se cortocircuiten. Estas técnicas requieren implantes de tipo p a una determinada dosis. Los detectores del CNM medidos tienen un aislamiento p-spray. El alto gradiente de dopaje entre estas zonas puede dar lugar a regiones de intenso campo eléctrico y como consecuencia microdescargas. Además se ha observado que estas microdescargas aparecen a voltajes más bajos para detectores no irradiados y este voltaje va aumentando a mayor irradiación, lo que muestra que la dosis del p-spray es moderada como efecto de la radiación.

Los siguientes detectores considerados son los provistos por Hamamatsu Photonics. En este caso, se evaluó los efectos de la radiación tanto de protones como de neutrones a diferentes flujos hasta 10^{15} cm^{-2}. Se disponía de detectores con aislamiento p-stop y p-stop+p-spray. Estos detectores mostraron un excelente comportamiento en términos de carga recogida y de aislamiento entre los strips. Sin embargo, estos detectores con silicio FZ también mostraron microdescargas. Investigaciones llevadas a cabo por Hamamatsu Photonics condujo a que estas microdescargas eran debidas al diseño asimétrico del p-stop utilizado para aislar los strips, que fue convenientemente corregido en posteriores procesados de detectores.

Comparando ambos tipos de detectores a la dosis esperada en la región de strips para el nuevo detector interno (representado en la figura 10.13) se muestra que ambos tipos de detectores tienen la suficiente eficiencia de recolección de carga para las condiciones del HL-LHC. Se dispone por tanto, de una tecnología de detectores que cumple con los requisitos necesarios para que el nuevo detector interno de ATLAS pueda operar en condiciones de luminosidad del HL-LHC.

También se observa que el silicio FZ es ligeramente superior en estos términos, sin embargo, la presencia de microdescargas con este tipo de sustrato hace necesaria una mayor investigación sobre los parámetros de diseño de estos detectores. Esta tesis pone de manifiesto como una adecuada decisión de los parámetros de diseño son esenciales para un correcto funcionamiento del detector: Una dosis adecuada de p-spray o una correcta geometría del p-stop.

Finalmente en esta tesis, se ha contribuido al actual funcionamiento del SCT de ATLAS. Se ha estudiado un posible escenario de pérdida de haz que impactara directamente sobre los detectores de silicio p^+n del actual SCT. Se ha simulado un dispositivo de silicio con las mismas características y se ha expuesto a altas densidades de carga. Se ha demostrado que el campo eléctrico es alterado y esta modificación supone una acumulación alta de carga en el implante p^+ y por tanto, un considerable riesgo de romper el óxido. Para proteger el óxido, estos detectores llevan en su diseño una estructura (PTP por sus siglas en inglés) que previene estas acumulaciones permitiendo una rápida descarga del sensor. Estos estudios permitieron establecer 150 000 mips por strip como límite para no romper el óxido.

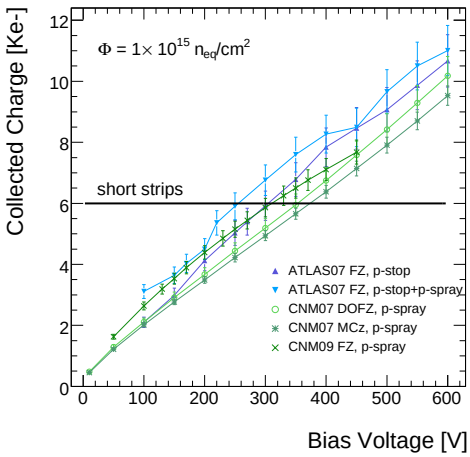

Figure 10.13: Carga recogida en función del voltaje aplicado para detectores de silicio n^{+}p. Detectores *ATLAS07* de Hamamatsu (en azul) y detectores CNM (en verde) son comparados. El límite establecido para la región short strips del detector interno de ATLAS como adecuado (6000 electrones a 500 V) es marcado como referencia.

Appendices

Appendix A

Silicon Properties and Fundamental Constants

A.1 Silicon Properties

Quantity	Value
Atomic concentration at 300 K	$5 \times 10^{22}\ cm^{-3}$
Atomic Weight	$28.086\ g/mol$
Density	$2.328\ g/cm^3$
Crystal structure	Diamond
Lattice constant at 300K	5.43095 Å
Dielectric constant	11.9
Energy gap at 300K	$1.12\ eV$
E (e-h pair)	$3.6\ eV$
Breakdown Field approx.	3×10^5
electron Mobility at 300 K and at low fields $E < 10^3\ V/cm$	$1350\ cm^2/Vs$
hole Mobility at 300 K and at low fields $E < 10^3\ V/cm$	$480\ cm^2/Vs$
electron Diffusion coefficient at 300 K	$\leq 36\ cm^2/s$
hole Diffusion coefficient at 300 K	$\leq 12\ cm^2/s$

Table A.1: Basic properties of silicon.

A.2 Fundamental constants

Quantity	Symbol	Value
Boltzmann constant	κ_B	$1.380\,6504(24) \times 10^{-23}\ J\ K^{-1}$
		$= 8.617\,343(15) \times 10^{-5}\ eV\ K^{-1}$
Elementary charge	q_0	$1.602\,176\,487(40) \times 10^{-19}\ C$
Electron rest mass	m_0	$0.510\,998\,910(13)\ MeV/c^2$
		$= 9.109\,382\,15(45) \times 10^{-31}\ kg$
Permittivity of the vacuum	ε_0	$8.854\,187\,817 \times 10^{-12}\ F\ m^{-1}$
Plank constant	h	$6.626\,068\,96(33) \times 10^{-34}\ J\ s$
Avogadro Constant	N_A	$6.022 \times 10^{23}\ atoms/mole$
Speed light in vacuum	c	$299\,792\,458\ ms^{-1}$

Table A.2: Fundamental constants as recommended by the CODATA Task Group (CODATA = Committee on Data for Science and Technology) [144].

Appendix B

Sentaurus device command file

An example of a complete command file for Sentaurus Device is presented (< $filename$ >_*des.cmd*). Each statement section is explained indivudually.

∗ Having loaded the device structure in Sentarus Device, it is necessary to specify which of the contacts are to be treated as electrodes. Electrodes in Sentaurus Device are defined by electrical boundary conditions and contain no mesh. Any contacts that are not defined as electrodes are ignored by Sentaurus Device. In this example the simulation starts off with no bias applied to the detector.

Electrode {
{*Name* = ”*backplane*” *Voltage* = 0.0 *Material* = ”*Aluminum*”}
{*Name* = ”$strip_1$” *Voltage* = 0.0 *Material* = ”*Aluminum*”}
{*Name* = ”$strip_2$” *Voltage* = 0.0 *Material* = ”*Aluminum*”}
{*Name* = ”$strip_3$” *Voltage* = 0.0 *Material* = ”*Aluminum*”}
}

∗ This sections gives the names of the mesh grid and doping files, and the output files you want to create.

File {

∗ input files:
Grid = ” < $filename$ > _*msh.grd*” ∗ this file defines the mesh and contacts
Doping = ” < $filename$ > _*msh.dat*” ∗ this file defines the doping profile data for the device structure)

∗ output files:
Current = ” < $filename$ > _*des.plt*” ∗ this is the file name for the final spatial solution variables

on the structure mesh
Plot = ” < $filename$ > $\_des.dat$” ∗ this is the file name for electrical ouput data, such as currents, voltages... at electrodes
Output = ” < $filename$ > $\_des.log$” ∗ this is the file name for the output log that is automatically created whenever Sentaurus Device is run
}

∗ This section allows a selection of the physical models to be applied in the device simulation.

Physics {

∗ standard physics models
Temperature= 300
Mobility(DopingDep Enormal HighFieldSaturation)
Recombination(SRH(DopingDep) Avalanche(ElectricField))
EffectiveIntrinsicDensity(Slotboom) }

∗ HeavyIon statement creates a particle track, with $80e^-/\mu m$ charge generated (i.e. $1.282 \times 10^{-5} pC/\mu m$), arriving at the device. Length is distance along track, wt_hi is the width of the Gaussian describing the track profile, and LET_f is the charge per μm. The impinging time is set to $0.02ns$.

HeavyIon (
Direction= $(0, 1)$
Location= $(100, 0)$
Time= $0.02e-9$
Length= [0 0.001 300 300.001]
wt_hi= [1.0 1.0 1.0 1.0]
LET_f= [0 $1.282E-5$ $1.282E-5$ 0]
Gaussian
Picocoulomb)
}

∗ It is possible to define different physical models for different regions and materials within a device structure. In this example a positive charge has been defined at the Oxide/silicon interface.

Physics(MaterialInterface= ”$Oxide/Silicon$”) {
Charge($Conc = 4e11$)
Recombination(surfaceSRH)
}

∗For radiation damage simulations, it is necessary to define a set of defects in silicon region.
Physics(Material= ”$Silicon$”) {
Traps(

(Acceptor Level fromCondBand Conc= @ < *Fluence* ∗ 1.613 > @ EnergyMid=0.42 eXsection= hXsection=)
(Acceptor Level fromCondBand Conc= @ < *Fluence* ∗ 0.9 > @ EnergyMid=0.46 eXsection= hXsection=)
(Donor Level fromValBand Conc= @ < *Fluence* ∗ 0.9 > @ EnergyMid=0.36 eXsection= hXsection=)
)
}

∗ The plot section specifies all the solution variables that are saved in the output plot files.

Plot {
Potential ElectricField Doping
Space Charge
eDensity hDensity eCurrent/Vector hCurrent/Vector
eMobility hMobility
eVelocity hVelocity
HeavyIonChargeDensity
}

∗ The CurrentPlot section is used to include selected mesh data into the current plot file (.plt).

CurrentPlot {

∗ Find the maximum electric field strength in the silicon
ElectricField(Maximum(*Material = "Silicon"*))
}

∗ Sentaurus Device solves the device equations (which are essentially a set of partial differential equations) self-consistently, on the discrete mesh, in an iterative fashion. For each iteration, an error is calculated and Sentaurus Device attempts to converge on a solution that has an acceptably small error. This example shows fairly standard math options. Many of these options are now default in Synopsys. The examples in the Sentaurus Device manual are a good guide [106].

Math {
Digits=5 ∗ it approximates the number of digits of accuracy to which an equation must be solved before being considered to have converged
Iterations=100 ∗ it specifies the maximum number of Newton iterations allowed per bias step
Method=Blocked ∗ it selects the linear solver to be used in the differential equations
Submethod=Pardiso
∗ A few standard options to control solving method:
Extrapolate
Derivatives
RelErrControl

}

∗ The solve section defines a sequence of solutions to be obtained by the solver.

Solve {
∗ Get initial state of the device without a bias applied (defined in the Electrode section)

Poisson

∗ The second step introduces the continuity equations for electrons and holes, with the initial bias conditions applied. In this case, the electron and hole current continuity equations are solved fully coupled to the Poisson equation, taking the solution from the previous step as the initial guess. The coupled command is based on a Newton solver. This is an iterative algorithm in which a linear system is solved at each step simulation.

Coupled{ Poisson electron hole }

∗ Internally, the Quasistationary ramp is controlled by a variable sweeping from 0 to 1. So, the max step corresponds to $0.05 * 100V = 2.5V$. The "$iterations = 8$" means that if we take more than 8 iterations to solve a step, it'll reduce the step size and try again.

Quasistationary (
InitialStep= $0.5e-3$ MaxStep= 0.05 Minstep= $1e-6$ Increment= 1.2
Goal {Voltage= -100 Name= *backplane* })
{
Coupled (iterations= 8, notdamped= 15) {Poisson electron hole}
}

∗ A simulation over time, to get the current signal produced by the MIP needs the Transient command.

Transient(
InitialTime= 0.0
FinalTime= $25.0e-9$
InitialStep= $0.25E-11$
MaxStep= $1e-9$
Increment= 1.1)
{
Coupled (iterations= 8, notdamped= 15) { Poisson Electron Hole }
}

}

∗ The next < *name* > *_des.cmd* file ilustrates a Mixed-Mode simulation. In this simulation, a 2D silicon device (defined as "sensor" is combined with a voltage source and two resistors to form a silicon module circuit.
∗ The sequence of command sections is different when comparing mixed-mode to single-device simulation. For mixed-mode simulations, the physical devices are defined in separate Device statement sections. Inside the Device statement, the Electrode, Physics, and most of the File sections are defined in the same way as in command files for single device simulations.

Device sensor {

Electrode {
{*Name* = "*nplus*1" *Voltage* = 0.0 *Material* = "*Aluminum*"}
{*Name* = "*pplus*2" *Voltage* = 0.0 *Material* = "*Aluminum*"}
{*Name* = "*implant*2" *Voltage* = 0.0}
}

File {
Grid = " < *filename* > *_msh.grd*"
Doping = " < *filename* > *_msh.dat*"
Current = " < *filename* > *_des.plt*"
Plot = " < *filename* > *_des.dat*"
}

Physics {
Temperature= 300
Mobility(DopingDep HighFieldSaturation Enormal)
Recombination(SRH(DopingDep))
EffectiveIntrinsicDensity(Slotboom)

HeavyIon (
Direction= (0, 1)
Location= (0, 0)
Time= $0.02e-9$ Length= [0 0.001 285 285.001]
wt_hi= [1.0 1.0 1.0 1.0]
LET_f= [0 $1.282E-5$ $1.282E-5$ 0]
Gaussian
Picocoulomb)
}

Physics(MaterialInterface= "*Oxide*/*Silicon*") {
Charge(*Conc* = 4*e*11)
}

Plot {
eDensity hDensity eCurrent/Vector hCurrent/Vector Potential
SpaceCharge ElectricField Doping
HeavyIonCharge HeavyIonChargeDensity
eVelocity hVelocity eMobility hMobility
}

Math {

Submethod=Pardiso

}

∗ End of ”sensor” device definition

}

∗ Global statements for all the circuit

Math {
Digits=5
Iterations=100
Method=Blocked
Extrapolate
Derivatives
RelErrControl
}

File{

Output = ” $< filename >$ *_des.log*”

}

∗ The circuit is defined in the System section, which uses a SPICE syntax.

System {

Vsource_pset vcp (cp 0) {dc=0}
∗ A voltage source is connected between the node ”*cp*” and ground node (0)

sensor diode (nplus1=cp implant2=i2 pplus2=c2)
∗ The previous defined device named *sensor* is instantiated with a tag diode. Each of its electrodes is connected to a circuit node.

Resistor_pset r (i2 0) resistance=1e6
∗ A resistor is connected between the node "*i*2" and the ground node (0)

Resistor_pset ram (c2 0) resistance=100
∗ A resistor is connected between the node "*c*2" and the ground node (0)

}

Solve {
Poisson
CoupledPoisson Electron Hole

Quasistationary (
InitialStep= 0.5*e* − 3 MaxStep= 0.05 Minstep= 1*e* − 6 Increment= 1.2
Goal {Parameter= *vcp.dc* Value= 100})
{
Coupled (iterations=8, notdamped=15) {Poisson} }

Transient(
InitialTime = 0.0
FinalTime= 15.0*e* − 9
InitialStep= 0.25*E* − 11
MaxStep= 1*e* − 9
Increment= 1.1
)
{Coupled (iterations=8, notdamped=15) { Poisson Electron Hole } }
}

Bibliography

[1] D. Perkins. *Introduction to High Energy Physics. Cambridge University Press, 4th edition*, 2000.

[2] C. Mariotti. *Search of the Standard Model Higgs at LEP*. *Nuclear Physics B - Proceedings Supplements*, 117:202–205, 2004.

[3] S. Weinberg. *A model of leptons*. *Phys. Rev. Lett.*, 19:1264–1266, 1967.

[4] P.W. Higgs. *Broken symmetries, Massless Particles and Gauge Fields*. *Phys. Rev. Lett. 12, 132-133*, 1964.

[5] P.W. Higgs. *Broken symmetries and the Masses of Gauge Bosons*. *Phys. Rev. Lett. 13, 508-509*, 1964.

[6] T. Hambye, K. Riesselmann. *Matching conditions and Higgs mass upper bounds revisited*. *Phy.Rev. D55*, pages 7255–7262, 1997.

[7] The LEP Collaborations ALEPH, DELPHI, L3, OPAL, the LEP Electroweak Working Group, the SLD Electroweak, and Heavy Flavour Groups. *A combination of preliminary electroweak measurements and constraints on the Standard Model*. *CERN-PH-EP/2006-042, LEPEWWWG/2006-01, ALEPH PHYSICS 2006-001, DELPHI 2006-014 PHYS 948, L3 Note 2833, OPAL PR 419, 2006. arXiv:hep-ex/0612034*, 2006.

[8] The CDF, D0 Collaborations, the TEVNPHWG Working Group. *Combined CDF and D0 Upper Limits on Standard Model Higgs Boson Production with up to* 8.2 fb^{-1} *of Data*. *arXiv:1103.3233[hep-ex]*, 2011.

[9] M.B. Popovic. *Upper limit on the Higgs Particle mass*. *arXiv:hep-ph/0106355*, 2008.

[10] S. Asai et al. *Prospects for the Search for a Standard Model Higgs Boson in ATLAS using Vector Boson Fusion*. *arXivv:hep-ph/0402254*. *Eur. Phy. J. C32S2* , pages 19–54, 2004.

[11] H. Georgi, S.L. Glashow. *Unity of All Elementary-Particle Forces*. *Phys. Rev. Lett.*, 32:438–441, 1974.

[12] D.I. Kazakov. *Beyond the Standard Model (In Search of Supersymmetry)*. *arXiv:hep-ph/0012288*, 2001.

[13] E. Komatsu et al.[WMAP Collaboration]. *Five-year Wilkinson Microwave Anisotropy Probe (WMAP) Observations: Cosmological Interpretation*. *arXiv:astro-ph/0803.0547]. Astrophys. J.Suppl. 180*, pages 330–376, 2009.

[14] G.C. Branco, P.M. Ferrerira, L. Lavoura, M.N. Rebelo, M. Sher and J.P. Silva. *Theory and phenomenology of two Higgs doublet models*. *arXiv:1106.0034 [hep-ph]*, 2011.

[15] S.P. Martin. *A supersymmetry Primer*. *hep-ph/9709356*, 1997.

[16] I. Antoniadis et al. *Direct collider signatures of large extra-dimensions*. *arXiv:hep-ph/9905311*. *Phys. Lett. B460*, pages 176–183, 1999.

[17] N. Brett at al. *Black hole production at the LHC: the Discovery reach of the ATLAS experiment*. *ATL-PHYS-INT-2007*, 2008.

[18] The LHC Study Group. *The Large Hadron Collider: Conceptual Design*. *CERN/AC/95-05(LHC)*, 1995.

[19] Lyndon Evans, Philip Bryant. *LHC Machine*. *JINST 3 S08001*, 2008.

[20] ATLAS Collaboration. *ATLAS: technical proposal for a general purpose pp experiment at the Large Hadron Collider at CERN*. *CERN-LHCC-94-43*, 1994.

[21] CMS Collaboration. *CMS technical proposal*. *CERN-LHCC-94-38*, 1994.

[22] LHCb Collaboration. *LHCb technical proposal*. *CERN-LHCC-98-004*, 1998.

[23] TOTEM Collaboration. *TOTEM, Total cross section, elastic scattering and diffractive dissociation at the LHC: Technical Proposal*. *CERN-LHCC-99-007*, 1999.

[24] ALICE Collaboration. *ALICE: Technical proposal for a Large Ion Collider Experiment at the CERN LHC*. *CERN-LHCC-95-71*, 1995.

[25] G. Aad et al.[ATLAS Collaboration]. *The ATLAS Experiment at the CERN Large Hadron Collider*. *JINST 3 S08003*, 2008.

[26] CMS Collaboration. *The CMS Experiment at the CERN LHC*. *JINST 3 S08004*, 2008.

[27] LHCb Collaboration. *The LHCb Detector at the LHC*. *JINST 3 S08005*, 2008.

[28] ALICE Collaboration. *The ALICE experiment at the CERN LHC*. *JINST 3 S08002*, 2008.

[29] G. Gorfine. *Tracking performance of the ATLAS pixel detector in the 2004 Combined Test Beam*. *Nucl. Instr. and Meth. A 565, 43-49*, 2006.

[30] A. Abdesselan et al. *The Barrel Modules of the ATLAS SemiConductor Tracker*. *Nucl. Instr. and Meth. A 568, 642-671*, 2006.

[31] A. Abdesselan et al. *The ATLAS SemiConductor tracker end-cap module*. *Nucl. Instr. and Meth. A 575, 353-389*, 2007.

[32] B. Dolgoshein. *Transition radiation detectors*. *Nucl. Instr. and Meth. A 326, 434-469*, 1993.

[33] T. Akesson et al. *Status of design and construction of the Transition Radiation Tracker (TRT) for the ATLAS experiment at the LHC*. *Nucl. Instr. and Meth. A 522, 131-145*, 2004.

[34] S. Baranov et al. *Estimation of Radiation Background, Impact of Detectors, Activation and Shielding Optimization in ATLAS*. *ATLAS-GEN-2005-001*, 2005.

[35] Academic training. *The LHC machine experiment interface*. *CERN*, April, 2005.

[36] F. Gianotti et al. *Physics potential and experimental challenges of the LHC luminosity upgrade*. *Eur. Phys. J.*, C39:293-33, 2005.

[37] J.R. Ellis. *Particle Physics at Furture Colliders*. *ArXiv:hep-ex*, 0210052, 2002.

[38] G. Azuelos et al. *Impact of energy and luminosity upgrades at LHC on the physics programme of ATLAS*. *J. Phys. G: Nucl.Part.Phys.*, 28:2453–2474, 2002.

[39] A. De Roeck, J.R. Ellis, and F. Gianotti. *Physics Motivations for future cern accelerators*. *CERN-TH-2001-023*, arXiv:hep-ex/0112004, 2001.

[40] K. Nagano. *ATLAS upgrade for the super LHC - Meeting the challenges of a ten-fold increase in collisions*. *Nucl. Instr. and Meth. A*, 623:394–396, 2010.

[41] V. Hedberg and M. Shupe. *Radiation and induced activation at high luminosity*. *CERN-ATL-COM-TECH-2004-003*, CERN, 2004.

[42] [Online]. Layout Requirements and Options for a new Inner Tracker for the ATLAS Upgrade. *available from: https://edms.cern.ch/document/809071/2*, 2007.

[43] Summary of the Current Status of Proposal [Online]. [Online]. *available from: http://atlas.web.cern.ch/Atlas/GROUPS/UPGRADES*, 2011.

[44] K.G. McKay. *Electron-Hole Production in Germanium by Alpha-Particles*. *Phys. Rev.*, 84(4):829–832, Nov 1951.

[45] J. Kemmer. *Fabrication of Low Noise Silicon Radiation Detectors by the Planar Process*. *Nucl. Instr. and Meth. A 169, 499*, 169:499–502, 1980.

[46] M. Moll. *Radiation Damage in silicon detector - microscopic defects and macroscopic properties*. PhD thesis, DESY-THESIS-1999-040, 1999.

[47] C. Kittel. *Introduction to Solid State Physics*, volume 8th Edition. John Wiley & Sons, 2005.

[48] W.R. Leo. *Techniques for Nuclear and Particle Physics Experiments*, volume 2nd Edition. Springer-Verlag, 1987.

[49] S.M. Sze. *Physics of Semiconductor Devices*, volume 2nd Edition. Wiley Interscience, 1981.

[50] C. Canali and G. Ottaviani. Saturation values of the electron drift velocity in silicon between 300k and 4.2k. *Physics Letters A*, 32(3):147 – 148, 1970.

[51] G. Lutz. *Semiconductors Radiation Detectors*, volume 2nd Edition. Springer, 1999.

[52] S.M. Sze. *Semiconductor Devices Physics and Technology*. John Wiley & Sons, 1995.

[53] G. Casse, P.P. Allport and A. Greenall. *Response to minimum ionising particles of p-type substrate silicon microstrip detectors irradiated with neutrons to LHC upgrade doses*. *Nucl. Instr. and Meth. A*, 581:318–321, 2007.

[54] G. Pellegrini, C. Fleta, F. Campabadal, M. Miñano, M. Lozano, J.M. Rafí, M. Ullán. *Technology of p-type microstrip detectors with radiation hard p-spray, p-stop and moderated p-spray isolations. Nucl. Instr. and Meth. A 579*, pages 599–603, 2007.

[55] P.P. Allport et al. *Radiation tests of ATLAS full-sized n-in-n prototype detectors*. *Nucl. Instr. and Meth. A*, 418:110–119, 1998.

[56] H. C. Theuerer. U.S patent 3,060. *123*, 1962.

[57] G.Lindströem et al.(The RD48 Collaboration). *Radiation hard silicon detectors - Developments by the RD48 (ROSE) Collaboration*. *Nucl. Instr. and Meth. in Phys. Res. A*, 466:308–326, 2001.

[58] J. Czochralski. *A new method for the measurement of crystallization rate of metals*. *Metalle. Z. Phys. Chem. 92:219*, 1918.

[59] V. Savolainen et al. *Simulation of large-scale silicon melt flow in magnetic Czochralski growth*. *Journal of Crystal Growth*, 243:243–260, 2002.

[60] Y. Unno et al. *Novel p-stop structure in n-side of silicon microstrip detector*. *Nucl. Instr. and Meth. A*, 541:40–46, 2005.

[61] Y. Unno et al. *Optimization of surface structures in n-in-p silicon sensors using TCAD simulation*. *Nucl. Instr. and Meth. A*, 636:118–124, 2011.

[62] G. Pellegrini,C. Fleta, F. Campabadal, S. Díez, M. Lozano, J.M. Rafí, M. Ullán. *Technology development of p-type microstrip detectors with radiation hard p-spray isolation*. *Nucl. Instr. and Meth. A 566, 360-365*, 2006.

[63] H. Spieler. *Semiconductor Detector Systems*. Oxford University Press, 2006.

[64] G.F. Knoll. *Radiation Detection and Measurement*, volume 3rd Edition. John Wiley & Sons, 2000.

[65] W. Shockley. *Currents to conductors induced by a moving point charge*. *J. Appl. Phys. 9, 635*, 1938.

[66] S. Ramo. *Currents induced by electron motion*. *Proceedings of the IRE, 27:584*, 1939.

[67] A. Peisert. *Silicon microstrip detectors*, volume Instrumentation on High Energy Physics. ed. F. Sauli, 1992.

[68] V.A.J. van Lint et al. *The Physics of radiation damage in particle detectors*. *Nucl. Instr. and Meth. A*, 253:453–459, 1987.

[69] J. W. Corbett and G. D. Watkins. *Production of Divacancies and Vacancies by Electron Irradiation of Silicon*. *Phys. Rev.*, 138(2A):A555–A560, Apr 1965.

[70] D.V. Lang. *Deep-level transient spectroscopy: A new method to characterize traps in semiconductors*. *J. Appl. Phys. 45, p.3023*, 1974.

[71] Wodean Project. Workshop on Defect Analysis in Silicon Detectors. *NIMP, Bucharest, 13-14, May*, 2010.

[72] G. Lindström. *Radiation Damage in Silicon Detectors*. *Nucl. Instr. and Meth. A*, 512:30–43, 2003.

[73] A.Vasilescu (INPE Bucharest) and G.Lindströem (University of Hamburg). *Displacement damage in Silicon on-line compilation*. *http://sesam.desy.de/members/gunnar/Si-dfuncs.html*, 2000.

[74] ROSE Collaboration. *Notes on the fluence normalization based on the NIEL scaling hypothesis*. *Technical Note ROSE/TN/2000-02, CERN*, 2000.

[75] M. Moll, E. Fretwurst, M. Kuhnke, G. Lindström. *Relation between microscopic defects and macroscopic changes in silicon detector properties after hadron irradiation*. *Nucl. Instr. and Meth. B 186*, pages 100–110, 2002.

[76] D. Zontar, V.Cindro et al. *Time development and flux dependence of neutron-irradiation induced defects in silicon pad detectors*. *Nucl. Instr. and Meth. A*, 426:51–55, 1999.

[77] Y. Unno et al. *p-Bulk silicon microstrip sensors and irradiation*. *Nucl. Instr. and Meth. A*, 579:614–622, 2007.

[78] The ROSE Collaboration. CERN-RD48 Collaboration. *http://rd48.web.cern.ch/RD48*, 1996.

[79] G. Casse et al. *Introduction of high oxygen concentrations into silicon wafers by high temperature diffusion*. *Nucl. Instr. and Meth. A*, 438:429–432, 1999.

[80] M.S. Alam et al. *The ATLAS silicon pixel sensors*. *Nucl. Instr. and Meth. A*, 456:217–232, 2001.

[81] R. Wunstorf et al. *Damage-induced surface effects in silicon detectors*. *Nucl. Instr. and Meth. A*, 377:290–297, 1996.

[82] R. Wunstorf, T. Rohe and A. Rolf. *Simulation of irradiation-induced surface effects in silicon detectors*. *Nucl. Instr. and Meth. A*, 388:308–313, 1997.

[83] M.Moll, E.Frewurst, G.Lindstroem. *Leakage current of hadron irradiated silicon detectors - material dependence*. *Nucl. Instr. and Meth. A*, 426:87–93, 1999.

[84] G. Lindström, M. Moll, E. Fretwurst, . *Radiation Hardness of silicon detectors. A challenge from High-Energy Physics*. *Nucl. Instr. and Meth. A 426*, pages 1–15, 1999.

[85] R. Wunstorf. *Ph.D. Thesis*. *Universitat Hamburg, DESY*, FHIK9201, 1992.

[86] M. Moll, E. Fretwurst, G. Lindström. *Investigation on the improved radiation hardness of silicon detectors with high oxygen concentration*. *Nucl. Instr. and Meth. A*, 439:282–292, 2000.

[87] G. Casse. *Prediction of the performances of finely segmented Si detector for tracking applications in future supercolliders after severe radiation damage*. *Nucl. Instr. and Meth. A*, 566, 2006.

[88] R. Wunstorf, W.M. Bugg, J. Walter, F.W. Garber, D. Larson. *Investigations of donor and acceptor removal and long term annealing in silicon with different boron/phosphorus*. *Nucl. Instr. and Meth. A*, 377:228–233, 1996.

[89] RD48 Collaboration. *Investigation on the improved radiation hardness of silicon detectors with high oxygen concentration*. *CERN/LHCC, LEB Status Report/RD 48*, 2000-009, 1999.

[90] V. Cindro, G. Kramberger, M. Lozano, I. Mandic, M. Mikuz, G. Pellegrini et al. *Trapping of electrons and holes in p-type silicon irradiated with neutrons*. *IEEE Nuclear Science Symposium*, 1:139-142, 2006.

[91] G. Kramberger, V. Cindro, I. Mandic, M. Mikuz and M. Zavrtanik. *Effective trapping time of electrons and holes in different silicon materials irradiated with neutrons, protons and pions*. *Nucl. Instr. and Meth.A*, 481:297–305, 2002.

[92] G. Casse et al. *First results on charge collection efficiency of heavily irradiated microstrip sensors fabricated on oxygenated p-type silicon*. *Nucl. Instr. and Meth. A, 518, 340*, 518:340–342, 2005.

[93] M. Lozano et al. *Comparison of radiation hardness of P-in-N, N-in-N, and N-in-P silicon pad detectors*. *IEEE Transactions on Nuclear Science*, 52-5, 2005.

[94] G. Casse, P.P. Allport and M. Hanlon. *Improving the radiation hardness properties of silicon detectors using oxygenated n-type and p-type silicon*. *IEEE Transactions on Nuclear Science*, 47-3, 2000.

[95] M. Moll et al. *Recent advances in the development of radiation tolerant silicon detectors for the super-LHC*. *Proc. Astroparticle, Particle and Space Physics Detectors and Medical Physics Applications*, 5:110–110, 2010.

[96] *Synopsis Inc.* available from: http://www.synopsis.com/products/tcad/tcad.html, 2007.

[97] W. Fichtner, D.J. Rose and R.E. Bank. *Semiconductor device simulation*. *IEEE Trans. Electron. Dev.*, 30(9), 1983.

[98] M.N.O. Sadiku. *A simple introduction to finite-element analysis of electromagnetic problems*. *IEEE Transactions on Education*, 32(2), 1989.

[99] R.E. Bank and D.J. Rose. *Global approximate Newton methods*. *Numerische Mathematik*, 37(2) p.279, 1981.

[100] J.W.Slotboom. *The pn-Product in Silicon*. *Solid State Electronics*, 20, 1997.

[101] D.J. Roulston, N.D. Arora, S.G. Chamberlain. *Modeling and Measurement of minority-carrier Lifetime versus doping in Diffused layers of n+-p Silicon Diodes*. *IEEE Transactions on Electron Devices*, ED-29-2, 1982.

[102] Siegfried Selberherr. *Analysis and Simulation of Semiconductor Devices. Wien*, 1984.

[103] J.G. Masseti, M. Severi, S. Solmi. *Modeling of Carrier Mobility Against Carrier Concentration in Arsenic-, Phosphorus-, and Boron-Doped Silicon*. *IEEE Transactions on Electron Devices*, ED-30-7 p.764, 1983.

[104] C. Lombardi et al. *A Physically Based Mobility Model for Numerical Simulation of Nonplanar Devices*. *IEEE Transactions on Computer-Aided Design*, 7-11, 1988.

[105] C. Canali et al. *Electron and Hole Drift Velocity Measurements in Silicon and Their Empirical Relation to Electric Field and Temperature*. *IEEE Transactions on Electron Devices*, ED-22-11 p.1045, 1975.

[106] *TCAD Sentaurus Device manuals*. available from: http://www.synopsis.com, 2005. Version X-2005.10.

[107] D. Pennicard et al. *Simulations of radiation-damaged 3D detectors for the Super-LHC*. *Nucl. Instr. and Meth. A*, 592:16–25, 2008.

[108] M. Petasecca, F. Moscatelli, D. Passeri and GU. Pignatel. *Numerical Simulation of Radiation Damage Effects in p-Type and n-Type FZ silicon sensors*. *IEEE Trans. Nucl. Sci.*, NS-53 (5) p.2971, 2006.

[109] M. Ahmed, S.J. Watts, J. Matheson, A. Holmes-Siedle. *Deep Level transient spectroscopy studies of silicon detector after 24GeV proton irradiation and 1MeV neutron irradiation*. *Nucl. Instr. and Meth. A*, 457:588–594, 2001.

[110] V. Cindro et al. Trapping of electrons and holes in p-type silicon irradiated with neutrons. *IEEE Nuclear Science Symposium (San Diego)*, volume 1, 2006.

[111] A. Chilingarov. *IV and CV measurements in Si diodes*. *RD50 Technical Note*, RD50-2003-03, 2004.

[112] N. L. Bruner et al. *Characterization procedures for double-sided silicon microstrip detectors*. *Nucl. Instr. and Meth. A*, 362:315–337, 1995.

[113] S. Löchner and M. Schmelling. *The Beetle Reference Manual*. *LHCb-2005-105*, 2006.

[114] L. Snoj, G. Zerovnik, A. Trkov. *Computational analysis of irradiation facilities at the JSI TRIGA reactor*. *Applied Radiation and Isotopes*, 70:2012, 483–488.

[115] E.S. Kristof. *Characterization of Neutron Flux in the Exposure Channel F19 of the TRIGA Mark II Reactor in Ljubljana*. *Proceedings of Nuclear Energy in Central Europe 98, Terme Catez, Slovenia, September 7-10*, 43-48, 1998.

[116] K. Boren, S. Janos et al. *Charge collection efficiency of irradiated silicon detector operated at cryogenic temperatures*. *Nucl. Instr. and Meth. A*, 440:5–16, 2000.

[117] M. Lozano, C. Fleta, et al. *IMB-CNM and IFIC activities in P-type detectors*. *8th RD50 Workshop on radiation hard semiconductor devices for very high luminosity colliders, Prague*, 25-26 June, 2006.

[118] I. Dawson. *Radiation Background*. *ATLAS Tracker Upgrade Workshop, Genova (Italy)*, July, 2005.

[119] G. Kramberger. *Trapping in Silicon Detectors*. *Workshop on Defect Analysis in Silicon Detectors (WODEAN), Hamburg (Germany)*, August, 2006.

[120] D. Bisello, A.Candelori et al. *Neutron Irradiation Effects on Standard and Oxygenated Silicon Diodes*. *IEEE Trans. Nucl. Sci.*, NS-49:1027–1034, 2002.

[121] G. Casse et al. *Charge Collection Efficiency Measurements for Segmented Silicon Detectors Irradiated to* 1×10^{16} *n cm*$^{-2}$. *IEEE Trans. Nucl. Sci.*, NS-55:1695–1699, 2008.

[122] M.K. Petterson et al. *Determination of the Charge Collection Efficiency in Neutron Irradiated Silicon Detectors*. *IEEE Trans. Nucl. Sci.*, NS-56:3828–3833, 2009.

[123] G. Casse et al. Effects of accelerated annealing on p-type silicon micro-strip detectors after very high doses of proton irradiation. *Nucl. Instr. and Meth. A*, 568:46–50, 2006.

[124] S.M. Sze. *Physics of Semiconductor Devices*. John Wiley & Sons, 2nd edition, 1981.

[125] I. Mandic, V. Cindro, G. Kramberger, M. Mikuz. *Measurement of anomalously high charge collection efficiency in* n^+p *strip detectors irradiated by up to* 10^{16} n_{eq}/cm^2. *Nucl. Instr. and Meth. A*, 603:263–267, 2009.

[126] A. Affolder, P. Allport, G. Casse. *Charge collection efficiencies of planar silicon detectors after reactor neutron and proton doses up to* 1.6×10^{16} n_{eq}/cm^2. *Nucl. Instr. and Meth. A*, 612:470–473, 2010.

[127] G. Casse, A. Affolder, P. Allport, H. Brown, M. Wormald. *Enhanced efficiency of segmented silicon detectors of different thicknesses after proton irradiations up to* 1.6×10^{16} n_{eq}/cm^2. *Nucl. Instr. and Meth. A*, 624:401–404, 2010.

[128] A. Ahmad et al. *The silicon microstrip sensors of the ATLAS semiconductor tracker*. *Nucl. Instr. and Meth. in Physics Research A*, 578:98–118, 2007.

[129] C. Leroy et al. *Study of Charge Collection and Noise in Non-Irradiated and irradiated Silicon Detectors*. *Nucl. Instr. and Meth. A*, 388:289–296, 1997.

[130] Y. Unno. *SLHC upgrade of the ATLAS SCT tracker*. *Nucl. Instr. and Meth. A*, 612:439–447, 2010.

[131] Y. Unno et al. *Development of n-in-p silicon sensors for very high radiation environments*. *Nucl. Instr. and Meth. A*, 636:S24–S30, 2010.

[132] K. Hara et al. *Beam splash effects on ATLAS silicon microstrip detectors evaluated using 1-w Nd:YAG laser*. *Nucl. Instr. and Meth. A*, 541:15–20, 2005.

[133] SCT ATLAS Collaboration. *Technical specification: Supply of Silicon Microstrip Sensors of previous termATLAS07 specification. 7th October*, 2007.

[134] K. Hara et al. *Testing of bulk radiation damage of n-in-p silicon sensors for very high radiation environments. Nucl. Instr. and Meth. A*, 636:83–89, 2011.

[135] G Aad et al. *The ATLAS Experiment at the CERN Large Hadron Collider. Journal of Instrumentation*, 3:S08003, 2008.

[136] A. Abdesselam et al. *The ATLAS semiconductor tracker end-cap module. Nucl. Instr. and Meth. in Physics Research A*, 575:353 – 389, 2007.

[137] F. Campabadal et al. *Beam tests of ATLAS SCT silicon strip detector modules. Nucl. Instr. and Meth. in Physics Research A*, 538:384–407, 2005.

[138] J. E. García. *Caracterización de los Detectores de Silicio del SCT de ATLAS*. Universitat de València, Spain, 2001.

[139] J. Kaplon. *Fast Bipolar and CMOS Rad-Hard Front-End Electronics for Silicon Strip Detectors*. AGH University of Science and Technology, Cracow, Poland, 2004.

[140] D. Robinson. private comunication, 2009.

[141] J. Macdougall. *The ABCD Hybrid Fatal Charge Dosage (HFCD) Experiment. CERN*, page 11, 2009.

[142] D. Robinson et al. *Silicon micro-strip detectors for the ATLAS SCT. Nucl. Instr. and Meth. in Physics Research A*, 485:84, 2002.

[143] Instituto de física corpuscular. Web page: http://ific.uv.es/ silicio/modules/.

[144] E.R. Cohen and B.N. Taylor. *The 1986 CODATA Recommended Values of the Fundamental Physical Constants. Journal of Research of the National Bureau of Standards*, 2:92, 1987.

List of Figures

List of Tables